SLAC-R-964

MEASUREMENT OF THE D_s^- LEPTONIC DECAY CONSTANT f_{D_s} AND OBSERVATION OF NEW RESONANCES DECAYING TO $D^{(*)}\pi$

A DISSERTATION
SUBMITTED TO THE DEPARTMENT OF PHYSICS
AND THE COMMITTEE ON GRADUATE STUDIES
OF STANFORD UNIVERSITY
IN PARTIAL FULFILLMENT OF THE REQUIREMENTS
FOR THE DEGREE OF
DOCTOR OF PHILOSOPHY

Jose Benitez
March 2011

Work supported in part by US Department of Energy contract DE-AC02-76SF00515.

SLAC National Accelerator Laboratory, Menlo Park, CA 94025

I certify that I have read this dissertation and that, in my opinion, it is fully adequate in scope and quality as a dissertation for the degree of Doctor of Philosophy.

(David Leith) Principal Adviser

I certify that I have read this dissertation and that, in my opinion, it is fully adequate in scope and quality as a dissertation for the degree of Doctor of Philosophy.

(Aaron Roodman)

I certify that I have read this dissertation and that, in my opinion, it is fully adequate in scope and quality as a dissertation for the degree of Doctor of Philosophy.

(Michael Peskin)

Approved for the University Committee on Graduate Studies.

Abstract

The absolute branching fractions for the decays $D_s^- \to \ell^- \bar{\nu}_\ell$ ($\ell = e$, μ, or τ) are measured using a data sample corresponding to an integrated luminosity of 521 fb^{-1} collected at center of mass energies near 10.58 GeV with the *BABAR* detector at the PEP-II e^+e^- collider at SLAC. The number of D_s^- mesons is determined by reconstructing the recoiling system $DKX\gamma$ in events of the type $e^+e^- \to DKXD_s^{*-}$, where $D_s^{*-} \to D_s^-\gamma$ and X represents additional pions from fragmentation. The $D_s^- \to \ell^-\nu_\ell$ events are detected by full or partial reconstruction of the recoiling system $DKX\gamma\ell$. The following results are obtained: $\mathcal{B}(D_s^- \to \mu^-\nu) = (6.02 \pm 0.38 \pm 0.34) \times 10^{-3}$, $\mathcal{B}(D_s^- \to \tau^-\nu) = (5.00 \pm 0.35 \pm 0.49) \times 10^{-2}$, and $\mathcal{B}(D_s^- \to e^-\nu) < 2.8 \times 10^{-4}$ at 90% C.L., where the first uncertainty is statistical and the second is systematic. The branching fraction measurements are combined to determine the D_s^- decay constant $f_{D_s} = (258.6 \pm 6.4 \pm 7.5)$ MeV.

In addition, a study has been performed of the $D^+\pi^-$, $D^0\pi^+$, and $D^{*+}\pi^-$ systems in inclusive $e^+e^- \to c\bar{c}$ interactions in a search for excited D meson states. The dataset used consists of $\sim$454 fb^{-1}. The mass spectra for these systems show, for the first time, candidates for the radial excitations of the D^0, D^{*0}, and D^{*+}, as well as the $L = 2$ excited states of the D^0 and D^+, where L is the orbital angular momentum of the quarks.

Finally, a prototype of a next generation Detector of Internally Reflected Cherenkov radiation (Focusing DIRC) has been tested using a 10 GeV electron beam at SLAC. The Focusing DIRC is based on the DIRC which was used in the *BABAR* detector, but has new pixel photon detectors which improve the resolution on the single photon time of propagation by about an order of magnitude allowing, for the first time, to correct the chromatic smearing in the Cherenkov angle. The Focusing DIRC may be used in a future Super-B factory.

Preface

The work presented in this thesis represents six years of work performed under the supervision of a few members of SLAC's experimental Group B, hence it contains three main topics depending on the person with whom I was working with.

I joined Group B at the end of my first year of graduate study (2005), at this time the group was very much involved in R&D efforts for an upgraded DIRC to be used in a future Super-B factory. From the experience with *BABAR* running, it was clear that a DIRC-type detector was very successful for particle identification. I joined the R&D effort which was lead by J. Va'Vra and had a working group of two scientists, two engineers, and two more graduate students (plus two postdocs who helped for data taking during the beam tests). I was part of the calibrations of the prototype, the data taking during the beam tests in 2005 and 2006, and the subsequent data analysis.

After the R&D work I joined the *BABAR* collaboration and began my service task as commissioner and later operations manager for the DIRC subsystem, this position lasted until the end of *BABAR* running in 2008. At the same time I begun learning about analysis of *BABAR* data with W. Dunwoodie and J. Coleman who were both working in Charm physics. As a first exercise I was assigned to search for an excited charm state which had only been seen by one experiment in the $D^{*+}\pi^-\pi^-$ final state. This took some time as I had to learn the *BABAR* analysis framework, when I finally looked at the mass region we did not find a sign of this state even though we had a much larger data sample. This was not too surprising since the claimed signal was too narrow for a strong decay. This was not the end of such studies as W. Dunwoodie, who always liked to understand everything about analyzes, instructed me to study the $D^{*+}\pi^-$ subsystem where we observed very nice signals for the known L=1 states ($D_1(2420)$ and $D_2^*(2460)$). Some hint of the new states was observed, however the analysis was primitive and was not optimized to search for higher resonances in this final state. I then embarked on a reanalysis of the $D^{*+}\pi^-$ final state, with full signal and generic Monte Carlo studies. At the end of this it was also clear we had found new resonances in this final state,

however much time was spent trying to model the backgrounds and it was clear that a complementary study needed to be performed on the $D^+\pi^-$ system since the mass and width parameters of the $D_2^*(2460)$ needed to be determined from $D^+\pi^-$ and fixed in the $D^{*+}\pi^-$ fit.

It took some more effort to get the data sets for $D^+\pi^-$ and by this time (November 2009) I had spent four years of graduate school. Moreover, my adviser D. Leith advised me to perform a measurement of something related to the Weak Interactions. This became an important highlight of my resume during my job search later. Just at this time J. Coleman found out about the $\sim 3\sigma$ discrepancy between experiment and a newly released calculation of the D_s^- decay constant. This became a hot topic for *BABAR* as the discrepancy could be a signal of New Physics and I was recruited to this working group, leaving the spectroscopy analysis on hold.

The measurement of f_{D_s} seemed like a formidable task given that an absolute measurement was necessary and this involved reconstructing events in hundreds of decay channels. This would have meant several more years of graduate school except for the resources which were given to it, which included, besides the computing priority, two other graduate students working full time and other senior analysts overseeing. At this time I had learned the *BABAR* analysis methods and performing this analysis went rather smooth, after about eight months we had most of the analysis framework in place but the analysis work did not finish until about a year later due to details. At this time the discrepancy with theory had gone down to about 2σ after more precise measurements by CLEOc. The measurement, using only $D_s^- \to \mu^- \bar{\nu}_\mu$, almost made it for the Moriond conference (in March 2010), when it was decided that we should add also the $D_s^- \to e^- \bar{\nu}_e$ and $D_s^- \to \tau^- \bar{\nu}_\tau$ modes. The additional modes would be completed by the other graduate student and the full analysis was ready by June in time for ICHEP. After releasing the paper, but unfortunately before finishing writing this thesis, a new theoretical calculation of f_{D_s} was released which further decreased the disagreement with experiment to only $\sim 1\sigma$.

In March I had switched to working most of my time again on the charm spectroscopy analysis, but I had joined forces with A. Palano who had been working the same subject, he brought in the charged final state $D^0\pi^+$. The new states were confirmed in this mode. Also by June, this analysis had been reviewed and was ready to go to ICHEP.

That is the story of how this thesis came to be.

Acknowledgments

I would like to thank the many people who have taught me and supported me throughout the years during which I worked towards this thesis. At the lab (SLAC) I have been sorrounded by many wise scientists from whom I have been able to learn the scientific methods and skills which were essential for the succesful completion of this work. At home I have been nourished both physically and spiritually by my family who have patiently endured this long and difficult journey.

At the lab I was embraced by Group B and always received kind treatment from my advisers David Leith, Blair Ratclif, William (Bill) Dunwoodie, David (Dave) Aston, and Jaroslav (Jerry) Va'vra. I first worked with Dave on a "rotation" project, where I learned about particle identification at BaBar, throughout the later years Dave always made sure I had an adequate computing system and helped me with software issues. I worked with Jerry for one and half years on the Focusing DIRC R&D. With him I learned everything I know about the DIRC and Cherenkov Radiation and had the opportunity to perform beam tests of the Focusing DIRC in the Endstation A. Later, Jerry always encouraged me with his interest on my work on charm spectroscopy. When I finally stopped working on the R&D it was time for Bill's lessons on physics analysis at BaBar. Bill was the person with most knowledge about experimental particle physics that I met during my Ph.D years. Bill was like an endless source of physics information, everytime I asked him a physics question I had to be ready to learn at least twice the amount of physics. For both the charm spectroscopy analysis and the D_s decay constant analysis, which filled my time until the end, he provided invaluable guidence. It was nice to have Blair in the group, I knew that I could always count on him for a good and friendly advice on just about any subject. He helped me most when trying to understand the work on the Focusing DIRC, and also guided me through the BaBar analyses. David was my main guide, he had an overview which I lacked and helped me move from one project to another without letting me fall too deeply into each subject. He made sure I had a proper education and supported me in anything I wanted to do.

There were other people who played important roles in my thesis work. Joe Schwiening (staff scientist) was an important part of the DIRC R&D team and helped with the data acquisiton system as well as with the subsequent analysis of the data. After the R&D work, I worked for the operations of the DIRC subdetector during the last couple of years of BaBar running, Joe was my principal adviser for this task. Jonathan (Jon) Coleman (a postdoc) was a person with a large impact on my thesis, he introduced me into the world of BaBar software for physics analysis. He also came up with both analysis projects, and as he was the convenor for my analysis work group, he was determined to see both of my projects come to completion. Kevin Yarritu (a graduate student) was my faithful office companion, we shared "the grad office" from the beginning. In some sense paved the path ahead for me as he also did his thesis in BaBar. He was a true friend and I always felt comfortable asking him any question no matter how silly it was.

There are many other people with whom I interacted throughout these long years and who helped me in some way or another or from whom I learned something. There was Adrienne Higashi (group B secretary); Veronique Ziegler, Jochen Kaminski, Kazuhito Susuki, and Niels van Bakel (group B postdocs); Matt McCulloch, Nicolas Narnaud, and Emmanuel Salvati (DIRC operations). Also, there were many friends which were brought together by the BaBar collaboration and with whom I spent many fun times. Most notable was Alejandro Perez (from Venezuela studying in France), Carlos Chavez (from Mexico working in England), Diego Milanes (from Colombia studying in Spain), Neuz Lopez (from Spain), and Wells Wulsin (Stanford student).

At home there were three persons who made my very existence possible, these were my wife Nancy and my daughters Denise and Ivonne. Without them this period of my life would have been a gloomy workful experience. I thank my wife for enduring this long and hard period along my side lighting up one day after another and for caring for my daughters so that I could concentrate on my work. I am lucky to have had two daughters with whom I could play with after work and who made me forget all the troubles at work. To my wife and daughters and to my mother, who has proudly watched me and supported me through these many years of study, I would like to dedicate this thesis.

Contents

List of Tables

List of Figures

Part I

MEASUREMENT OF THE D_s^- LEPTONIC DECAY CONSTANT f_{D_s}

Chapter 1

Introduction

1.1 Standard Model Theory Review

At present, elementary particle physics is described by the Standard Model (SM) theory, which was developed during the last century. The SM is a fundamental theory describing the properties of the three known families of fermions and their interactions through gauge bosons (see Figure 1.1). Each fermion family consists of four particles: an up-type quark u, a down-type quark d, a charged lepton ℓ, and a neutral lepton neutrino ν_ℓ. A total of four different gauge bosons are known: the gluon g mediating the Strong interactions, the photon γ mediating the Electro-Magnetic interactions, and the $W^\pm$ and Z^0 mediating the Weak interactions [1].

At the base of the SM theory is a Lagrangian density written in terms of fermion and boson fields which accounts for their total energy,

$$\begin{aligned}
\mathcal{L}_{SM} &= \sum_{i=1}^{3} \left(\bar{E}_L^i i\not{\partial} E_L^i + \bar{e}_R^i i\not{\partial} e_R^i + \bar{Q}_L^i i\not{\partial} Q_L^i + \bar{u}_R^i i\not{\partial} u_R^i + \bar{d}_R^i i\not{\partial} d_R^i \right) \\
&- \left[(1 + \frac{h}{v}) \sum_{i=1}^{3} \left(m_e^i \bar{e}_L^i e_R^i + m_u^i \bar{u}_L^i u_R^i + m_d^i \bar{d}_L^i d_R^i \right) - \text{h.c.} \right] \\
&+ g \sum_{i=1}^{3} \sum_{a=1}^{8} G_\mu^a \left(\bar{Q}_L^i \gamma^\mu t^a Q_L^i + \bar{u}_R^i \gamma^\mu t^a u_R^i + \bar{d}_R^i \gamma^\mu t^a d_R^i \right) \\
&+ \left[\frac{e}{\sqrt{2} sin\theta_w} W_\mu^+ \left(\sum_{i=1}^{3} \bar{\nu}_L^i \gamma^\mu e_L^i + \sum_{i,j=1}^{3} \bar{u}_L^i \gamma^\mu V_{CKM}^{ij} d_L^j \right) + \text{c.c.} \right] \\
&+ ...
\end{aligned} \tag{1.1}$$

[1] We will not discuss the gravitational force in this text due to its negligible effect on the physics of interest here.

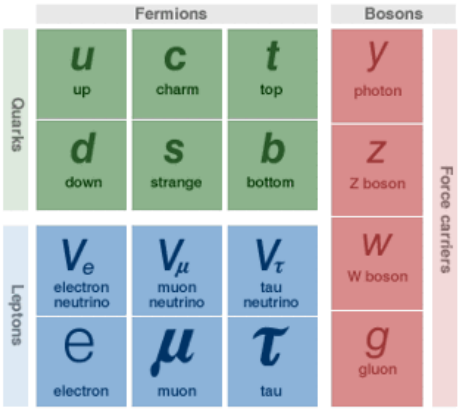

Figure 1.1: The left three columns show the three fermion families of quarks and leptons while the last column shows the gauge bosons through which the fermions interact. The Higgs boson is omitted as it has not yet been detected.

Where we follow the notation conventions by M. Peskin and D. Schroeder [2]. In this equation the first line represents the kinetic energy of the fields, and the second line shows the mass terms generated through the simplest Higgs mechanism. The third line represents the Strong interactions which affect only the quarks and the fourth line represents the Weak interactions which couple the leptons and quarks. Additional terms of the Lagrangian accounting for the Electro-Magnetic interactions, the self interactions of the gluon fields G^a_μ, and Weak neutral current interactions have been left out as they play important but peripheral roles in this analysis. For a more complete description the reader is referred to [2].

An important aspect of the charged current Weak interaction mediated by the W^+_μ is the fact that it only couples left handed fermions. This is described in the SM Lagrangian where the left handed fermions are represented by SU(2) doublets

$$E^i_L = \begin{pmatrix} \nu^i_L \\ e^i_L \end{pmatrix}, \qquad Q^i_L = \begin{pmatrix} u^i_L \\ d^i_L \end{pmatrix} \tag{1.2}$$

while the right handed fermions are SU(2) singlets. This property leads to interesting features in the reactions studied below.

The three fermion families are enumerated as follows,

$$\nu^i = \{\nu_e, \nu_\mu, \nu_\tau\} \qquad u^i = \{u, c, t\} \tag{1.3}$$

$$e^i = \{e, \mu, \tau\} \qquad d^i = \{d, s, b\} \tag{1.4}$$

However, only the leptons have been observed free in nature, the quarks carry an additional quantum number (*color*) and only color neutral combinations of quarks (mesons and baryons) are observed in nature. This $confinement$ property of the Strong interaction is accounted for by assigning the quarks to an non-Abelian SU(3) group representation in which the coupling constant g increases as the distance between quarks increases.

Another important property of the SM Lagrangian is the mixing of quark families through the Cabibbo-Kobayashi-Maskawa (CKM) matrix V_{CKM} which arises from the transformation of the fermion fields when diagonalizing the couplings to the Higgs field [2]. The CKM matrix contains the couplings between up-type quarks and down-type quarks:

$$V_{CKM} = \begin{pmatrix} V_{ud} & V_{us} & V_{ub} \\ V_{cd} & V_{cs} & V_{cb} \\ V_{td} & V_{ts} & V_{tb} \end{pmatrix} \tag{1.5}$$

Through the use of its unitarity condition, the CKM matrix can be rewritten in the Wolfenstein parametrization using only four independent parameters,

$$V_{CKM} = \begin{pmatrix} 1-\lambda^2/2 & \lambda & A\lambda^3(\rho - i\eta) \\ -\lambda & 1-\lambda^2/2 & A\lambda^2 \\ A\lambda^3(1-\rho-i\eta) & -A\lambda^2 & 1 \end{pmatrix} + \mathcal{O}(\lambda^4) \tag{1.6}$$

This parametrization shows that $V_{cs} \approx V_{ud}$ which will be useful in later calculations [3]. The different matrix elements are measured independently using various meson and baryon decay processes described in [17]. Using the measured rates and (in most cases) aided by QCD calculations of the unknown parts of the process, the following values have been obtained,

$$V_{CKM} = \begin{pmatrix} 0.97419(22) & 0.2257(10) & 0.00359(16) \\ 0.2256(10) & 0.97334(23) & 0.0415(11) \\ 0.00874(37) & 0.0407(10) & 0.999133(44) \end{pmatrix} \tag{1.7}$$

It is worth mentioning that the V_{cs} matrix element can be measured using the leptonic decays $D_s^- \to \ell^- \nu_\ell$, however, semi-leptonic decays $D \to K\ell\nu_\ell$ are now more precise due to their larger branching fractions. This thesis presents a study of the leptonic decays of the D_s^- meson.

[2] This mechanism of mixing does not occur in the lepton sector due to the absence of right-handed neutrinos [2].

[3] Current values of the parameters are $\lambda = 0.2257$, A=0.814, $\bar{\rho} = 0.135$ and $\bar{\eta} = 0.349$ [17].

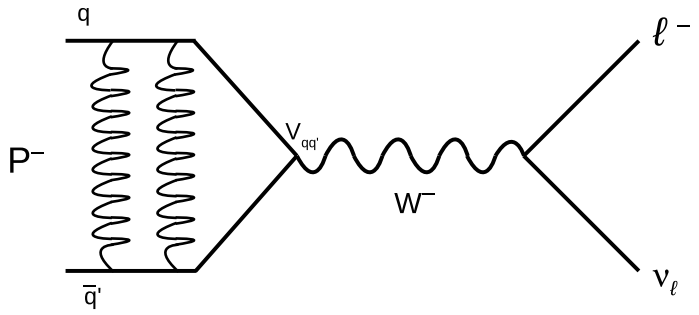

Figure 1.2: Feynman diagram for the leptonic decay of a pseudo-scalar meson P.

1.2 Pseudo-Scalar Leptonic Decays

In the SM theory the purely leptonic decays of pseudo-scalar mesons are of great interest due to their relative theoretical simplicity which makes the predictions reliable and a good testing ground of the SM. For a general pseudo-scalar meson P, the decay process $P^- \to \ell^- \nu_\ell$ can be calculated at tree-level as shown by the Feynman diagram in Figure 1.2. The decay width can be calculated using the general formula for 2-body decays of unstable particles,

$$\begin{aligned} \Gamma(P^- \to \ell^- \nu_\ell) &= \frac{1}{2M_P} \int \frac{d^3p_\ell}{(2\pi)^3 2E_\ell} \frac{d^3p_\nu}{(2\pi)^3 2E_\nu} (2\pi)^4 \delta^4(p_P - p_\ell - p_\nu) \\ &\quad \times |\mathcal{M}(P^- \to \ell^- \nu_\ell)|^2 \\ &= \frac{1}{16\pi M_P} \left(1 - \frac{m_\ell^2}{M_p^2}\right) |\mathcal{M}(P^- \to \ell^- \nu_\ell)|^2 \end{aligned} \tag{1.8}$$

Where M_P and m_ℓ are the masses of the meson and the lepton, the small mass of the neutrino can be ignored. The 4-vectors are evaluated in the rest frame of the decaying meson: $p_P = (M_P, 0)$, $p_\ell = (E_\ell, \vec{p}_\ell)$, and $p_\nu = (|p_\ell|, -\vec{p}_\ell)$. In this frame the energy and momentum of ℓ are given by $E_\ell = \frac{M_P}{2}(1 + \frac{m_\ell^2}{M_P^2})$ and $|\vec{p}_\ell| = \frac{M_P}{2}(1 - \frac{m_\ell^2}{M_P^2})$. The second formula above was derived using the fact the amplitude $\mathcal{M}$ has no angular dependence since P is a scalar.

The computation of the amplitude is complicated by the fact that the strong interactions on the left of the Feynman diagram are not easily computed using Feynman rules. This part of the amplitude is parametrized with a *decay constant* f_P. The remainder of the amplitude follows from simple Feynman rules,

$$\begin{aligned}\mathcal{M}^{ss'} &= \left(\frac{-ie(V_{qq'}f_p p_P^\mu/2)}{\sqrt{2}sin\theta_W}\right)\left(\frac{-ig_{\mu\lambda}}{M_W^2}\right)\left(\bar{\ell}_L^s(p_\ell)\frac{-ie\gamma^\lambda}{\sqrt{2}sin\theta_W}\nu_L^{s'}(p_\nu)\right) \\ &= \frac{ie^2V_{qq'}f_P}{4sin^2\theta_W M_W^2}\bar{\ell}^s(p_\ell)\not{p}_P\frac{(1-\gamma^5)}{2}\nu^{s'}(p_\nu)\end{aligned} \tag{1.9}$$

In the first line, the first term is an ansatz for the $q-\bar{q}$ annihilation vertex written in terms of the only available 4-vector p_P^μ and the decay constant parameter. The second term is the W boson propagator and the last term is the leptonic vertex. The total amplitude can be computed by summing over the final state spins and using the rules for γ matrices:

$$\begin{aligned}|\mathcal{M}|^2 &= \sum_{s,s'}|\mathcal{M}^{ss'}|^2 \\ &= \frac{e^4|V_{qq'}|^2f_P^2}{16sin^4\theta_W M_W^4}\sum_{s,s'}\bar{\nu}^{s'}(p_\nu)\not{p}_P\frac{(1-\gamma^5)}{2}\ell^s(p_\ell)\bar{\ell}^s(p_\ell)\not{p}_P\frac{(1-\gamma^5)}{2}\nu^{s'}(p_\nu) \\ &= \frac{e^4|V_{qq'}|^2f_P^2}{16sin^4\theta_W M_W^4}\mathrm{tr}[\not{p}_P\frac{(1-\gamma^5)}{2}(\not{p}_\ell - m_\ell)\not{p}_P\frac{(1-\gamma^5)}{2}\not{p}_\nu] \\ &= \frac{e^4|V_{qq'}|^2f_P^2}{16sin^4\theta_W M_W^4}\frac{1}{2}tr[\not{p}_P\not{p}_\ell\not{p}_P\not{p}_\nu] \\ &= \frac{e^4|V_{qq'}|^2f_P^2}{16sin^4\theta_W M_W^4}2(2p_P.p_\ell p_P.p_\nu - M_P^2 p_\ell.p_\nu) \\ &= \frac{e^4|V_{qq'}|^2f_P^2}{16sin^4\theta_W M_W^4}2M_P^2|\vec{p}_\ell|(E_\ell - |\vec{p}_\ell|) \\ &= \frac{e^4|V_{qq'}|^2f_P^2M_P^2m_\ell^2}{16sin^4\theta_W M_W^4}\left(1-\frac{m_\ell^2}{M_p^2}\right)\end{aligned} \tag{1.10}$$

Substituting the above formula into Eq.1.9 one obtains the final formula for the decay width

$$\Gamma(P^- \to \ell^-\nu_\ell) = \frac{G_F^2|V_{qq'}|^2M_P}{8\pi}\left(1-\frac{m_\ell^2}{M_P^2}\right)^2 m_\ell^2 f_P^2, \tag{1.11}$$

where $G_F = \frac{\sqrt{2}e^2}{8M_W^2\sin^2\theta_W}$ is the Fermi constant. This formula shows an interesting dependence on the lepton mass m_ℓ. The factor of $(1-m_\ell^2/m_P^2)$ accounts for the phase space suppression when the mass of the lepton is close to the parent mass, this is only important for decays of D mesons to τ leptons since the mass ratio is close to one. More importantly,

the width is proportional to the square of the lepton mass which indicates that, for example, decays to electrons are much suppressed with respect to decays to muons or taus. This *helicity* suppression results from the fact that the charged Weak interactions only couple the left handed fermions. Finally, the width also depends strongly on the value of the CKM element $V_{qq'}$ which can vary by more than two orders of magnitude. These three dependencies result in large variations of the pseudo-scalar decay rates to purely leptonic final states, generally favoring the tau or muon modes and making the electron mode unobservable in heavy meson decays at current experiments.

1.3 Determinations of the Decay Constants and Comparison with Experiment

In order to be able to compare the SM predictions of pseudo-scalar leptonic decays with experimental measurements the decay constant f_P must be calculated. Several methods have been used in the past including QCD sum rules and Lattice QCD (LQCD) to calculate f_P from the defining relation

$$< 0|\bar{q}\gamma^{\mu}\gamma^{5}q|P(p) >\equiv f_P p^{\mu}. \tag{1.12}$$

However, the recent LQCD calculations by the HPQCD and UKQCD Collaborations [5] claim to have a much improved precision ($< 2\%$) with respect to previous calculations. While previous LQCD calculations ignored the contribution of sea quarks in the gluon fields (*quenched* calculations) due to limitations in computing power, the new un-quenched calculations include these contributions and are able to compute strong interaction effects more accurately. Figure 1.3 compares several 'gold-plated' quantities demonstrating the agreement between LQCD calculations and experiment before and after the inclusion of sea quarks.

Once the decay constant is known one can compute the decay rate $B(P^- \to \ell^-\nu_\ell) = \tau_P\Gamma(P^- \to \ell^-\nu_\ell)$ where τ_P is the lifetime of the meson. Except for f_P, all parameters appearing in the formula are known to better than 1%. Using this formula the decay rates for the leptonic decays of pseudo-scalar mesons have been calculated in this analysis and are compared with the current experimental measurements in Table 1.1.

Starting from the top in this table we see that the predicted decay rates for the pion and Kaon are in excellent agreement with experiment. Next, $D^- \to \mu^-\nu_\mu$ has been

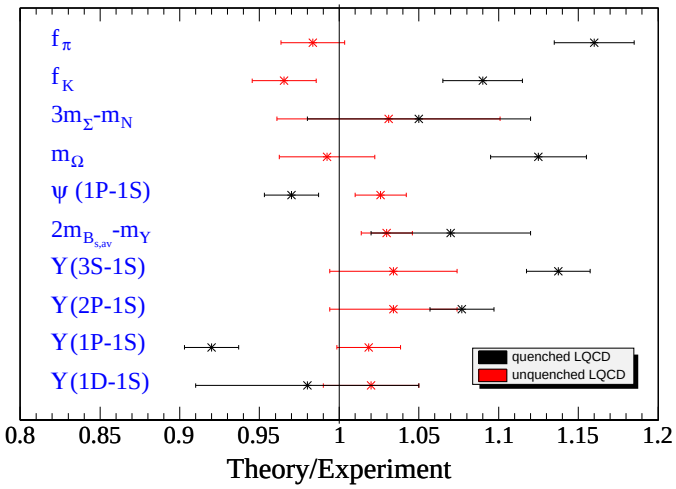

Figure 1.3: Ratio of theoretical prediction and experimental measurement for quenched and unquenched LQCD for several 'gold-plated' quantities.

Table 1.1: Comparison of pseudo-scalar meson leptonic decay constants and rates. The predicted decay constants are obtained from unquenched LQCD calculations in [5] and [7]. The predicted decay rates are calculated using Eq. 1.11 with the measured masses and couplings from the PDG [17] and assuming $V_{cs} = V_{ud}$. The measured D^- decay rates and the D_s^- decay rates to $e^-\ \nu_e$ and $\tau^-\ \nu_\tau$ are from the CLEOc collaboration [11] [10]. The $D_s^- \to \mu^-\nu_\mu$ decay rate is an error weighted average of the recent measurements by CLEOc [10] and the BELLE collaboration [12]. The rest are obtained from the PDG.

Process	**Predicted f_P**	**Predicted Rate**	**Measured Rate**
$\pi^- \to e^-\nu_e$	f_π=132 ± 2 MeV	(1.29 ± 0.04) $\times 10^{-4}$	(1.230 ± 0.004)$\times 10^{-4}$
$\pi^- \to \mu^-\nu_\mu$		0.999871 ± 0.000004	0.9998770 ± 0.0000004
$K^- \to e^-\nu_e$	f_K=157 ± 2 MeV	(1.65 ± 0.04) $\times 10^{-5}$	(1.55 ± 0.07) $\times 10^{-5}$
$K^- \to \mu^-\nu_\mu$		0.641 ± 0.017	0.6354 ± 0.0014
$D^- \to e^-\nu_e$		(9.11 ± 0.37) $\times 10^{-9}$	$< 8.8 \times 10^{-8}$
$D^- \to \mu^-\nu_\mu$	f_D=207 ± 4 MeV	(3.87 ± 0.16) $\times 10^{-4}$	(3.82 ± 0.33) $\times 10^{-4}$
$D^- \to \tau^-\nu_\tau$		(1.03 ± 0.41) $\times 10^{-3}$	$< 1.2 \times 10^{-3}$
$D_s^- \to e^-\nu_e$		(1.17 ± 0.03) $\times 10^{-7}$	$< 1.2 \times 10^{-4}$
$D_s^- \to \mu^-\nu_\mu$	f_{D_s}=241 ± 3 MeV	(4.95 ± 0.14) $\times 10^{-3}$	(5.81 ± 0.43) $\times 10^{-3}$
$D_s^- \to \tau^-\nu_\tau$		(4.83 ± 0.14) $\times 10^{-2}$	(6.42 ± 0.83) $\times 10^{-2}$
$B^- \to e^-\nu_e$		(1.12 ± 0.25) $\times 10^{-11}$	$< 9.8 \times 10^{-6}$
$B^- \to \mu^-\nu_\mu$	f_B=216 ± 22 MeV	(4.77 ± 1.06) $\times 10^{-7}$	$< 1.7 \times 10^{-6}$
$B^- \to \tau^-\nu_\tau$		(1.06 ± 0.24) $\times 10^{-4}$	(1.4 ± 0.4) $\times 10^{-4}$

measured and is also in good agreement with the predicted value. The $D^- \to e^-\nu_e$ mode is below experimental sensitivity and the τ^- ν_τ mode is hard to detect due to poor kinematic constraints, a consequence of the decay of the τ^- to additional neutrinos. The leptonic decays of the B^- meson are currently poorly measured due to their low rates and therefore provide poor tests of the theory.

The D_s^- case is particularly interesting and is the main subject of this thesis. The measurement of the decay rate of $D_s^- \to \mu^-\bar{\nu}_\mu$ has been done by the CLEOc and BELLE collaborations and is currently at a precision of 7.4% while the uncertainty on the predicted value is neglible. The predicted rate by LQCD calculations published in 2008 [5] was lower than the experimental value by about 2 standard deviations. A similar disagreement occurred in the case of $D_s^- \to \tau^-\bar{\nu}_\tau$. A more precise test of the theory can be made by computing the decay constant f_{Ds} of both modes from their measured decay rates and combining the values. One obtains the values

$$f_{Ds}^{\mu\nu} = 261.0 \pm 9.8, \qquad f_{Ds}^{\tau\nu} = 277.7 \pm 18.1 \tag{1.13}$$

and an error weighted average of $f_{Ds}^{avg} = 264.8 \pm 8.6$. The disagreement between this measured value and the theoretical value was about 2.6 standard deviations and caused much speculation amongst the particle physics community. This provided the main motivation for the work in this part of the thesis. The disagreement with theory is now only at about one standard deviation after an update of the LQCD calculations in August 2010 [6]. Given the precision of the theoretical value it is important to try to improve on the current experimental uncertainty since this may allow to detect possible small effects due to non SM physics.

1.4 Scenarios of Non Standard Model Physics

There are several theoretical scenarios in which non SM particles may modify the leptonic decay rates of the D_s^- meson. Akeroyd and Chen point out that the decay rates could be modified by two-Higgs doublet models (2HDM) [19]. There are multiple forms of the 2HDM which differ by the allowed Higgs-fermion interactions [20],[21],[22]. The 2HDM introduces a factor r_q to the width formula Eq. 1.11:

$$r_q = \left[1 + \left(\frac{1}{m_c + m_q}\right)\left(\frac{M_D}{M_{H^-}}\right)^2 (m_c - m_q \tan^2\beta)\right]^2 \tag{1.14}$$

where M_{H^+} is the mass of the charged Higgs, M_{D_q} is the mass of the D meson (containing a light quark q), m_c is the charm quark mass, m_q is the light quark mass and $\tan\beta$ is the ratio of the vacuum expectation values of the two-Higgs doublets. In the case of the D^+ meson, the change in the decay rate due to the Higgs is small because $m_d \sim 0$. That is not the case for m_s and hence the effect in the D_s^+ can be significant.

Dobrescu and Kronfeld have also proposed models that might interfere with the SM process. They suggest three possibilities for the charge of a boson (+1,+2/3,-1/3) for the four-fermion operators that describe the $D_s^- \to l\nu_l$ decay. The diagrams are shown in Figure 1.4. The +1 charge corresponds to the two-Higgs doublet model, while the $-1/3$ and $+2/3$ charges correspond to leptoquarks.

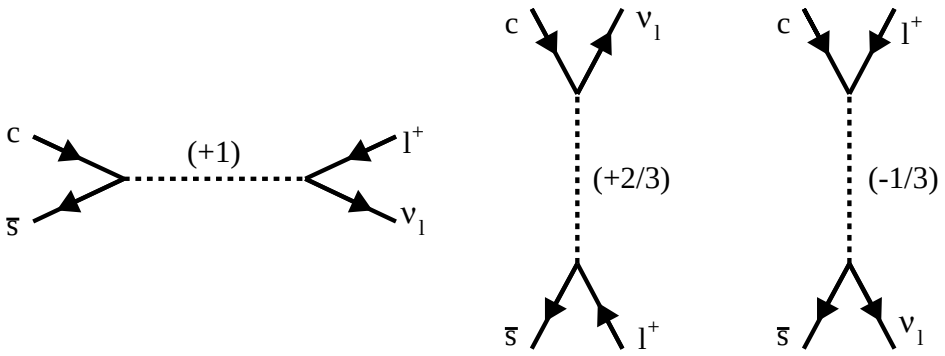

Figure 1.4: Decay diagram for the two-Higgs doublet model and leptoquark models.

Chapter 2

The *BABAR* Experiment

The measurements presented in this thesis have been performed using the data collected in the *BABAR* experiment. *BABAR* is located at the PEP-II asymmetric energy collider at SLAC. While the main motivation for the construction of the *BABAR* experiment was the precise study of CP violation in the B meson system, the data set collected is just as rich in $c\bar{c}$ events and makes *BABAR* as competitive as the specialized charm factory, CLEOc, in many charm topics. The design of *BABAR* is optimized for the study of CP violation, however, it is also well suited for the measurements of charm properties. The strength of *BABAR* derives from it's unprecedented accumulated luminosity which amounts to more than half an inverse attobarn and balances with the stronger kinematic constraints of the charm factory which operates at the threshold for production of $D\bar{D}$ pairs.

2.1 The SLAC Accelerator and PEP-II collider

PEP-II primarily collides electrons and positrons with energies 9.0 GeV and 3.1 GeV respectively at total center-of-mass (CM) energy of 10.58 GeV corresponding to the $\Upsilon(4S)$[1]. The asymmetry between the electron and positron energies is necessary in order to measure the time of flight of the B mesons, a necessary condition in order to measure B^0-$\overline{B}^0$ mixing and to study time-dependent CP violation. The CM of mass frame of the e^+e^- system moves with a speed of about 0.49 times the speed of light along the direction of the electrons. Figure 2.1 shows a schematic of the different parts of the collider. The electrons and positrons are produced by the SLAC two-mile-long Linear Accelerator

[1]The collider also collected data at energies right below (∼40 MeV) the $\Upsilon(4S)$resonance as well as at the $\Upsilon(3S)$and $\Upsilon(2S)$

(Linac) and are stored in the PEP-II high-energy and low-energy rings (HER and LER). The collisions take place at the IR2 region.

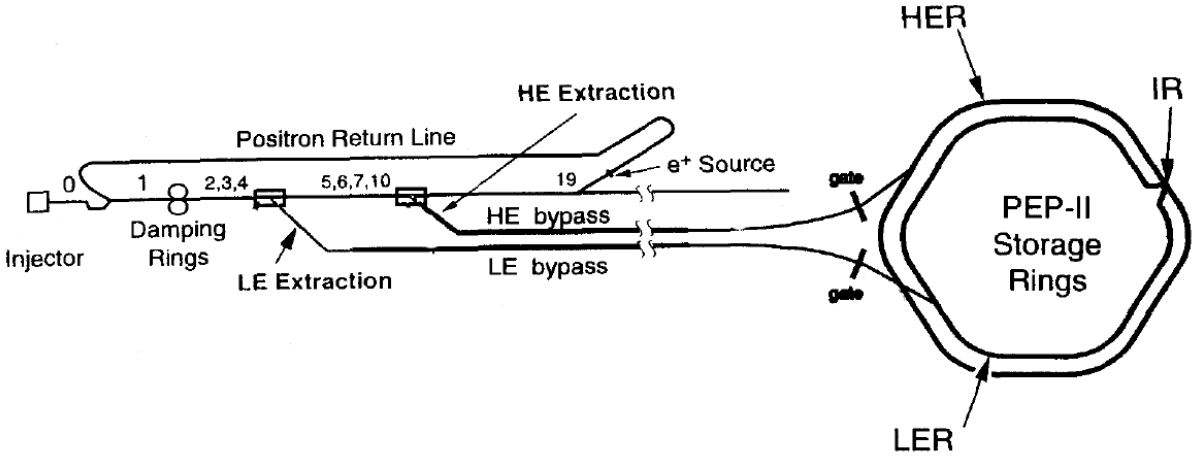

Figure 2.1: Electrons and positrons are accelerated in bunches until they are extracted at the bypass lines. They eventually combine at the *BABAR* detector, located at IR-2.

Electron bunches, containing about 5×10^{10} electrons per bunch, are produced at the start of the Linac in the electron injector and are accelerated to about 1 GeV before passing through the damping rings which reduce the emmittance and size of the beam. The electrons are then accelerated to their target energy of 9.0 GeV before some are extracted into the HER bypass beam-line. Subsequently the electrons are injected into the PEP-II HER ring where they are stored for later collisions. The electron bunches remaining in the Linac are accelerated to 30 GeV before being extracted for production of positrons. The high energy electrons hit a fixed target producing bremsstrahlung γ's which subsequently convert to electron-positron pairs. Positron bunches (with about the same number of particles per bunch) are then transported by the positron return line to the start of the Linac where they start acceleration. After passing through the damping rings the positrons are accelerated to their target energy of 3.1 GeV before being extracted into the LER bypass beam-line. The positrons are then injected and stored in the PEP-II LER.

The HER and LER both hold approximately 1700 bunches when fully filled and carry about 1.8 and 2.9 Amperes of current respectively. The injection of the electrons and positrons into PEP-II used a *trickle injection* system where the bunches are continuously being injected thereby maintaining a long beam lifetime.

The collisions occur in the IR-2 region, Figure 2.2 shows a schematic of the region near

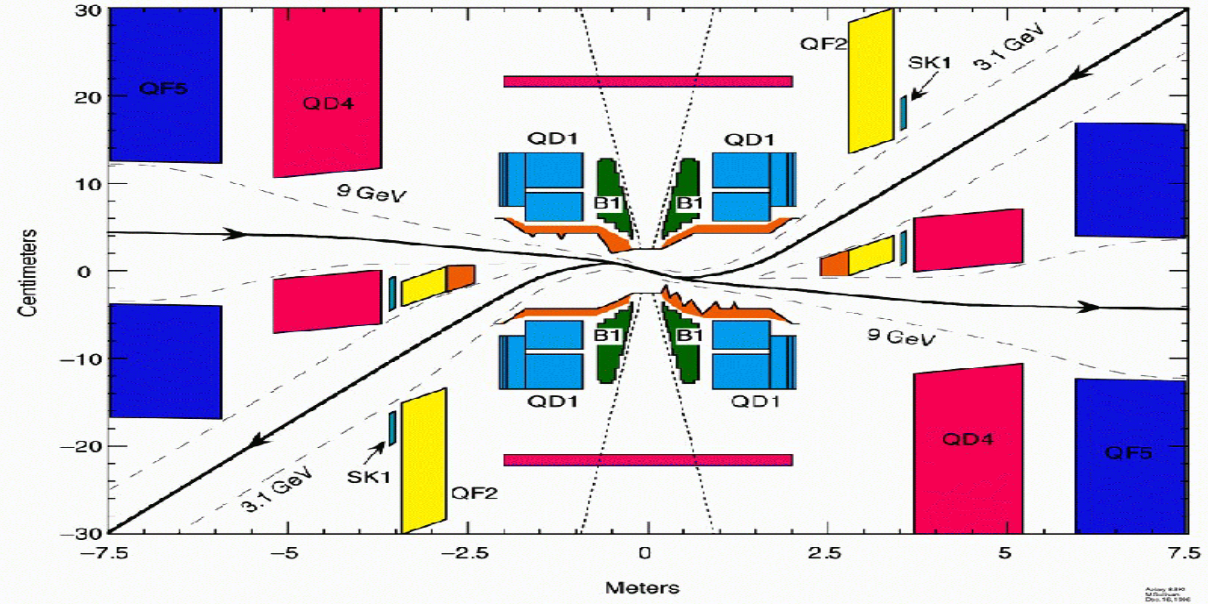

Figure 2.2: IR-2 region. The dipoles (B1) and quadrupoles (QD1) provide the bending of LER needed to collide with the HER. The remaining quadrupoles QF2, QD4 and QF5 are needed to focus and separate the beams.

the collision point. This diagram shows the trajectories of the electrons and positrons in the x-z plane, where the z-axis nearly coincides with the direction of the e^- beam and the x-axis is pointing towards the top (away from the rings center). The complex arrangement of dipole, quadrupole and sextuple magnets is required in order to bring the beams into head-on collision. The instantaneous luminosity achieved by the PEP-II collider quickly surpassed its design luminosity of $3 \times 10^{-33} cm^2 s^{-1}$ and was typically at about $9 \times 10^{-33} cm^2 s^{-1}$ and reached upto $12 \times 10^{-33} cm^2 s^{-1}$.

At the CM energy of the e^+e^- collisions the production of different fermion-anti-fermion pairs occurs through a virtual γ [2], the cross-sections for the different processes are shown in Table 2.1.

2.2 The *BABAR* Detector

The *BABAR* detector surrounds the interaction point (IP) and has an angular acceptance of more than 90% in the CM frame. A diagram of the full detector is shown in Figure 2.2. The e^+e^- beams traverse the center of detector on an axis which is almost

[2]The interaction can also proceed through a virtual Z^0 and produces a measurable ($\sim$0.5%) forward-backward asymmetry in rates.

Table 2.1: Cross-sections for production of the different fermion-anti-fermion pairs at PEP-II.

$e^+e^- \rightarrow$	Cross-section
$b\overline{b}$	1.1 nb
$c\bar{c}$	1.3 nb
$s\overline{s}$	0.35 nb
$d\overline{d}$	0.35 nb
$u\overline{u}$	1.39 nb
$\tau^+\tau^-$	0.94 nb
$\mu^+\mu^-$	1.16 nb

parallel to the axis defined by the detector. The asymmetric energies of the e^+e^- beams require the detector to be asymmetric extending farther in the forward (e^-) direction thereby making the coverage symmetric in the CM frame.

The detector is composed of 5 main sub-detectors which perform the track reconstruction, photon energy measurements and particle identification. The detectors are layered from the with increasing radius from the IP and consist of a silicon tracker for precise vertex reconstruction, a drift chamber for track reconstruction and momentum measurement, a detector of Cherenkov radiation for particle identification, an electro-magnetic calorimeter for photon detection and an instrumented flux return for muon identification.

2.2.1 Silicon Vertex Tracker (SVT)

The innermost component of BABAR is the silicon vertex tracker (SVT), located just outside the beryllium beam pipe, and inside a support tube with a radius of about 22 cm, whose central section is fabricated from a carbon-fiber epoxy composite. The SVT provides a vertex resolution of 80 μm or better for a fully reconstructed B decay. It also serves as a stand-alone tracking system for particles with transverse momentum less than 120 MeV, the minimum that can be measured reliably in the DCH alone. The SVT consists of five layers of 300 μm thick, double-sided silicon strip sensors organized in 6, 6, 6, 16, and 18 modules, respectively. Each module consists of four (layer 1 and 2) to eight (layer 5) sensors. The strips on the opposite sides of the module are orthogonal to each other. The strips that are parallel to the beam axis measure ϕ of a hit (ϕ strips). The ones that are transverse to the beam axis measure z position (z strips). The modules of the inner three layers are straight, while the modules of layer 4 and 5 are arch-shape. The schematic views of SVT are shown in Fig.2.5 and 2.6. The modules are divided

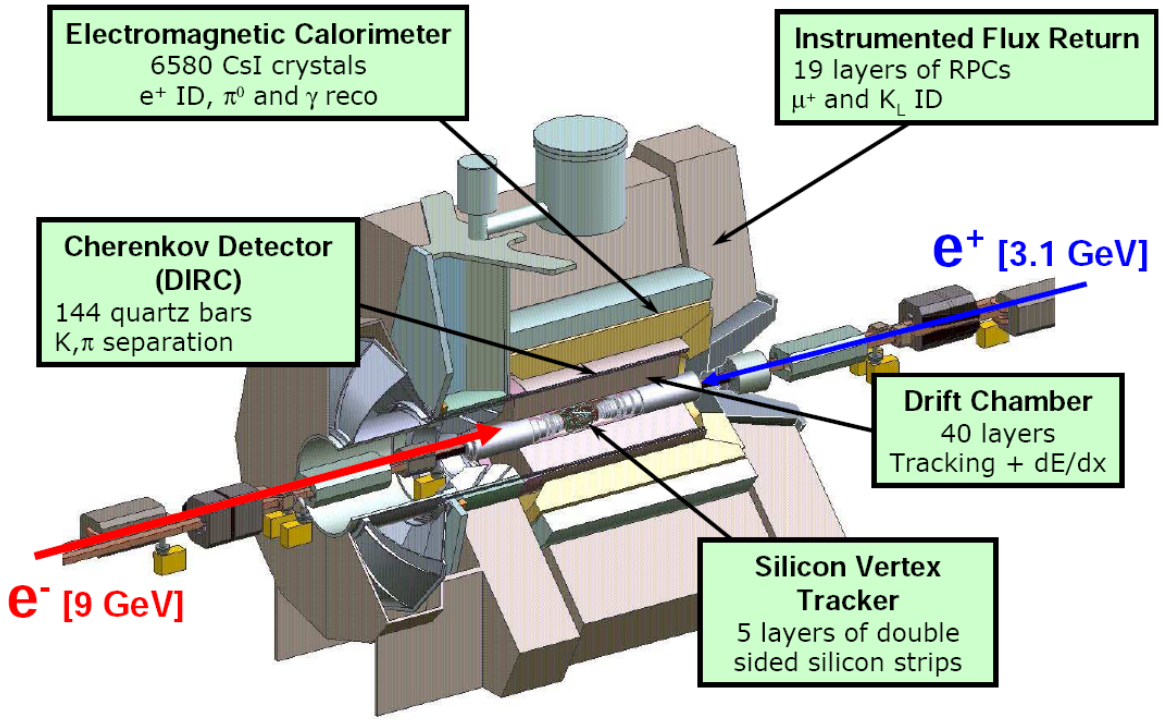

Figure 2.3: An overview of the *BABAR* detector. Starting at the collision axis and moving radially outward, the sub-detectors are the Silicon Vertex Tracker (SVT), the Drift CHamber (DCH), the Detection of Internally Reflected Cherenkov Detector (DIRC) particle identification system, the ElectroMagnetic Calorimeter (EMC), and the Instrumented Flux Return (IFR). The solenoid provides a 1.5 T magnetic field that is necessary to perform momentum measurements of charged particles.

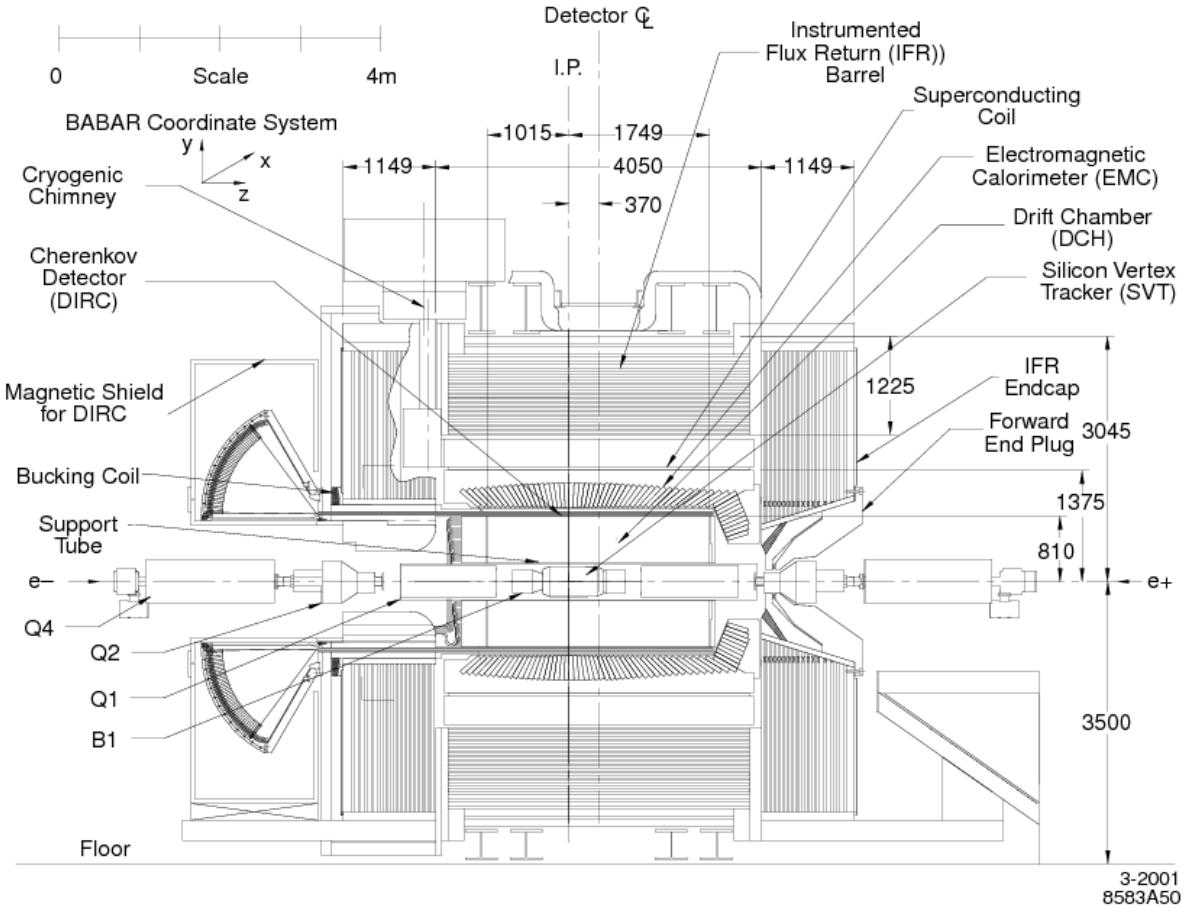

Figure 2.4: Longitudinal cross-section of the *BABAR* detector.

electrically into two half-modules, which are read out at the ends. The sensors have five different shapes, sizes ranging from 43×42 mm^2 ($z \times \phi$) to 68×53 mm^2. Two identical trapezoidal sensors are added to form the arch modules. The ϕ strips of sensors in the same half-module are electrically connected with wire bonds to form a single readout strip. This results in a total strip length up to 140 mm (240 mm) in the inner (outer) layers. The length of the z strip is about 50 mm in inner layers. For layer 4 and 5 the number of z strips exceeds the number of electronics channels available, requiring two z strips on different sensors to be electrically connected (ganged) to a single electronics channel. The total length of these strips is about 100 mm. The readout pitch for z strips is 100 μm (210 μm) for layer 1,2 and 3 (layer 4, 5) and for ϕ 100 μm (110 μm) for layer 1, 4, 5 (layer 2, 3) with one floating strip between readout strips. Parts of the ϕ sides of layer 1 (2) are bounded at 50 μm (55 μm) pitch with no floating strip. The total number of readout channels is approximately 150,000. The total active silicon area is 0.96 m2 and the material traversed by particles is about 4% of a radiation length. The geometrical acceptance of the SVT is 90% of the solid angle in the c.m. system, typically 86% is used in charged particle tracking. The combined hardware and software efficiencies are about 97%, excluding defective readout sections (9 out of 208) that were damaged during the installation.

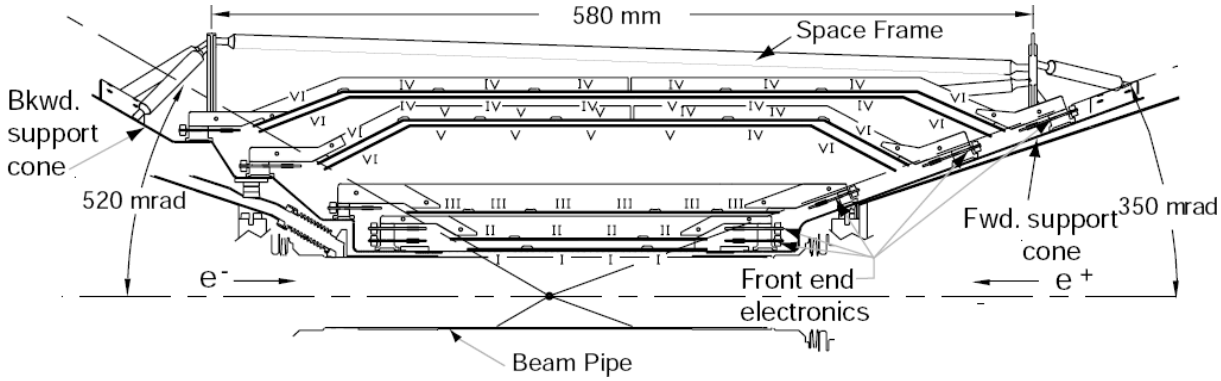

Figure 2.5: A schematic side view of the SVT.

2.2.2 Drift Chamber (DCH)

Outside the support tube is the drift chamber (DCH). The principal purpose of the DCH is the efficient detection of charged particles and the measurement of their momenta and angles with high precision. The DCH also supplies information for the charged particle

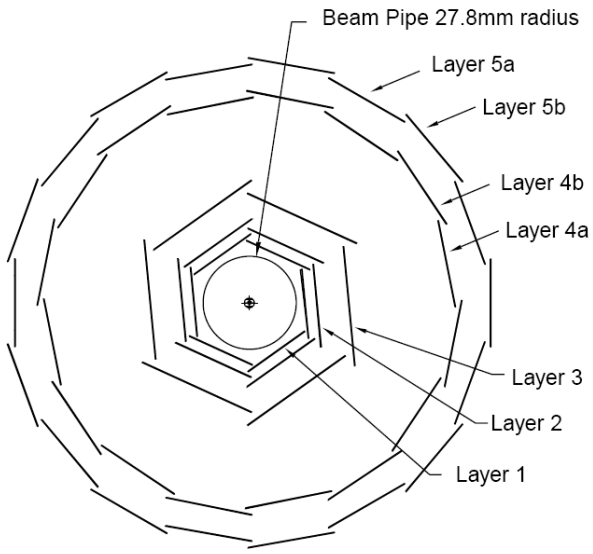

Figure 2.6: A transverse view of the SVT.

trigger with a maximum time jitter of 0.5 μs (Sec. 4.9). For low momentum particles, the DCH also provide particle identification by measurement of ionization energy loss (dE/dx). Figure 2.7 shows the longitudinal cross section of the DCH with principal dimensions. The DCH has 40 layers of small hexagonal cells providing up to 40 spatial and ionization loss measurements for charged particles with transverse momentum greater then 180 MeV. Longitudinal position information is obtained by placing the wires in 24 of the 40 layers at small angles with respect to the z-axis. Particles emitted at polar angles between 17.2^o and 152.6^o traverse at least half of the layers of the chamber before exiting through the endplates. The gas used in the DCH is a 80:20 mixture of helium:isobutane.

The DCH consists of a total of 7,104 small hexagonal drift cells of 11.9 mm by approximately 19.0 mm, arranged in 40 cylindrical layers. The layers are grouped by four into ten superlayers. The stereo angles of the superlayers alternate between axial (A) and stereo (U,V) pairs, in the order AUVAUVAUVA, as shown in Fig. 2.8. Each cell consists of one sense wire surrounded by six field wires. The sense wires are made of tungsten-rhenium with 20 μm diameter. The field wires are made of aluminum with a diameter of 120 μm. All wires are coated with gold. A positive high voltage (nominal value is 1960 V) is applied to the sense wires, and the field wires are at ground potential. The dE/dx, for charged particles traversing the DCH is derived from measurement of the total charge collected in each drift cell through an extraction algorithm with various corrections. The RMS resolution of the measured dE/dx is typically 7.5%.

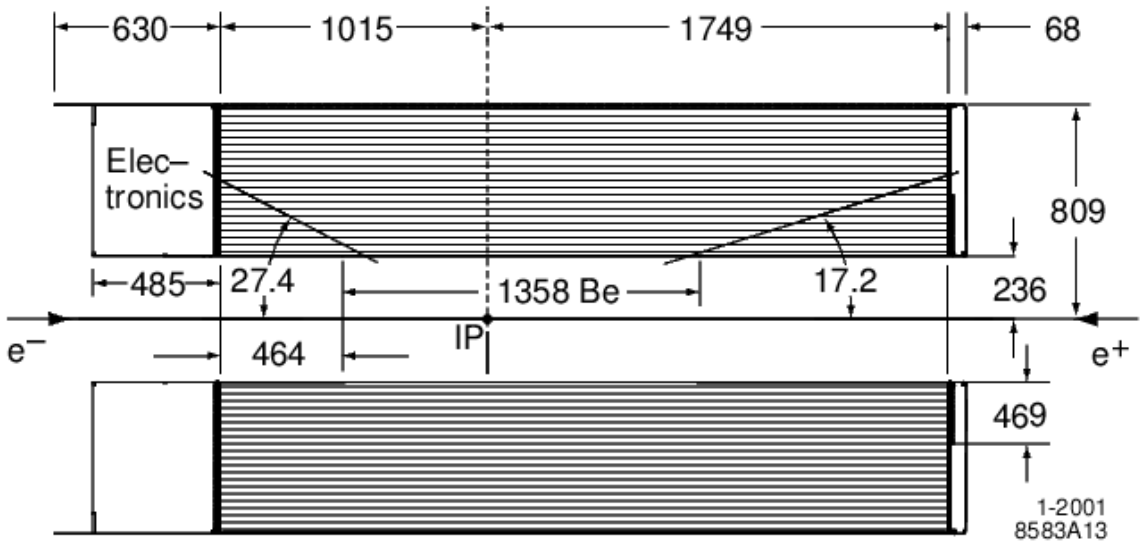

Figure 2.7: A longitudinal view of the drift chamber with the units given in mm. The IP is offset by 370 mm from the chamber center to account for the asymmetric beams.

2.2.3 Detector of Internally Reflected Cherenkov Light (DIRC)

The detector of internally reflected Cherenkov light (DIRC) is a novel ring-imaging Cherenkov detector, located outside the outer shell of the DCH. The principal purpose of the DIRC is to provide good π/K separation from 0.7 to 4 GeV/c. Figure 2.10 shows a schematic of the DIRC geometry that illustrates the principles of light production, transport, and imaging. The radiator is a set of long, thin bars made of synthetic, fused silica, with rectangular cross section. These bars also serve as light guides for the light trapped in the radiator by total internal reflection. The magnitudes of light angles are preserved by the parallel flat surfaces of the bars.

The mean index of refraction (n) of fused silica is 1.473. The Cherenkov angle (θ_C) is related to n and the speed of charged particle (v) through the familiar relation cos θ_C = 1/nβ, where β = v/c, and c = velocity of light. Therefore, by measuring θ_C and the momentum of the track, one can identify the mass of the particle.

For particles with $\beta \sim$1, some photons will always lie within the limits of total internal reflection, and will be transported to either or both ends of the bar, depending on the incident angle. A mirror is placed at the forward end, perpendicular to the bar axis, to reflect incident photons to the backward end, where is instrumented. Most photons that arrive at the instrumented end will emerge into a water-filled expansion region, called the

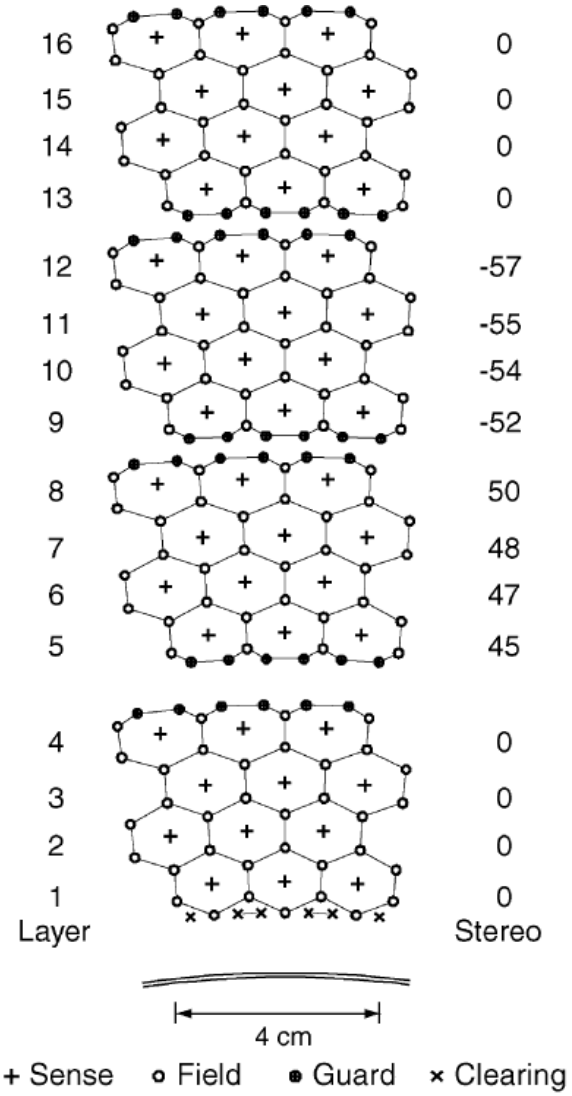

Figure 2.8: Schematic layout of the drift cells for the four innermost superlayers. Layers have been drawn between field wires to illustrate the cell boundaries. The numbers on the right side give the stereo angles (mrad) of the sense wires, while the 1 mm beryllium boundary is shown on the bottom.

Superlayer number	Number of cells	Radius (mm)	Width (mm)	Angle (mrad)
1	96	260.4	17.0-19.4	0
2	112	312.4	17.5-19.5	45-50
3	128	363.4	17.8-19.6	-(53-57)
4	144	422.7	18.4-20.0	0
5	176	476.6	16.9-18.2	56-60
6	192	526.1	17.2-18.3	-(63-57)
7	208	585.4	17.7-18.8	0
8	224	636.7	17.8-18.8	65-69
9	240	688.0	18.0-18.9	-(72-76)
10	256	747.2	18.3-19.2	0

Table 2.2: The specifications of the superlayer structure of the DCH. Listed is the number of cells per layer, the radius of the innermost sense wire, cell widths and wire angles. Widths and radii are specified at the center of the chamber.

standoff box. The photons are detected by an array of densely packed photo-multiplier tubes (PMTs), which are placed at a distance of about 1.2 m form the bar end.

The bars are placed into 12 hermetically sealed containers called bar boxes. The bar boxes are arranged in a 12-sided polygonal barrel. Each bar box contains 12 bars, for a total of 144 bars. Within a bar box the 12 bars are optically isolated by a 150 μm air gap between neighboring bars. The bars are 17 mm-thick, 35 mm- wide, and 4.9 m-long. Each bar is assembled from four 1.225 m pieces that are glued end-to-end.

The standoff box is made of stainless steel, consisting of a cone, cylinder, and 12 sectors of PMTs. It contains about 6,000 liters of purified water, with an average index of refraction of about 1.346. Each of the 12 PMT sectors contains 896 PMTs with 20 mm-diameter, in a closely packed array inside the water volume. A hexagonal light catcher cone is mounted in front of the photocathode of each PMT, which results in an effective active surface area light collection fraction of about 90%. The support structure and geometry of the DIRC are shown in Fig.2.9. The radiator bars subtend a solid angle corresponding to about 94% of the azimuth and 83% of the c.m. polar angle. The geometric contribution to the single photon Cherenkov angle resolution due to the sizes of the bars and PMTs is about 7 mrad. This value is slightly larger than the rms spread of the photon production and transmission dispersions. The overall single photon resolution is estimated to be about 10 mrad.

About 80% of the light is maintained after a few hundreds of bounces along the bars. The overall detection efficiency is dominated by the quantum efficiency of PMTs

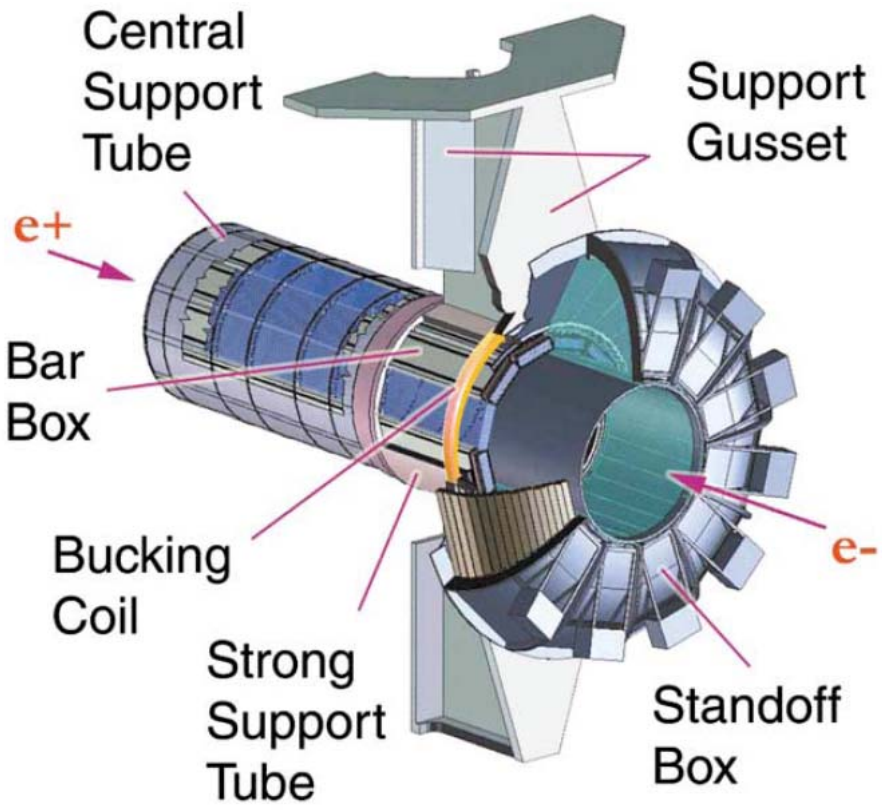

Figure 2.9: An illustration of the DIRC particle identification system. The bar boxes house the fused silica bars which as serve radiators for the traversing particles. They are supported by the Central Support Tube (which also supports the DCH). The whole structure is supported by the Strong Support Tube.

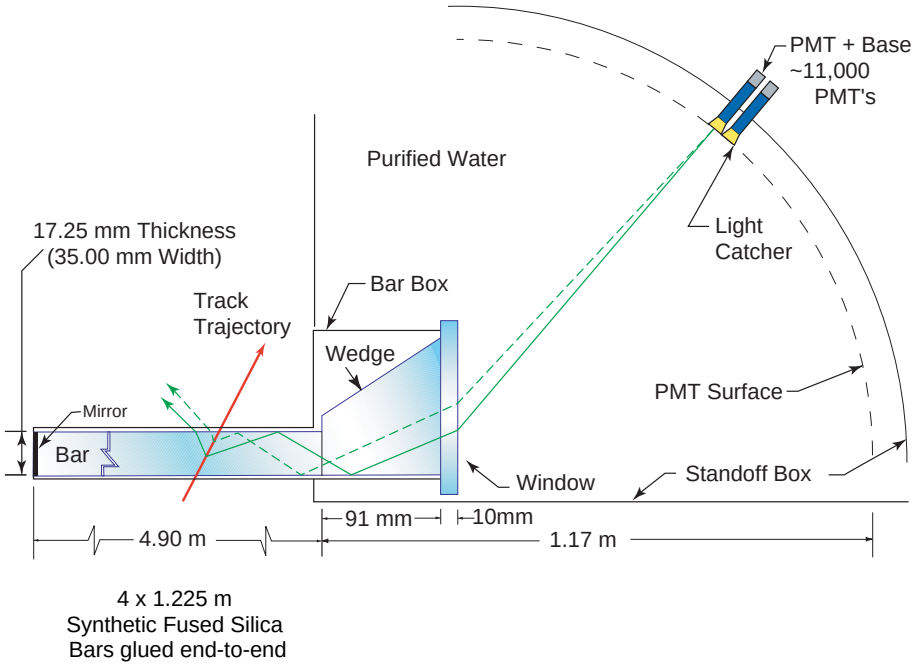

Figure 2.10: A schematic of the DIRC bar. Cherenkov radiation emitted by the particle is channeled to the PMTs, which produce a signal to be read out by the front-end electronics.

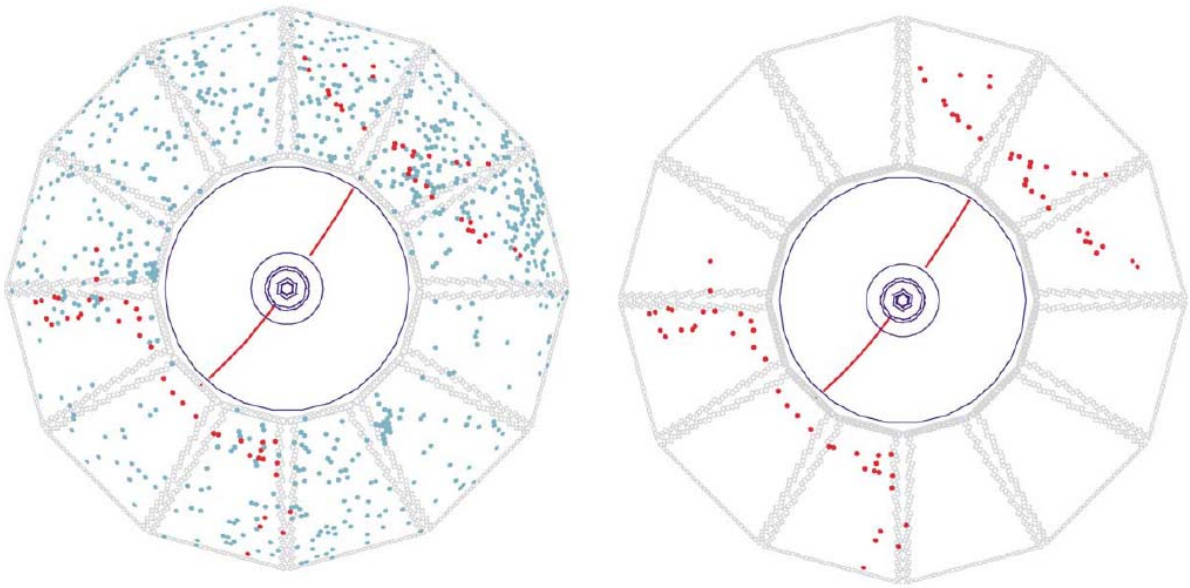

Figure 2.11: A reconstructed dimuon event with PMT signals that have a measured time within the ±300 trigger window (left) and within 8 ns of the expected Cherenkov photon arrival time (right).

(O(20%)). The expected number of photoelectrons (N_{pe}) is about 28 for a $\beta = 1$ particle entering normal to the surface at the center of a bar, and increases by over a factor of two in the forward and backward direction. An unbinned maximum likelihood formalism is used to incorporate all information provided by the space and time measurements form the DIRC. Currently a likelihood value of each of the five stable particle types (e, μ, π, K, p) is calculated if the track passes through the active volume of the DIRC. The expected separation between kaon and pions is about 4.2 σ at 3 GeV/c and about 2.5 σ at 4.2 GeV/c.

To distinguish between signal and background, a selection based on the difference between the measured and expected photon arrival time is made. This is calculated using the time-of-flight of the track, the propagation time of the photon in the DIRC bar, and the measured time of the candidates signal in the PMT. As illustrated in Fig.2.11 this selection is very powerful in removing background photons.

2.2.4 Electromagnetic Calorimeter (EMC)

The electromagnetic calorimeter (EMC) is designed to measure electromagnetic showers with excellent efficiency, energy and angular resolution over the energy range from 20 MeV to 9 GeV. This capability allows the detection of photons from π^0 and η decays as well as from electromagnetic and radiative processes. The EMC is also a major component for electron identification. The EMC consists of 6,580 Thallium-doped CsI crystals, of which 5,760 crystals are contained in a cylindrical barrel support structure arranged in 48 distinct rings, and 820 crystals arranged in eight rings. The EMC has full coverage in azimuth and extends in polar angle from 15.8^o to 141.8^o corresponding to a solid-angle coverage of 90% in the c.m. system (see Fig. 2.12). CsI crystals are doped with 0.1% thallium. They are machined into tapered trapezoids. The transverse dimensions of the crystals vary. The typical area of the front face is 4.7×4.7 cm^2 and the back face area is 6.1×6.0 cm^2. The length of the crystals increases from 29.6 cm in the backward direction to 32.4 cm in the forward direction. The surface of the crystal is polished and wrapped with two layers of diffuse white reflector. A schematic of the crystal is shown in Fig. 2.13. The light yield is required to be uniform to within ±2% in the front half of the crystal; the limit increases linearly to ±5% at the rear face. The photons of electromagnetic showers in a crystal are detected by two 21 cm^2 silicon PIN diodes. The diodes have a quantum efficiency of 85% for the CsI(Tl) scintillation light. The depletion voltage is about 70 V, at which voltage the typical leakage current is 4 nA and capacitance is 85 pF; the diodes

are operated at 50 V. For each crystal-diode assembly, the light yield is measured with the 1.836 MeV photon line from a ^{88}Y radioactive source. The resulting signal distribution has a mean and RMS of 7300 and 890 photoelectrons/MeV. The electronics system has an equivalent noise energy of less than 250 keV, which has negligible impact on the energy resolution of electromagnetic showers from 20 MeV to 9GeV.

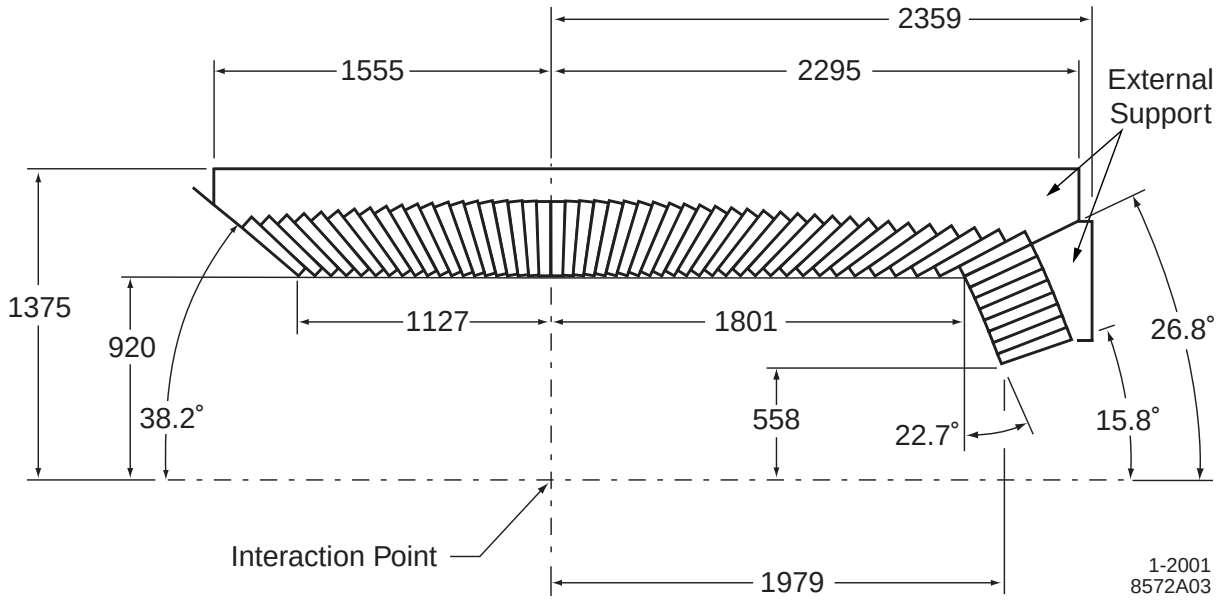

Figure 2.12: A longitudinal view of the top-half of the EMC with the dimensions given in mm. Displayed are the 56 axially-symmetric rings which compose the detector. The endcap is placed at the forward end to account for the asymmetric beam conditions.

A typical electromagnetic shower spreads over several crystals, called a cluster. The reconstruction algorithm requires that at least one crystal in a cluster exceeds 10 MeV and the surrounding crystals pass certain thresholds. A cluster can contain multiple local energy maxima, called bumps. An iterative algorithm is used to determine the energy of the bumps, by calculating the weight of each crystal associated with a certain bump according to the distances between crystals and the centroid of the bump, and calculating the bump centroid according to the weights. The position of a bump is calculated using a center-of-gravity method with logarithmic, rather than linear weights. To determine whether a bump is associated with a charged particle, the track is projected onto the inner surface of the EMC. If the centroid of the bump is consistent with the angle and momentum of the track, the bump is associated with this charged particle, otherwise, it is assumed to originate from a neutral particle. The energy resolution can be measured with or inferred from several sources, including radioactive sources, mass resolutions of

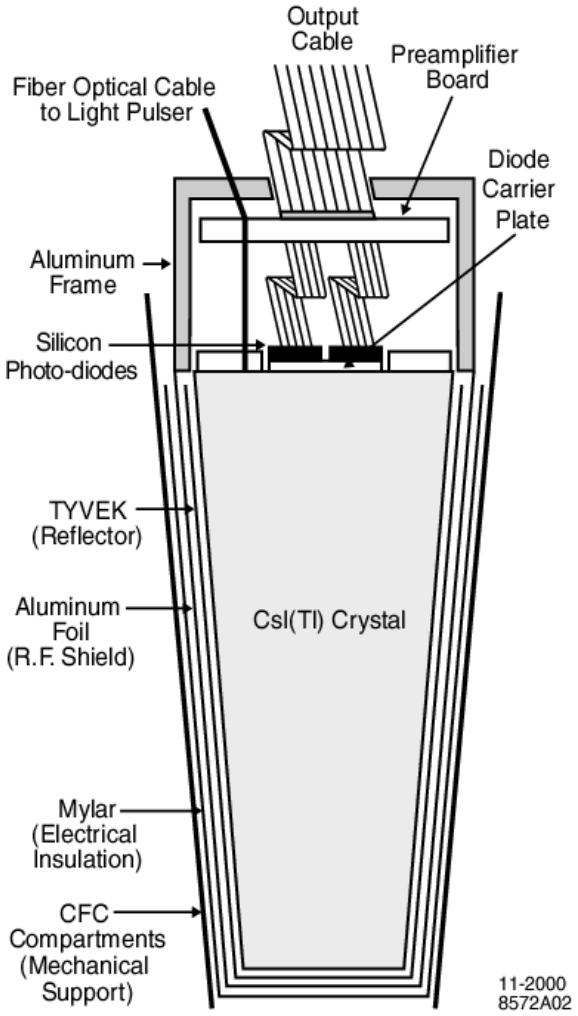

Figure 2.13: A schematic of a crystal. The readout is mounted on the back end.

π^0 and η mesons decaying to two photons, the decay of $\chi_{c1} \to J/\psi\gamma$, and electrons from Bhabha scattering. A fit to the energy dependence with an empirical function results in

$$\frac{\sigma_E}{E} = \frac{(2.32 \pm 0.30)\%}{(E(GeV))^{1/4}} \oplus (1.85 \pm 0.12)\% \tag{2.1}$$

The measurement of the angular resolution is based on the analysis of π^0 and η decays to two photons of approximately equal energy. The resolution varies between about 12 mrad at low energies and 3 mrad at high energies. A fit with an empirical parametrization of energy dependence results in

$$\sigma_\theta = \sigma_\phi = \left(\frac{3.87 \pm 0.07}{\sqrt{E(GeV)}} \pm 0.00 \pm 0.04 \right) mrad \tag{2.2}$$

2.2.5 Instrumented Flux Return (IFR)

The main purpose of the Instrumented Flux Return (IFR) is to identify muons with high efficiency and good purity, and to detect neutral hadrons (primarily K_L and neutrons) over a wide range of momenta and angles.

The active detectors in the IFR are single gap resistive plate chambers (RPCs) with two-coordinate readout. They are installed in the gaps of 18 steel plates in the barrel and the end doors of the flux return, as illustrated in Fig. 2.14. There are 19 RPC layers with 342 modules in the barrel and 18 RPC layers with 432 modules in two end doors. The thickness of the steel plates ranges from 2 cm for the inner nine layers to 10 cm for the outermost ones. The gap between the steel plates is 3.5 cm in the inner layers of the barrel and 3.2 cm elsewhere. In addition, two layers of cylindrical RPCs with 32 modules are installed between the EMC and the magnet cryostat to detect particles exiting the EMC. RPCs detect streamers from ionizing particles via capacitive readout strips.

The RPCs consist of two 2-mm-thick bakelite (phenolic polymer) sheets, separated by a gap of 2 mm, in which a gas mixture, typically 56.7% Argon, 38.8% Freon 134a, and 4.5% isobutane is filled. The external surfaces of bakelite sheets are coated with graphite and are connected to high voltage ($\sim$8 kV) and ground. The bakelite surfaces facing the gap are treated with linseed oil except on the cylindrical RPCs. A cross section of an RPC is shown schematically in Fig. 2.15. The widths of the strips are between 16 mm and 38 mm. To calculate the efficiency in a given chamber, nearby hits in a given layer and hits in different layers are combined to form clusters. The residual distributions from straight line fits to two-dimensional clusters typically have an RMS width of less than 1 cm. An

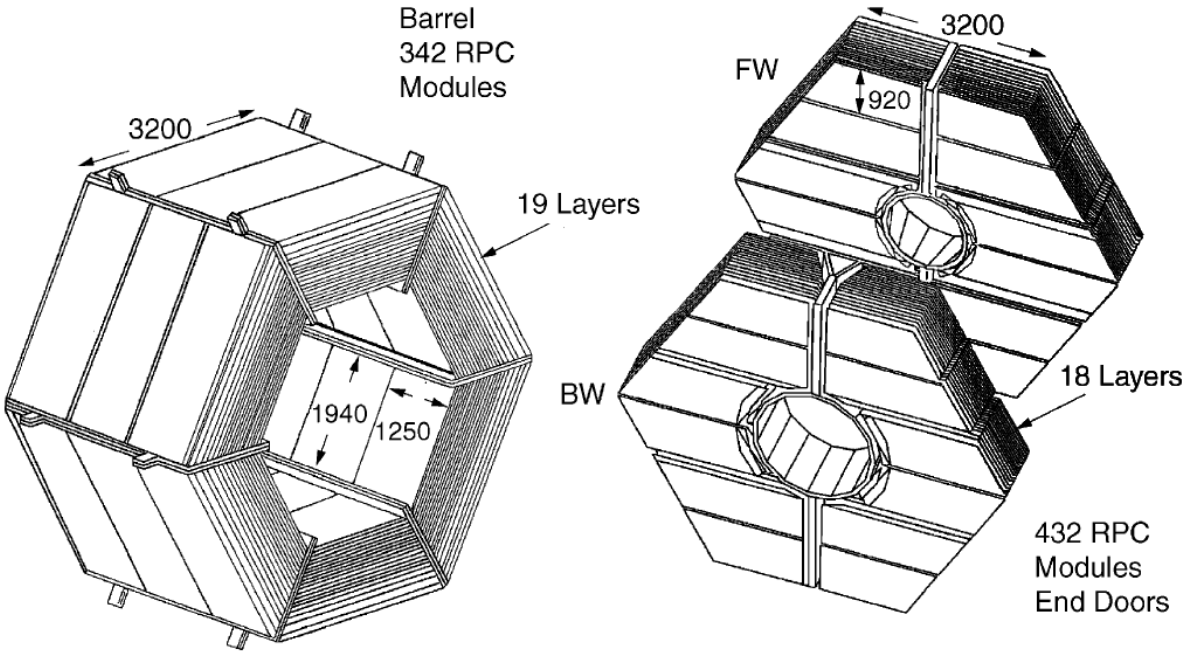

Figure 2.14: An overview of the IFR, in which the barrel and endcaps are indicated. All dimensions are given in millimeters.

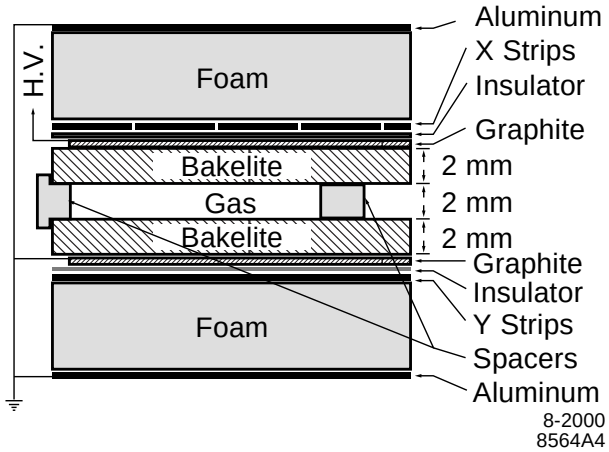

Figure 2.15: Cross section of a planar RPC.

RPC is considered efficient if a signal is detected at a distance of less than 10 cm from the fitted straight line to either of the two readout planes. Of the active RPC modules, 75% exceed an efficiency of 90%. Muons can penetrate many layers of steel plates while other particles (except for non-detectable neutrinos) can't. This property enable the IFR to separate muons from other particles.

The barrel RPC's performance degraded from the beginning of the experiment, and were replaced by limited streamer tubes (LSTs). From 2000 to 2005 the muon efficiency and pion rejection rates steadily declined. For example, for a sample of high energy muons (2 GeV/c < p < 4 GeV/c), and a pion rejection rate of 96%, the muon efficiency decreased from 88% to 76%. The installation of the LST's began in 2004. It was completed in the fall of 2006. The inner 18 layers of the IFR were used for LST installation. However, to add in absorbing material, 6 of those layers contain brass, while the other 12 contain the LST tubes. A schematic of a tube is shown in Fig 2.16. Each tube consists of about 7 or 8 cells, whose dimensions are 17mm wide, 15mm high, and 380 mm long. In the center of each resides a gold-plated anode wire, which is held in place by six wire holders placed around the cell. The walls are coated internally with graphite paint and held at ground, while the wire is at 5.5 kV. The inside of each cell also contains a gas mixture which is argon, isobutane, and carbon dioxide in the ratio 3:8:89. A particle passing through the gas ionizes it and causes a streamer discharge, which can be readout from the wire, while also inducing charge a plane below the tube. Taken together with position of the layer, the full 3D information from the hit can be determined. The installation of the LST's increased the muon efficiency to 92% for the same pion rejection rate.

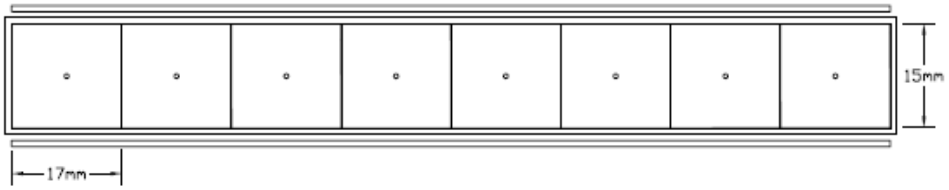

Figure 2.16: Cross section of an LST module.

2.2.6 Solenoid and Magnets

The BABAR magnet system consists of a superconducting solenoid, a segmented flux return and a field compensating coil. Figure 2.2 shows major components of the magnets. The main purposes of the magnet system are to provide magnetic field for measuring

charged particle momentum, serve as hadron absorber for separating muons and hadrons, and provide the overall structure and support for BABAR detector elements. The flux return consists of a hexagonal barrel and forward and backward doors. The coil cryostat is mounted inside the barrel. The coil is made of 16 strand niobium- titanium Rutherford cable with aluminum stabilizer. Each strand has a diameter of 0.8 mm and is wound from thin filaments, each less than 40 μm in diameter. The coil is cooled to 4.5 K by liquid helium and the operating current is 4596 A. The structure of the flux return is designed to sustain the forces produced by the magnetic field, and earthquakes. The central field produced by the coil is 1.5 T. The samarium-cobalt B1 and Q1 magnets are located inside the solenoid as shown in Fig. 2.2. They cannot sustain high radial magnetic field. The radial component at Q1 and r = 200mm is kept below 0.25 T. The stray field leaking into the conventional iron quadrupole Q2, Q4 and Q5 is less than 0.01 T averaged over their apertures. The magnetic field is mapped by five sets of B_r and B_z, and two B_ϕ movable Hall probes. One NMR probe located at r = 89mm provides a very precise field reference near the z-axis. In the tracking volume, B_r and B_z fields vary by less than 0.05 T, and Bϕ is less than 1 mT. The variation of bending field for high momentum tracks is less than 2.5% along the path.

2.2.7 Trigger

The trigger system is designed to select events of interest, while at the same time efficiently rejecting background events. The trigger efficiency for $c\bar{c}$ events is required to be at least 95%. The beam backgrounds must be held to a minimum, as the total event rate must be under 120 Hz. The trigger is implemented in two stages. The first stage, L1, is in hardware, while the second, L3, is based in software. The L1 trigger uses three detectors as input, which are the drift chamber trigger (DCT), the electromagnetic trigger (EMT), and the instrumented flux return trigger (IFT). The former two satisfy all of the trigger requirements independently with high efficiency, and so are largely redundant, while the IFT is used mainly for diagnostic purposes. All three L1 triggers generate trigger primitives, which contain information about the position and energy of a particle. These primitives are passed to the global trigger (GLT) every 134 ns, which processes them and sends them to the Fast Control and Timing System (FCTS). This system can mask or prescale any trigger. If one remains, then an L1 accept signal is sent out for the event to be readout.

The input to the DCT consist of one bit for each of the 7104 DCH cells, where the bit

contains time information from the sense wire associated with that cell. This information is passed to 24 Track Segment Finder (TSF) modules, which find track segments in an adjacent set of cells that span all four layers of a superlayer. The Binary Link Tracker (BLT) then receives these track segments and forms complete tracks. In addition, eight transverse momentum discriminators (PTDs), determine if the track segments have a pt greater than some minimum value. The output of the DCT is a set of trigger primitives which categorize of the output of the BLT and PTDs into short tracks (tracks reaching DCH superlayer 5), long tracks (tracks reaching DCH superlayer 10), and high pt tracks (pt $>$ 800 MeV/c).

The EMT treats the calorimeter as if it divided into 280 towers, 7θx40ϕ . The barrel has 240 towers, each of which contains 24 crystals in a 8θx3ϕ array. The endcap contains 40 towers, each of which contains 19-22 crystals. All crystal energies in each tower above 20 MeV are sent to the EMT. 10 Trigger Processor Boards (TPBs) determine the energies in the 40 ϕ-sectors and different ranges in θ. The output of the EMT is five trigger primitives which categorize the crystal energies using different minimum thresholds, and locations in the EMC. The function of the L3 trigger software is to reconstruct and classify events using the output of the L1 triggers, as well as the complete event data. The trigger is executed in three phases. The first phase defines the L3 input lines. In the second, classification tests are performed which produce pass-fail output flags. These tests are comprised of two algorithms, which are a track finding algorithm for the DCH and a clustering algorithm for the EMC. The DCH algorithm determines the five track helix parameters with those tracks with pt $>$ 250 MeV/c, while the EMC algorithm identifies energy clusters such that minimum ionizing particles can be found. In the last phase, L3 output lines are formed.

2.3 Data Acquisition

The BABAR data acquisition system is a chain from the common front-end electronics through the embedded computing processors, to the logging of event data. The data acquisition chain supports an L1 trigger accept rate of up to 2 kHz, with an average event size of $\sim$32 kbytes, and a maximum output rate of 120 Hz. It should contribute less than a time-average 3% to dead time during normal data acquisition. The data acquisition system consists of the following major subsystems: Online Dataflow, for communication with and control of the detector systems' front-end electronics, and the acquisition and

building of event data from them; Online Event Processing, for processing of complete events, including L3 triggering, data quality monitoring, and the final stages of calibration; and Logging Manager, for receiving selected events sent from the Online Event Processing and writing them to disk files for use as input to the Online Prompt Reconstruction processing. The entire system is coded primarily in the C++ language, with some Java for graphical user interfaces. The data from the front-end electronics are routed via optical fiber links to a set of 157 custom VME readout modules (ROMs), which are then grouped and housed in 23 data acquisition VME crates. One ROM in each crate aggregates the data and forwards them for event building to 32 commercial Unix workstations. The crates and farm computers communicate via full-duplex 100 Mbits/s Ethernet, linked by a network switch. The 32 online farm computers host the Online Event Processing and L3 trigger software. The events accepted by the trigger are logged via TCP/IP to a logging server and written to a disk buffer for later reconstruction and archival storage.

The data acquisition normally worked at an efficiency of greater than 96% and accumulated almost the full luminosity delivered by PEP. Figure 2.17 shows the integrated luminosity delivered and recorded over the lifetime of the experiment from 1999 to 2008.

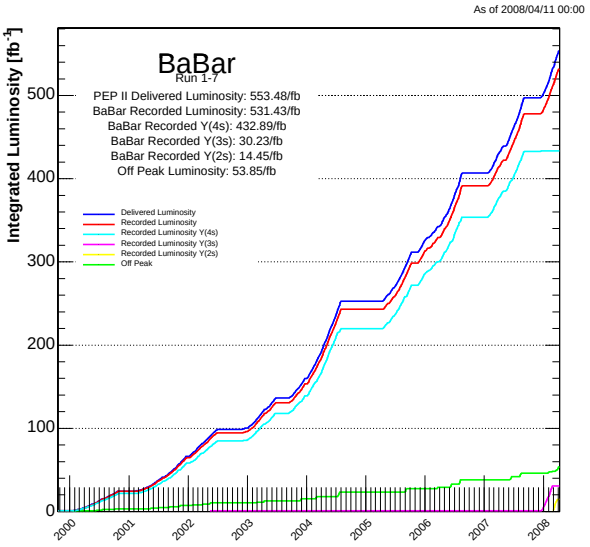

Figure 2.17: Integrated luminosity delivered and recorded in the *BABAR* experiment.

Chapter 3

Particle Identification, Track and Vertex Reconstruction at *BABAR*

Particle identification (PID) is an essential part of any measurement at *BABAR*. PID selections help remove large amounts backgrounds. Especially for $c\bar{c}$ events which contain relatively large track multiplicities due to the additional fragmentation pions. As an example consider the decay of $D^0 \to K^-\pi^+$ where one creates D^0 candidates by combining two tracks. The 4-momentum of true signal candidates is reconstructed correctly by assigning the K^- *hypothesis* to one track and the π^+ hypothesis to the other track [1], however, one must consider all track pair combinations in the event and this leads a large number *combinatorial* background candidates. PID selectors can usually pick out the track which is a true K^- thereby removing many combinations. For decays with more particles in the final state the combinatorial background becomes very larger.

Three types of particle identification will be discussed below: track identification, neutral identification, and *composites*. There are five kinds of particles which produce tracks in *BABAR*, these are the long lived charged particles $e^\pm, \mu^\pm, \pi^\pm, K^\pm$, and $p^\pm$. All of these will be used in this analysis. The methods by which the tracks are reconstructed from the DCH and SVT information will be briefly discussed. Neutral particles include γ's (detected by the EMC) and K^0_L (detected by the EMC and IFR), however only the γ identification will be discussed as K^0_L are not used in this analysis. Finally, I will discuss the reconstruction of K^0_S, which decay to two tracks, and π^0 and η, which decay two photons. The reconstruction of these latter composites will also serve to introduce *Vertex*

[1] The 3-momentum of each track is determined by the measured curvature in the DCH and SVT and the 4-momentum of each track is fully determined once the energy is determined after assigning a mass hypothesis, the parent 4-momentum can be determined by adding the individual tracks.

reconstruction.

3.1 $e^{\pm}, \mu^{\pm}, \pi^{\pm}, K^{\pm}$, and p Identification (Track Reconstruction)

Long lived charge particles leave energy deposits along their trajectory through the subdetectors enabling their track reconstruction and identification.

The reconstruction of a charged particle begins with the determination of its geometrical path (track) within the subdetectors. This is performed using a sophisticated technique called a Kalman Filter [27] which iterates over the measured track segments beginning with the outer hits in the DCH. The filter then iteratively incorporates the inner hits and SVT hits to determine the track parameters and momentum.

The properties of the energy deposits in the subdetectors depend on the mass of the particle. The SVT and DCH both provide a similar means of identification by measuring the energy loss (dE/dx) of the track. The energy loss of charged particles traversing matter follows the Bethe-Bloch formula

$$-\frac{dE}{dx} \propto \frac{1}{\beta^2}\left[ln\left(C\beta\gamma\right) - \beta^2 - \frac{\delta(\beta\gamma)}{2}\right] \tag{3.1}$$

where the constant C and the density correction, $\delta(\beta\gamma)$, are defined in [17], β and γ are the speed of the particle (in units of c) and its lorentz factor. A one-to-one correspondence between β and the particle mass can be made given that the momentum is known. Figure 3.1 shows the dE/dx distributions from a sample of generic tracks. The dE/dx measurements are most useful for separation between pions, Kaons and protons. There is very little separation between muons and pions due to their similar mass values. Also, electrons are only separated at very low momentum values, however, most analysis require electrons at higher momentum. The identification of leptons is described below.

Due to the different properties between the SVT and DCH the Bethe-Bloch curves for the DCH remain more separated in the intermediate momentum range where the SVT looses its power. The DCH dominates for most purposes also because dE/dx is better measured due to the larger number of hits with respect to the SVT. However, the DCH also looses its $\pi - K$ separation at about 0.9 GeV and separation at higher momentum is mainly possible by the DIRC, above 1.5 GeV the DCH also provides some $\pi - K$ separation due to the relativistic rise of the Bethe-Block curves. The angle of

the Cherenkov radiation emitted by the track depends on the type of particle for a fixed momentum value. The angle follows the relation

$$cos\theta_C = \frac{1}{n\beta} \tag{3.2}$$

where n is the index of refraction of the radiator bars. Figure 3.2 shows a distribution of θ_C as a function of momentum for a generic sample of tracks. The DIRC provides more than 2σ separation between pions and Kaons upto 4 GeV/c. Similarly, the separation of protons is possible for the entire momentum range by combining the information from the SVT, DCH and DIRC.

The information from the SVT, DCH, and DIRC is combined using sophisticated algorithms which use an Error Correcting Output Code [28] (labeled KM selectors) or Bagged Decision Trees (labeled BDT selectors) [29]. For pions and protons the KM selector is used while for Kaons the BDT selector is used. The KM selectors have 4 levels of tightness: SuperLoose, VeryLoose, Loose, Tight, VeryTight, and SuperTight. The BDT selectors have only 4 levels: VeryLoose, Loose, Tight, and VeryTight. The levels are designed to balance purity against efficiency. For 1 GeV/c tracks the selector levels have approximately the following efficiencies:

Selector	SuperLoose	VeryLoose	Loose	Tight	VeryTight	SuperTight
pion KM	99.0%	98.6%	98.0%	94.0%	87.5%	85.0%
Kaon BDT		95.0%	89.0%	87.0%	82.0%	
proton KM	99.5%	99.5%	99.5%	99.0%	92.0%	90.0%.

For the Kaon and proton selectors the large backgrounds arise from charged pions due to their large abundance. For 1 GeV/c tracks the rate of pions faking a Kaon or proton are the following:

Selector	SuperLoose	VeryLoose	Loose	Tight	VeryTight	SuperTight
Kaon BDT		6.0%	2.5%	1.5%	1.0%	
proton KM	$< 0.5\%$	$< 0.5\%$	$< 0.5\%$	$< 0.5\%$	$< 0.5\%$	$< 0.5\%$

The identification of muons is possible through the use of the IFR information. Due to the strong interactions of charged hadrons only muons are able to penetrate the iron layers of the IFR. Electrons tend to loose most of their energy in the EMC and also

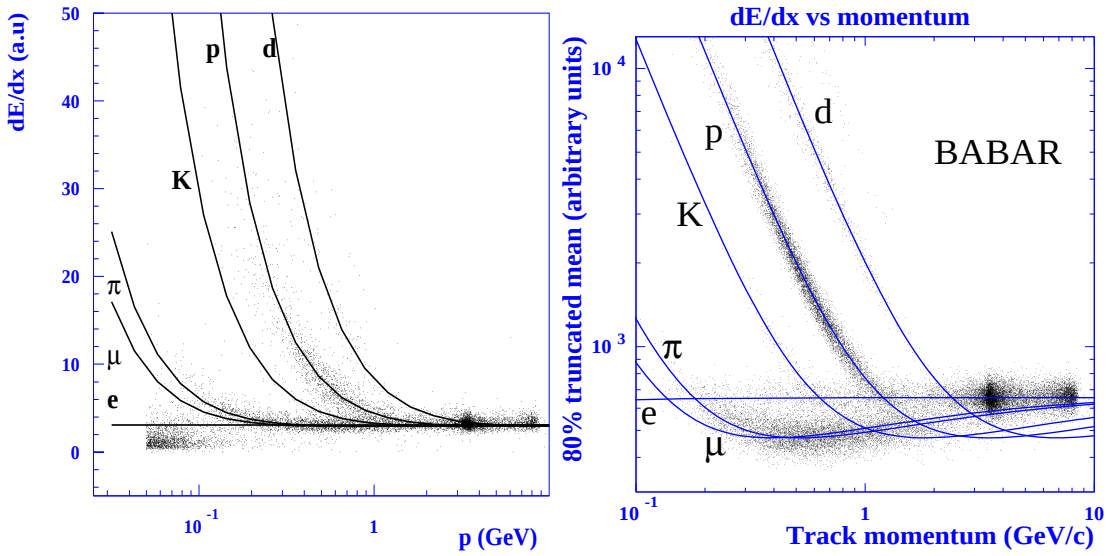

Figure 3.1: SVT and DCH dE/dx distributions (left and right) from a sample of tracks obtained when *BABAR* was running at very low luminosity and the detected tracks originated from beam gas or beam pipe interactions. The curves are the Bethe-Bloch expectations for the different particles.

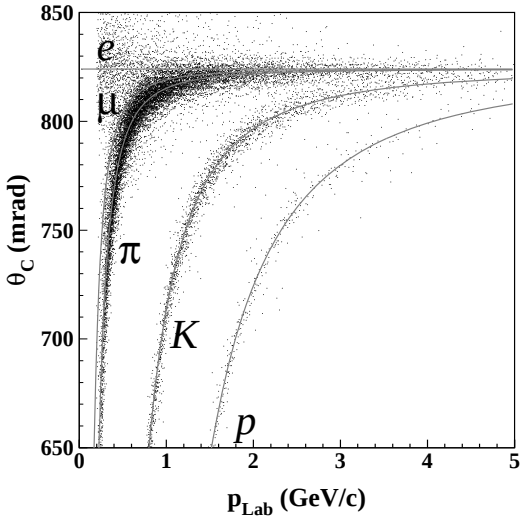

Figure 3.2: DIRC θ_C distributions from a generic sample of tracks in *BABAR*. The curves are the expectations for the different particles.

do not penetrate the IFR. Hence the observation of a track continuing into the IFR (a minimum of 2 IFR layers is required) identifies a muon, the drawback, however, is that a minimum momentum of about 0.7 GeV/c is required for muons to reach the IFR. In addition, the energy deposited in the EMC contains separating power from electrons. Figure 3.3 compares the distribution of the energy deposited in the EMC for muons and electrons.

Electron identification is performed mainly using the energy deposited in the EMC. Electrons, much like photons, deposit most of their energy in the EMC through electromagnetic interactions. A variable, E/p, is defined using the raw energy deposited by the track in the EMC and track momentum. This variable is calibrated such that it peaks at a value of 1 for electrons as shown in Figure 3.4 and is required to be in the range 0.89 to 1.2. Electron identification also uses the dE/dx information from the DCH and SVT. In addition, the lateral moment (LAT) of energy cluster in the EMC is defined using the formula

$$LAT = \frac{\sum_{i=3} E_i r_i}{\sum_{i=3} E_i r_i + E_1 r_0 + E_2 r_0} \tag{3.3}$$

where the energies E_i correspond to the crystals in the cluster and are ordered from smallest to largest, r_0 is the distance between crystals. A requirement of LAT<0.6 (See Figure 3.5)takes advantage of the fact that clusters made by hadronic particles have a larger spread.

The information of the sub-detectors is combined using a BDT algorithm for the selection of muons and a KM algorithm for the identification of electrons. The following are the efficiencies of the muon and electron selectors:

Selector	SuperLoose	VeryLoose	Loose	Tight	VeryTight	SuperTight
muon BDT		84%	70%	61%	45%	
electron KM	99%	98%	97%	94%	92%	90%

The corresponding pion fake rates for these selectors are the following:

Selector	SuperLoose	VeryLoose	Loose	Tight	VeryTight	SuperTight
muon BDT		60%	27%	15%	9%	
electron KM	1%	0.5%	0.4%	0.14%	0.06%	0.05%

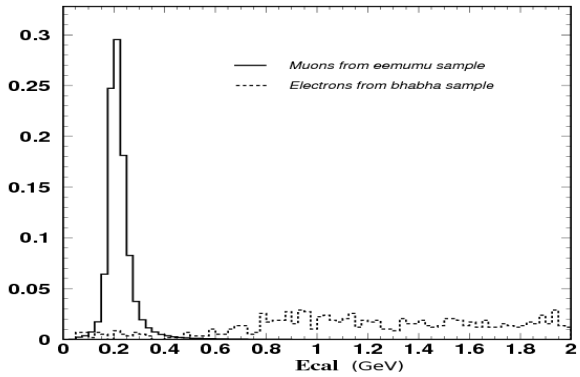

Figure 3.3: Distribution of energy deposited in the EMC by muons (solid curve) and electrons (dashed curve). The muons and electrons are obtained from high purity control samples.

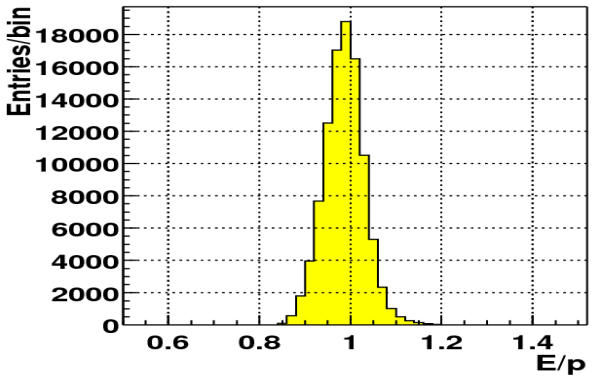

Figure 3.4: E/p Distribution for electrons in the $\gamma\gamma \to e^+e^-e^+e^-$ control sample.

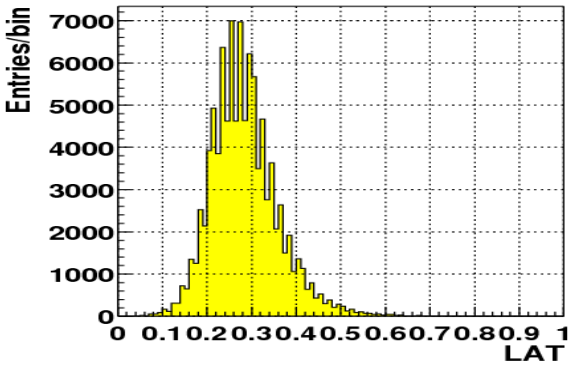

Figure 3.5: LAT Distribution for electrons in the $\gamma\gamma \to e^+e^-e^+e^-$ control sample.

3.2 γ Detection

Photons are reconstructed using EMC energy clusters. The energy is determined from the energy deposited while their momentum vector is assigned from the line of flight between the cluster center and the IP unless the production vertex is known from additional tracks produced by the parent. Photon reconstruction usually suffers from large backgrounds due to the many possible ways to deposit energy in the EMC. Most tracks and K_L^0 leave some amount of energy in the EMC and this can be misidentified as a photon. There are also machine backgrounds due to stray particles hitting the beam pipe. For these reasons only clusters with energies greater than 30 MeVare considered. An important selection against fake photons is the requirement of isolation, where it is required that the cluster not be consistent with the extrapolated path of a charged particle. In addition, a default requirement of LAT<0.8 is applied in order to discriminate against hadronic interactions. The shape of energy clusters from photons is similar to the shape for electrons shown in Figure 3.5.

3.3 K_S^0 Reconstruction (Vertex Reconstruction)

Due to their relatively long lifetime, K_S^0 particles decay mostly within the tracking detectors (SVT and DCH). The reconstruction from the $\pi^+\pi^-$ mode is almost always exclusively used since the $\pi^0\pi^0$ mode has low efficiency, high backgrounds and the decay vertex cannot be determined due to the four photons.

The K_S^0 decay vertex can be determined from the $\pi^+\pi^-$ tracks through the use of vertexing tools. For a simple approximation one can just use the point of closest approach of the two tracks and compute K_S^0 momentum using the momentum of the tracks at that point, however this leads to poor resolution on the reconstructed mass of the K_S^0. Improved resolution can be obtained through a sophisticated algorithm where one *fits* for the K_S^0 decay vertex point and momentum vector using a χ^2 minimization computed using the measured track parameters. The $\chi 2$ is define as follows

$$\chi^2 = (\alpha - \alpha_{\mathbf{0}})^T V^{-1} (\alpha - \alpha_{\mathbf{0}}) + 2\lambda^T (D(\alpha - \alpha_{\mathbf{A}}) + \mathbf{d}) \tag{3.4}$$

Where $\alpha_{\mathbf{0}}$ is a vector containing all the measured track parameters and α is vector containing the true track parameters to be determined from the fit. V is a the error matrix on the measurements. The second term in this formula imposes the physical constraints

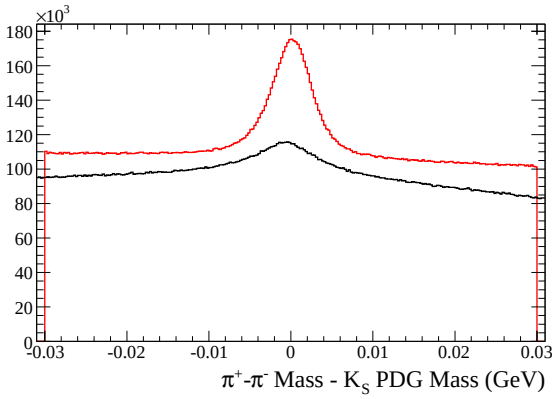

Figure 3.6: Comparison of the K^0_S mass distribution before (lower histogram) and after (upper histogram) the vertex fit in an inclusive event sample.

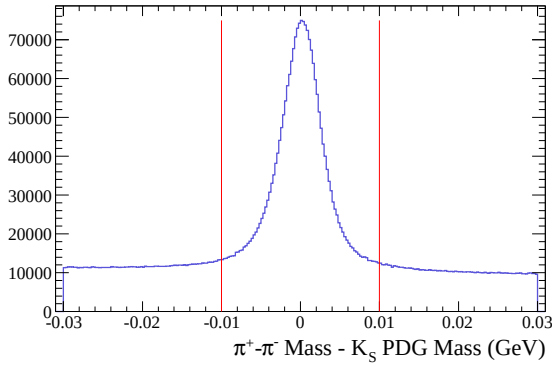

Figure 3.7: Distribution of the K^0_S mass distribution after applying the selection on the flight distance. The vertical lines show a typical selection on the K^0_S candidate mass.

on the true track parameters using Lagrange multipliers (λ). The constraint equations $H(\alpha) = 0$ are linearized about a convenient point $\alpha_{\mathbf{A}}$, $D = dH/d\alpha$ and $d = H(\alpha)$ describe this linearized form. A comparison between the mass distribution of K^0_S candidates with and without the vertex fitting is shown in Figure 3.6.j

Once the K^0_S vertex has been measured we remove many of the fake candidates by requiring a flight distance from the IP of at least 3 standard deviations. In $c\bar{c}$ events, this requirement removes much of the combinatorial background due to other tracks originating from the IP region coming from fragmentation pions or other D meson decays.

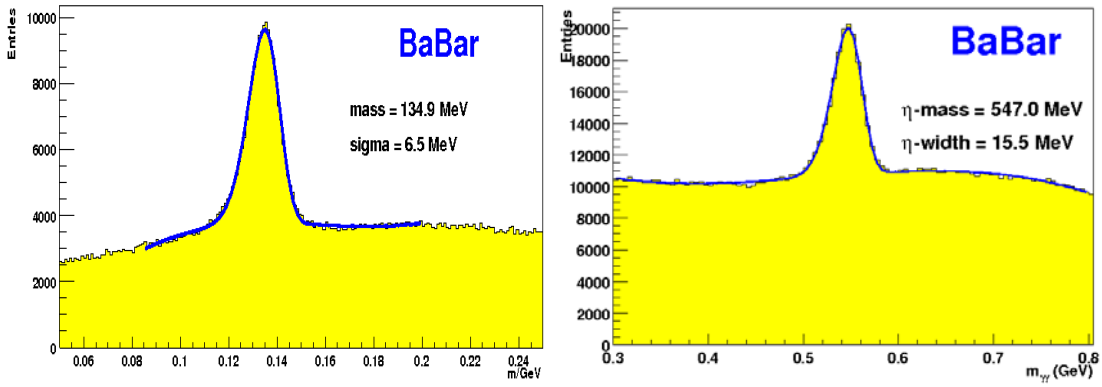

Figure 3.8: Invariant mass distributions of vertexed π^0 and η candidates in a generic sample.

3.4 π^0 and η Reconstruction

π^0 and η particles in this analysis are reconstructed from their decays to two γ's. A precise determination of the decay vertex cannot be performed for these particles because one cannot obtain the direction of the photon momentum from the EMC information, only its energy. One therefore assumes that the photons originate from IP region; this assumption is usually good enough for most applications because the π^0 and η have very short lifetimes ($< 10^{-16}$ s) and decay within this region. Figure 3.8 shows mass distributions of π^0 and η candidates in generic event samples. We apply a selection on the mass peak of about 3 standard deviations. Alternatively one can apply a mass constraint during the vertex fit, where the mass of the candidates is fixed to the known value. The latter has two effects, 1) it induces a somewhat better resolution on the momentum vector of the π^0 or η, and 2) it removes candidates with mass values far from the nominal mass after applying an appropriate selection on the fit probability.

Chapter 4

Analysis Overview and Event Samples

4.1 Strategy

This chapter describes the procedure used for the reconstruction of the events containing D_s^- mesons. The reconstruction method follows a method similar to the one used by the *Belle* collaboration [12], in this method we attempt to reconstruct $e^+e^- \to c\bar{c}$ events which contain D_s^- mesons produced through the following reactions,

$$e^+e^- \to c\bar{c} \to DKXD_s^*,\ D_s^* \to D_s\gamma.$$

In these reactions one of the charm quarks hadronizes into a D_s^- meson on the signal side of the event while the other charm quark hadronizes generically into a charm hadron. The charm hadron can be a D^0, D^+, Λ_c^+, or a D_s^+ meson; we denote this charm hadron by the D symbol. As will be seen later the reconstructed sample of signal events consists of about 97% from D^0 and D^+ (hence the notation) while the D_s^- modes are not used due to low purity as a result of backgrounds arising from the signal side. The symbol K is used to denote a K^+ or K_S, which is required to balance the strangeness in the event. In addition, for the Λ_c^+ modes, we require an anti-proton in order to conserve baryon number. The X symbol represents additional pions in the event which arise from the additional free energy in the hadronization process.

The method uses only signal D_s^- mesons which have been produced through a parent D_s^{*-} so we require a photon consistent with decay $D_s^{*-} \to D_s^-\gamma$. The requirement of the photon from the D_s^{*-} decay is necessary for obtaining a resolution on the recoil mass below

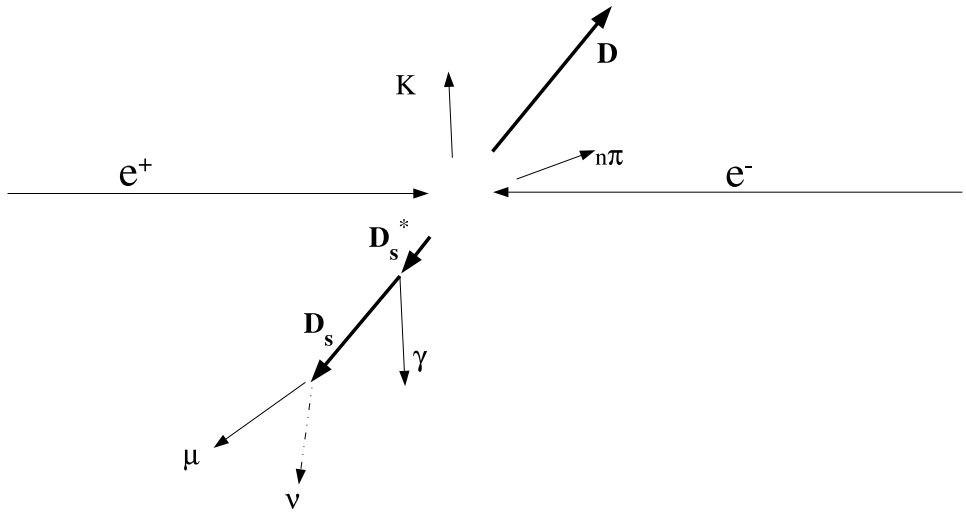

Figure 4.1: Topology for events containing a $D_s^- \to \mu^- \nu$ decay. The symbols are defined in the text.

which allows us to distinguish the signal events from the high backgrounds. In the first stage of the analysis no requirements are placed on the daughters of the signal D_s^- meson in order to obtain a fully inclusive sample of D_s^- events which is used for normalization in the calculation of the branching fractions. The event yield for this inclusive sample is extracted from the distribution of events in the variable $m_{recoil}(DKX\gamma)$, which is defined as the mass recoiling against the $DKX\gamma$ system. This variable is computed using the missing 4-momentum in the event:

$$p_r = p_{e^+} + p_{e^-} - p_D - p_K - p_X - p_\gamma \tag{4.1}$$

$$m_{recoil}(DKX\gamma) = \sqrt{p_r^2} \tag{4.2}$$

Once the inclusive sample of D_s^- events has been selected, we use this sample to reconstruct the fraction of events where the D_s^- decays to the final states $\mu^- \bar{\nu}_\mu$, $e^- \bar{\nu}_e$, and $\tau^- \bar{\nu}_\tau$ by requiring an additional muon or electron in the rest of the event. For the τ, the e or μ track identifies its decay to $\tau^- \to e^- \bar{\nu}_e \nu_\tau$ or $\tau^- \to \mu^- \bar{\nu}_\mu \nu_\tau$. The events corresponding to $\mu^- \bar{\nu}_\mu$ and $e^- \bar{\nu}_e$ decays are extracted using the recoil mass against a $DKX\gamma\ell$ system, while for the τ modes we use the extra neutral energy in the event.

The reconstruction efficiencies for each mode are determined from MC samples of events containing the signal decays. The branching fraction can then be computed by correcting the D_s and $\ell\nu$ yields by their corresponding efficiency:

$$B(D_s \to \ell\nu) = \frac{N_{\ell\nu}^{prod.}}{N_{D_s}^{prod.}} = \frac{\left(\frac{N_{\ell\nu}^{rec.}}{\varepsilon_{\ell\nu}}\right)}{\left(\frac{N_{D_s^-}^{rec.}}{\varepsilon_{D_s}}\right)} = \frac{N_{\ell\nu}^{rec.}}{N_{D_s}^{rec.}\frac{\varepsilon_{\ell\nu}}{\varepsilon_{D_s}}} \tag{4.3}$$

In addition to the leptonic branching fractions the hadronic decay $D_s^- \to K^+K^-\pi^-$ has been measured as a cross-check of the analysis method and the result is compared to the precise measurement by CLEO-c.

4.2 Data Samples

The data sample used for the measurements corresponds to the full data set collected by *BABAR*. About 470 fb^{-1} were collected on the $\Upsilon(4S)$ resonance, 10% of which was collected 40 MeV below (Off-Peak). In addition we use about 50 fb^{-1} collected at the $\Upsilon(3S)$ and $\Upsilon(2S)$ resonances. The physics of the $c\bar{c}$ events does not depend significantly on these energy variations of the e^+e^- beams.

For the determination of reconstruction efficiencies and for studies of backgrounds we use signal and generic MC event samples. All MC samples are generated using the EvtGen and JETSET packages [30, 31]. Final state radiation by charged particles is simulated using the PHOTOS package [33]. The events are then passed through a detailed GEANT4 [32] simulation of the detector which tracks the real run-by-run conditions of the sub-detectors, including backgrounds and aging.

Generic samples are generated for the production of each $q\bar{q}$ flavor. The quarks are then hadronized by JETSET according to the known production and decay rates of mesons and baryons. The signal event samples are generated similarly, but with the condition that the signal decay process be produced in every event.

Table 4.1 lists the number of events for data and the MC samples which are used in this analysis. The equivalent luminosity of each sample is listed on Table 4.2.

Table 4.1: Events used for this analysis (in millions). The *On* and *Off* written in the left-most column refer to data taken on and below the Υ resonance energy. All the D_s^- samples have a $D_s^* \to D_s\gamma$ requirement.

Type	Run1	Run2	Run3	Run4	Run5	Run6	Run7 (Y2S)	Run7 (Y3S)	Total
Data On	292.8	958.7	501.1	1593.0	2103.8	1262.6	419.5	718.5	7849.9
Data Off	33.8	101.1	35.2	149.1	208.4	115.3	43.8	89.5	776.3
$e^+e^- \to$									
$c\bar{c}$ On	55.3	164.7	88.3	267.3	344.6	208.7	37.7	88.5	1255.1
$c\bar{c}$ Off	5.9	17.6	6.5	21.3	37.8	20.5	3.9	9.9	123.1
B^+B^- On	34.9	105.6	56.0	166.8	215.2	130.3	0.0	0.0	708.8
$B^0\bar{B}^0$ On	34.9	104.3	57.9	169.8	216.1	135.2	0.0	0.0	718.3
$\tau\tau$ On	19.7	57.2	49.0	180.1	237.1	139.4	12.2	28.9	723.7
$\tau\tau$ Off	1.9	6.8	9.0	14.5	25.8	14.1	1.3	3.2	76.6
$u\overline{u}, d\overline{d}, s\overline{s}$ On	44.6	185.9	137.5	421.8	554.3	327.0	30.0	67.8	1769.0
$u\overline{u}, d\overline{d}, s\overline{s}$ Off	4.5	20.2	21.1	34.0	60.3	33.0	3.1	8.8	185.1
$D_s \to$									
$\mu\nu$ On	0.98	2.84	1.65	5.06	6.66	3.93	1.45	1.73	24.29
$\mu\nu$ Off	0.13	0.35	0.13	0.41	0.72	0.40	0.20	0.16	2.49
$e\nu$ On	0.39	1.14	0.75	2.03	2.67	1.57	0.19	1.75	10.48
$e\nu$ Off	0.05	0.15	0.05	0.16	0.29	0.16	0.05	0.17	1.07
$\tau\nu; \tau \to$									
$\mu\nu\bar{\nu}$ On	0.634	1.82	0.958	3.034	3.996	2.358	0.372	1.072	14.236
$\mu\nu\bar{\nu}$ Off	0.078	0.218	0.076	0.248	0.436	0.238	0.046	0.116	1.456
$e\nu\bar{\nu}$ On	0.634	1.82	0.958	3.034	3.996	2.358	0.372	1.072	14.236
$e\nu\bar{\nu}$ Off	0.078	0.218	0.076	0.248	0.436	0.238	0.046	0.116	1.456
$KK\pi$ On	1.96	5.69	3.31	10.11	13.32	7.83	0.23	2.44	44.88
$KK\pi$ Off	0.25	0.69	0.25	0.81	1.45	0.79	0.04	0.24	4.53

Table 4.2: Luminosity for each of the generic MC samples (in fb^{-1}). The following cross-sections [41] have been used to convert the number of events to Luminosity: $c\bar{c} = 1.3, B^+B^- = 0.5025, B^0\bar{B}^0 = 0.5025, \tau^+\tau^- = 0.94, uds = 2.09$ (in nb).

Data-Type	Run1	Run2	Run3	Run4	Run5	Run6	Run7 (Y2S)	Run7 (Y3S)	Total
Data On	20.60	62.10	32.70	100.90	133.90	79.00	14.40	28.50	472.10
Data Off	2.60	7.00	2.50	10.20	14.50	7.90	1.50	2.70	49.00
$c\bar{c}$ On	42.50	126.71	67.94	205.62	265.06	160.51	28.99	68.09	965.42
$c\bar{c}$ Off	4.30	13.51	5.02	16.38	29.09	15.80	3.00	7.60	94.69
B^+B^- On	66.43	201.07	106.73	317.68	409.84	248.26	0.00	0.00	1350.02
$B^0\bar{B}^0$ On	66.55	198.76	110.26	323.43	411.60	257.57	0.00	0.00	1368.17
$\tau\tau$ On	20.94	60.84	52.13	191.57	252.23	148.32	13.03	30.79	769.86
$\tau\tau$ Off	2.05	7.27	9.57	15.42	27.43	14.96	1.36	3.44	81.49
$u\overline{u}, d\overline{d}, s\overline{s}$ On	21.33	88.95	65.81	201.82	265.22	156.47	14.37	32.45	846.42
$u\overline{u}, d\overline{d}, s\overline{s}$ Off	2.14	9.67	10.11	16.28	28.87	15.77	1.50	4.22	88.56

Chapter 5

D_S^- Tagging

5.1 Reconstruction of the Charm Hadron D

The event reconstruction begins by creating a list of charm hadron candidates on the tag side of the event using D^0, D^+, and Λ_c^+ decay channels. We use a total of 15 hadronic channels, listed in Table 5.1, which are expected to have high signal yields due to their large branching fractions and efficiencies. Only modes with up to one π^0 are used to avoid large backgrounds.

5.1.1 Basic Selections

The following is a list of initial requirements applied:

- The Kaon candidate tracks used to create each D candidate are required to pass the VeryLoose level of the particle identification algorithm while the pion and proton tracks are required to pass the SuperLoose selector.

- The photons in π^0 decays must have an energy at least 100 MeV in the lab frame and the $\gamma\gamma$ invariant mass must be within 3σ of the mean value for the π^0 signal.

- K_S candidates must have a flight distance from the IP which is at least 3 times its uncertainty.

- For each D candidate the decay products are kinematically fitted to a common vertex. The momentum vector of the D candidate is required to originate from the IP region. The fit probability is required to be larger than 10^{-5}.

- Backgrounds from B meson decays are removed by requiring that the momentum of the D candidate be greater than 2.0 GeV/c.

With these selections we study the purity of the D signal using a small event sample corresponding to about 1/3 of Run 3 OnPeak data. The mass distributions for all D channels are shown in Figures 5.1, 5.2, and 5.3. For all modes the backgrounds are linear and the signal peaks are nearly Gaussian. In the optimization below we use the mean and width of the signal peak, therefore the mass distributions are fit to a simple function consisting of a Gaussian function added with a linear polynomial. These fits are shown in the same Figures and the results of the fits are listed in Table 5.2. The total D signal has a composition of 74.0% D^0, 22.4% D^+, and 3.4% Λ_c^+.

• $D^0 \to K^-\pi^+$	• $D^+ \to K_S\pi^+$	• ${\Lambda_c}^+ \to pK^-\pi+$
• $D^0 \to K^-\pi^+\pi^0$	• $D^+ \to K^-\pi^+\pi^+$	• ${\Lambda_c}^+ \to pK^-\pi^+\pi^0$
• $D^0 \to K_S\pi^+\pi^-$	• $D^+ \to K_S\pi^+\pi^0$	• ${\Lambda_c}^+ \to pK_S$
• $D^0 \to K^-\pi^+\pi^-\pi^+$	• $D^+ \to K^-\pi^+\pi^-\pi^0$	• ${\Lambda_c}^+ \to pK_S\pi^+\pi^-$
• $D^0 \to K_S\pi^-\pi^+\pi^0$	• $D^+ \to K_S\pi^+\pi^-\pi^+$	
• $D^0 \to K^-\pi^+\pi^-\pi^+\pi^0$		

Table 5.1: List of D decay channels used.

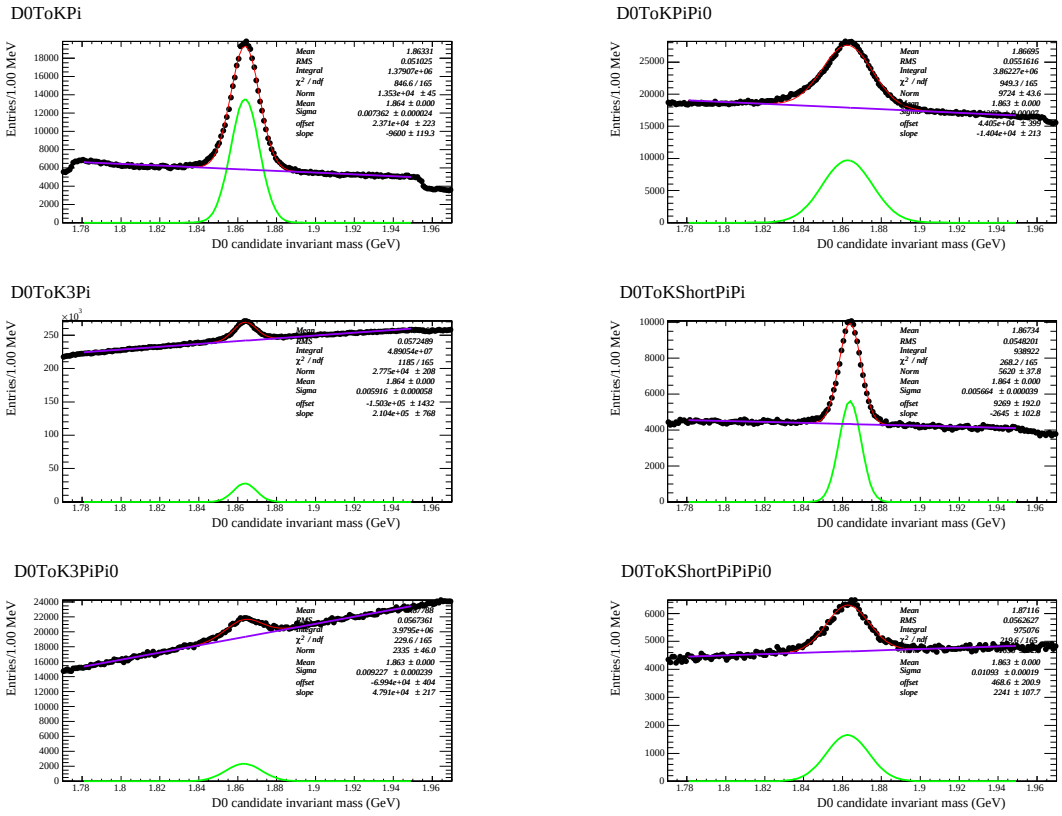

Figure 5.1: Fitted D^0 mass plots. Black points represent data. The red line is the combined Gaussian and linear fit function. The purple line is the linear background and the green line is the signal Gaussian, drawn again for clarity.

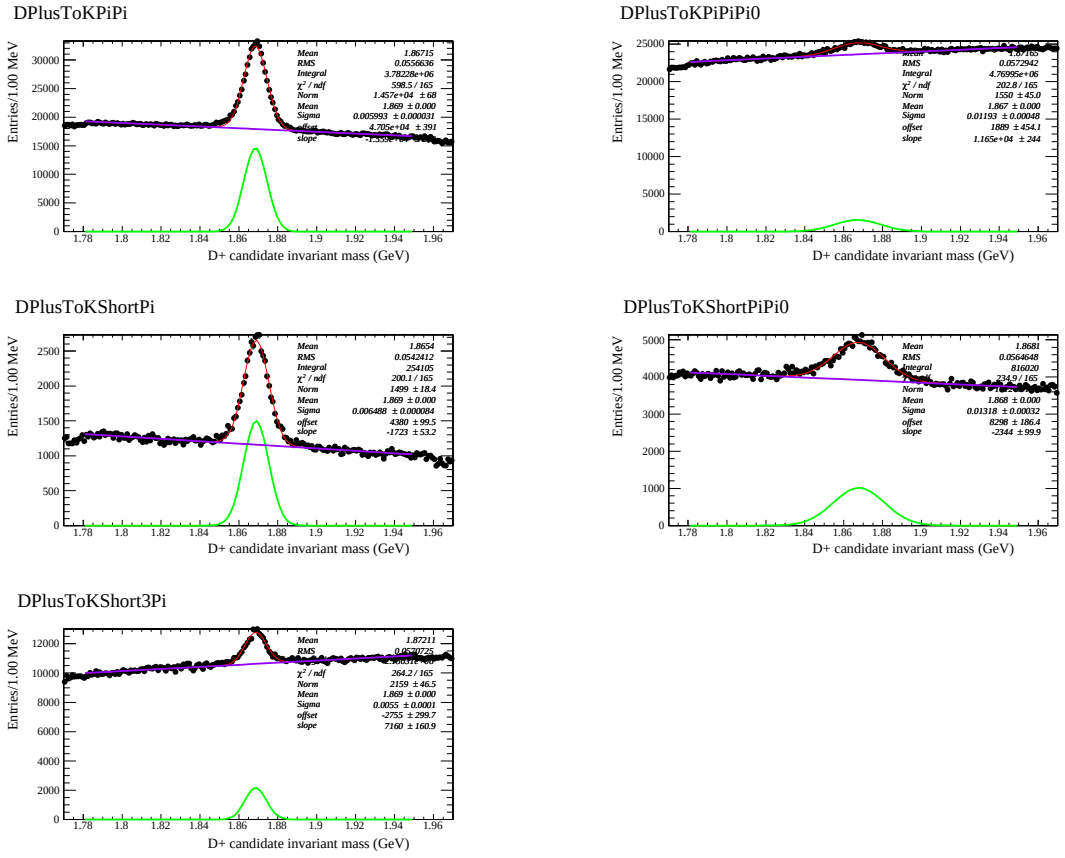

Figure 5.2: Fitted D^+ mass plots. Black points represent data. The red line is the combined Gaussian and linear fit function. The purple line is the linear background and the green line is the signal Gaussian, drawn again for clarity.

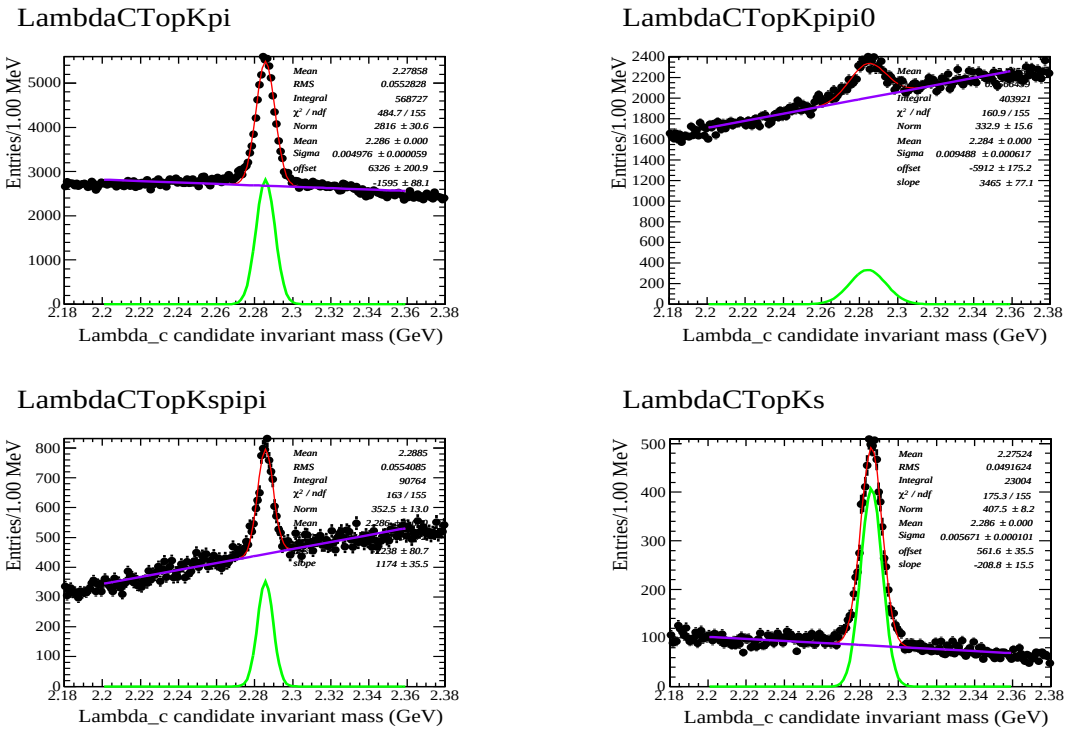

Figure 5.3: Fitted Λ_c mass plots. Black points represent data. The red line is the combined Gaussian and linear fit function. The purple line is the linear background and the green line is the signal Gaussian, drawn again for clarity.

Mode	Mean (GeV)	Sigma (MeV)	Signal Yield	Purity $\frac{S}{(S+B)}$	Significance $\frac{S}{\sqrt{(S+B)}}$	Signal yield (%)
$D^0 \to K^-\pi^+$	1.8638	7.4	248996	0.49	350.1	15.42
$D^0 \to K^-\pi^+\pi^0$	1.8626	12.9	312741	0.18	240.2	19.37
$D^0 \to K^-\pi^+\pi^-\pi^+$	1.8637	5.9	410438	0.05	136.9	25.42
$D^0 \to K_S\pi^+\pi^-$	1.8639	5.7	79578	0.35	167.0	4.93
$D^0 \to K^-\pi^+\pi^-\pi^+\pi^0$	1.8631	9.2	53864	0.05	50.8	3.34
$D^0 \to K_S\pi^+\pi^-\pi^0$	1.8627	10.9	45247	0.13	76.5	2.80
$D^+ \to K^-\pi^+\pi^+$	1.8685	6.0	218352	0.25	235.1	13.52
$D^+ \to K^-\pi^+\pi^+\pi^0$	1.8672	11.9	46206	0.03	35.1	2.86
$D^+ \to K_S\pi^+$	1.8689	6.5	24303	0.35	92.2	1.51
$D^+ \to K_S\pi^+\pi^0$	1.8678	13.2	33354	0.10	56.9	2.07
$D^+ \to K_S\pi^+\pi^+\pi^-$	1.8687	5.5	29685	0.08	48.1	1.84
$\Lambda_c^+ \to p^+K^-\pi^+$	2.2857	5.0	35031	0.30	103.3	2.17
$\Lambda_c^+ \to p^+K^-\pi^+\pi^0$	2.2843	9.5	7895	0.06	22.6	0.49
$\Lambda_c^+ \to p^+K_S$	2.2859	5.7	5776	0.67	62.1	0.36
$\Lambda_c^+ \to p^+K_S\pi^+\pi^-$	2.2856	4.1	3639	0.25	30.1	0.23

Table 5.2: Quantities obtained from the fit to each D mode. The purity and significance in this table is computed on a $\pm 3\sigma$ window about the mean of the peak.

5.1.2 Optimization of the D Signal

In order to improve the signal-to-background ratio of the D candidates, we apply tighter requirements to the D candidate selections.

The purity of K_S candidates is improved by applying a vertex fit with a mass constraint to the nominal mass and requiring a fit probability greater than 10^{-3}. In addition, the distribution of flight distance significance shows much background near 0 due to combinatorial background from the large number of pions originating from the IP (see figure 5.4. A requirement on this variable to be greater than 10 removes most of this background. Likewise the purity of the π^0 candidates is improved by applying a kinematic fit with the mass constrained to the nominal mass and fit probability greater than 10^{-2}.

In addition to the above refinements we optimize the significance of each D decay mode by searching for a set of selections on the following variables:

- Kaon, pion, and proton PID selector level,
- minimum lab energy of π^0 candidate photons,
- size of the window on the D candidate invariant mass,
- CM momentum of the D candidate mass,
- vertex fit probability of the D candidate.

An iteration algorithm is applied to search simultaneously for the selections on these variables which maximize the significance ($S/\sqrt{S+B}$). The background, B, under the D signal in the invariant mass distribution is determined by selecting a side-band region of equal size as shown in Figure 5.5. The definition of the range for each variable during the optimization are listed in Table 5.3. Graphs showing the difference in the D candidate mass distribution before and after the optimization are shown in Figures 5.6 - 5.8. Large improvements on the signal purity are observed for modes with many tracks or π^0s.

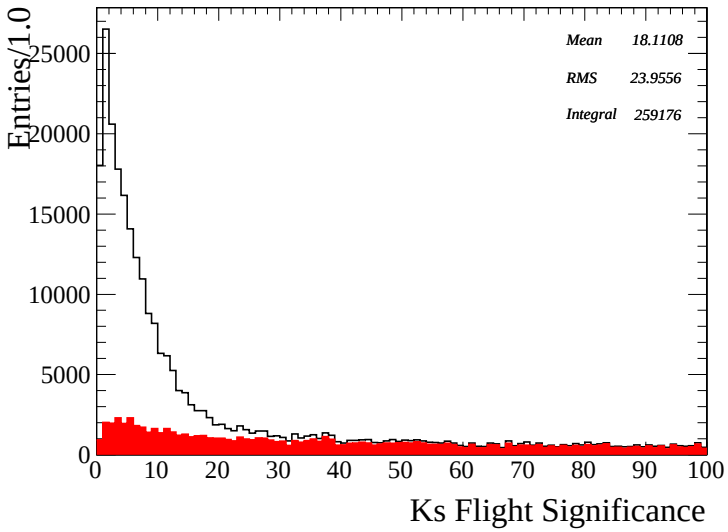

Figure 5.4: Distribution of the K_S candidate flight significance from the IP for generic MC. The open histogram shows the total distribution, the red-filled distribution are true K_S decays.

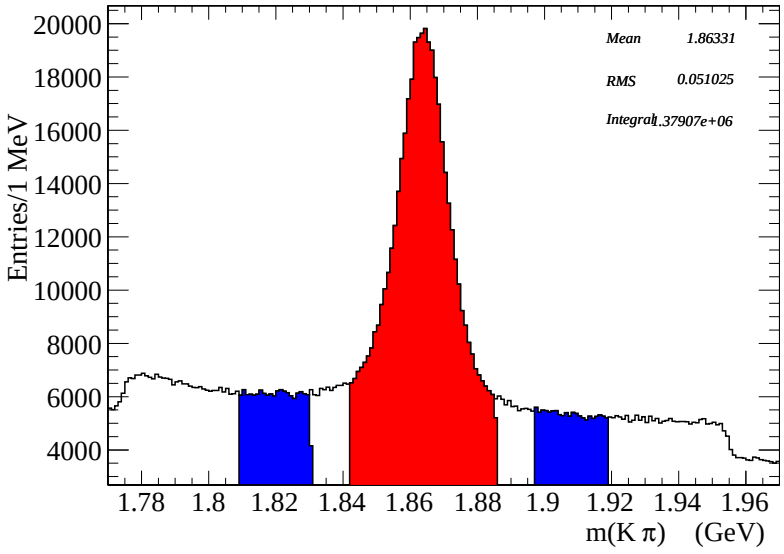

Figure 5.5: Definition of signal and sideband regions. This example plot (for $D^0 \to K^+\pi^-$) shows how S and B were computed for each of the D modes during optimization.

Optimization Variable	Definition	Range Values
pidkmin	Tightest selector passed by K^+ candidate. The track with lower value is used when there is more than one.	• VeryLoose, • Loose, • Tight, • VeryTight
pidpimin	Tightest selector passed by π^+ candidate. The track with lower value is used when there is more than one pion.	• SuperLoose, • VeryLoose, • Loose, • Tight, • VeryTight, • SuperTight
pidprmin	Tightest selector passed by the *proton* candidate.	• SuperLoose, • VeryLoose, • Loose, • Tight, • VeryTight, • SuperTight
probmin	log(D vertex fit probability)	[-5,-1]
pmin	CM momentum of D	[2 GeV,3 GeV]
mwin	size of signal region in D mass (one sided)	1.5 - 3.0 σ (where σ is from the 1 Gauss fit
pi0gamemin	Minimum energy of photons in π^0	100 - 200 MeV

Table 5.3: Definition of the optimization variables. The final selections appear on Figures 5.6 - 5.8.

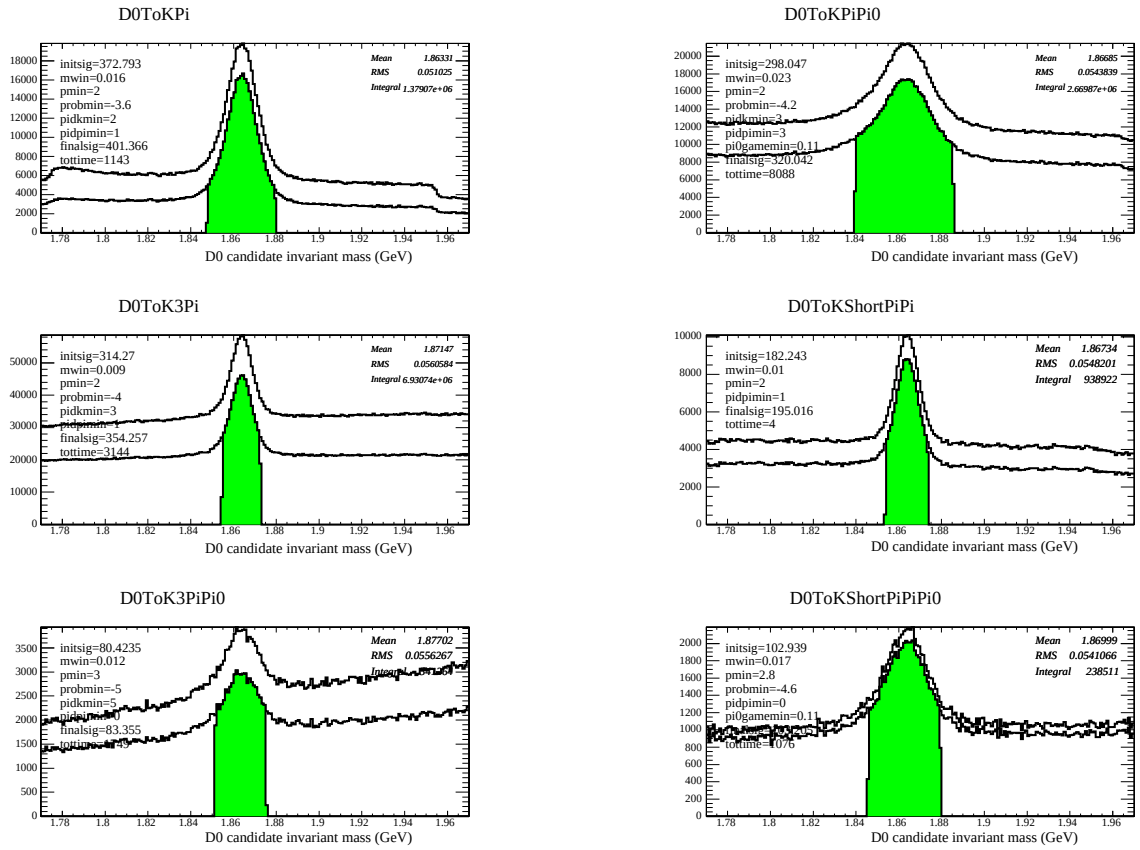

Figure 5.6: Optimized D^0 mass plots. The upper histogram shows the raw D mass distribution. The lower histogram shows the D mass distribution after optimization. The green region shows the optimal mass window.

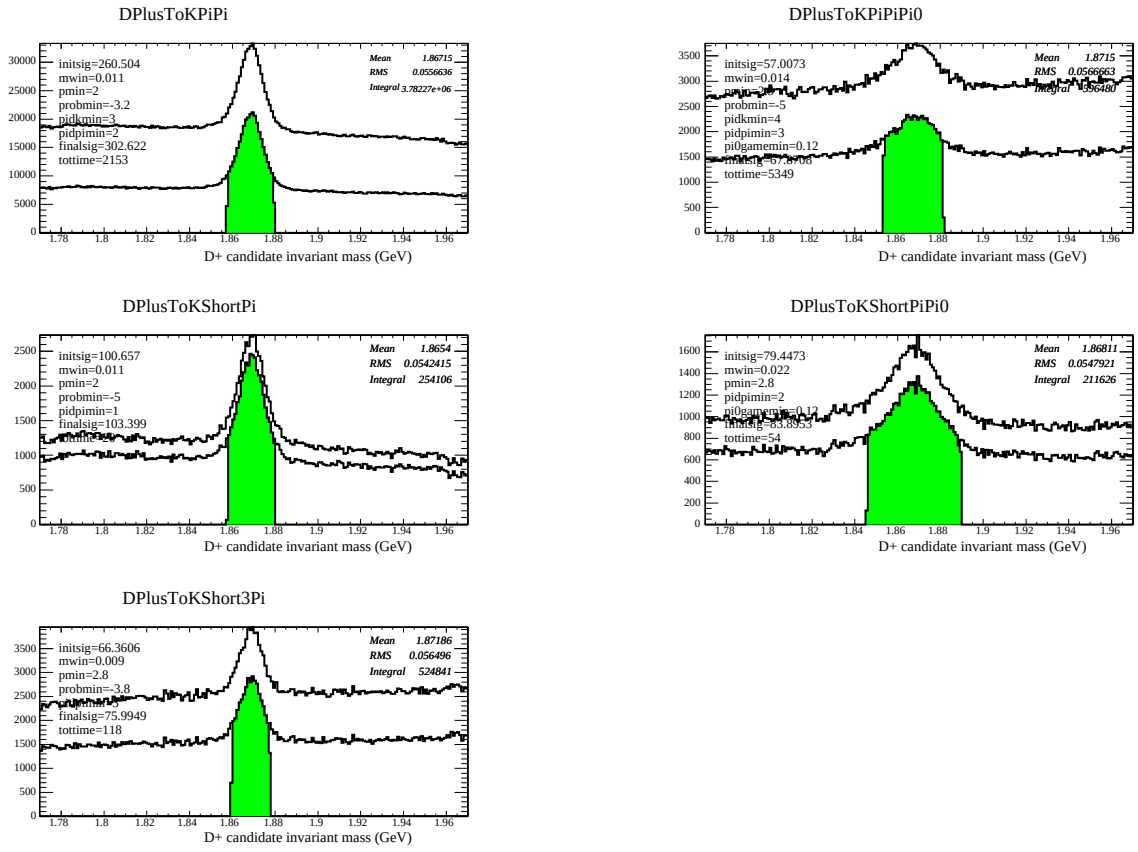

Figure 5.7: Optimized D^+ mass plots. The upper histogram shows the raw D mass distribution. The lower histogram shows the D mass distribution after optimization. The green region shows the optimal mass window.

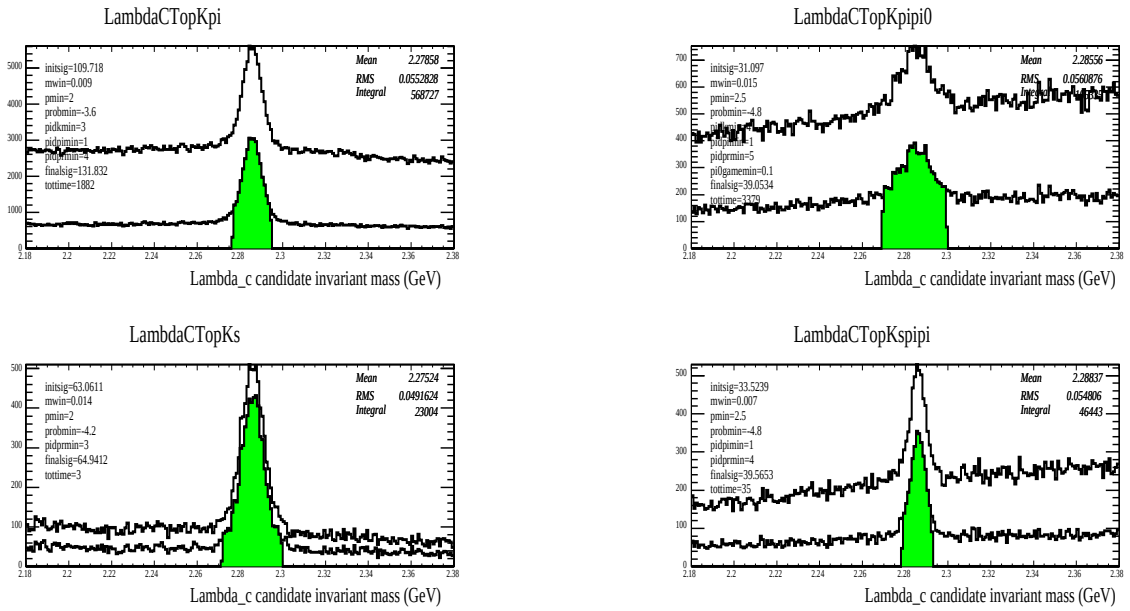

Figure 5.8: Optimized Λ_C mass plots. The upper histogram shows the raw D mass distribution. The lower histogram shows the D mass distribution after optimization. The green region shows the optimum mass window.

5.1.3 Reconstruction of D^* Decays

Once the charm hadron has been reconstructed, D^0 and D^+ mesons originating from D^* decays are identified by reconstructing the decays $D^{*+} \to D^0\pi^+$, $D^{*0} \to D^0\pi^0$, $D^{*+} \to D^+\pi^0$, and $D^{*0} \to D^0\gamma$. The motivation for this reconstruction is to clean up the subsequent $K - X - \gamma$ reconstruction; by absorbing one more particle one will remove subsequent combinatoric background. Also, reconstructing $D^{*+} \to D^0\pi^+$ helps in determining the quark content of D^0 modes which contain a K_S.

The selections for each mode are listed in Table 5.4: The D^* decay is vertexed with constraint requiring the vertex to be within the IP region and requiring a fit probability greater than 10^{-5}. Figure 5.9 shows the distributions of the mass difference between the D^* candidates and the D candidates, Δm. The fraction of D candidates which are assigned to a D^* decay is only about 25% and therefore D mesons which are not identified to come from a D^* are retained in the event analysis.

D* mode	π/γ Selection	Δm selection (MeV)
$D^{*+} \to D^0\pi^+$	π^+ track originating from IP, π^+ momentum $> 100MeV$	143.92 $<\Delta$m$<$ 146.92 MeV
$D^{*0} \to D^0\pi^0$	γ energy $>$ 30 MeV, $115 < m(\gamma\gamma) < 150$ MeV, π^0 energy $>$ 200 MeV	139.12 $<\Delta$m$<$ 145.12 MeV
$D^{*+} \to D^+\pi^0$	γ energy $>$ 30 MeV, $115 < m(\gamma\gamma) < 150$ MeV, π^0 energy $>$ 200 MeV	137.64 $<\Delta$m$<$ 143.64 MeV
$D^{*0} \to D^0\gamma$	γ energy $>$ 250 MeV	131 $<\Delta$m$<$ 151 MeV

Table 5.4: Selections for the D^* reconstruction. The energy cuts are in the Lab frame. The Δm cuts are shown in Figure5.9

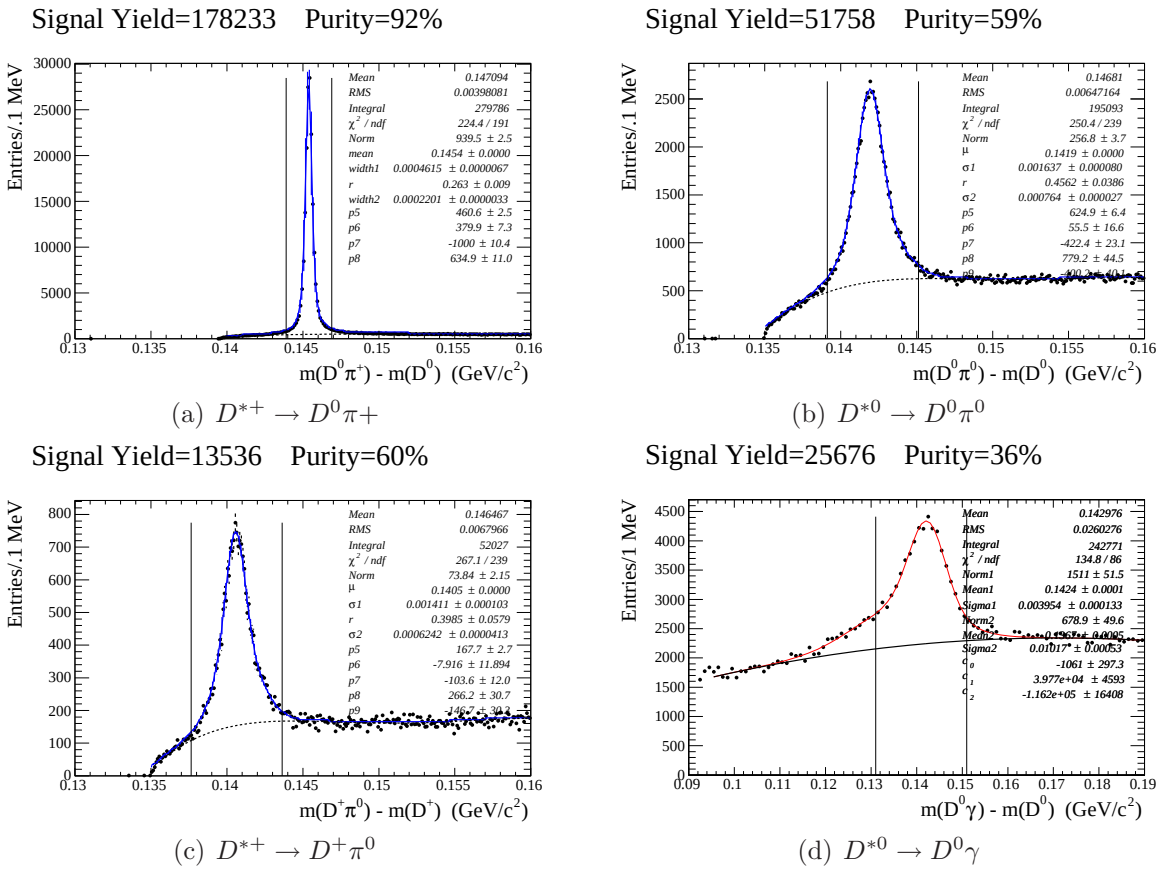

(a) $D^{*+} \to D^0\pi+$ (b) $D^{*0} \to D^0\pi^0$

(c) $D^{*+} \to D^+\pi^0$ (d) $D^{*0} \to D^0\gamma$

Figure 5.9: Δm distributions for each $D*$ mode. Each plot sums over all $D^0/D+$ modes. The fits are done with 2 Gaussians for the Signal and a polynomial background. This study has been done with 1/3 of Run3 On-Peak Data.

5.2 Reconstruction of the Flavor Balancing Kaon: K

Once the charm hadron on the tag side of the event has been reconstructed, a strangeness balancing kaon is required in the tracks in the event which do not overlap with the D candidate. Note that here and below the symbol D represents a charm tag: $D^0, D^+, D^* or \Lambda_c$. Both $K^\pm$ and K_S are used.

- The selection of the K^+ is as follows:
  - The track is required to pass the `VeryLoose` PID selector.
  - the track trajectory must originate from the IP region.
- The selection of the K_S is as follows:
  - The oppositely charged pions are kinematically fitted to a common vertex and with an invariant mass constrained to the nominal K_S value; a fit probability greater than 0.1% is required.
  - The momentum of the K_S must point from the IP.
  - The flight significance from the IP is required to be greater than 5.

The purity of these K^+ and K_S candidates is shown in Figures 5.10 and 5.11. In the case of the Λ_c^+ tags we require an anti-proton in addition to the Kaon, with similar selections as the above K^+, in order to balance the baryon content of the event. From the list of D candidates and the list of K candidates a list of DK combinations is created without any check on the charge or flavor of the mesons. Each DK combination is at this stage an event candidate.

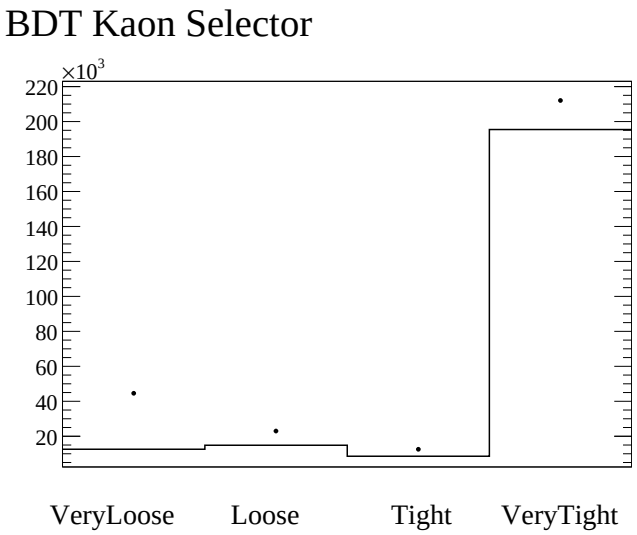

Figure 5.10: Points show the total number of reconstructed events as a function of the tightest selector passed by the flavor balancing K^+ generic MC. The bottom histogram shows the number where the K^+ is truth-matched.

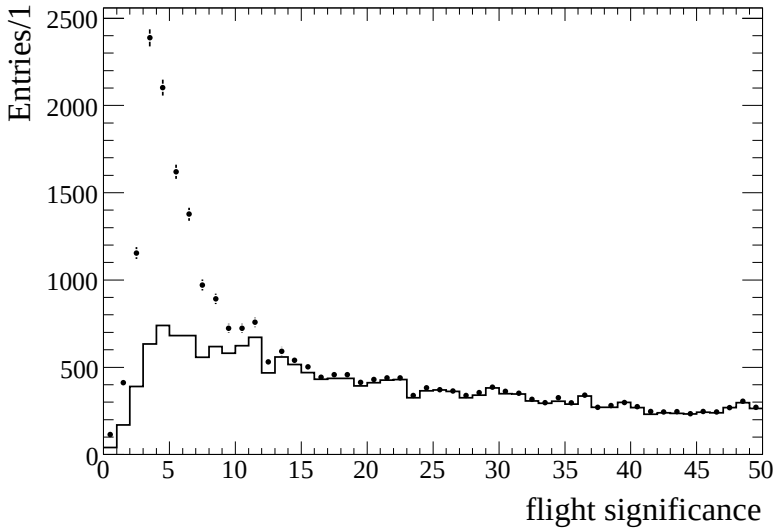

Figure 5.11: Points show the total number of reconstructed events as a function of flight significance of the flavor balancing K_S generic MC. The bottom histogram shows the number where the K_S is truth-matched.

5.3 Reconstruction of the Fragmentation Pions: X

From the remaining tracks and π^0 candidates in the event we construct X candidates in the following modes:

• no pions • $\pi^\pm$ • $\pi^\pm\pi^\pm$ • $\pi^\pm\pi^\pm\pi^\pm$ • π^0 • $\pi^0\pi^\pm$ • $\pi^0\pi^\pm\pi^\pm$

We define the variables n_X^R and n_X^T as the total number of reconstructed pions and the true number of generated pions, respectively. Only modes with upto three charged pions and up to one π^0 are used in order to avoid large combinatoric or photon backgrounds. All charged pions must originate from the IP region and have momentum in the Lab frame of at least 100 MeV, but no PID requirements are necessary because at this point most remaining tracks are pions and other types are mostly removed by the kinematic requirements later. For the π^0 candidates the energy of the photons is required to be greater than 100 MeV, and the $\gamma\gamma$ invariant mass must be within 12 MeVof the mean value 133.3 MeV (determined from a Gaussian fit to the π^0 candidate mass). The purity of the π^+ sample is shown in figure 5.12 and a π^0 mass distribution is shown in figure 5.13.

At this stage no requirement is applied to the total charge of the X system and a list of candidates is created. The list of X candidates is then combined with the list of DK candidates to create every possible DKX combination requiring only that X does not overlap with the DK candidate. Since there are on average several X candidates and several DK candidates, this leads to a large number of DKX candidates per event. For high multiplicity events there can be hundreds of candidates. However, the definition of the Right-Sign and Wrong-Sign samples described later will select only certain charge combinations into each sample. Also the selections after the kinematic fit to the whole event greatly reduce the number of event candidates.

5.4 Reconstruction of the Signal γ

Due to the kinematics of the D_s^{*-} decay the energy of this photon in the Lab is less than 650 MeV. It is merged with photons from π^0 and η decays which are present even in signal events. It also suffers from backgrounds from fake EMC clusters produced from "split-offs" due to tracks and K_L interacting with the EMC. It is therefore responsible for much background in tagging D_s^- events. It is also not kinematically constrained as this is the final particle before the fit for the D_s^- signal yield.

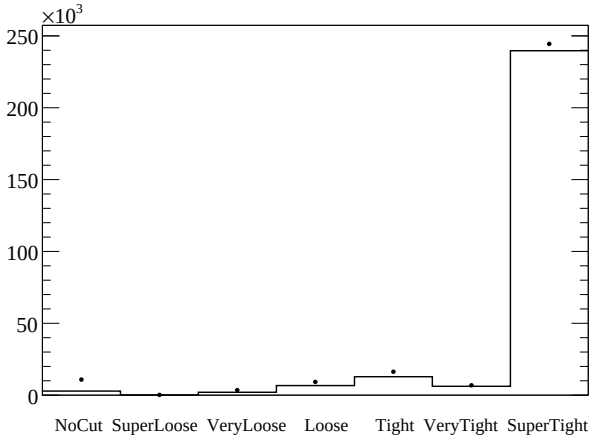

Figure 5.12: Points show the total number of reconstructed events as a function of the tightest selector passed by the worst charged pion in X. The bottom histogram shows the number where the track is a true pion. This plot is produced from the generic MC.

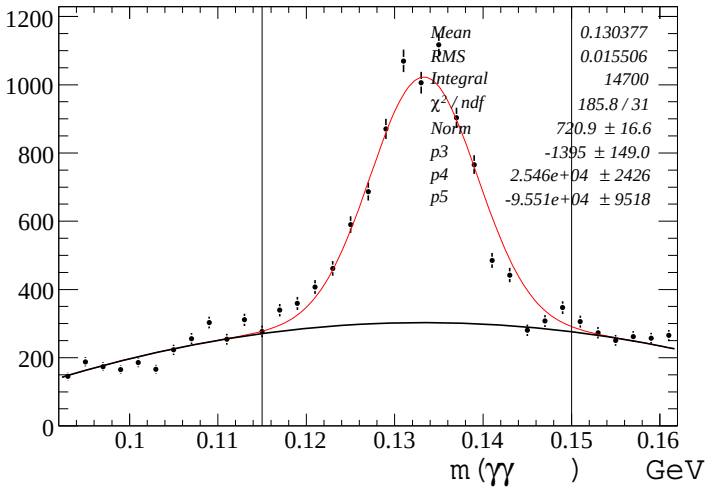

Figure 5.13: Fit to the π^0 candidate mass distribution, vertical lines show the selection on this mass. This plot is produced from the Ds Signal MC.

The energy of this photon candidate is required to be greater than 120 MeV(Figure 5.14). Also, the angle in the CM frame between its momentum direction and the D momentum direction is required to be less 90 degrees since this photon should be on the signal side of the event. Any candidate which overlaps with the list of reconstructed π^0's or η's in the event is vetoed. A large component in the background comes from fake clusters. These clusters are truth-matched to K_L and energy deposits by tracks. To further reduce these backgrounds we apply additional quality cuts to the EMC cluster.

- We require $\cos(\theta)<0.94$ where θ is the angle of the candidate in the Lab. This removes the last few EMC crystals which give mostly background.
- The lateral moment of the EMC cluster is required to be in the range .01 to .6 .
- The distance to the nearest bump is required to be greater than 15 cm.
- The distance to the nearest track is required to be greater than 15 cm.

These cuts are shown in figure 5.15.

We combine the list of photon candidates created above and the list of DKX candidates to create a list of $DKX\gamma$ candidates where the only additional requirement is that the γ candidate does not overlap with the DKX system.

5.5 Definition of Wrong-Sign and Right-Sign samples

Up to now no restrictions have been made on the charge configuration of the $DKX\gamma$ combinations that have been created in the event. A Right-Sign (RS) sample, from which the D_s signal yield will be extracted, is now selected by the following requirements:

- the total charge of the DKX must be +1, consistent with recoiling from a D_s^-,
- the charm-strange quark content of the DK system must balance that of the signal D_s^-.

Event candidates for which the quark flavor cannot be determined due to a K_S are retained. The RS sample requirements attempt to select the following signal configurations:

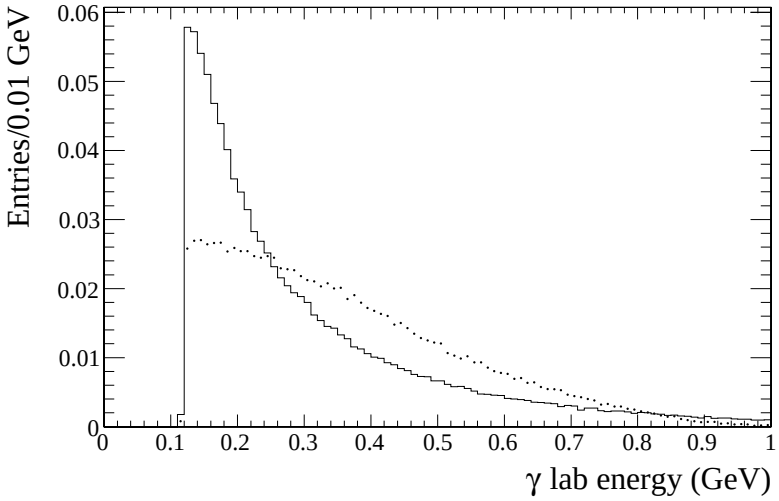

Figure 5.14: γ lab energy distribution for signal photons (points) and background γ candidates (histogram) in the Signal Ds MC.

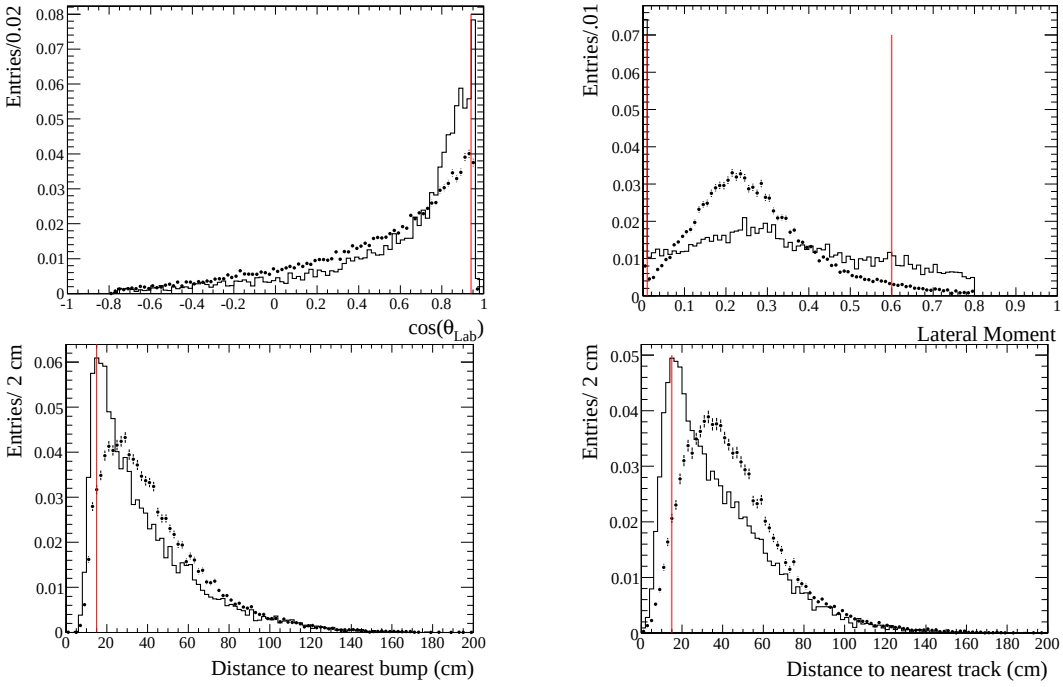

Figure 5.15: Variables used to refine the basic photon selection, the cuts are shown with a vertical line. The points show the Signal distributions and histogram shows the background (track/K_L) distributions. This study has been done with Run3 Ds Signal MC.

- D^0, K^+, X^0
- D^0, K_S, X^+
- D^+, K_S, X^0
- D^+, K^+, X^-

In a similar manner we define a Wrong-Sign (WS) sample from which the shape of the RS background is extracted. For this sample we impose the same charge requirement as for the RS sample, but now we require that the charm-strange quark content of DK be the same as the D_s^- candidate. This requirement is used to reject signal events and retain event candidates which are kinematically similar to the RS background events. The list of the DKX combinations in the WS sample are the following:

- $\overline{D}^0$, K^-, X^{2+}
- $\overline{D}^0$, K_S, X^+
- D^-, K_S, X^{2+}
- D^-, K^-, X^{3+}

The Wrong-Sign definition does not reject all signal events for two reasons:

- Events which have been misreconstructed and the reconstructed charge is incorrect so that the D_s quark flavor is incorrectly assigned.
- If the tag-D is reconstructed in a D^0 which decays to a K_S we cannot tell the flavor of the charm quark except when a D^* has been reconstructed, also when the K is a K_S we cannot tell the flavor of the strange quark.

The main contribution comes from the charge misreconstruction. The amount of signal leaking into the WS sample is about 10% relative to the signal passing into RS sample. These events create a peaking component which will be removed in the fit. The Wrong-Sign sample defined in this way, where one removes the leaking signal events, has been found to model the background very well in the MC.

5.6 Kinematic Fit to the DKX and $DKX\gamma$ Systems

Having fully defined the event candidates, a kinematic fit is performed to the DKX and $DKX\gamma$ systems. For signal events these fits correspond to the recoiling D_s^{*-} and D_s^- mesons, respectively. The fit to the DKX system is performed as follows:

- the D candidate mass is constrained to the nominal value,
- the DKX vertex is required to be within the IP region,
- a beam-energy constraint is applied on the DKX system in order to determine the D_s^{*-} 4-momentum as the missing 4-momentum in the event,
- the fit probability is required to be greater than 10^{-5}.

The fit to the $DKX\gamma$ system is performed in a similar way in order to determine the 4-momentum of the D_s^-. In this fit mass recoiling against the DKX system is constrained to the D_s^{*-} nominal mass value.

5.7 Final Selections on the D_s^{*-} and D_s^- Candidates

In Signal MC events we can observe a well defined D_s^{*-} peak from which we can determine the resolution of reconstructed events. This resolution depends on the X decay mode. Table 5.5 lists the fitted values for the mean and sigma of the reconstructed D_s^{*-} mass peak for different X decay modes determined from the distributions in Figures 5.16 and 5.17. The fit is done with a simple Gaussian plus 2nd order polynomial. Only candidates within $\pm 2.5\sigma$ of the mean value are selected. Finally, the CM momentum (p^*) of the D_s^- candidate is required to be greater than 3.0 GeV and the mass must greater than 1.82 GeV.

X **pion content**	**Mean (MeV)**	**Sigma (MeV)**
$0\pi^{\pm}$, 0 π^0	2116	63.3
$1\pi^{\pm}$, 0 π^0	2116	49.9
$2\pi^{\pm}$, 0 π^0	2116	46.2
$3\pi^{\pm}$, 0 π^0	2116	37.3
$n\pi^{\pm}$, 1 π^0	2144	55.1

Table 5.5: Fitted mean and sigma values for the reconstructed D_s^* mass peak in the signal MC.

After these final selections the number of $DKX\gamma$ candidates per event is reduced to about 1.7 per event as shown in Figures 5.18-5.20. The majority of background candidates are due to fake signal γ candidates and is therefore irreducible. In order to provide a true count of the reconstructed signal events each D_s^- (or $DKX\gamma$) candidate is deweighted by $w = 1/n$ where n is the number of candidates in the event in the fits for signal yields described later. The mass distribution of the D_s^- candidates in signal MC is shown in Figure 5.21 and shows the different backgrounds which form a long tail in the distribution.

The distribution of D_s^- candidates for generic MC is shown in Figures 5.22 and 5.23. The MC shows a small peaking background under the D_s^- signal, this background arises from $D^{*0} \to D^0\gamma$ decays which are kinematically similar to the D_s^{*-} decays. As will be seen later the WS sample models the backgrounds well, including this peaking component.

A important part of the analysis in the branching fraction calculation later is the correction of the MC efficiencies for the mismodeling of the fragmentation functions which affect the number of pions in the X system. Figures 5.24 and 5.25 show the distribution of events as a function the number of reconstructed pions in X for MC and Data. It is evident that the signal events have a larger weight at lower number of pions.

The background model for the RS background is determined from the WS sample, Figures 5.26 and 5.27 show the mass distributions as a function of n_X^R. Due to the definition of the WS sample, which requires X to be charged, at least one charged pion must be included and no events pass for the n_X^R=0 bin.

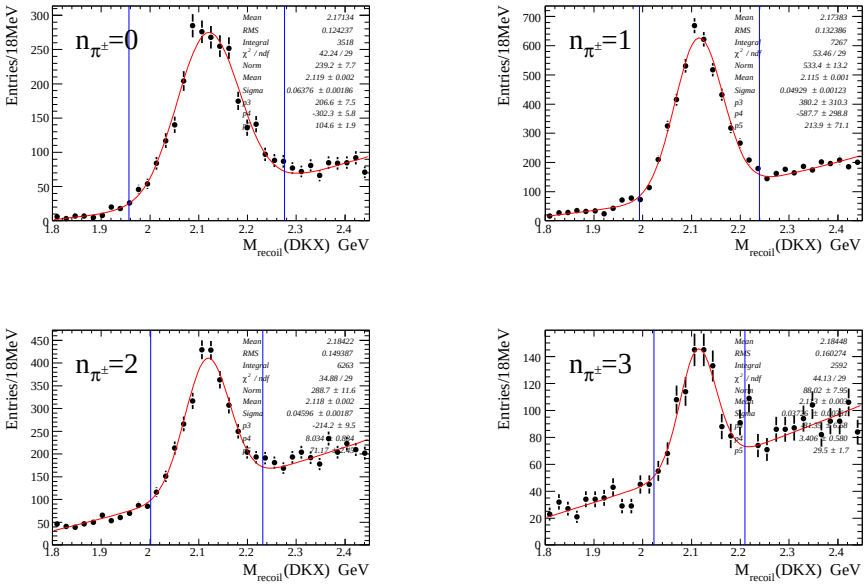

Figure 5.16: D_s^* mass distribution of Signal MC events where the mass constraint on the D_s^{*-} has been removed as a function of the number of charged pions in X. Only X decay modes without π^0's are shown. This study was done with 10% of total Signal MC.

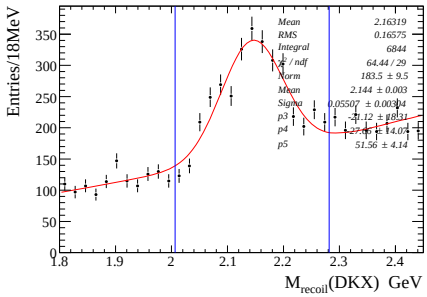

Figure 5.17: D_s^* mass distribution of Signal MC events where the mass constraint on the D_s^{*-} has been removed. This plot is for all the X modes which have 1 π^0. This study was done with 10% of total Signal MC.

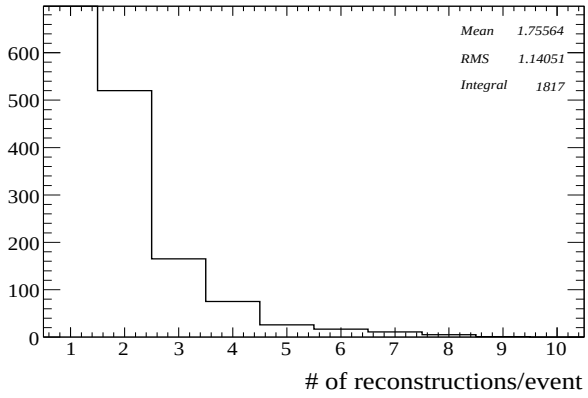

Figure 5.18: Reconstruction multiplicity for signal MC events.

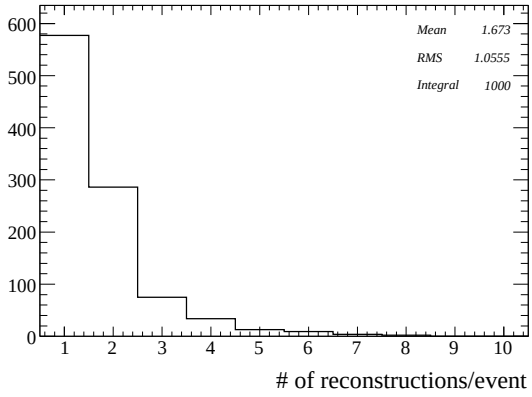

Figure 5.19: Reconstruction multiplicity in generic MC.

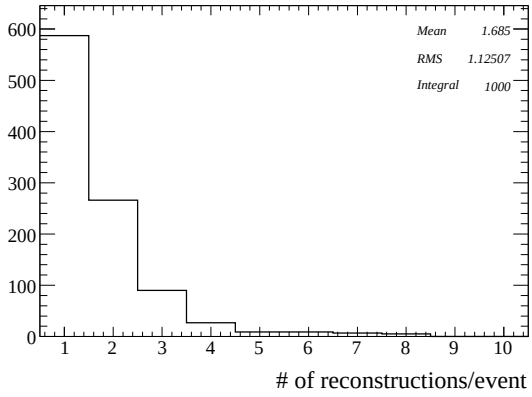

Figure 5.20: Reconstruction multiplicity for Data.

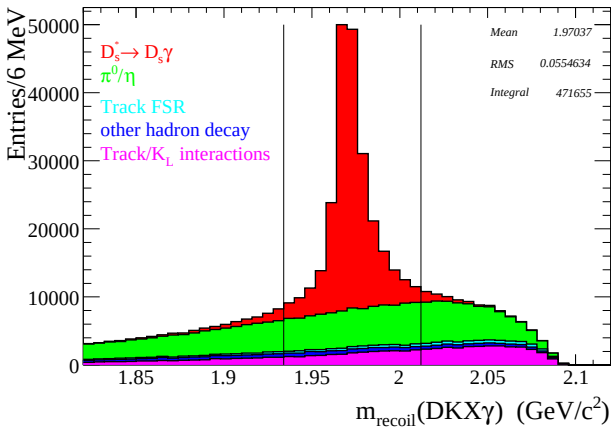

Figure 5.21: Reconstructed D_s mass categorized by the source of the signal γ. From top to bottom:
Red = true γ from D_s^* decay,
Green = π^0/η decays,
Light-Blue = photons radiated by a track,
Blue = photons from meson/baryon decays $(\eta', D*^0, D_s(2460), \Omega, \Sigma^0)$,
Pink = fake photons from tracks/K_L hitting the EMC.

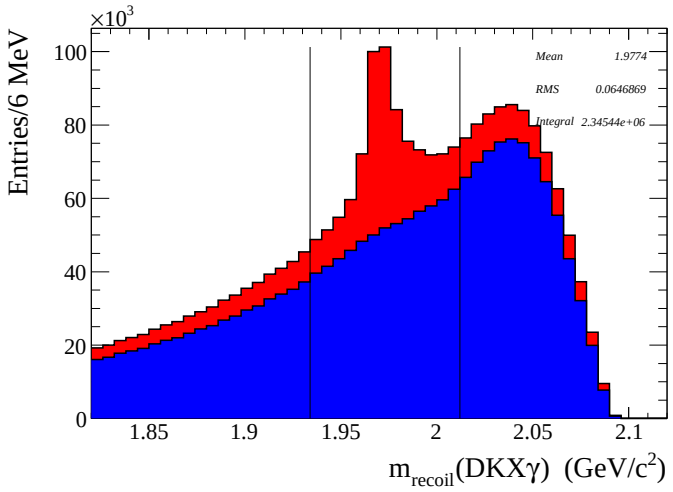

Figure 5.22: Reconstructed D_s^- mass distribution in the generic MC RS sample. red) Signal Events, blue)the rest.

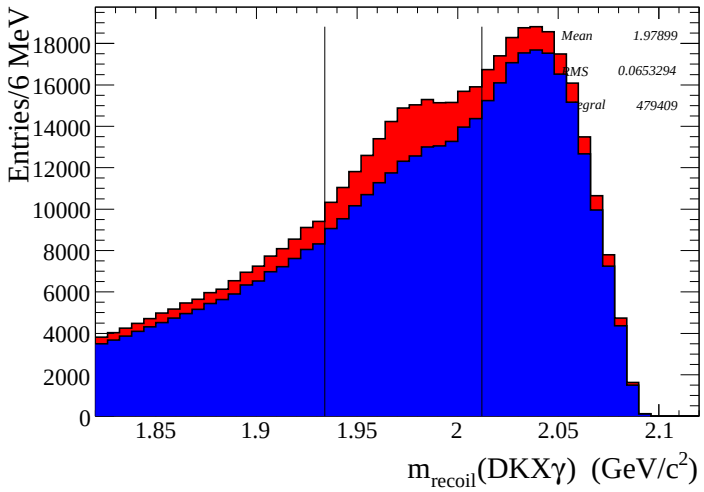

Figure 5.23: Reconstructed D_s^- mass distribution in the generic MC WS sample. red) Signal Events, blue)the rest.

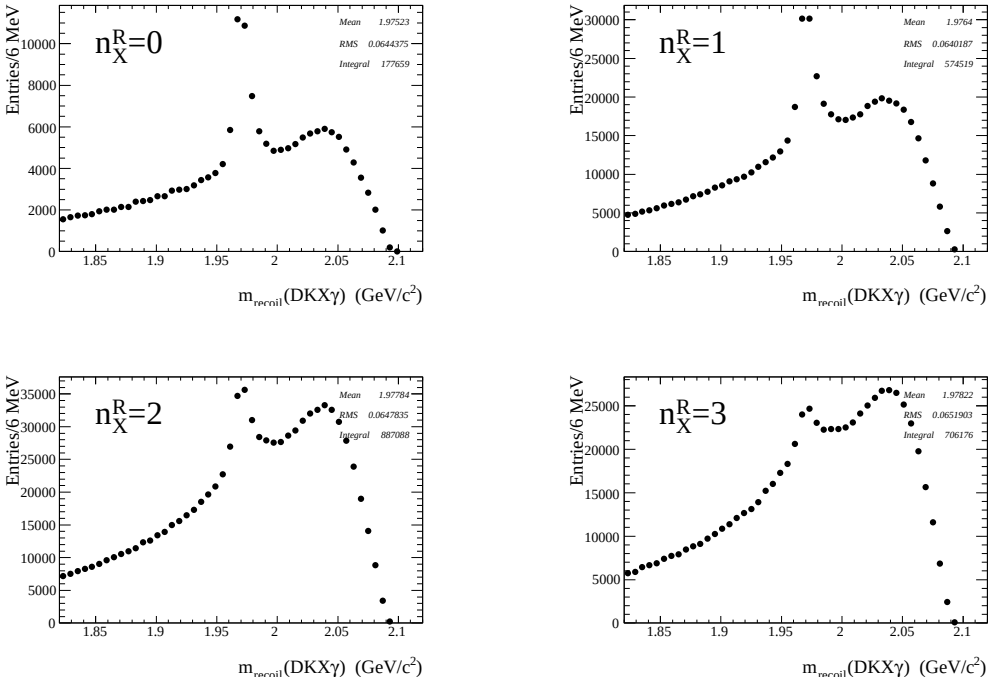

Figure 5.24: Reconstructed D_s^- mass distribution in the generic MC RS sample categorized by n_X^R.

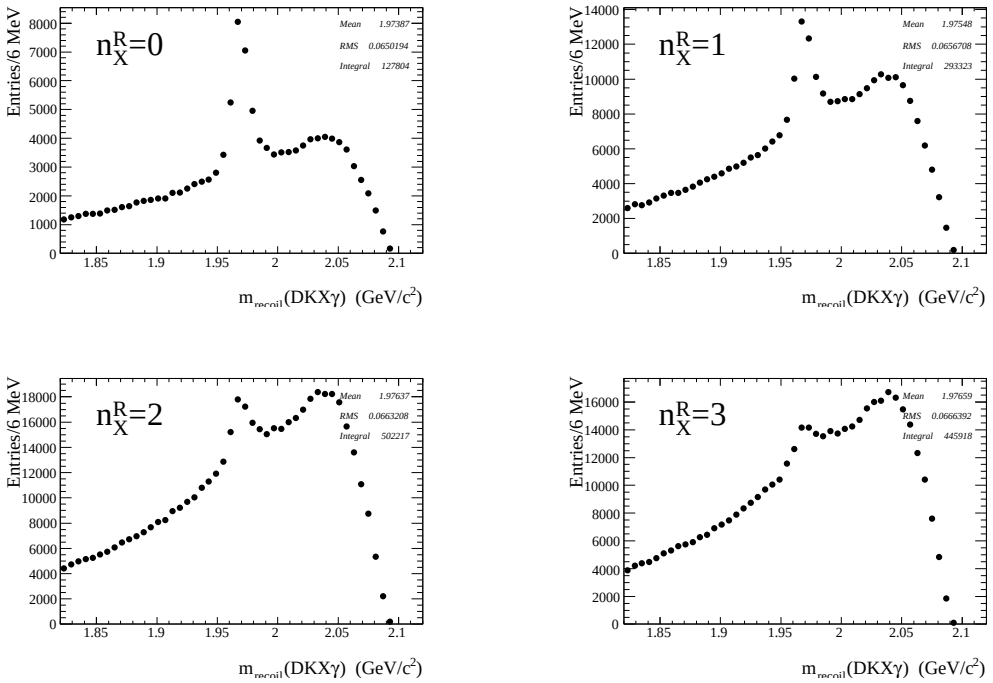

Figure 5.25: Reconstructed D_s^- mass distribution in the data RS sample categorized by n_X^R.

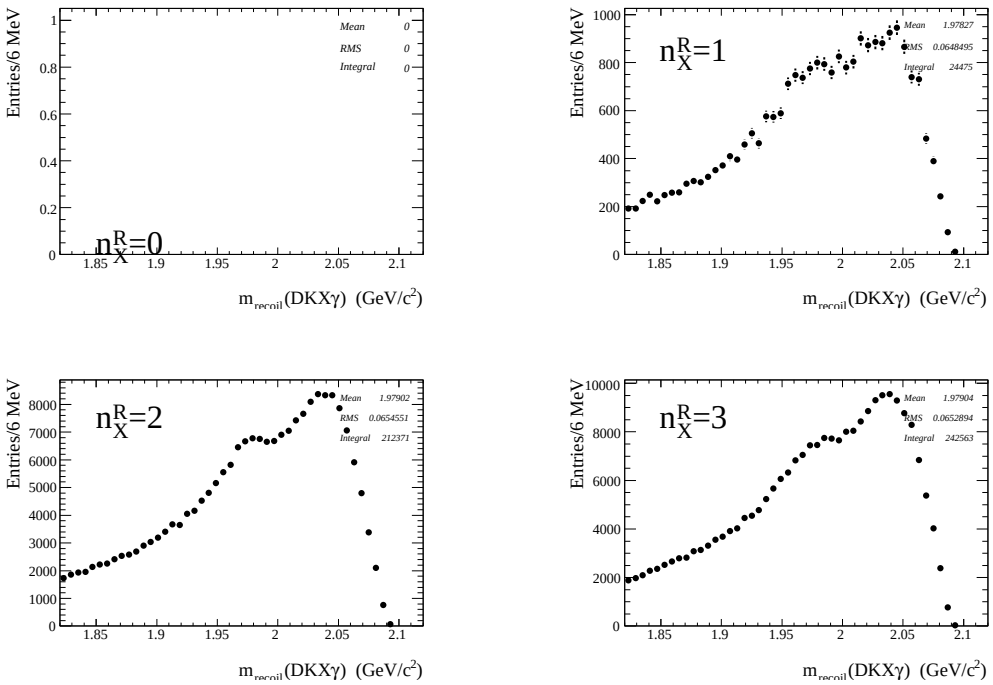

Figure 5.26: Reconstructed D_s^- mass distribution in the generic MC WS sample categorized by n_X^R.

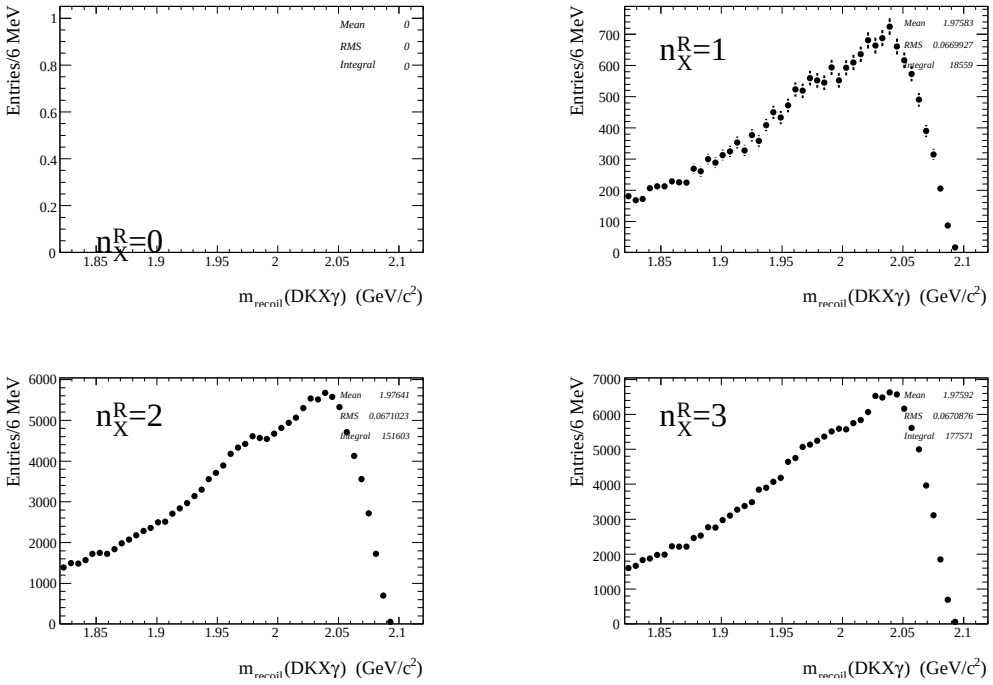

Figure 5.27: Reconstructed D_s^- mass distribution in the data WS sample categorized by n_X^R.

5.8 Fit for the D_s^- yield and Weights

The discrepancy between MC and Data in the distribution of the number of fragmentation pions (mentioned in the previous section) is expected since it is known that JETSET does not model charm hadron momentum distributions well and this affects the free energy for production of fragmentation pions. Therefore, the efficiency for signal events is determined from the MC for each value of n_X^T. In addition we extract the D_s^- signal yield as a function of n_X^T and during the branching fraction calculations later each signal yield is corrected by the corresponding efficiency in order to remove the mismodeling by the MC. The reconstructed events, however, do not directly determine the value of n_X^T due to misreconstruction of the X system. Significant crossfeed from a given value of n_X^T to different values of n_X^R is observed as shown in Figure 5.28. The extraction of the inclusive D_s^- signal yield as a function of n_X^T must be determined indirectly by performing a by fit to the 2-dimensional distribution of $m_{recoil}(DKX\gamma)$ v.s. n_X^R. Figures 5.29 and 5.30 show the 2-D distribution of the RS sample for MC and Data. In addition, a similar fit to the WS sample is performed simultaneously to determine the background shape for each value of n_X^R, Figures 5.31 and 5.32 show the 2-D distribution of the WS samples.

In order to perform the RS fit, the RS signal MC is separated into seven n_X^T components and a non-parametric probability distribution function (histogram PDF) is created from each sample: $S_j^{RS}(m, n_X^R)$ $(j = n_X^T = 0...6)$. These signal PDFs are shown in figure 5.33. These PDF's are then added with undetermined coefficients (weights) to create the total signal PDF:

$$S_{Tot}^{RS}(m, n_X^R) = \sum_{j=0}^{6} w_j^{RS} S_j^{RS}(m, n_X^R) \tag{5.1}$$

The weights are defined so that they are normalized to unity:$\sum_{j=0}^{6} w_j = 1$. A plot of this model is shown later in Figure 5.35.

Initially, a fit has been attempted where all the weights above have been floated independently, however MIGRAD cannot find a well defined solution and returns an unconverged result with ill-defined covariance matrix. These problems are attributed to the cross-feed in the n_X distributions. In order to extract a well defined distribution for the weights, they are constrained by the following parametrization:

$$w_j^{RS} = \frac{(j-\alpha)^\beta e^{-\gamma j}}{\sum_{k=0}^{6}(k-\alpha)^\beta e^{-\gamma k}} \tag{5.2}$$

where the sum in the denominator imposes the unit normalization of the weights. The

parameters α, β, and γ can all be determined in the fit to the MC, however we find that Data is not sensitive to α; MINUIT returns $\alpha = -3 \pm 20$, but the fit does not converge properly. This feature can be understood by noting that the Data prefers a distribution in n_X^T which is at lower values compared with the MC, the distribution is highest at $n_X^T = 0$ and falls at higher values, by contrast the MC rises then decreases giving the sensitivity. A simple fit to the MC weights (Figure 5.35) gives $\alpha = -1.32 \pm .08$, this parameter will be fixed to this value in the nominal fit to Data.

A similar signal PDF is constructed for the WS fit in order to remove the peaking component in this sample:

$$S_{Tot}^{WS}(m, n_X^R) = \sum_{j=0}^{6} w_j^{WS} S_j^{WS}(m, n_X^R) \tag{5.3}$$

These signal PDFs are shown in Figure 5.34. However, none of these weights are floated because the amount of peaking signal is small and the fit cannot determine them. These weights are fixed to the MC values shown in Figure 5.36 and table 5.6.

The total background PDF for RS fit is constructed such that the background yields for each n_X^R can float:

$$B_{Tot}^{RS} = \sum_{i=0}^{3} b_i B_i^{RS} \tag{5.4}$$

where $b_3 = (1 - \sum_{i=0}^{2} b_i)$ for normalization. The individual background PDF's B_i^{RS} are be determined during the fit as described below.

The total PDF for the RS fit is then:

$$P(m, n_X^R) = y^{RS} S_{Tot}^{RS}(m, n_X^R) + (1 - y^{RS}) B_{Tot}^{RS}(m, n_X^R) \tag{5.5}$$

where y^{RS} is the fractional signal yield. The RS sample is fit by minimizing the χ^2 on the 2D binned histogram:

$$\chi^2 = \sum_{i}^{all\ bins} \frac{(N_i - N_{Tot}^{RS} P_i)^2}{(\sigma_i^N)^2 + (N_{Tot}^{RS} \sigma_i^P)^2} \tag{5.6}$$

Where the normalization constant N_{Tot}^{RS} is just the total number of events, $\sigma_i^N = \sqrt{N_i}$ is statistical error on the i'th bin, and P_i is the value of the total PDF at the ith bin. The extra error σ_i^P is the statistical error, for the i'th bin, from the limited size of the samples used to create the signal and background PDFs.

The fit is then performed by the following steps:

1. an initial guess is made for the total RS signal yield: y^{RS},

2. using the MC value for (WS signal yield)/(RS signal yield), the total WS signal yield is determined,

3. the total WS signal PDF is scaled to the WS signal yield and then subtracted from the WS sample,

4. the remaining 2D WS distribution is composed of three 1D distributions, one for each n_X^R see figure 5.37. After normalizing these distributions to unit integral they are labeled B_i^{WS}.

5. The RS background distributions are now defined as:

$$B_0^{RS} = C(m)\frac{1}{3}\sum_{i=1}^{3} B_i^{WS}, \quad B_1^{RS} = \frac{1}{3}\sum_{i=1}^{3} B_i^{WS}, \quad B_2^{RS} = B_2^{WS}, \quad B_3^{RS} = B_3^{WS} \quad (5.7)$$

   Where for $n_X^R = 0$ and $n_X^R = 1$ the PDF is an average of the other distributions. These distributions do not vary much (see Figure 5.38). $C(m)$ is a mass dependent factor that corrects for a discrepancy between the true RS background and the model created this way (see Figures 5.39 and 5.40), this correction is determined from MC. Although there exists a WS background distribution for $n_X^R = 1$ the statistical errors are large for this bin therefore the average gives better precision.

6. After assigning values for the RS weight parameters β and γ, and background parameters b_i, the total RS PDF is evaluated and the χ^2 is computed.

The above algorithm is implemented with MINUIT, and MIGRAD iterates changing the values of the D_s yield, weight parameters, and background parameters until the χ^2 is minimum.

In the procedure above the ratio WS-to-RS signal yield is fixed to the MC value. In the MC where the statistical precision is good the fit can determine the WS yield precisely , however in the Data this yield has a 50% error because the peaking component is less prominent and because the Data size is only about half the size of the MC.

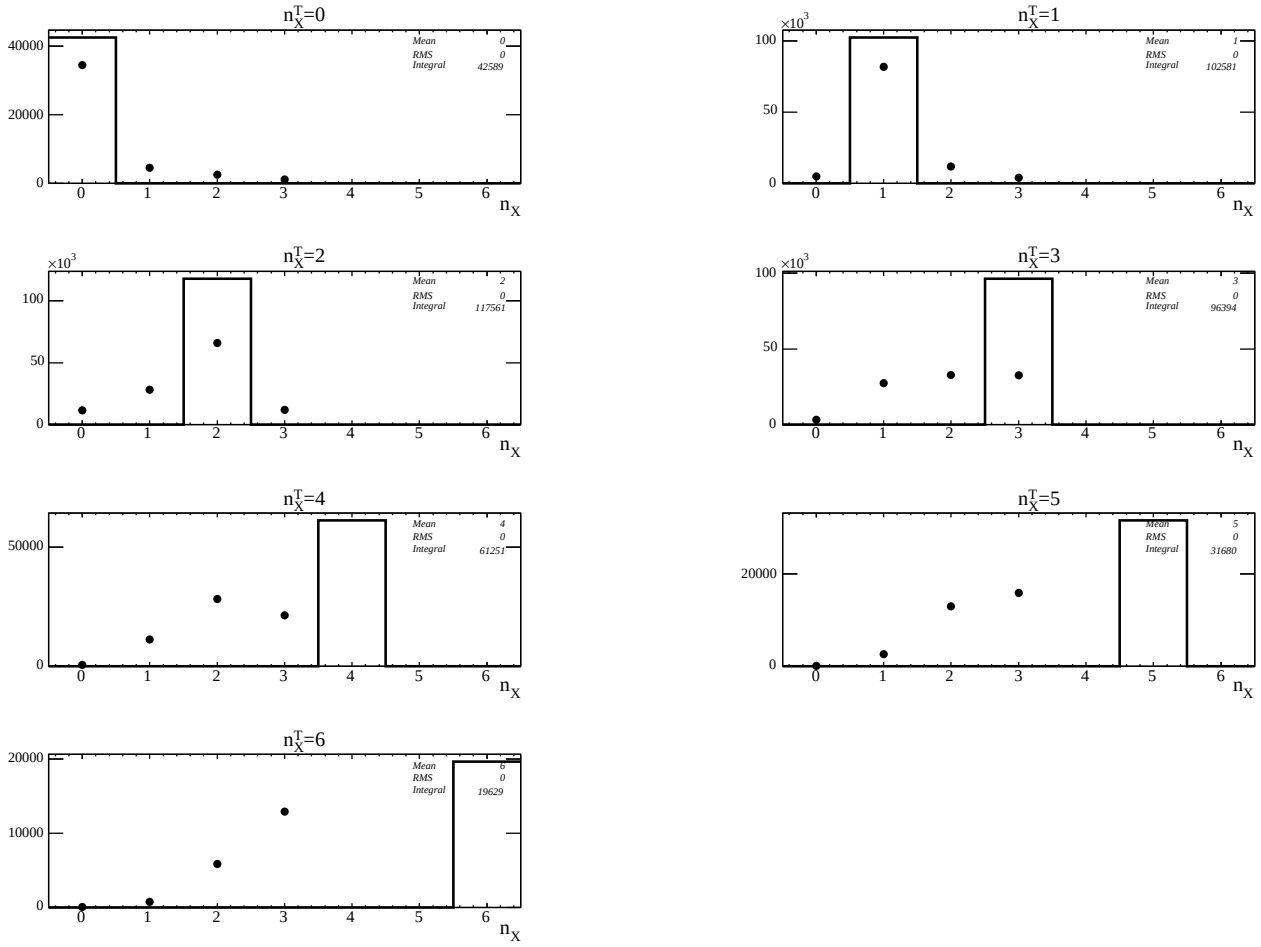

Figure 5.28: Number of pions in X for events which pass the full selection criteria. The 1 bin histogram in each plot shows where the true number of pions was generated, the points show where those were reconstructed.

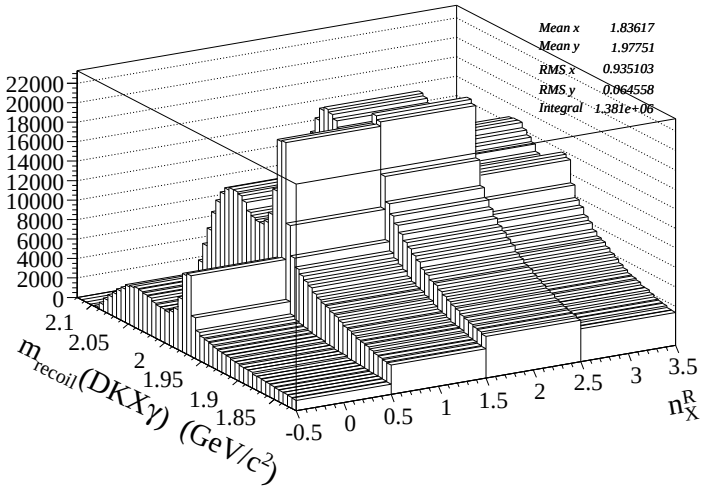

Figure 5.29: Reconstructed 2D distribution of RS MC events.

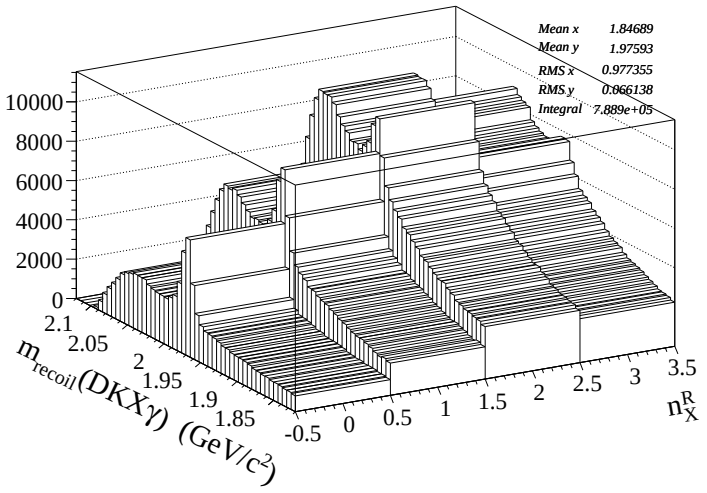

Figure 5.30: Reconstructed 2D distribution of RS Data events.

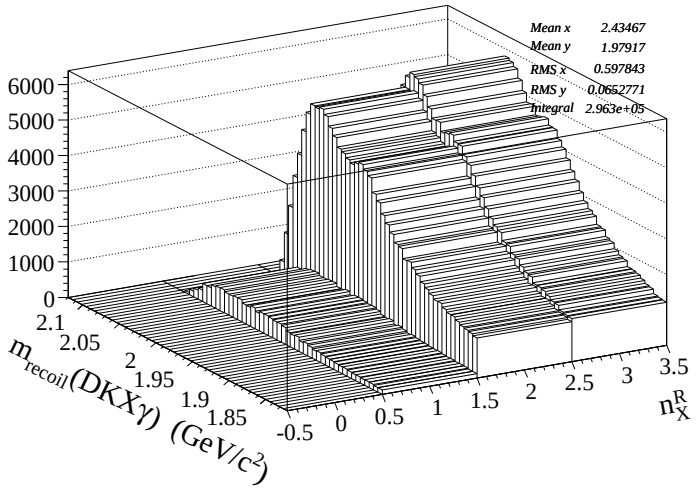

Figure 5.31: Reconstructed 2D distribution of WS MC events.

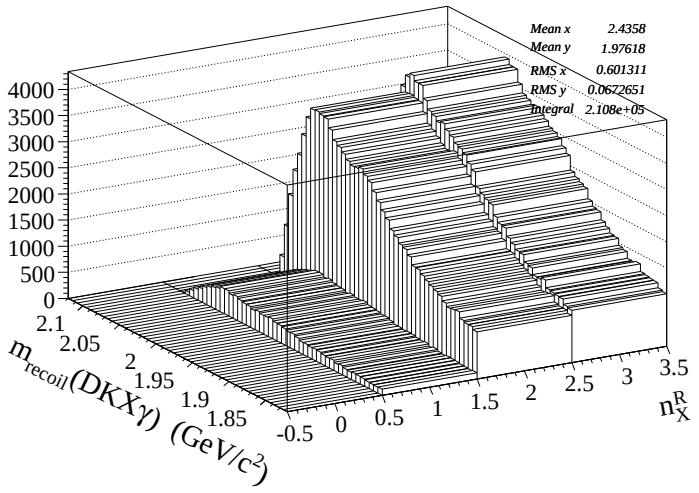

Figure 5.32: Reconstructed 2D distribution of WS Data events.

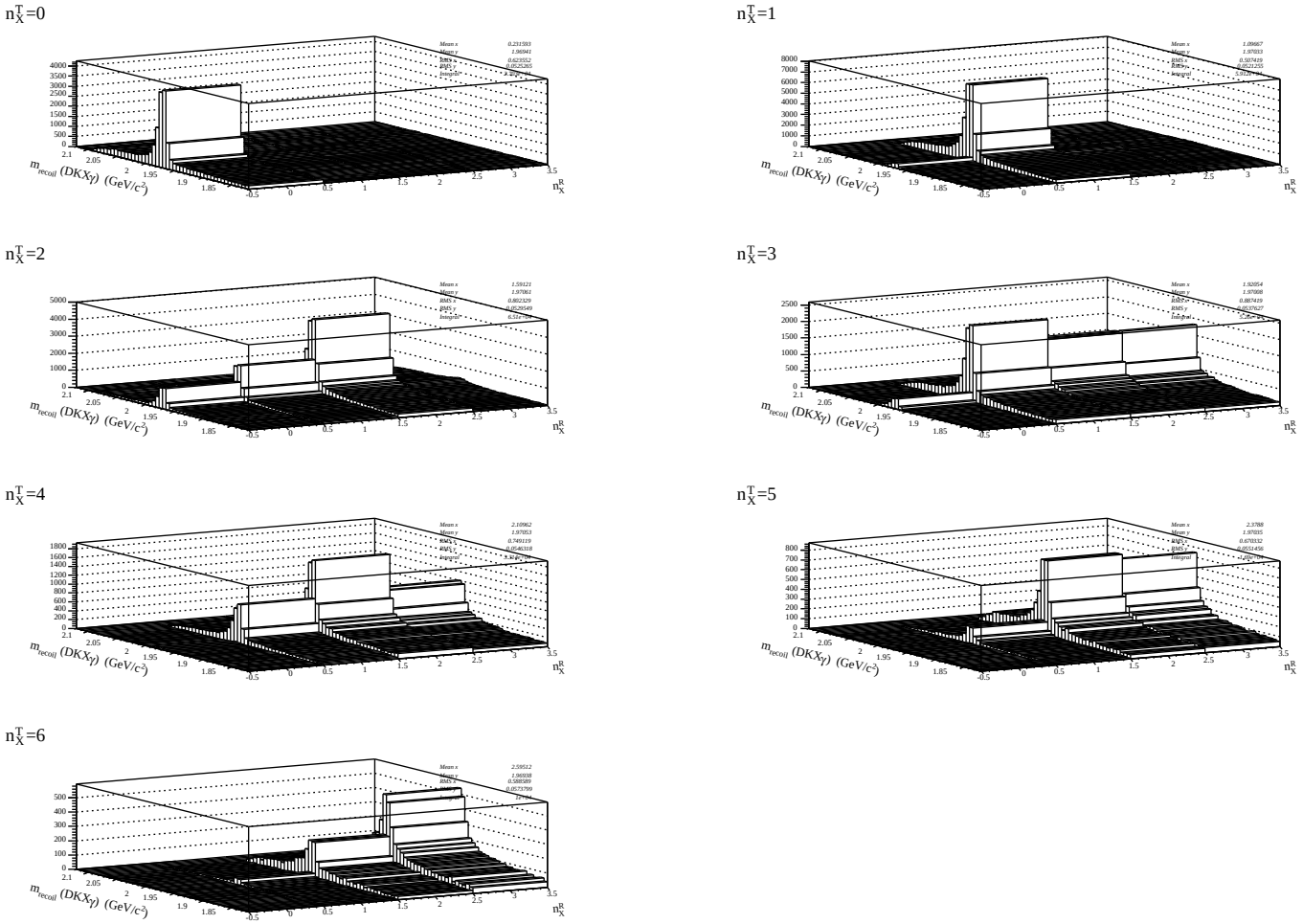

Figure 5.33: 2D RS Signal PDF's, determined from the signal MC, used to fit the signal component in the RS Data.

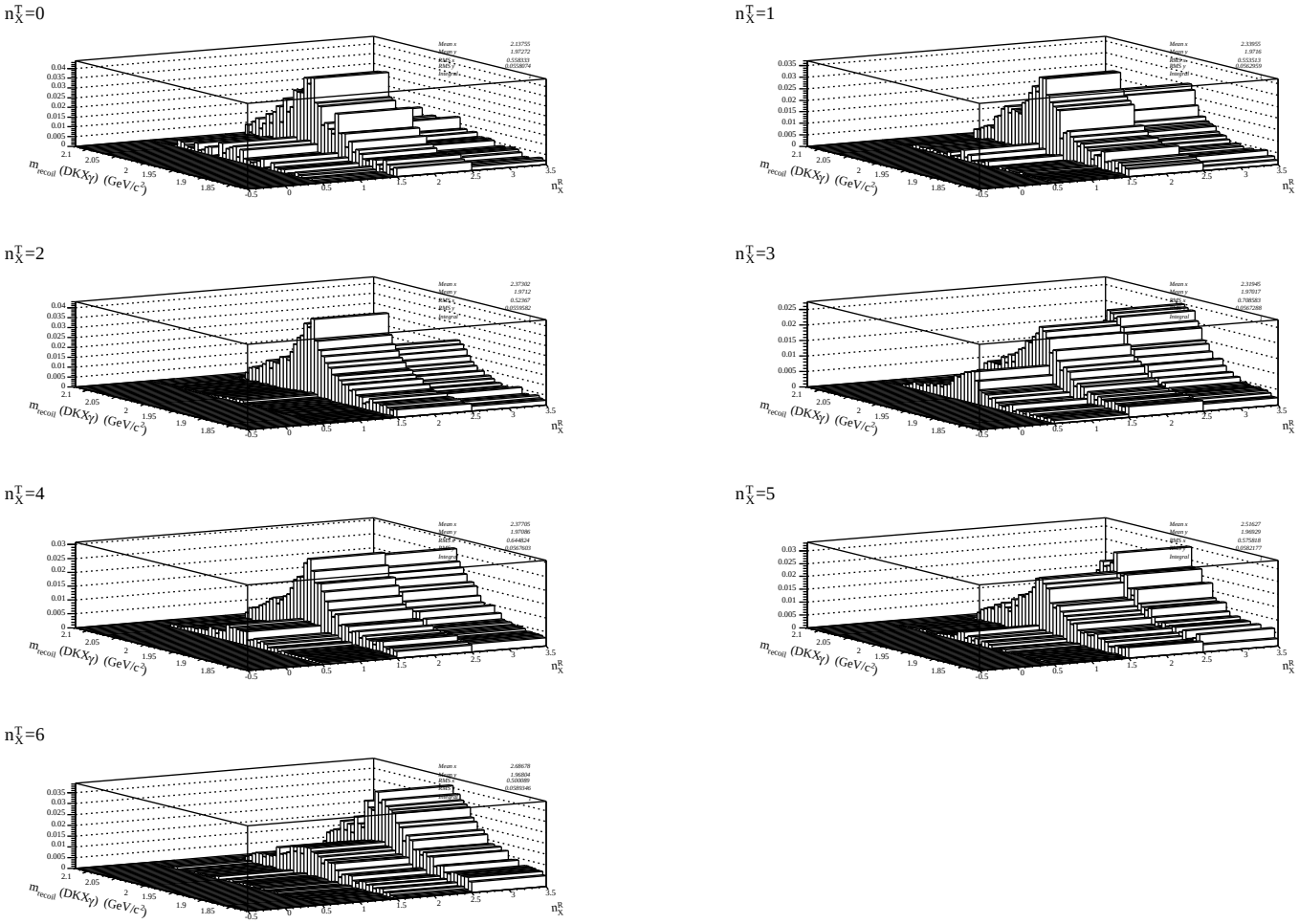

Figure 5.34: 2D WS signal PDF's, determined from the signal MC, used to fit the signal component in the WS Data.

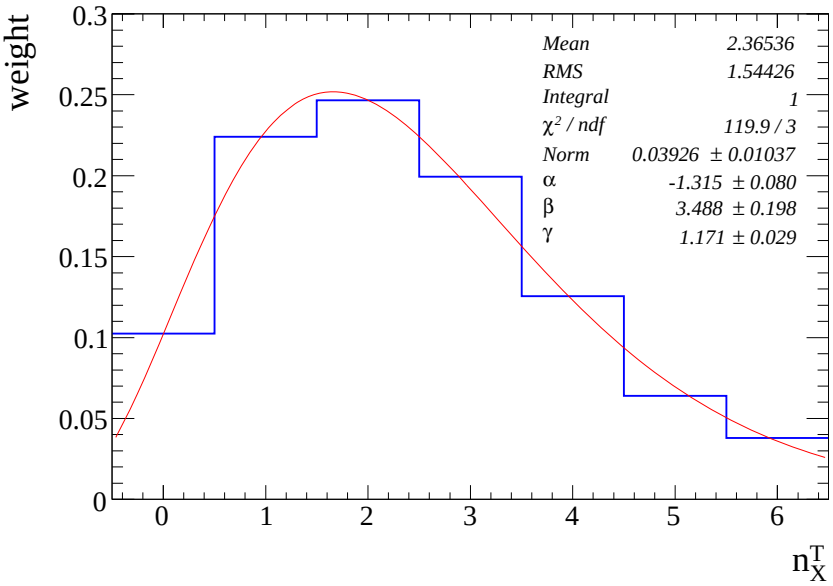

Figure 5.35: Distribution of reconstructed signal events as a function of n_X^T in the RS sample. The curve is a fit to this histogram using the function in equation 5.2.

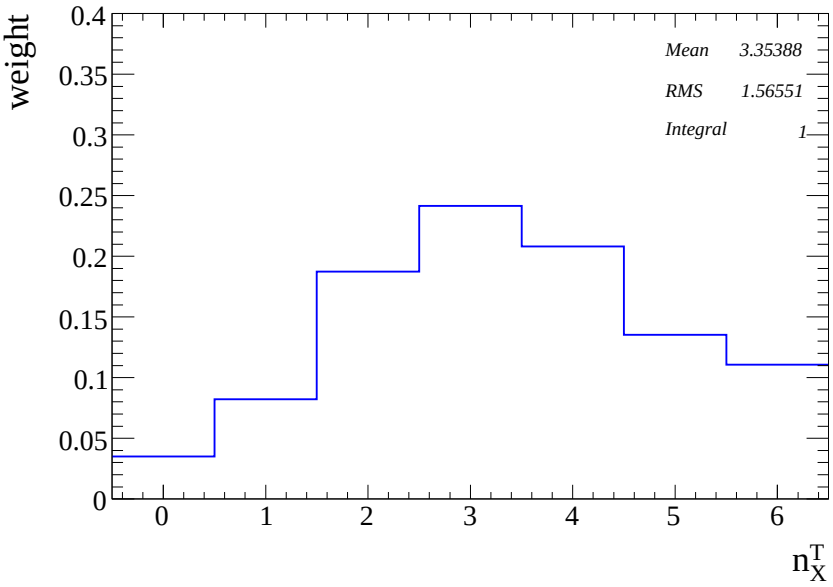

Figure 5.36: Distribution of reconstructed signal events as a function of n_X^T in the WS sample.

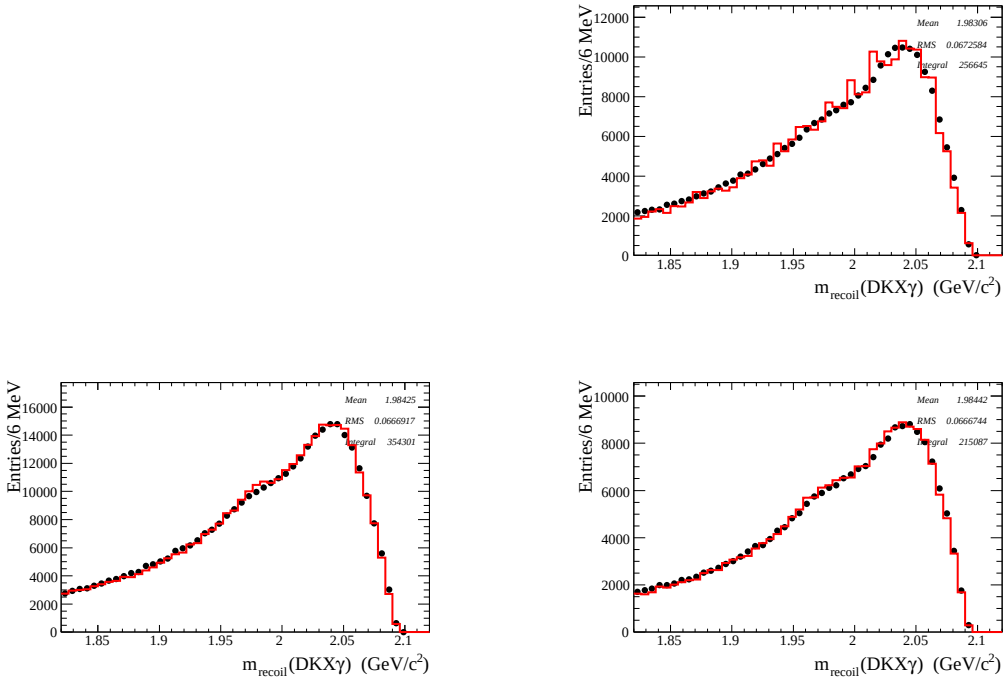

Figure 5.37: MC comparison of the WS background distribution (red) to the RS background distribution (black) for each n_X^R: $n_X^R = 0$(empty)(top-left), $n_X^R = 1$(top-right), $n_X^R = 2$(bottom-left) and $n_X^R = 3$(bottom-right).

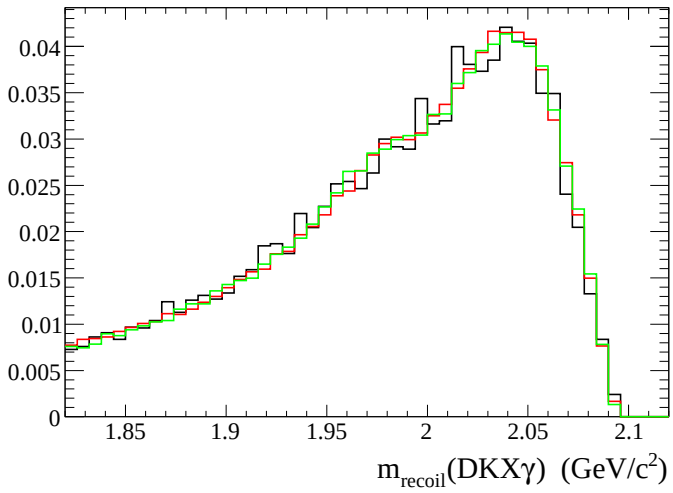

Figure 5.38: Comparison of the three MC WS background shapes: n_x^R=1(black), n_x^R=2(red),n_x^R=3(green).

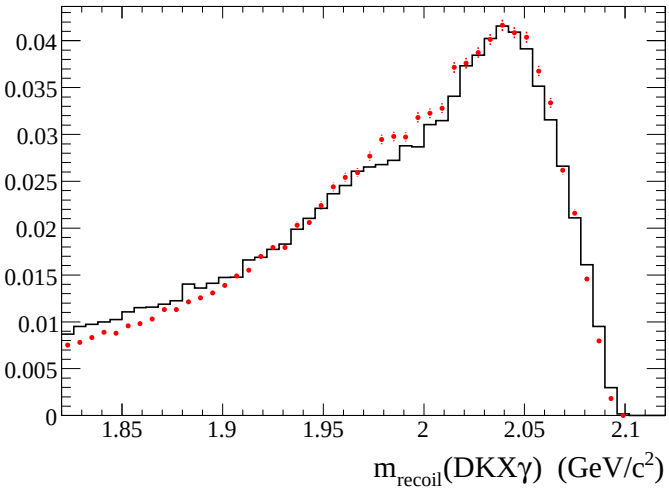

Figure 5.39: Comparison of the background shape constructed by averaging the last three MC WS background distributions to the true MC RS background for $n_X^R = 0$.

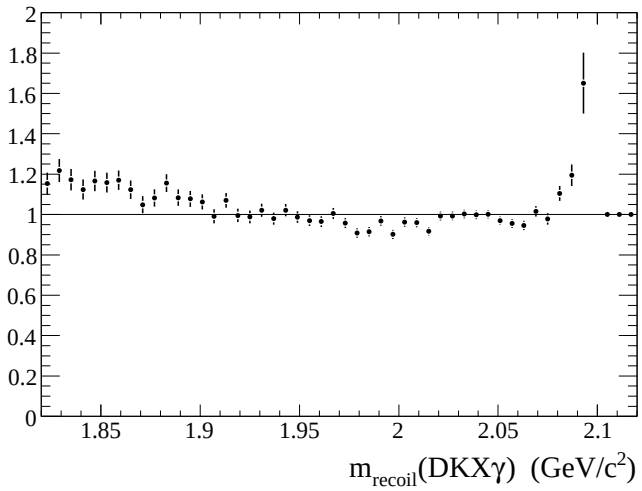

Figure 5.40: Ratio of distributions in Figure 5.39. Correction factor for the $n_X^R = 0$ background.

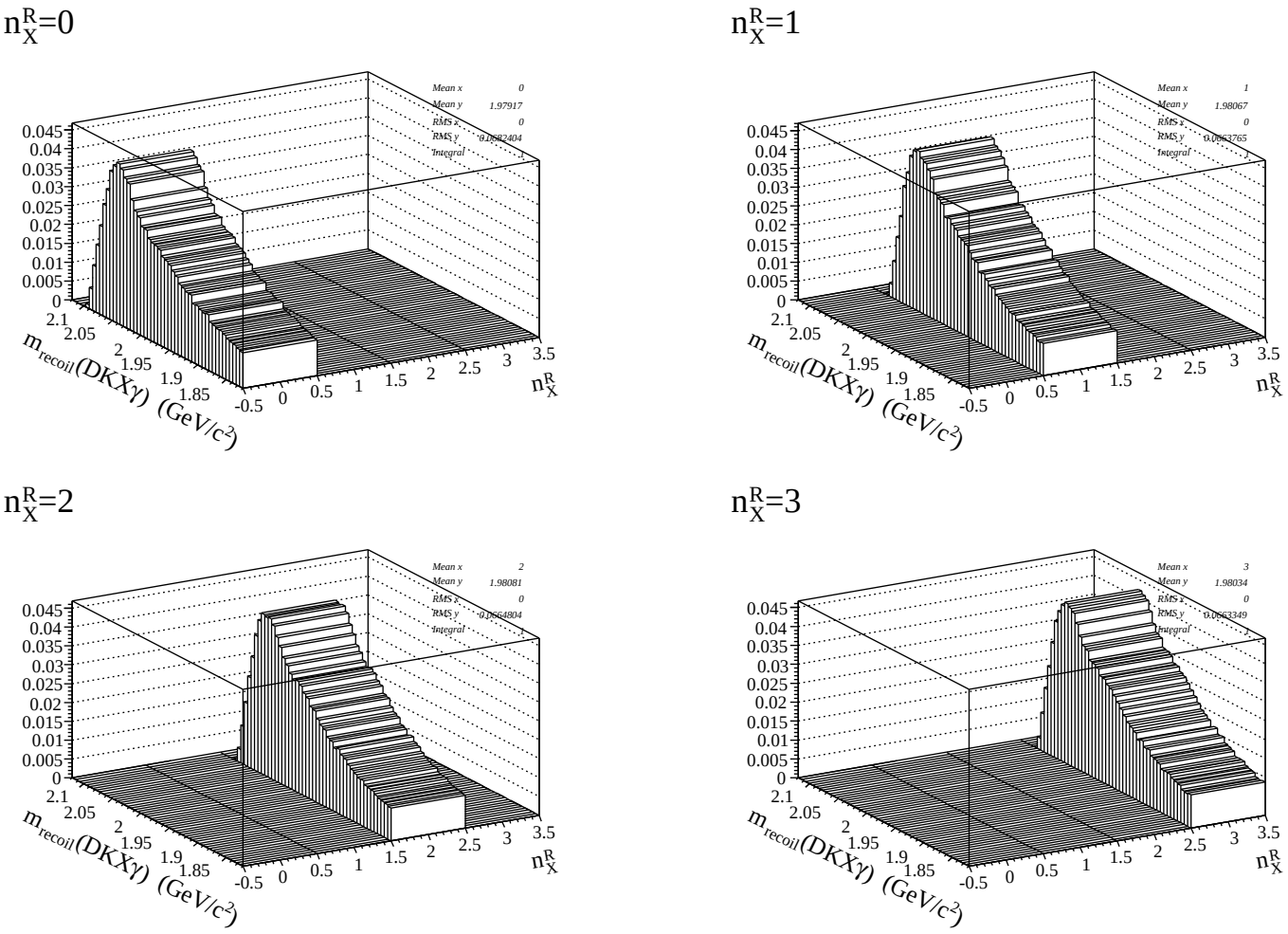

Figure 5.41: 2D RS Background PDF's determined during the fit to Data: $n_X^R = 0$(top-left), $n_X^R = 1$(top-right), $n_X^R = 2$(bottom-left) and $n_X^R = 3$(bottom-right).

5.8.1 Results for the fit to MC

The fit procedure is applied to the MC samples and a fit quality of $\chi^2/\text{NDF} = 238/181$ is achieved. Figures 5.42 and 5.43 show the 2D normalized residuals. Figures 5.44 to 5.47 show the projections of the fit onto $m_{recoil}(DKX\gamma)$. The fitted weight parameters are in good agreement with the true values as shown in Table 5.6. The poor quality of this fit derives from the imperfect modeling of the RS backgrounds by the WS distributions, in the fit to data we apply a correction to the WS shapes to correct for the RS background model.

Parameter	**True value**	**Fitted value**
$N_{Tot}^{RS} y^{RS}$	263.9 x10^3	258.6 ± 3.9 x10^3
α	-1.32	fixed
β	3.49	3.38 ± 0.16
γ	1.17	1.15 ± 0.06
b_0	0.0781	0.0775 ± 0.0006
b_1	0.2426	0.2431 ± 0.0011
b_2	0.3790	0.3793 ± 0.0010
$\left(\frac{N_{Tot}^{WS} y^{WS}}{N_{Tot}^{RS} y^{RS}}\right)$	0.1186	fixed
w_0^{WS}	0.0350	fixed
w_1^{WS}	0.0822	fixed
w_2^{WS}	0.1873	fixed
w_3^{WS}	0.2414	fixed
w_4^{WS}	0.2081	fixed
w_5^{WS}	0.1354	fixed
w_6^{WS}	0.1106	fixed
$N_{Tot}^{RS} y_{cut}^{RS}$	162.7 x10^3	159.5 ± 2.4 x10^3
w_0^{RS}	0.1024	0.1074
w_1^{RS}	0.2240	0.2297
w_2^{RS}	0.2467	0.2452
w_3^{RS}	0.1993	0.1899
w_4^{RS}	0.1256	0.1221
w_5^{RS}	0.0641	0.0695
w_6^{RS}	0.0379	0.0363

Table 5.6: Comparison between fitted and true parameter values. y_{cut}^{RS} is defined by the signal events which are in the small region around the peak between 1.934 and 2.012 GeV, y^{RS} is for the full histogram range. Parameters above the horizontal line are part of the fit, the ones below are derived quantities.

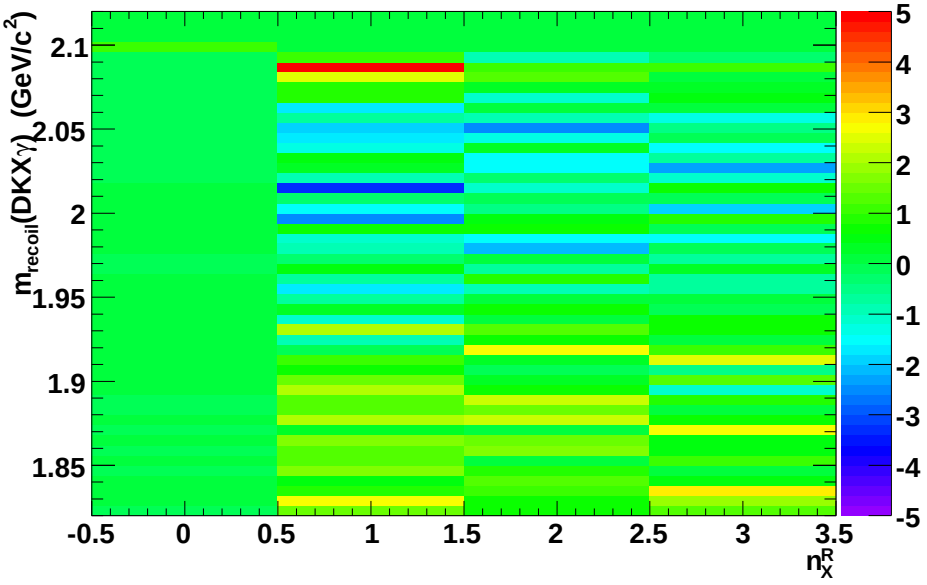

Figure 5.42: Normalized fit residuals: (Data - Fit) / Error.

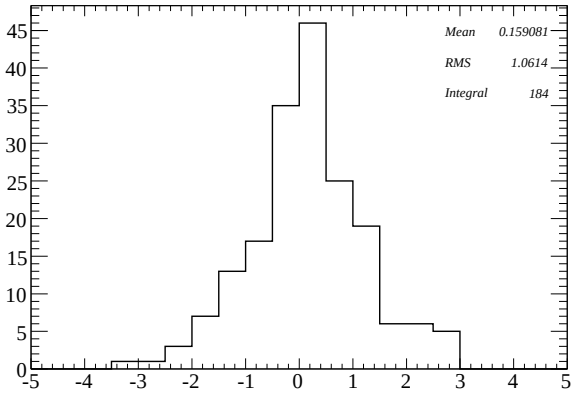

Figure 5.43: The histogram shows the collection of fit residuals from Figure 5.42. This histogram is filled with the bin content of each bin in Figure 5.42.

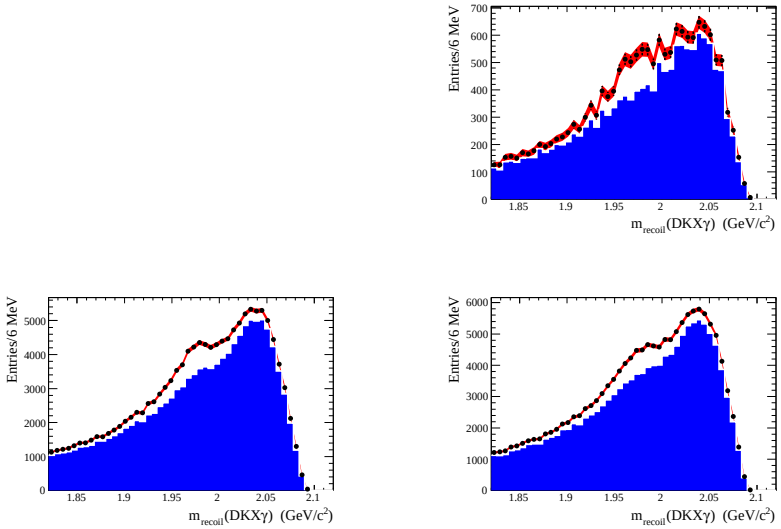

Figure 5.44: Projections of the fitted D_s^- mass distribution in the WS sample for each n_X: $n_X^R = 0$(top-left), $n_X^R = 1$(top-right), $n_X^R = 2$(bottom-left) and $n_X^R = 3$(bottom-right). The dark blue regions represent the fitted background. The red bands show the total pdf, the width of the band represents the statistical error on the total pdf.

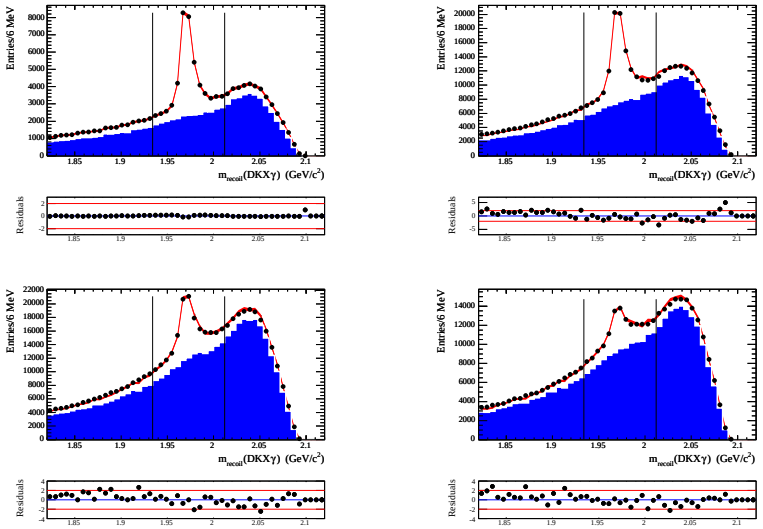

Figure 5.45: Projections of the fitted D_s^- mass distribution in the RS sample for each n_X: $n_X^R = 0$(top-left), $n_X^R = 1$(top-right), $n_X^R = 2$(bottom-left) and $n_X^R = 3$(bottom-right). The dark blue regions represent the fitted background. The red bands show the total pdf, the width of the band represents the statistical error on the total pdf.

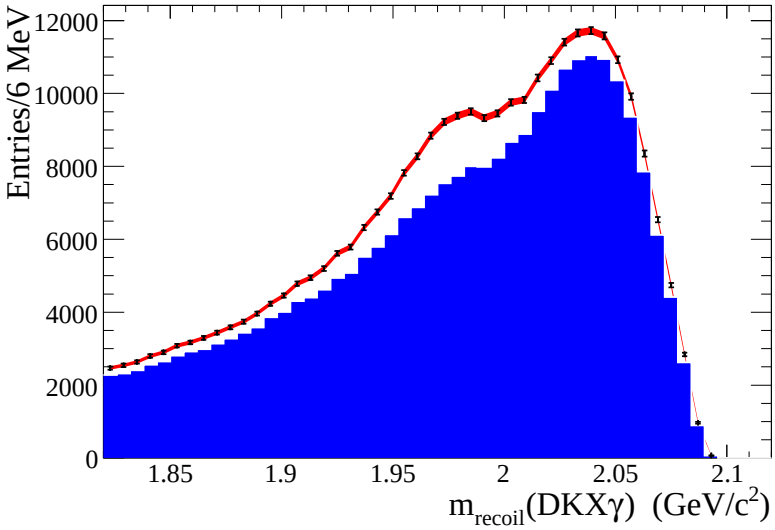

Figure 5.46: Projection of the fit onto the WS D_s^- mass.

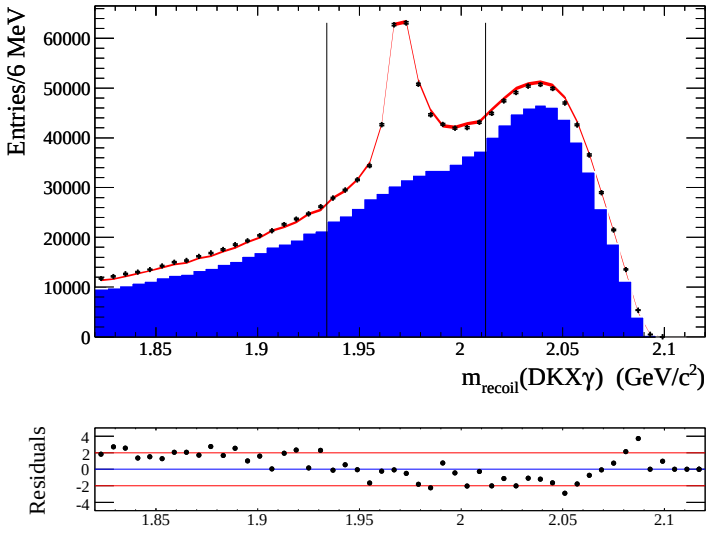

Figure 5.47: Projection of the fit onto the RS D_s^- mass.

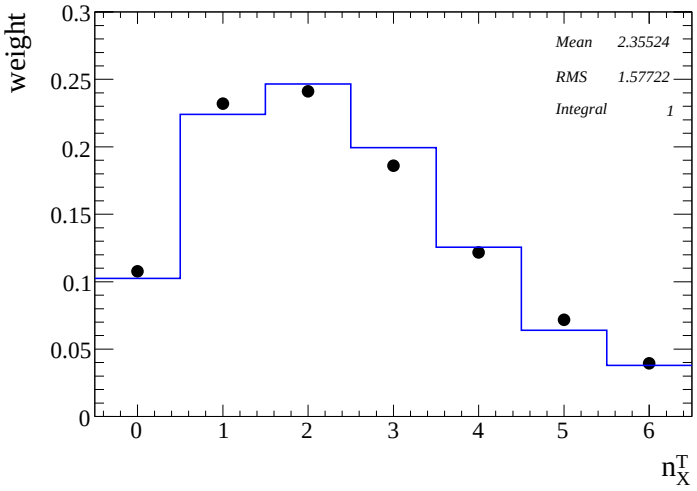

Figure 5.48: Points show the fitted n_X^T weights. Blue histogram shows the true values.

5.8.2 Results for the fit to Data

The fit to Data achieves a quality of χ^2/NDF=216/181, the 2D normalized residuals are shown in Figures 5.49 and 5.50. Figures 5.51 to 5.54 show the projections of the fit onto $m_{recoil}(DKX\gamma)$ for both the WS and RS samples. The parameters extracted for Data are shown in Table 5.7, a large discrepancy is observed for the n_X^T weights between MC and Data.

Parameter	**Data Fitted value**
$N_{Tot}^{RS} y^{RS}$	108.9 ± 2.4
α	-1.32
β	0.27 ± 0.17
γ	0.28 ± 0.07
b_0	0.0930 ± 0.0008
b_1	0.2180 ± 0.0011
b_2	0.3707 ± 0.0011
$N_{Tot}^{RS} y_{cut}^{RS}$	67.2 ± 1.5
w_0^{RS}	0.2274
w_1^{RS}	0.2010
w_2^{RS}	0.1681
w_3^{RS}	0.1370
w_4^{RS}	0.1100
w_5^{RS}	0.0874
w_6^{RS}	0.0690

Table 5.7: Parameters extracted from Data. Errors are statistical only. Parameters above the horizontal line are part of the fit, the ones below are derived quantities. Parameters missing in this table are fixed to the MC values found in the corresponding MC table.

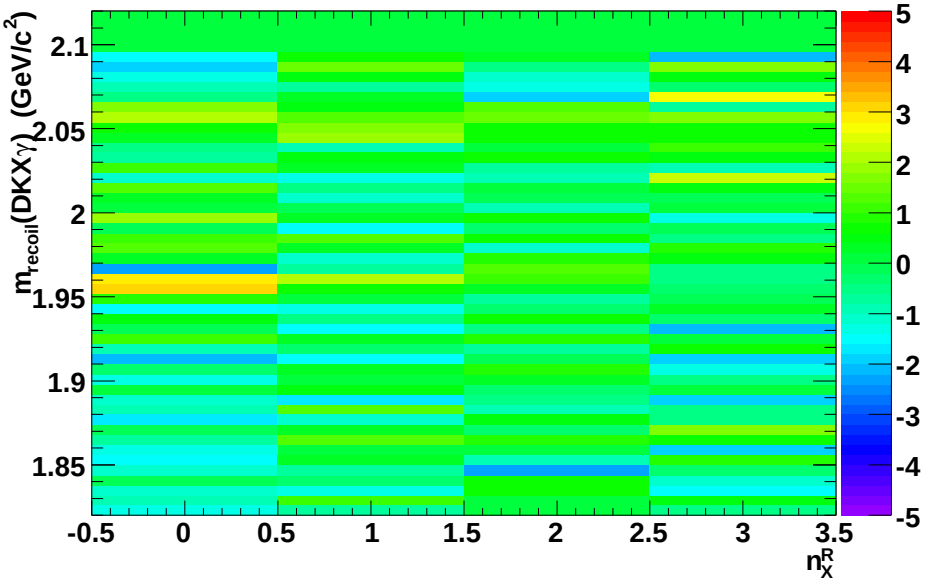

Figure 5.49: Normalized fit residuals: (Data - Fit) / Error.

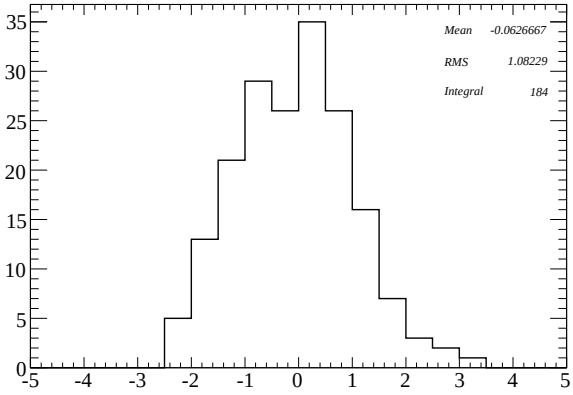

Figure 5.50: Collected normalized fit residuals from Figure 5.49.

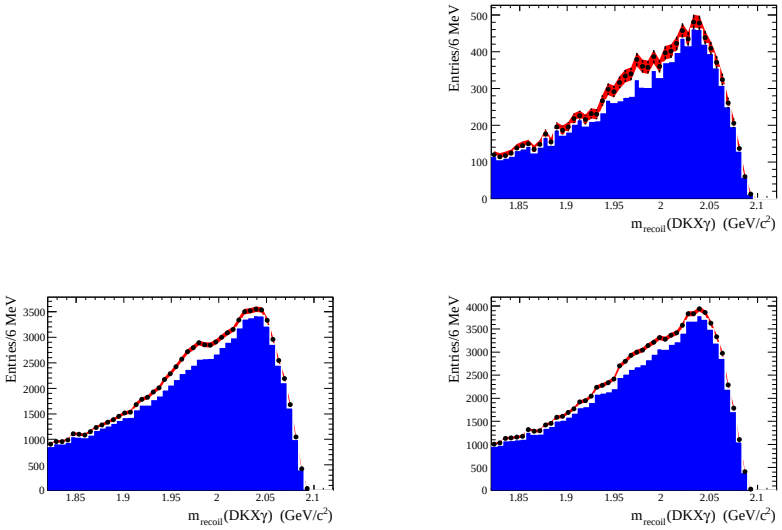

Figure 5.51: Projections of the fitted D_s^- mass distribution in the WS sample: $n_X^R = 0$(top-left), $n_X^R = 1$(top-right), $n_X^R = 2$(bottom-left) and $n_X^R = 3$(bottom-right). The dark blue regions represent the fitted background. The red bands show the total pdf, the width of the band represents the statistical error on the total pdf.

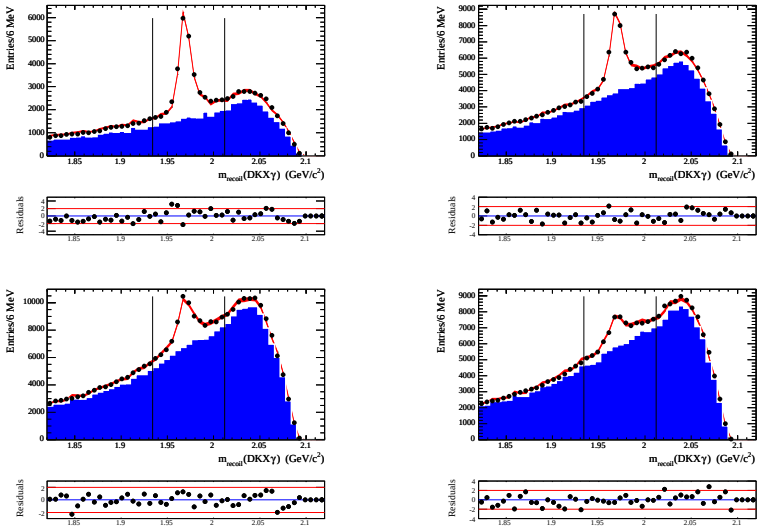

Figure 5.52: Projections of the fitted D_s^- mass distribution in the RS sample: $n_X^R = 0$(top-left), $n_X^R = 1$(top-right), $n_X^R = 2$(bottom-left) and $n_X^R = 3$(bottom-right). The dark blue regions represent the fitted background. The red bands show the total pdf, the width of the band represents the statistical error on the total pdf.

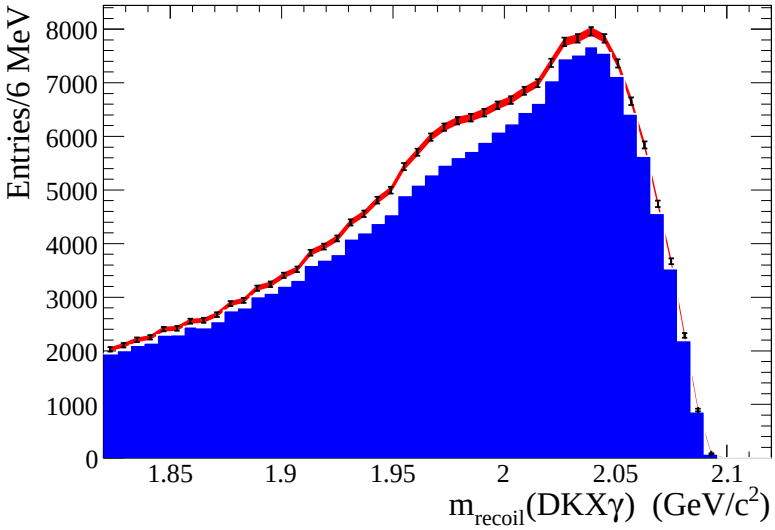

Figure 5.53: Projection of the fit onto the WS D_s^- mass.

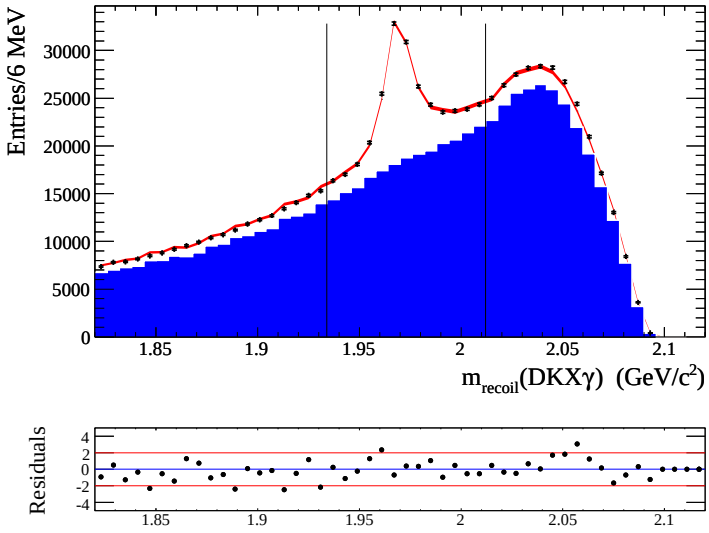

Figure 5.54: Projection of the fit onto the RS D_s^- mass.

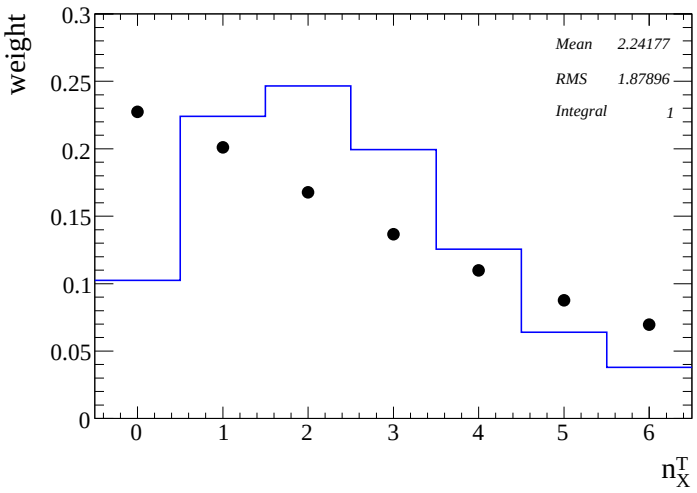

Figure 5.55: Points show the fitted n_X^T weights. Blue histogram shows the true values in the MC.

5.8.3 Systematic Uncertainties on the Inclusive D_s^- Yield

In the fit to the inclusive sample above the signal and background distributions have been modeled according to the procedure defined for the MC while making several assumptions, for example several parameters have been fixed to the MC values. In this section systematic uncertainties are assigned to account for those assumptions. For each systematic error determined below the Data is refitted and new values for the D_s yield and the RS n_X^T weight parameters are determined. In the calculation of the systematics on the branching fractions later the nominal parameters are replace by the ones determined in this section.

The following systematic uncertainties have been considered:

- WS n_X^T weights The n_X^T weights used in the WS signal PDF are fixed to the MC true values. From the fit to the Data we observe that the signal prefers lower n_X. A systematic is estimated by multiplying the MC values by a linear function with a 80% gradient which favors the lower n_X^T weights.

- RS n_X^T weights The RS weights are constrained to a model whose formula is determined from the MC. While the model itself is flexible and should not bias the shape of the weights we find the Data is not sensitive to the α parameter. This parameter is varied from the MC value to the values -10 and -.5 as a systematic crosscheck.

- D_s Signal Shape An uncertainty is assigned for a possible difference in the resolution of the D_s peak. This is done by randomizing the measured mass value using a Gaussian with 2 MeV sigma. A 3 MeV sigma has been tried but it produces a fit which degrades the fit quality significantly.

- Peaking Backgrounds Two possible sources of peaking backgrounds exist. The WS/RS signal fraction in the MC, which is fixed in the Data fit, can be different in the Data sample. This would cause either a peak or a hole in the background. Also, events with the decay process $D^{*0} \rightarrow D^0\gamma$ cause a peaking bump under the signal in the D_s mass distribution. This bump is well modeled by the WS background according to the MC. In order to estimate a systematic error for these backgrounds we vary the WS/RS signal fraction by $\pm 10\%$.

- Background Model A background model systematic is estimated by modifying the background PDF's according to the discrepancies observed in Figure 5.38, this estimates how well the WS sample models the RS sample backgrounds.

- n_X Resolution The signal PDFs used for each n_X^T account for the resolution (or crossfeed) in n_X, however this resolution could be different in the Data. In order to estimate a systematic error we have degraded the resolution of each n_X^T PDF by shifting 10% of the bin contents in the main n_X^R bin into the other bins (see Figure 5.28).

- Signal Photon Backgrounds The RS signal PDF includes a non-peaking component due to photons from signal events but coming from π^0/η decays as well as from Tracks/K_L interactions in the EMC (Fig 5.21). The fraction of this component is taken from the signal MC simulation. The event reconstruction multiplicity provides a handle on possible mismodeling of this fraction because the reconstruction multiplicity of the signal events depends on the amount of these background photons. The large amount of the background is the main reason for having a large reconstruction multiplicity per event. By modifying the amount of this background photons in the Signal MC one can create a map of the reconstruction multiplicity vs. amount of this background. This map is shown in Figure 5.58. Next we determine the reconstruction multiplicity of signal events of the *Data*. The reconstruction multiplicity in signal Data events is not the same as the multiplicity of the Data sample because this sample contains background events with different multiplicity as is found in the MC analysis. We therefore perform a background subtraction as follows:

  1. We start with the reconstruction multiplicity distribution of the WS Data sample.
  2. We use the reconstruction multiplicity distribution of the signal MC WS sample and normalize it to the number of WS signal events fitted in the Data then subtract this from the reconstruction multiplicity distribution of the WS Data.
  3. We then construct a correction histogram as the ratio of (Background MC RS sample)/(Background MC WS sample) and apply this correction to the histogram obtained from step 2. This becomes a model for the reconstruction multiplicity distribution of the Background in the RS Data sample.
  4. We normalize this model to the number of background events in the Data and subtract it from the reconstruction multiplicity distribution of the Data RS sample. This gives the pure reconstruction multiplicity distribution of the signal events in Data.

Figure 5.56 shows a comparison between the total Data sample and background which is subtracted. Figure 5.57 shows a comparison between background subtracted Data and the signal MC. The average value of the reconstruction multiplicity in the resulting signal Data distribution is plotted in Figure 5.58 as a red line. From the intercept with the map we estimate that the MC should within about 5% from the true amount of fake photon background in the Data. We modify this component of the signal PDF by ±5% and redo the fit.

Tables 5.8 and 5.9 show the differences in the D_s yield obtained from each systematic variation. Note that we define two sets of systematic errors, one set for the full mass range and one set for the range which is selected in the leptonic reconstructions later. The systematics on the full mass range are necessary for the measurement of the hadronic decay to $K^+K^-\pi^-$ as described later.

Systematic	**Difference in D_s Yield (x10^3)**	**Difference/Nominal**
WS n_X^T weights	(-0.00,+0.66)	(-0.00,+0.98)%
RS n_X^T weights	(-0.10,+0.06)	(-0.15,+0.09)%
D_s Signal Shape	(-1.04,+1.04)	(-1.55,+1.55)%
Peaking Backgrounds	(-1.38,+1.40)	(-2.05,+2.08)%
Background Model	(-0.00,+0.04)	(-0.00,+0.05)%
n_X Resolution	(-1.05,+1.17)	(-1.56,+1.74)%
Signal Photon Backgrounds	(-1.63,+1.65)	(-2.43,+2.46)%
Total	**(-2.60,+2.75)**	**(-3.86,+4.09)%**

Table 5.8: Summary of Denominator systematic errors determined for the limited signal range around the peak.

Systematic	**Difference in D_s Yield (x10^3)**	**Difference/Nominal**
WS n_X^T weights	(-0.00,+1.04)	(-0.00,+0.95)%
RS n_X^T weights	(-0.21,+0.12)	(-0.20,+0.11)%
D_s Signal Shape	(-1.70,+1.70)	(-1.56,+1.56)%
Peaking Backgrounds	(-2.32,+2.36)	(-2.13,+2.16)%
Background Model	(-0.01,+0.09)	(-0.01,+0.09)%
n_X Resolution	(-2.06,+2.32)	(-1.89,+2.13)%
Signal Photon Backgrounds	(-4.16,+4.21)	(-3.82,+3.87)%
Total	**(-5.47,+5.72)**	**(-5.02,+5.25)%**

Table 5.9: Summary of Denominator systematic errors computed on full range of D_s mass.

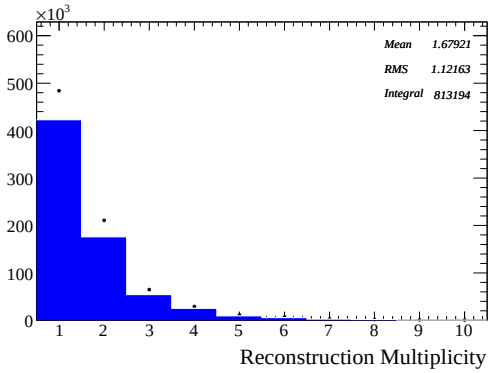

Figure 5.56: Comparison of the Data(points) and the background model(blue). The background model has been normalized to the number of background events determined from the nominal fit.

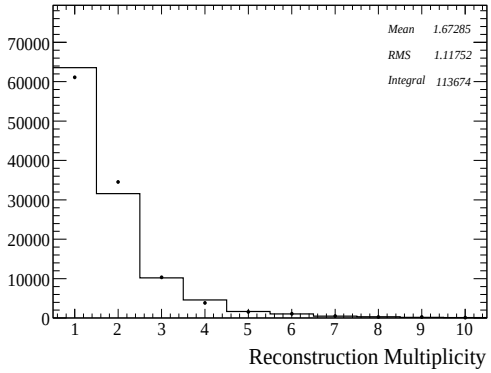

Figure 5.57: Comparison of the background subtracted Data(points) and the Signal MC.

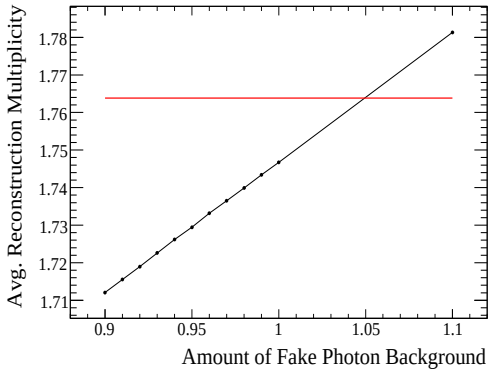

Figure 5.58: Black line shows the reconstruction multiplicity in Signal MC vs. amount fake photons. Red line shows the value obtained for the Data signal events.

Chapter 6

Measurement of the Leptonic D_S^- Decays

Within the inclusive sample of D_s^- tagged events the decays $D_s^- \to \mu^- \bar{\nu}_\mu$ and $D_s^- \to e^- \bar{\nu}_e$ can be reconstructed by detection of the muon or electron and by the determination of the missing mass in the event which should be consistent with that of the neutrino. In addition, $D_s^- \to \tau^- \bar{\nu}_\tau$ events can be detected by reconstructing the decay products of the tau, however, due to multiple neutrinos the missing mass in the event cannot be used to extract these events. Nevertheless, $D_s^- \to \tau^- \bar{\nu}_\tau$ events can be extracted by using the extra neutral energy in the event which peaks towards zero for signal events.

6.1 $D_s^- \to \mu^- \bar{\nu}_\mu$

6.1.1 Reconstruction and Selections

The reconstruction of $D_s^- \to \mu^- \bar{\nu}_\mu$ decays is performed by requiring one more track in the event. This track must pass the VeryLoose PID selector for muons. Besides the neutrino this is the last particle produced in the event and therefore events with more than one track are rejected. Also, no additional neutral particles should exist in the event and the remaining energy in the EMC, E_{extra}, should be consistent with zero. E_{extra} is calculated from the remaining clusters which are not associated with any reconstructed track. In practice the particles from the rest of the event leave energy deposits in the EMC so E_{extra} is not exactly zero. A requirement of $E_{extra} < 1$ GeV removes most of the background events which have additional neutral partiles. The E_{extra} distributions are shown in Figures 6.1 to 6.2.

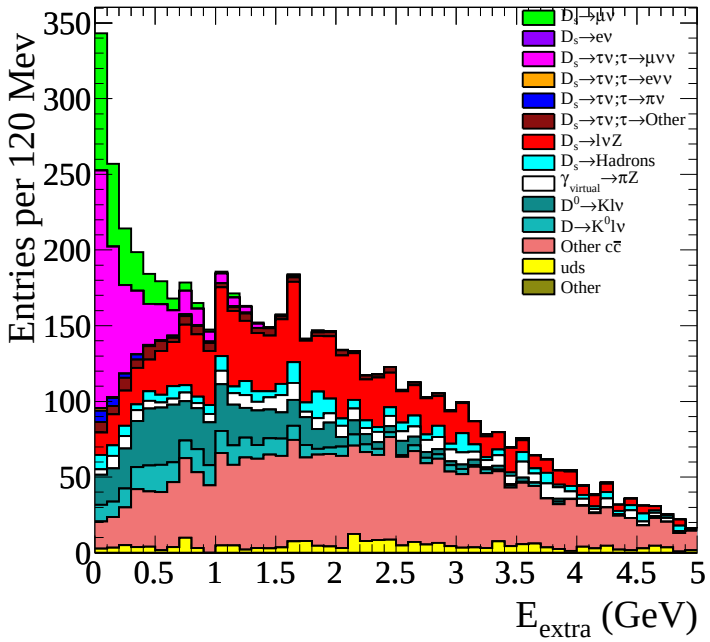

Figure 6.1: E_{extra} distribution for $D_s^- \to \mu^- \bar{\nu}_\mu$ candidates in the generic MC.

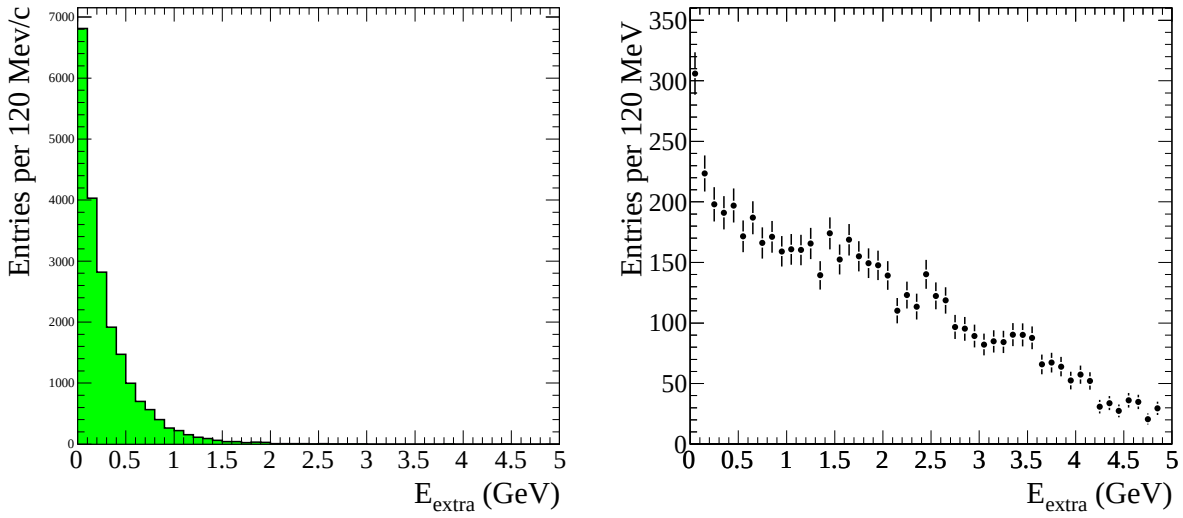

Figure 6.2: E_{extra} distribution for $D_s^- \to \mu^- \bar{\nu}_\mu$ candidates in the signal MC (left) and Data (right).

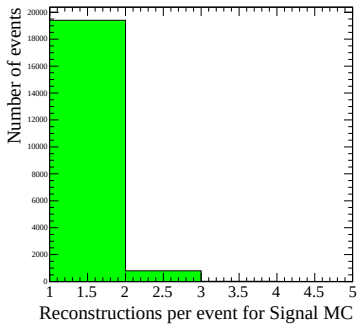

Figure 6.3: Number of candidates per event for signal MC.

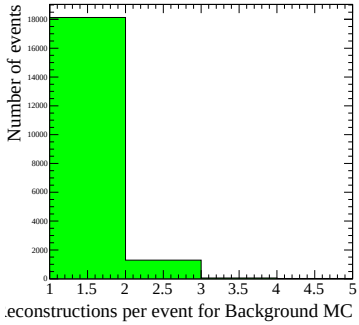

Figure 6.4: Number of candidates per event for generic MC.

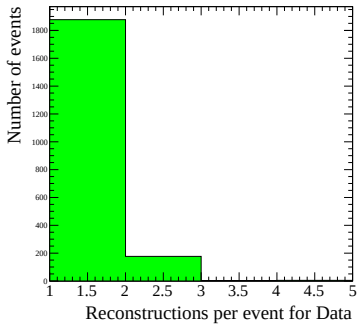

Figure 6.5: Number of candidates per event for Data.

A kinematic fit is then performed to the $DKX\gamma\mu$ candidates in which the particles are required to originate from the IP region and the 4-momentum of the missing neutrino is determined by requiring 4-momentum conservation in the event. A fit probability greater than 10^{-5} is required. After this final selection the number of $DKX\gamma\mu$ candidates per event is reduced to only about 1.05 as shown in Figures 6.3 to 6.5. In the fit for the signal yield the candidates are deweighted by 1/n to assign a count of 1 to each event. The missing mass squared, $m^2_{recoil}(DKX\gamma\mu)$, distribution for signal MC events is plotted in Figure 6.7 and shows a well defined peak with a resolution of about 0.05 GeV^2. For the generic MC sample the $m^2_{recoil}(DKX\gamma\mu)$distribution is shown in Figure 6.6. This distribution exhibits a peak at zero corresponding to $D_s^- \to \mu^-\bar{\nu}_\mu$ events and a broad background distribution extending upto about 3.5 GeV^2. The backgrounds surviving the selections are mainly from $D_s^- \to \tau^-\bar{\nu}_\tau$ decays where $\tau^- \to \mu^-\bar{\nu}_\mu\nu_\tau$ and from the semileptonic decays $D^0 \to \mu^-\nu K^+$, $D^- \to \mu^-\nu K^0$, and $D_s^- \to \mu^-\nu\eta$.

6.1.2 Fit for the Signal Yield

The signal yield in Data is extracted by fitting the $m^2_{recoil}(DKX\gamma\mu)$ distribution. Signal events are modeled using a histogram PDF determined from the reconstructed signal MC. The background is modeled using the reconstructed generic MC sample (Figure 6.6) with signal events removed. Due to the low statistics of the Data sample a binned maximum likelihood fit is performed, shown in Figure 6.7. The signal yield is 274±17 events.

6.1.3 Determination of $\mathcal{B}(D_s^- \to \mu^-\bar{\nu}_\mu)$

The calculation of the branching fraction for $D_s^- \to \mu^-\bar{\nu}_\mu$ must account for the mismodeling of the fragmentation functions in the MC because the efficiency is expected to vary as a function of n_X^T. The momentum of the D_s^- is correlated with the number fragmentation pions and therefore an additional correction for mismodeling of the momentum distribution is not necessary. A formula for the calculation can be derived in terms of the total $D_s^- \to \mu^-\bar{\nu}_\mu$ yield, the D_s^- yield for each n_X^T and the reconstruction efficiencies for each n_X^T component in the following way.

- The number of produced $D_s^- \to \mu^-\bar{\nu}_\mu$ events, $n^j_{\mu\nu}$, for a given value of $j = n_X^T$ is given by

$$n^j_{\mu\nu} = n^j_{D_s}\mathcal{B}(D_s^- \to \mu^-\bar{\nu}_\mu)$$

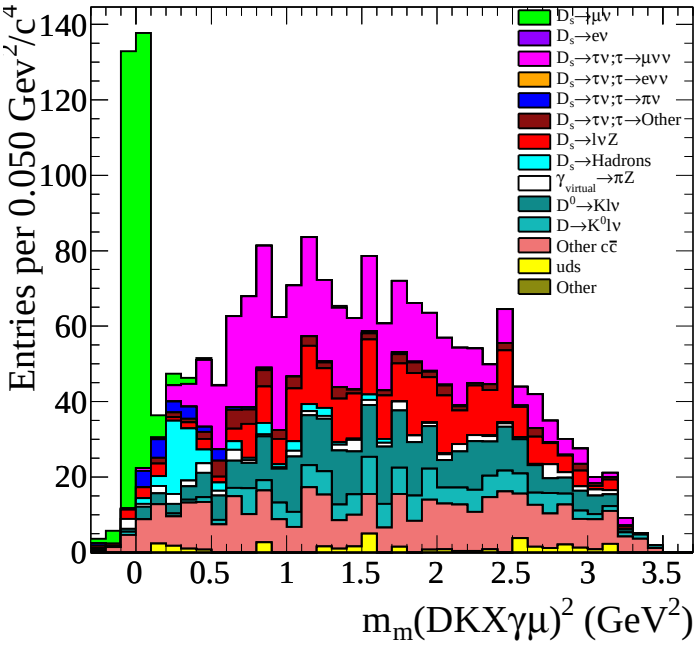

Figure 6.6: $m^2_{recoil}(DKX\gamma\mu)$ distribution for $D_s^- \to \mu^- \bar{\nu}_\mu$ candidates in generic MC.

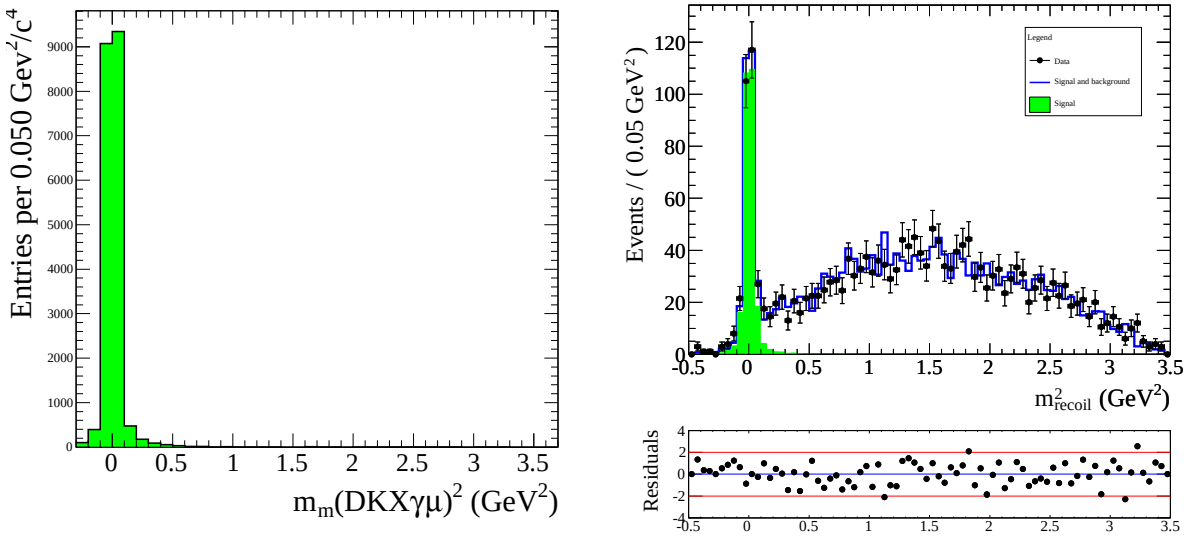

Figure 6.7: Left: $m^2_{recoil}(DKX\gamma\mu)$distribution for $D_s^- \to \mu^- \bar{\nu}_\mu$ candidates in the signal MC. Right: Fit to the $m^2_{recoil}(DKX\gamma\mu)$ distribution in Data.

where $n^j_{D_s}$ is the number of produced D_s^- events.

- In terms of the reconstructed numbers $N^j_{\mu\nu}$ and $N^j_{D_s}$, this equation becomes

$$\frac{N^j_{\mu\nu}}{\varepsilon^j_{\mu\nu}} = \frac{N^j_{D_s}}{\varepsilon^j_{D_s}} B(D_s \to \mu\nu)$$

where $\varepsilon^j_{\mu\nu}$ and $\varepsilon^j_{D_s}$ are the reconstruction efficiencies for $D_s^- \to \mu^-\bar{\nu}_\mu$ and D_s^- tagged events, respectively.

- This equation can be rewritten in terms of the total number of reconstructed $D_s^- \to \mu^-\bar{\nu}_\mu$ events as follows:

$$N_{\mu\nu} = \sum_j N^j_{\mu\nu} = B(D_s \to \mu\nu) \sum_j \frac{N^j_{D_s}\varepsilon^j_{\mu\nu}}{\varepsilon^j_{D_s}}$$

- Finally, this last equation can be used to calculate the branching fraction:

$$\mathcal{B}(D_s \to \mu\nu) = \frac{N_{\mu\nu}}{\sum_{j=0}^{6} N^j_{D_s} \frac{\varepsilon^j_{\mu\nu}}{\varepsilon^j_{D_s}}} = \frac{N_{\mu\nu}}{N_{D_s} \sum_{j=0}^{6} w_j \frac{\varepsilon^j_{\mu\nu}}{\varepsilon^j_{D_s}}} \tag{6.1}$$

where $w_j = N^j_{D_s}/N_{D_s}$ are the weights determined from the fit to the inclusive D_s^- sample, and N_{D_s} is the total number of inclusive D_s^- events.

The efficiencies as a function of n_X^T , $\varepsilon^j_{D_s}$ and $\varepsilon^j_{\mu\nu}$, have been determined from the signal MC samples of inclusive D_s^- events and exclusive $D_s^- \to \mu^-\bar{\nu}_\mu$ events, respectively. These individual efficiencies are on the order of 0.2% due to the large number of particles required to fully reconstruct the signal events. The efficiency ratios $\frac{\varepsilon^j_{\mu\nu}}{\varepsilon^j_{D_s}}$ are approximately the efficiencies for reconstructing the single muon in D_s^- tagged events. The values are listed in Table 6.1.

The dependence on the value of n_X^T derives from the fact that as more pions are produced the D_s^- has lower momentum and therefore the muon has lower momentum. Muons with lower energy are less probable to reach the IFR and therefore the efficiency drops significantly.

Using the inclusive D_s^- yield from section 5.8.2, the total $D_s^- \to \mu^-\bar{\nu}_\mu$ yield from section 6.1.2, and the above efficiencies the following value is obtained:

$$\mathcal{B}(D_s^- \to \mu^-\bar{\nu}_\mu) = (6.02 \pm 0.38) \times 10^{-3} \tag{6.2}$$

n_X^T	$\varepsilon^j_{\ell\nu}/\varepsilon^j_{D_s}$
0	0.868 ± 0.018
1	0.760 ± 0.011
2	0.672 ± 0.010
3	0.621 ± 0.011
4	0.510 ± 0.012
5	0.461 ± 0.017
6	0.332 ± 0.019

Table 6.1: Efficiency ratio, ε^j, for each n_X^T value. The errors are due to the size of the signal MC sample.

where the error is determined from the statistical errors on the $D_s^- \to \mu^- \bar{\nu}_\mu$ yield, the inclusive D_s^- yield, and the weights w_j. The correlations between the weights and the D_s^- yield are accounted for by using the covariance matrix obtained from the fit to the inclusive sample.

As a cross-check to the analysis procedure the same calculation has been performed using the signal yields in the generic MC. Using the corresponding yields the following result is obtained:

$$\mathcal{B}_{MC}(D_s^- \to \mu^- \bar{\nu}_\mu) = (6.24 \pm 0.36) \times 10^{-3} \tag{6.3}$$

This value is within one statistical sigma of the true value, 6.16×10^{-3} , which was used in the generation of the MC.

Another important cross-check to this measurement has been performed by measuring the branching fraction for the hadronic decay $D_s^- \to K^+K^-\pi^-$. The analysis of this channel is documented in Appendix A. The branching fraction for this decay channel has been measured precisely by CLEO-c: $\mathcal{B}(D_s^- \to K^+K^-\pi^-) = (5.50 \pm 0.23(stat) \pm 0.16(syst))\%$ [35]. The value obtained in this analysis: $B(D_s^- \to K^+K^-\pi^-) = (5.78 \pm 0.20(stat) \pm 0.30(syst))\%$, is consistent with the value obtained by CLEO-c.

6.1.4 Systematic Uncertainties for $\mathcal{B}(D_s^- \to \mu^- \bar{\nu}_\mu)$

Systematic uncertainties on the branching fraction are assigned due to the systematic uncertainties on the inclusive D_s^- sample which were described in section 5.8.3. In addition, there are systematic uncertainties due to possible biases in the fit for the $D_s^- \to \mu^- \bar{\nu}_\mu$ events. These include uncertainties on the signal model and background model.

- For the signal model, a conservative uncertainty is assigned by replacing the nominal

signal PDF by one which has a resolution degraded by about 10%. An independent variation is performed using a signal PDF whose mean value is shifted from the nominal by about 10% of the resolution.

- For the background model, the different decays which compose the background in the generic MC are varied according to the errors on their branching fractions. Also, the statistical errors on each bin are taken into account by refitting the $m^2_{recoil}(DKX\gamma\mu)$ distribution using a χ^2 minimization method which incorporates these errors into the fit.

Finally, there are uncertainties associated with the efficiencies. Although the efficiency associated with D_s^- tagging may be mismodeled by the MC, this possible bias will cancel in the efficiency ratio and therefore only differences associated with the muon reconstruction are relevant.

- A possible difference between Data and MC in the efficiency for the reconstruction of one track is determined from a sample of $e^+e^- \to \tau\tau$ events which have a 3-1 topology and for which the production cross-sections and branching fractions are well known.

- Lastly, a systematic uncertainty arises from differences in the PID selectors when applied to Data. A high statistics sample of $e^+e^- \to \mu\mu\gamma$ events is used compare the PID efficiencies in Data to those in MC. The differences have been used to correct the efficiencies used in the branching fraction calculation and the statistical errors on those corrections are used to determine a systematic uncertainty on the branching fraction.

A summary of all the systematic uncertainties and the total is shown in Table 6.2.

Systematic	**Difference in the B.F.** ($\times 10^{-3}$)	**Difference/Nominal**
WS n_X^T weights	(-0.07,+0.00)	(-1.08,+0.00)%
RS n_X^T weights	(-0.00,+0.00)	(-0.04,+0.00)%
D_s Signal Shape	(-0.09,+0.09)	(-1.45,+1.45)%
Peaking Backgrounds	(-0.10,+0.10)	(-1.64,+1.67)%
Background Model	(-0.02,+0.01)	(-0.34,+0.23)%
n_X Resolution	(-0.03,+0.03)	(-0.51,+0.48)%
Signal Photon Backgrounds	(-0.14,+0.14)	(-2.24,+2.32)%
$\mu\nu$ background model	(0.14)	(2.21)%
$\mu\nu$ Signal model	(0.16)	(2.56)%
μ Tracking Efficiency	(0.05)	(0.83)%
μ PID Efficiency	(0.12)	(1.88)%
Total	(0.34)	(5.44)%

Table 6.2: Systematic uncertainties for $\mathcal{B}(D_s^- \to \mu^- \bar{\nu}_\mu)$.

6.2 $D_s^- \to e^- \bar{\nu}_e$

6.2.1 Reconstruction and Selections

For the reconstruction of $D_s^- \to e^- \bar{\nu}_e$ candidates a similar procedure is followed as for $D_s^- \to \mu^- \bar{\nu}_\mu$. Only events with one additional track are selected and the track is required to pass the KM VeryLoose PID selector for electrons. Also, the E_{extra} for the event candidate must be less than 1 GeV. After these selections a kinematic fit is performed to the $DKX\gamma e$ system in order to determine the 4-momentum of the missing neutrino candidate. A fit probability greater than 10^{-5} is required. The distributions of $m^2_{recoil}(DKX\gamma e)$ for signal MC and generic MC are shown in Figures 6.8 and 6.9. The reconstruction of $D_s^- \to e^- \bar{\nu}_e$ signal events has a worse resolution when compared to the $D_s^- \to \mu^- \bar{\nu}_\mu$ reconstruction as is evident from the tail on the high side of the signal MC distribution. This tail arises from the larger amount of final state radiation by the electron track which is modeled by the PHOTOS package in the event generator. The distribution of generic MC events shows no signal component since the $D_s^- \to e^- \bar{\nu}_e$ decays are not included in the generation due to the very low expected rate; this rate is $\sim 10^{-6}$ in SM theory.

6.2.2 Fit for the Signal Yield

To determine a possible signal contribution in Data, a fit is performed to the $m^2_{recoil}(DKX\gamma e)$ distribution. Signal events are modeled using a histogram PDF determined from the reconstructed signal MC. The background events are modeled using the reconstructed generic MC. Due to the low statistics of the Data sample, a binned maximum likelihood fit is performed as shown in Figure 6.10. The signal yield obtained from this fit is consistent with zero: $n = 6.1 \pm 2.9 \pm 4.3$, where the first error is statistical and the second is systematic.

The systematic uncertainty on the signal yield has been calculated by varying the signal and background PDFs in the nominal fit.

- The signal PDF is varied by degrading the resolution and by shifting the mean value similarly as in the $D_s^- \to \mu^- \bar{\nu}_\mu$ analysis.

- For the background model, the uncertainties due to the limited size of the MC sample are accounted for by varying the bin contents of the PDF according to their errors. Also, the uncertainties on the individual components in the background

arising from the errors on the branching fractions of the D_s^- are accounted for by varying these components.

6.2.3 Upper Limit on $\mathcal{B}(D_s^- \to e^- \bar{\nu}_e)$

An upper limit can be placed on the value for $\mathcal{B}(D_s^- \to e^- \bar{\nu}_e)$ based on the null result obtained for the signal yield. A Bayesian approach is used with a prior which defines the probability for the branching fraction to be uniform for positive values and zero for negative values. A likelihood function can then be constructed based on the formula for the branching fraction calculation Equation 6.1 and which accounts for the uncertainties on the measured yield. From the inclusive D_s^- yield the expected number of signal events is given by

$$\mu = \mathcal{B} N_{D_s} \sum_{j=0}^{6} w_j \frac{\varepsilon_{e\nu}^j}{\varepsilon_{D_s}^j}$$

where $\varepsilon_{e\nu}^j$ is the efficiency for reconstructing $D_s^- \to e^- \bar{\nu}_e$ events. The $D_s^- \to e^- \bar{\nu}_e$ branching fraction, $\mathcal{B}$, is to be considered as a variable in this formula. The efficiency ratios are listed in Table 6.3. These values are larger than the corresponding values for the $D_s^- \to \mu^- \bar{\nu}_\mu$ reconstruction due to the fact that electrons do not need to penetrate the IFR and can be identified by the EMC.

n_X^T	$\varepsilon^j_{D_s^- \to e^- \bar{\nu}_e} / \varepsilon^j_{D_s}$
0	0.930 ± 0.028
1	0.819 ± 0.018
2	0.709 ± 0.016
3	0.630 ± 0.017
4	0.565 ± 0.020
5	0.444 ± 0.025
6	0.324 ± 0.029

Table 6.3: Efficiency ratio for each n_X^T value for the $D_s^- \to e^- \bar{\nu}_e$ mode. The errors are due to the size of the signal MC sample.

The likelihood function is now written explicitly as

$$\mathcal{L}(\mathcal{B}) \propto e^{-\frac{(\mu-n)^2}{2\sigma_n^2}} \begin{cases} 0, & \text{if } \mathcal{B} < 0; \\ 1, & \text{if } \mathcal{B} > 0 \end{cases} \tag{6.4}$$

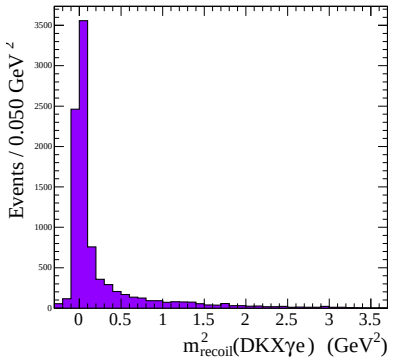

Figure 6.8: The $m^2_{recoil}(DKX\gamma e)$ distribution for signal MC.

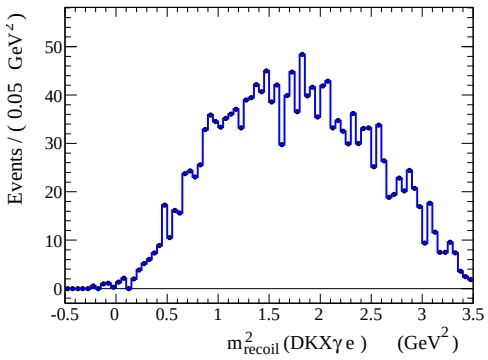

Figure 6.9: The $m^2_{recoil}(DKX\gamma e)$ distribution for generic MC.

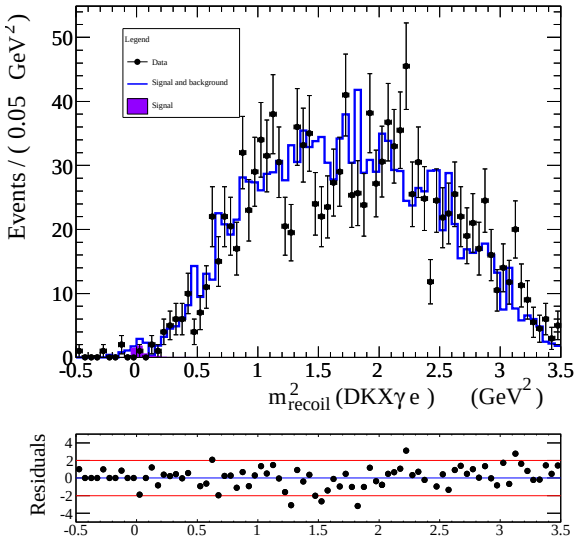

Figure 6.10: Fitted $m^2_{recoil}(DKX\gamma e)$ distribution for Data.

where n is the signal yield and σ_n is the total uncertainty on the signal yield. Uncertainties on the inclusive D_s^- yield and on the efficiencies are on the order of a few percent and do not affect significantly the upper limit estimate.

The upper limit is calculated by integrating the likelihood function upto the value of $\mathcal{B}$ which corresponds to 90% of the integral, as shown in Figure 6.11. The following upper limit is obtained:

$$\mathcal{B}(D_s^- \to e^- \bar{\nu}_e) < 2.8 \times 10^{-4} \quad (@90\%\,\text{confidence level}) \tag{6.5}$$

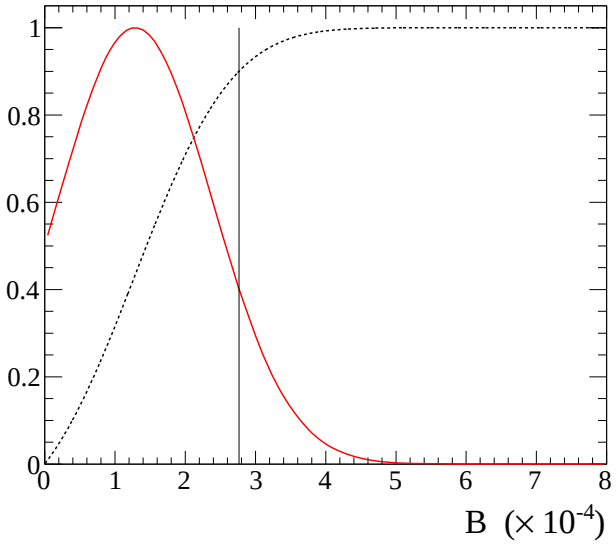

Figure 6.11: Likelihood function $\mathcal{L}(\mathcal{B})$ (solid curve) and its integral (dotted curve). The vertical black line shows the value which encloses 90% of the likelihood function.

6.3 $D_s^- \to \tau^- \bar{\nu}_\tau$

The detection of $D_s^- \to \tau^- \bar{\nu}_\tau$ events has the disadvantage of additional neutrinos in the final state. The decay of the τ gives at least one additional neutrino depending on whether the decay is hadronic or leptonic. Therefore the method for the extraction of the signal events used in the $D_s^- \to \mu^- \bar{\nu}_\mu$ analysis is not applicable since the missing mass in the event is not a single value. Nevertheless, $D_s^- \to \tau^- \bar{\nu}_\tau$ events can be extracted by fitting the E_{extra} distribution after reconstructing the visible energy in the event. Due to higher backgrounds present at the center of mass energy of *BABAR* (compared to CLEO-c) hadronic modes such as $\tau^- \to \pi^- \nu_\tau$ are very hard to extract because the requirement of a pion does not suppress the backgrounds arising from fragmentation pions or other hadronic decays. By contrast background events with additional leptons are not too abundant, and therefore the leptonic decays $\tau^- \to e^- \bar{\nu}_e \nu_\tau$ and $\tau^- \to \mu^- \bar{\nu}_\mu \nu_\tau$ are good reconstruction channels. These channels also do not have additional tracks and therefore combinatoric backgrounds are avoided.

6.3.1 Reconstruction and Selection of the $\tau^- \to e^-$ and $\tau^- \to \mu^-$ samples

To detect $D_s^- \to \tau^- \bar{\nu}_\tau$ decays, event candidates are required to have exactly one more charged track which is either identified as an electron or a muon by the corresponding PID selector. This lepton tags the $\tau^- \to e^- \bar{\nu}_e \nu_\tau$ or $\tau^- \to \mu^- \bar{\nu}_\mu \nu_\tau$ decay. The E_{extra} distribution for signal MC events in both samples peaks towards zero as shown in Figures 6.12 and 6.13. In the μ^- sample events from $D_s^- \to \mu^- \bar{\nu}_\mu$ decays cause a peaking background in the E_{extra} distribution since they have no additional missing energy. These events can be removed by determining the missing mass in the event and selecting only events with $m^2_{recoil}(DKX\gamma\mu)$ greater than 0.5 GeV^2 as shown in Figures 6.14 and 6.15. After this final selection, the E_{extra} distribution for $D_s^- \to \tau^- \bar{\nu}_\tau$ candidates in generic MC, Figures 6.16 and 6.17, show substantial separation between signal and background events.

6.3.2 Fit for the Signal Yields

A binned maximum likelihood fit is performed to the E_{extra} distributions in Data to determine the signal yield for each sample. The signal events are modeled by histogram PDFs from the reconstructed signal MC samples. The backgrounds are modeled using the reconstructed generic MC for each sample after removing the component due to signal

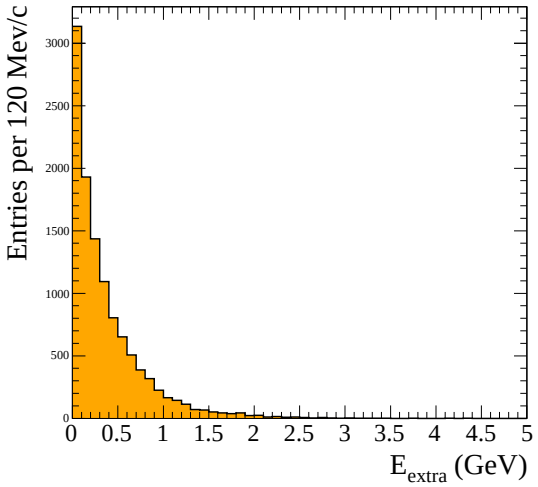

Figure 6.12: E_{extra} distribution for $\tau^- \to e^- \bar{\nu}_e \nu_\tau$ candidates in the signal MC.

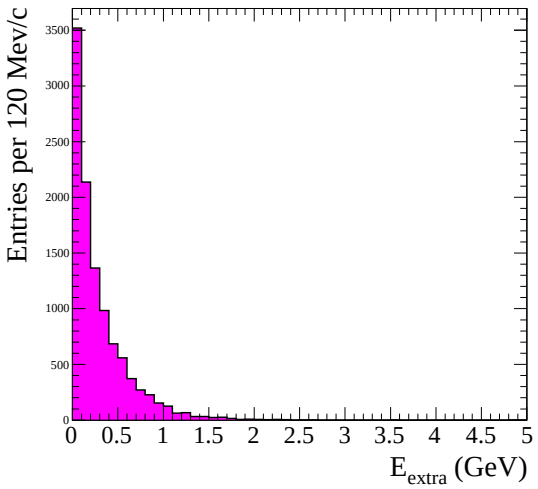

Figure 6.13: E_{extra} distribution for $\tau^- \to \mu^- \bar{\nu}_\mu \nu_\tau$ candidates in the signal MC.

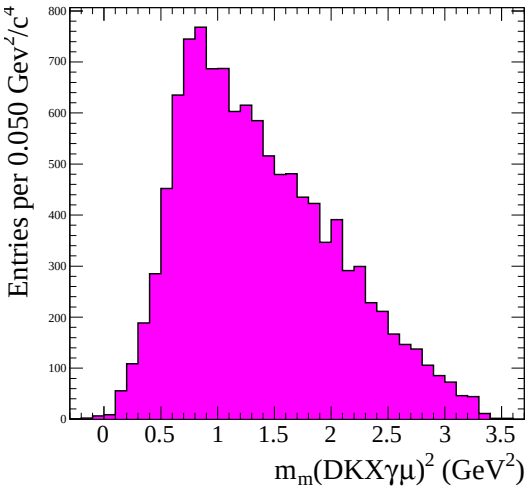

Figure 6.14: $m^2_{recoil}(DKX\gamma\mu)$ distribution for $\tau^- \to \mu^-\bar{\nu}_\mu\nu_\tau$ candidates in the $D_s^- \to \tau\nu; \tau \to \mu\nu\nu$ signal MC.

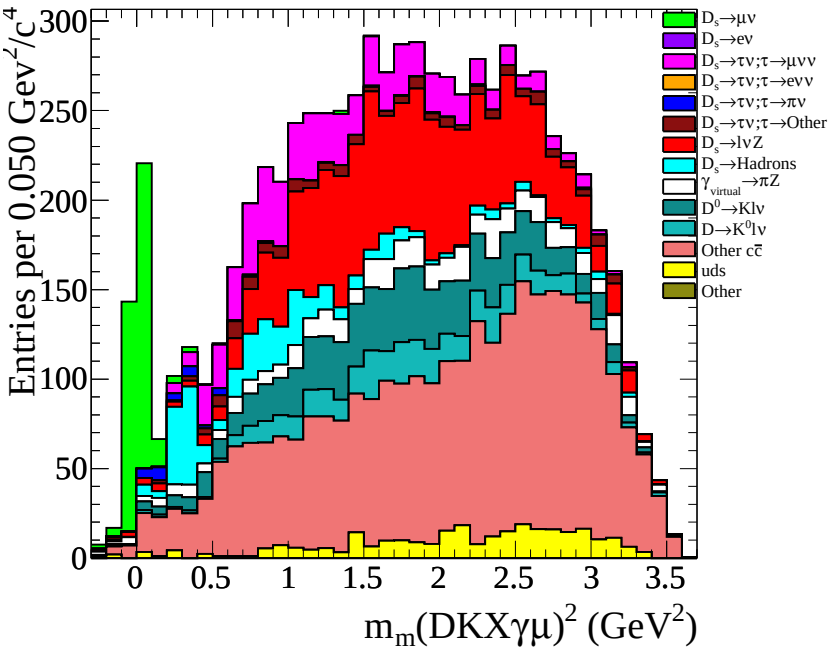

Figure 6.15: $m^2_{recoil}(DKX\gamma\mu)$ distribution for $\tau^- \to \mu^-\bar{\nu}_\mu\nu_\tau$ candidates in the generic MC.

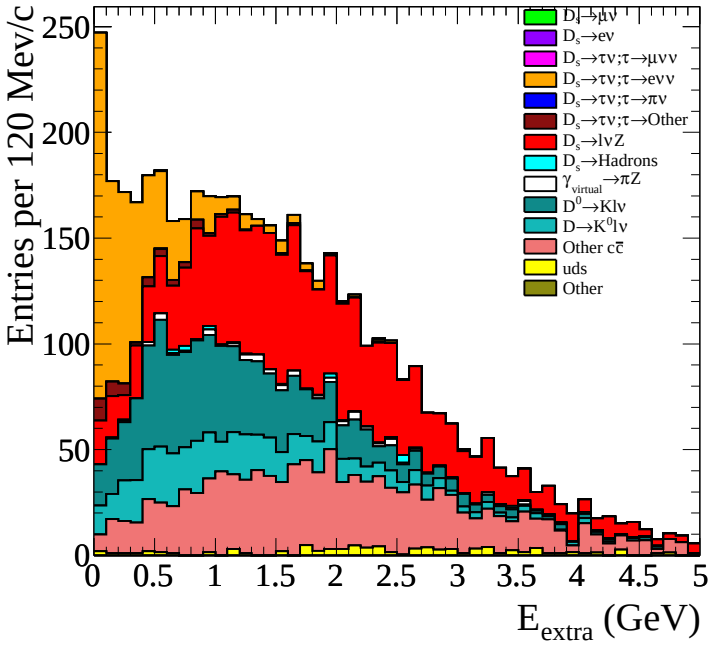

Figure 6.16: E_{extra} distribution for $\tau^- \to e^- \bar{\nu}_e \nu_\tau$ candidates in the generic MC.

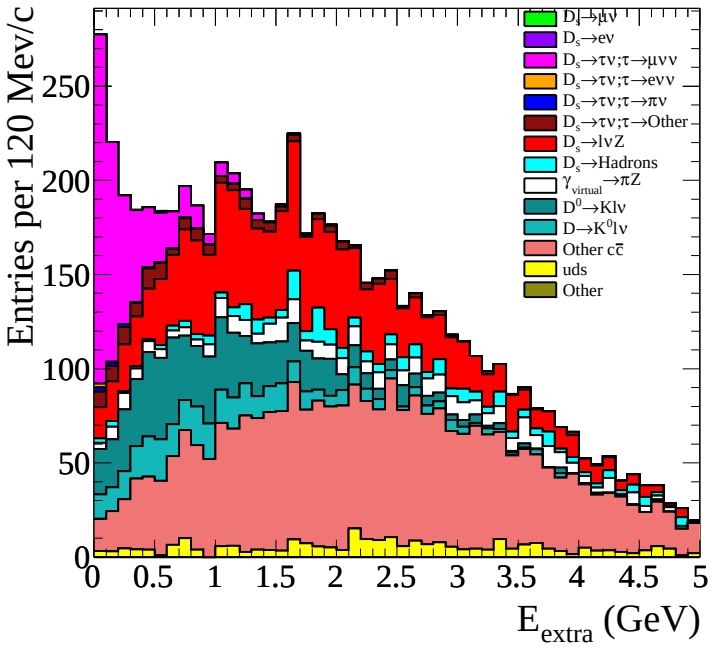

Figure 6.17: E_{extra} distribution for $\tau^- \to \mu^- \bar{\nu}_\mu \nu_\tau$ candidates in the generic MC.

events. These fits are shown in Figures 6.18 and 6.19. The signal yields for the $\tau^- \to e^-\bar{\nu}_e\nu_\tau$ and $\tau^- \to \mu^-\bar{\nu}_\mu\nu_\tau$ samples are 408 ± 42 and 340 ± 33, respectively.

6.3.3 Determination of $\mathcal{B}(D_s^- \to \tau^-\bar{\nu}_\tau)$ for the e^- and μ^- samples

The determination of the branching fraction for $D_s^- \to \tau^-\bar{\nu}_\tau$ is done following the method used for $D_s^- \to \mu^-\bar{\nu}_\mu$. However, for $D_s^- \to \tau^-\bar{\nu}_\tau$ a correction factor is applied to the denominator of Equation 6.1 to account for the partial reconstruction of the τ decay:

$$\mathcal{B}(D_s \to \tau\nu) = \frac{N_{\tau\nu}}{N_{D_s} \sum_{j=0}^{6} w_j \frac{\varepsilon_{\tau\nu}^j \mathcal{B}(\tau \to \ell\nu\nu)}{\varepsilon_{D_s}^j}} \tag{6.6}$$

where $\ell = e$ or μ. The branching fractions of the tau, $\mathcal{B}(\tau \to e\nu\nu)$ and $\mathcal{B}(\tau \to \mu\nu\nu)$, are known at the level of 10^{-3} [17] and do not introduce significant uncertainty. The efficiency ratios for reconstructing $D_s^- \to \tau^-\bar{\nu}_\tau$ events in the e^- and μ^- samples are listed in Tables 6.4 and 6.5. The values for $\mathcal{B}(D_s^- \to \tau^-\bar{\nu}_\tau)$ obtained from each sample are the following:

$$\mathcal{B}(D_s^- \to \tau^-\bar{\nu}_\tau) = (5.07 \pm 0.52) \times 10^{-2} \quad (\tau \to e\nu\nu) \tag{6.7}$$

$$\mathcal{B}(D_s^- \to \tau^-\bar{\nu}_\tau) = (4.91 \pm 0.47) \times 10^{-2} \quad (\tau \to \mu\nu\nu) \tag{6.8}$$

where the errors are statistical only. As a crosscheck the calculations are performed using the signal yields obtained in the generic MC sample and the following values are obtained:

$$\mathcal{B}_{MC}(D_s^- \to \tau^-\bar{\nu}_\tau) = (7.12 \pm 0.52) \times 10^{-2} \quad (\tau \to e\nu\nu) \tag{6.9}$$

$$\mathcal{B}_{MC}(D_s^- \to \tau^-\bar{\nu}_\tau) = (6.80 \pm 0.48) \times 10^{-2} \quad (\tau \to \mu\nu\nu) \tag{6.10}$$

These values are within one statistical sigma of the true value, 6.4×10^{-2} , used in the generation of the MC.

6.3.4 Systematic Uncertainties on $\mathcal{B}(D_s^- \to \tau^-\bar{\nu}_\tau)$

Most of the systematic uncertainties on $\mathcal{B}(D_s^- \to \tau^-\bar{\nu}_\tau)$ are common with the $D_s^- \to \mu^-\bar{\nu}_\mu$ channel and are listed in Tables 6.6 and 6.7. In the $D_s^- \to \tau\nu; \tau \to e\nu\nu$ sample the PID systematic uncertainty is smaller due to the better performance of the EMC in identifying electrons. However, the $D_s^- \to \tau^-\bar{\nu}_\tau$ modes have larger uncertainties due to the extraction of the signal from the E_{extra} distributions. The systematic uncertainty for

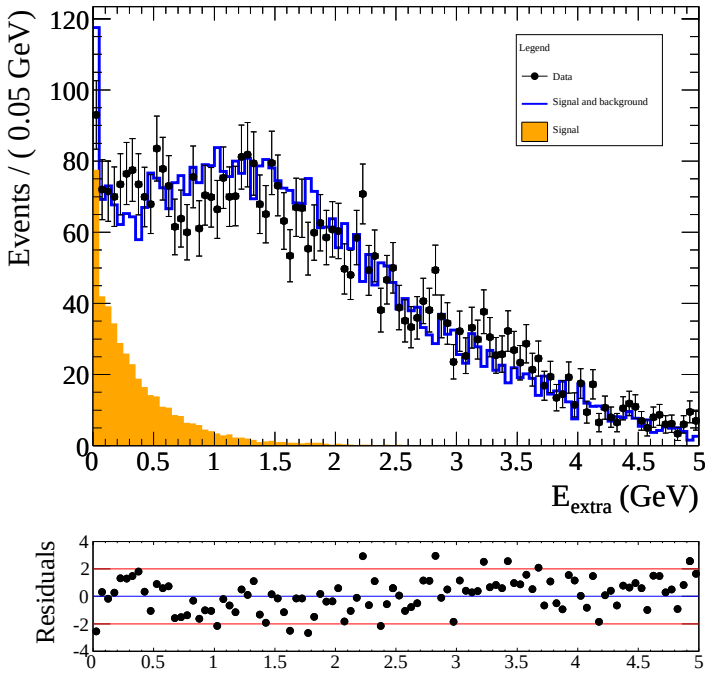

Figure 6.18: Fit to the E_{extra} distribution of $\tau^- \to e^- \bar{\nu}_e \nu_\tau$ candidates in Data .

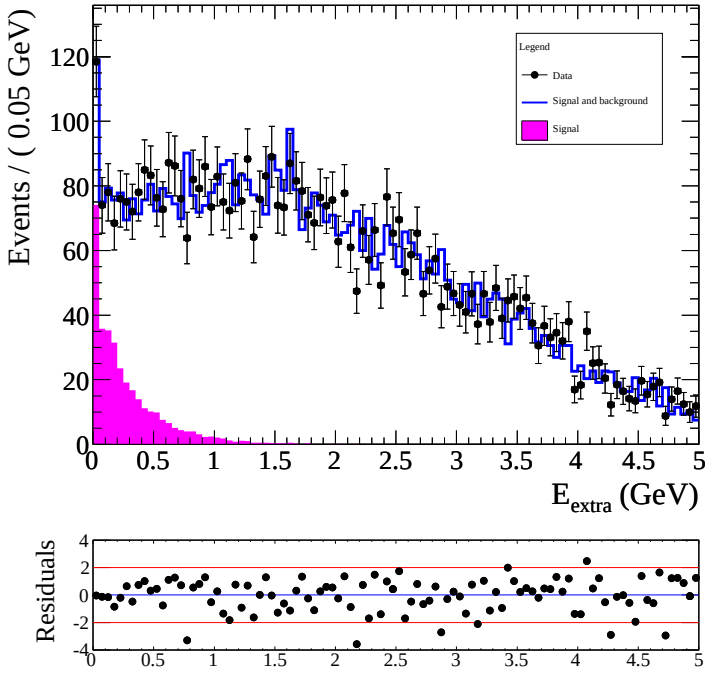

Figure 6.19: Fit to the E_{extra} distribution of $\tau^- \to \mu^- \bar{\nu}_\mu \nu_\tau$ candidates in Data .

n_X^T	$\varepsilon^j_{\tau\nu}/\varepsilon^j_{D_s}$
0	0.843 ± 0.022
1	0.782 ± 0.014
2	0.686 ± 0.013
3	0.604 ± 0.014
4	0.562 ± 0.017
5	0.441 ± 0.021
6	0.346 ± 0.025

Table 6.4: Efficiency ratio, ε^j, for each n_X^T value for the $D_s^- \to \tau\nu; \tau \to e\nu\nu$ mode. The errors are due to the size of the signal MC sample.

n_X^T	$\varepsilon^j_{\tau\nu}/\varepsilon^j_{D_s}$
0	0.771 ± 0.021
1	0.675 ± 0.013
2	0.605 ± 0.012
3	0.534 ± 0.013
4	0.467 ± 0.015
5	0.406 ± 0.020
6	0.306 ± 0.023

Table 6.5: Efficiency ratio, ε^j, for each n_X^T value for the $D_s^- \to \tau\nu; \tau \to \mu\nu\nu$ mode. The errors are due to the size of the signal MC sample.

the signal model is assigned by replacing the nominal model with an exponential function which was shown to fit the signal MC. The background systematic is assigned by varying the background components in the generic MC and by the statistical errors on the bin contents.

Systematic	**Difference in the B.F.** ($\times 10^{-2}$)	**Difference/Nominal**
WS n_X^T weights	(-0.05,+0.00)	(-1.09,+0.00)%
RS n_X^T weights	(-0.00,+0.00)	(-0.04,+0.00)%
D_s Signal Shape	(-0.07,+0.07)	(-1.45,+1.45)%
Peaking Backgrounds	(-0.08,+0.08)	(-1.64,+1.67)%
Background Model	(-0.01,+0.01)	(-0.34,+0.23)%
n_X Resolution	(-0.02,+0.02)	(-0.48,+0.46)%
Signal Photon Backgrounds	(-0.11,+0.11)	(-2.24,+2.32)%
$e\nu\nu$ Background Model	0.57	(11.65)%
$e\nu\nu$ Signal Model	0.39	(5.48)%
e Tracking Efficiency	0.06	(0.83)%
e PID Efficiency	0.01	(0.14)%
Total	**0.68**	(13.4)%

Table 6.6: Summary of systematic errors on $\mathcal{B}(D_s^- \to \tau^- \bar{\nu}_\tau)$ in the $\tau^- \to e^- \bar{\nu}_e \nu_\tau$ sample.

Systematic	**Difference in the B.F.** ($\times 10^{-2}$)	**Difference/Nominal**
WS n_X^T weights	(-0.05,+0.00)	(-1.08,+0.00)%
RS n_X^T weights	(-0.02,+0.00)	(-0.04,+0.00)%
D_s Signal Shape	(-0.07,+0.07)	(-1.45,+1.45)%
Peaking Backgrounds	(-0.08,+0.08)	(-1.62,+1.64)%
Background Model	(-0.02,+0.12)	(-0.35,+0.24)%
n_X Resolution	(-0.02,+0.21)	(-0.46,+0.43)%
Signal Photon Backgrounds	(-0.11,+0.11)	(-2.23,+2.31)%
$\mu\nu\nu$ Background Model	0.49	(9.60)%
$\mu\nu\nu$ Signal Model	0.23	(1.77)%
μ Tracking Efficiency	0.06	(0.83)%
μ PID Efficiency	0.13	(1.91)%
Total	**0.54**	(11.1)%

Table 6.7: Summary of systematic errors on $\mathcal{B}(D_s^- \to \tau^- \bar{\nu}_\tau)$ in the $\tau^- \to \mu^- \bar{\nu}_\mu \nu_\tau$ sample .

6.3.5 Average Value of $\mathcal{B}(D_s^- \to \tau^- \bar{\nu}_\tau)$

An error-weighted average of the two $D_s^- \to \tau^- \bar{\nu}_\tau$ branching fractions is determined using the method in Ref. [34]. The average is calculated as follows:

$$\mathcal{B}_{Avg} = \sum_i w_i \mathcal{B}_i, \quad where \quad w_i = \frac{\sum_j (V^{-1})_{ij}}{\sum_{k,l} (V^{-1})_{kl}} \tag{6.11}$$

where V is the total covariance matrix. The statistical and systematic errors are calculated as follows:

$$\sigma^2_{stat} = \sum_{i,j} w_i V^{stat}_{ij} w_j \quad and \quad \sigma^2_{syst} = \sum_{i,j} w_i V^{syst}_{ij} w_j \tag{6.12}$$

where V^{stat} and V^{syst} are the statistical and systematic parts: $V = V^{stat} + V^{syst}$. The indexing is in the order $1{=}\tau^- \to e^- \bar{\nu}_e \nu_\tau$, $2{=}\tau^- \to \mu^- \bar{\nu}_\mu \nu_\tau$. The following sources of correlations are accounted for in the covariance matrices:

- the statistical error due to the common denominator,
- the systematic error due to the common denominator,
- the systematic error due to tracking
- the systematic error due to the signal model variation to an exponential model,
- and the systematic error due to the background model,

The diagonal elements in the matrices are just the square of the total statistical or systematic errors. The offdiagonal element in V^{stat} is computed as

$$\sigma^e_{stat} * \sigma^\mu_{stat}$$

where σ^e_{stat} is the statistical error on the branching fraction (in the electron sample) resulting from the total statistical error on the denominator; similarly for σ^μ_{stat}. The off-diagonal element in the V^{syst} is computed as

$$\sigma^e_{syst} * \sigma^\mu_{syst} + \sigma^e_{track} * \sigma^\mu_{track} + \sigma^e_{sig} * \sigma^\mu_{sig} + \sigma^e_{bkg} * \sigma^\mu_{bkg}.$$

where σ^e_{syst} is the systematic error on the branching fraction (in the electron sample) resulting from the total systematic error on the denominator. The rest are defined similarly.

The numerical values of the covariance matrices are the following:

$$V^{stat} = \begin{pmatrix} 0.250 & 0.003 \\ 0.003 & 0.230 \end{pmatrix}, \qquad V^{syst} = \begin{pmatrix} 0.436 & 0.141 \\ 0.141 & 0.292 \end{pmatrix}$$

The weights for each mode determined from Eq. 6.11 are $w_e = 0.411$ and $w_\mu = 0.589$ and the resulting average value is the following:

$$\mathcal{B}_{Avg}(D_s^- \to \tau^- \bar{\nu}_\tau) = (5.00 \pm 0.35 \pm 0.49) \times 10^{-2} \tag{6.13}$$

6.3.6 Test of Lepton Universality

The ratio of branching fractions: $\mathcal{B}(D_s^- \to \tau^- \bar{\nu}_\tau)/\mathcal{B}(D_s^- \to \mu^- \bar{\nu}_\mu)$, can be used as a test of lepton universality. For this calculation the average value for the $D_s^- \to \tau^- \bar{\nu}_\tau$ branching fraction obtained in the previous section is used:

$$r = \frac{\mathcal{B}(D_s^- \to \tau^- \bar{\nu}_\tau)}{\mathcal{B}(D_s^- \to \mu^- \bar{\nu}_\mu)} = \frac{w_e \mathcal{B}(D_s^+ \to \tau_{e\nu\nu}\nu) + w_\mu \mathcal{B}(D_s^+ \to \tau_{\mu\nu\nu}\nu)}{\mathcal{B}(D_s^- \to \mu^- \bar{\nu}_\mu)}, \tag{6.14}$$

where the weights are obtained from the previous section. The statistical and systematic errors are calculated as follows:

$$\sigma^2_{stat} = \sum_{i,j=0}^{2} \frac{dr}{dx_i}\frac{dr}{dx_j} V^{ij}_{stat}, \quad and \quad \sigma^2_{syst} = \sum_{i,j=0}^{2} \frac{dr}{dx_i}\frac{dr}{dx_j} V^{ij}_{syst} \tag{6.15}$$

where $x_0 = \mathcal{B}(D_s^- \to \mu^- \bar{\nu}_\mu)$, $x_1 = \mathcal{B}(D_s^+ \to \tau_{e\nu\nu}\nu)$, and $x_2 = \mathcal{B}(D_s^+ \to \tau_{\mu\nu\nu}\nu)$. The correlations listed in the previous section as well as a for the correlated PID systematic between the $D_s^- \to \mu^- \bar{\nu}_\mu$ and $D_s^+ \to \tau_{\mu\nu\nu}\nu$ modes are accounted for in the covariance matrices. The covariance matrices obtained are the following:

$$V^{stat} = \begin{pmatrix} 0.0144 & 0.0040 & 0.0038 \\ 0.0040 & 2.7040 & 0.0324 \\ 0.0038 & 0.0324 & 2.2090 \end{pmatrix} \times 10^{-5} \quad and \quad V^{syst} = \begin{pmatrix} 0.0116 & 0.0353 & 0.0438 \\ 0.0353 & 4.6240 & 1.4109 \\ 0.0438 & 1.4109 & 2.9160 \end{pmatrix} \times 10^{-5}$$

and the result for the ratio is the following,

$$\frac{\mathcal{B}(D_s^- \to \tau^- \bar{\nu}_\tau)}{\mathcal{B}(D_s^- \to \mu^- \bar{\nu}_\mu)} = (8.27 \pm 0.77 \pm 0.85) \tag{6.16}$$

This value is consistent with the Standard Model value of 9.76.

6.4 Determination of f_{D_s}

The value of f_{D_s} is determined using the expression for the branching fraction in equation 1.9. Inverting this equation and noting that $\mathcal{B}(D_s^- \to \ell^- \bar{\nu}_\ell) = \tau_{D_s^+} \Gamma(D_s^- \to \ell^- \bar{\nu}_\ell)$, where $\tau_{D_s^+}$ is the D_s^- lifetime, gives

$$f_{D_s^+} = \frac{1}{G_F m_\ell \left(1 - \frac{m_\ell^2}{M_{D_s^+}^2}\right) |V_{cs}|} \sqrt{\frac{8\pi B(D_s^+ \to \ell\nu)}{M_{D_s^+} \tau_{D_s^+}}} \tag{6.17}$$

To second order in the Wolfenstein parametrization $|V_{cs}|$ can be assumed to be equal to $|V_{ud}|$, which has been measured very precisely. The values for the additional parameters are given in table 6.8.

Quantity	PDG Value
$M_{D_s^+}$	1968.49(34) MeV
m_μ	105.658367(9) MeV
m_τ	1776.84(17) MeV
$\tau_{D_s^+}$	$500(7) \times 10^{-15} s$
G_F	$1.16637(1) \times 10^{-5}$ GeV^{-2}
$\lvert V_{ud} \rvert$	0.97418(27)

Table 6.8: Additional parameters used to compute $f_{D_s^+}$.

Table 6.9 lists a summary of the measurements of $\mathcal{B}(D_s^- \to \ell^- \bar{\nu}_\ell)$ and the values obtained for f_{D_s}. The systematic uncertainty due to the additional parameters needed to calculate f_{D_s} is about 1.9 MeV and arises from the uncertainty in the D_s^- lifetime. An error-weighted average of f_{D_s} measurements is obtained using the technique described in section 6.3.5. In addition to the correlations listed there the correlation in the systematic error due to PID between $D_s^- \to \mu^- \bar{\nu}_\mu$ and $D_s^- \to \tau^- \bar{\nu}_\tau (\tau^- \to \mu^- \bar{\nu}_\mu \nu_\tau)$ modes is accounted for. The numerical values of the covariance matrices are the following:

$$V^{stat} = \begin{pmatrix} 70.56 & 2.13 & 2.10 \\ 2.13 & 169.00 & 1.95 \\ 2.10 & 1.95 & 144.00 \end{pmatrix}, \qquad V^{syst} = \begin{pmatrix} 62.90 & 19.00 & 24.49 \\ 19.00 & 292.61 & 85.05 \\ 24.49 & 85.05 & 199.61 \end{pmatrix}$$

where the indexing is in the order 1=$D_s^- \to \mu^- \bar{\nu}_\mu$, 2=$D_s^- \to \tau\nu; \tau \to e\nu\nu$, and 3=$D_s^- \to$

$\tau\nu;\tau \to \mu\nu\nu$. The weights are: $\mu\nu$=0.66, $\tau^- \to e^-\bar{\nu}_e\nu_\tau$=0.14, and $\tau^- \to \mu^-\bar{\nu}_\mu\nu_\tau$=0.19. The average value is shown in Table 6.9.

Table 6.9: Results for $\mathcal{B}(D_s^- \to \ell^-\bar{\nu}_\ell)$ and f_{D_s}. The first error is statistical and the second is systematic. The systematic error due to the PDG parameters is included in the second error.

Channel	$\mathcal{B}(D_s^- \to \ell^-\bar{\nu}_\ell)$	Signal Yield	f_{D_s}(MeV)
$D_s^- \to \mu^-\bar{\nu}_\mu$	$(6.02 \pm 0.38 \pm 0.34) \times 10^{-3}$	274.04 ± 16.85	$265.7 \pm 8.4 \pm 7.7$
$D_s^- \to \tau\nu;\tau \to e\nu\nu$	$(5.07 \pm 0.52 \pm 0.66) \times 10^{-2}$	407.99 ± 41.65	$247 \pm 13 \pm 17$
$D_s^- \to \tau\nu;\tau \to \mu\nu\nu$	$(4.91 \pm 0.47 \pm 0.54) \times 10^{-2}$	340.04 ± 32.35	$243 \pm 12 \pm 14$
$D_s^- \to \ell^-\bar{\nu}_\ell$ combined		1022.07	$258.6 \pm 6.4 \pm 7.5$

Chapter 7

Conclusions

In this part of this thesis, a measurement of the leptonic decays of the D_s^- meson has been presented. These decays allow for a precise determination of the decay constant f_{D_s}. This measurement uses the full data set collected by the *BABAR* detector and the value obtained for f_{D_s} has a precision comparable to the world average. The individual measurement of $\mathcal{B}(D_s^- \to \mu^- \bar{\nu}_\mu)$ has an uncertainty which is better than the measurement performed by the BELLE collaboration using a data set of about the same size. The better precision obtained in this analysis is due to a larger signal yield which leads to a smaller statistical error.

The value for the D_s^- decay constant obtained in this analysis is higher than the current theoretical value [6] by only one standard deviation and therefore no evidence for effects of physics beyond the SM is found. The statistical uncertainty due to the low $D_s^- \to \mu^- \bar{\nu}_\mu$ yield remains as the limiting factor preventing a more precise comparison with theory. In the future, more precise comparisons between theory and experiment may be available after BELLE performs a final analysis of their full data-set. In addition, the upgraded charm factory BESIII which has just started running in Beijing, China expects to accumulate about an order of magnitude more Data than the previous CLEO-c experiment. Finally, the Super-B and Super-BELLE experiments expected to turn on in a few years will eventually accumulate data sets about an order of magnitude larger than their current ones. The analyzes of these future data sets will provide the most sensitive searches for new fundamental particles which may affect the leptonic D_s^- decays.

Part II

OBSERVATION OF NEW RESONANCES DECAYING TO $D^{(*)}\pi$

Chapter 8

Introduction

8.1 Motivation and Theory

Charm spectroscopy, to this date, remains poorly explored. Many D meson states predicted in the 1980's have not been observed experimentally. Part II of this thesis is devoted to the search for excited states of a system consisting of a charm quark and an up or down quark.

Predictions of the bound states in these systems were done in 1985 by S. Godfrey and N. Isgur [36] using a chromodynamic relativistic potential model. This model had great success in predicting qualitatively the observed spectra of mesons and baryons. Figure 8.1 shows the predicted spectrum for a $c\bar{u}$ system, the spectrum for a $c\bar{d}$ system is shifted to higher mass by a small amount not noticeable on this scale. The excited states tend to have large widths (>10MeV) because they can decay strongly through pion emission, one exception is the D^* because it is very close to threshold therefore its width is suppressed to about 0.1 MeV. The next excitations are the angular momentum excited states with L=1 (P states), where L is the angular momentum of the quarks; there exist 2 "narrow" and 2 broad states depending on their decay mechanism. The decay rates of the narrows ones are suppressed by angular momentum barrier factors since they decay through D-waves and therefore have widths of about 20-40 MeV. The broad ones have widths on the order of hundreds of MeV because they can decay through S-waves [37]. Table 8.1 lists the predicted states together with their predicted and experimentally observed masses.

The ground states, D^0 and D^+, and spin excitations, D^{*0} and D^{*+}, were first observed in 1976 and 1979 respectively. The narrow L=1 orbital excitations were not observed until 1989 owing to their lower production rates and larger widths. The broad L=1 states have

only recently been observed by BELLE and *BABAR* in B meson decays where they can be separated from the backgrounds through kinematic constraints. However, the sample of $e^+e^- \to c\bar{c}$ events collected by *BABAR* is now orders of magnitude larger than the data-sets of previous charm factories, one therefore expects to have much better sensitivity to higher resonances despite their large widths and smaller production rates.

To search for higher D meson excitations a study of the $D\pi$ and $D^*\pi$ final states has been performed where are these final states are produced inclusively in the $c\bar{c}$ hadronization. These channels are expected to be the preferred decay modes given their allowed phase-space.

8.2 $D\pi$ Decay Properties

The decays of any excited state D^{**} with arbitrary quantum numbers J^P into two pseudoscalars (Dπ) are restricted by angular momentum and parity conservation.

- By angular momentum conservation $l = J$, where l is the angular momentum of the $D\pi$ system,
- and by parity conservation $P_D * P_\pi * (-1)^l = P \Rightarrow (-1)^J = P$, where P_D and P_π are the parity of the D and pion.

Table 8.2 lists the allowed decays of each predicted state.

8.3 $D^*\pi$ Decay Properties

Decays to $D^*\pi$ are considerably more interesting because the D^* is a spin-1 particle. In $D\pi$ decays if a resonance is observed one can merely classify it as belonging to a class of possible J^P quantum numbers. In $D^*\pi$ decays the initial J^P value can select a z-component of the D^* spin state and the subsequent decay of the D^* will then have a particular angular distribution in the helicity angle θ_H defined as shown in Figure 8.2. An angular analysis of these decays is performed in the rest frame of the D^* with the z-axis is chosen to coincide with the direction of the D^{**} momentum.

- In this frame the initial state is described by its spin angular momentum $|J, M>$ and parity P (the quantum numbers of the D^{**}).

- The intermediate state ($D^*\pi$) is described by orbital angular momentum, $|l, m_l>$, plus the spin of the D^*, $|S = 1, m_s>$. By definition $m_l = 0$ because the pion is moving in the z-direction, it follows that $m_s = M$.

With these requirements one can write the general form of the condition of angular momentum conservation ($\vec{J} = \vec{S} + \vec{l}$):

$$|J, M >= \sum_{l=|J-1|}^{J+1} A_l C^{1lJ}_{M0M} |1, M > |l, 0 >$$

Where A_l are undetermined amplitudes for each possible partial wave and the C coefficients are the Clebsch-Gordon coefficients. Because the initial state of the D^{**} is unpolarized one must average over M to obtain the observable angular probabilities, the $D^*\pi$ system is then described by the following probability distribution:

$$\sum_{M=-J}^{J} \left| \sum_{l=|J-1|}^{J+1} A_l C^{1lJ}_{M0M} |1, M > |l, 0 > \right|^2$$

Where the sum is subject to the condition of parity conservation: $P_{D^*} * P_\pi * (-1)^l = P \Rightarrow (-1)^l = P$. For different values of J and P the Clebsch-Gordon coefficients will choose different D^* spin states ($|1, M >$).

The D^* decays to two pseudoscalars, $D\pi$, so the angular distribution of the second pion is determined by the spin state of the D^* with the same probability distribution as above. As an example consider an excited state with $J^P = 2^+$. By angular momentum conservation l can be 1,2, or 3, but parity requires $(-1)^l = +1$ so l must be 2. The Clebsch-Gordon coefficients are $C^{122}_{-10-1} = 1/\sqrt{2}$, $C^{122}_{000} = 0$, $C^{122}_{101} = -1/\sqrt{2}$ and we find the probability distribution $\propto |\frac{1}{\sqrt{2}} Y_1^{-1}(\theta, \phi)|^2 + |\frac{-1}{\sqrt{2}} Y_1^1(\theta, \phi)|^2 \propto sin^2(\theta)$. Where the spherical harmonics (Y_l^m) arise from the D^* spin states. The angular distributions have been calculated for each of the predicted D meson excited states and are listed in Table 8.2.

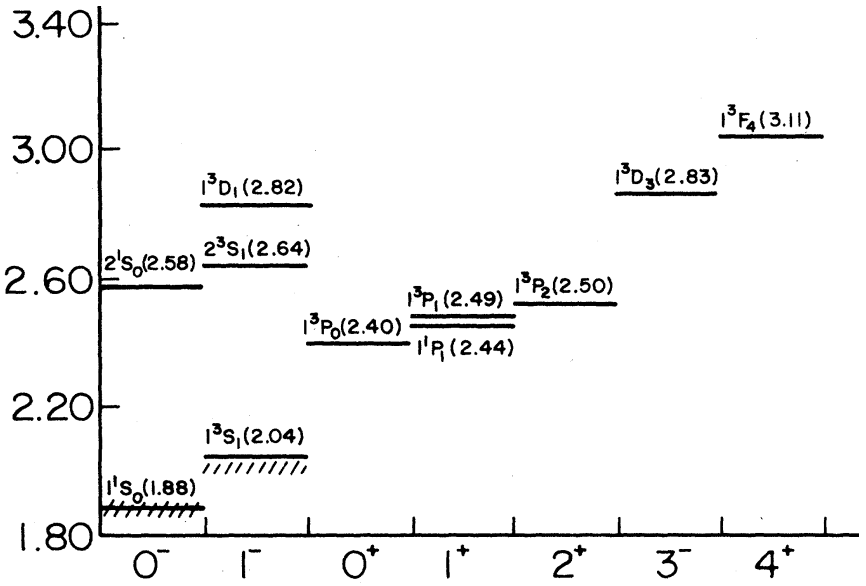

Figure 8.1: Bound states of a $c\bar{u}$ or $c\bar{d}$ system predicted by S. Godfrey and N. Isgur [36]. The y-axis gives the predicted mass and the x-axis labels the J^P quantum numbers.

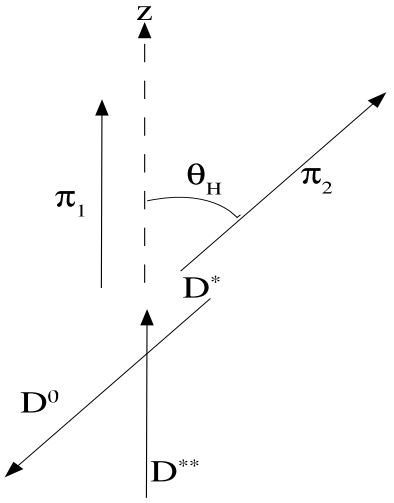

Figure 8.2: Definition of the helicity angle θ_H. The angle is calculated in the rest frame of the D^* and the z-axis is chosen as the direction of the D^{**}.

Table 8.1: Mass and Width properties extracted from [36],[17] and [39]. A "-" indicates the state has not been observed.

Label $D_J^{(2S+1)}(nL)$	PDG Name	Expected Mass (GeV)	Observed Mass (GeV)	Observed Width (MeV)
$D_0^1(2S)$	-	2.58	-	-
$D_1^3(2S)$	-	2.64	-	-
$D_1^1(1P)$	$D_1(2420)$	2.44	2.422 ± 0.002	20 ± 2
$D_0^3(1P)$	$D_0^*(2400)$	2.40	2.300 ± 0.015	310 ± 15
$D_1^3(1P)$	$D_1'(2430)$	2.49	2.427 ± 0.030	380 ± 100
$D_2^3(1P)$	$D_2^*(2460)$	2.50	2.459 ± 0.001	44 ± 2
$D_2^1(1D)$	-	$\sim$2.83	-	-
$D_1^3(1D)$	-	2.82	-	-
$D_2^3(1D)$	-	$\sim$2.83	-	-
$D_3^3(1D)$	-	2.83	-	-

Table 8.2: J^P quantum numbers and angular momentum properties of the decays. The 3rd and 4th columns indicate the allowed angular momentum of the $D\pi$ and $D^*\pi$ decay products. A "-" indicates the decay is not allowed by parity conservation. The last column shows the angular distribution of the helicity angle defined in $D^*\pi$ decays.

Label $D_J^{2S+1}(nL)$	PDG Name	J^P	$D\pi$ Angular Momentum	$D^*\pi$ Angular Momentum	$D^*\pi$ Helicity Distribution
$D_0^1(2S)$		0^-	-	P	$\propto cos^2(\theta)$
$D_1^3(2S)$		1^-	P	P	$\propto sin^2(\theta)$
$D_1^1(1P)$	$D_1(2420)$	1^+	-	S,D	$\propto 1 + Acos^2(\theta)$
$D_0^3(1P)$	$D_0^*(2400)$	0^+	S	-	-
$D_1^3(1P)$	$D_1'(2430)$	1^+	-	S,D	$\propto 1 + Acos^2(\theta)$
$D_2^3(1P)$	$D_2^*(2460)$	2^+	D	D	$\propto sin^2(\theta)$
$D_2^1(1D)$		2^-	-	P,F	$\propto 1 + Acos^2(\theta)$
$D_1^3(1D)$		1^-	P	P	$\propto sin^2(\theta)$
$D_2^3(1D)$		2^-	-	P,F	$\propto 1 + Acos^2(\theta)$
$D_3^3(1D)$		3^-	F	F	$\propto sin^2(\theta)$

Chapter 9

Analysis Overview

9.1 Strategy

The *BABAR* data-set is rich in events of the type $e^+e^- \to c\bar{c}$ where the charm quarks can hadronize into excited D meson states due to the large available energy of the collision. To search for the excited states we reconstruct events of the kind:

$$e^+e^- \to c\bar{c} \to D^{**}X \to D^{(*)}\pi X$$

Where X represents any additional system produced in the event. A diagram showing the event topology for signal events is shown in Figure 9.1.

The requirement of only the $D\pi$ or $D^*\pi$ system without restriction on the additional system is referred to as an *inclusive* reconstruction and is the method used to obtain the largest possible signal yield. Decays to $D\pi$ are reconstructed in the neutral $D^+\pi^-$ and charged $D^0\pi^+$ final states. Decays to $D^*\pi$ are reconstructed in the neutral $D^{*+}\pi^-$ final state only. Charge conjugate modes for all particles are implied throughout this

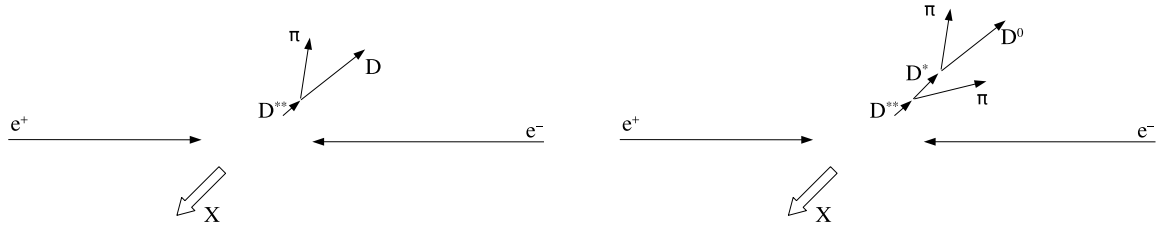

Figure 9.1: Event topology for signal events in the $D\pi$ (left) and $D^*\pi$ (right) final states.

analysis unless otherwise stated. These final states are chosen because they can be fully reconstructed using tracks only, thereby avoiding large backgrounds inherent with neutral particles. The decay chain reconstructed for each final state is as follows:

- $D^{**0} \to D^{+}\pi^{-}$ where $D^{+} \to K^{-}\pi^{+}\pi^{+}$
- $D^{**+} \to D^{0}\pi^{+}$ where $D^{0} \to K^{-}\pi^{+}$
- $D^{**0} \to D^{*+}\pi^{-}$ where $D^{*+} \to D^{0}\pi^{+}$ and $D^{0} \to (K^{-}\pi^{+}$ or $K^{-}\pi^{+}\pi^{-}\pi^{+})$

Backgrounds from B meson decays as well as much of the combinatoric backgrounds are rejected through a selection on the CM momentum of the $D^{(*)}\pi$ system. Another important selection is applied on the angle of the primary pion requiring it to be belong to the signal hemisphere in order to remove pions from the opposite jet. For each final state, dedicated signal MC events are used to determine the efficiency and resolution as a function of the invariant mass of the $D^{(*)}\pi$ system. Backgrounds are studied using a sample of generic MC events which incorporate the known resonances; also, the mass distributions for the wrong-sign samples, $D^{+}\pi^{+}$ and $D^{*+}\pi^{+}$, are studied in data.

9.2 Event Samples

For this analysis 454 fb^{-1} of data from Runs 1 to 6 are used. Both, the on-peak data and the off-peak data are used since the physics of $c\bar{c}$ events does not depend on this energy variation. This data-set corresponds to about 590 million produced $c\bar{c}$ events. The sample of generic MC events corresponds to about twice the data luminosity. The MC sample incorporates the narrow resonances, $D_1(2420)$, $D_2^*(2460)$, and the broad resonances, $D_0^*(2400)$ and $D_1'(2430)$. The numbers of events and luminosity for the samples are listed in Tables 9.1 and 9.2. Dedicated signal MC samples, consisting of about one million events, were generated for the $D_1(2420)$ and $D_2^*(2460)$ resonances in the decay chains which are reconstructed. These event samples are defined by requiring that each event contain the desired decay chain on one side of the event while the other side contain a generic hadronization of the charm quark. The resonances in the MC are generated using non-relativistic Breit-Wigner functions, their parameters are listed in Table 9.3.

Table 9.1: Events used for this analysis, in millions of events. The *On* and *Off* written in the left-most column refer to data taken on or below the Υ resonance energy. The subscript on the D denotes its decay channel.

Type	Run1	Run2	Run3	Run4	Run5	Run6	Total
Data On	280.4	911.8	479.8	1482.3	1963.7	1028.7	6146.7
Data Off	32.6	93.8	34.2	137.2	194.4	65.5	557.6
$e^+e^- \to c\bar{c}$ On	58.9	168.8	84.0	252.8	366.8	156.9	1088.2
$e^+e^- \to c\bar{c}$ Off	2.1	10.6	3.7	13.4	32.2	10.9	72.9
$D_2^{*0} \to D^+_{K\pi\pi}\pi^-$ On	0.043	0.123	0.066	0.203	0.267	0.156	0.858
$D_2^{*0} \to D^+_{K\pi\pi}\pi^-$ Off	0.006	0.015	0.005	0.016	0.03	0.015	0.087
$D_2^{*+} \to D^0_{K\pi}\pi^+$ On	0.083	0.25	0.132	0.403	0.534	0.313	1.715
$D_2^{*+} \to D^0_{K\pi}\pi^+$ Off	0.011	0.028	0.011	0.034	0.058	0.032	0.174
$D_1^0 \to D^{*+}\pi^-, D^{*+} \to D^0_{K\pi}\pi^+$ On	0.043	0.125	0.066	0.203	0.265	0.156	0.858
$D_1^0 \to D^{*+}\pi^-, D^{*+} \to D^0_{K\pi}\pi^+$ Off	0.006	0.015	0.005	0.016	0.03	0.015	0.087
$D_1^0 \to D^{*+}\pi^-, D^{*+} \to D^0_{K3\pi}\pi^+$ On	0.043	0.125	0.066	0.203	0.267	0.15	0.854
$D_1^0 \to D^{*+}\pi^-, D^{*+} \to D^0_{K3\pi}\pi^+$ Off	0.006	0.015	0.005	0.016	0.03	0.015	0.087
$D_2^{*0} \to D^{*+}\pi^-, D^{*+} \to D^0_{K\pi}\pi^+$ On	0.043	0.125	0.066	0.203	0.267	0.156	0.86
$D_2^{*0} \to D^{*+}\pi^-, D^{*+} \to D^0_{K\pi}\pi^+$ Off	0.006	0.015	0.005	0.016	0.03	0.015	0.087
$D_2^{*0} \to D^{*+}\pi^-, D^{*+} \to D^0_{K3\pi}\pi^+$ On	0.043	0.125	0.066	0.203	0.267	0.156	0.86
$D_2^{*0} \to D^{*+}\pi^-, D^{*+} \to D^0_{K3\pi}\pi^+$ Off	0.006	0.015	0.005	0.016	0.03	0.015	0.087

Table 9.2: Luminosity for Data and MC (fb^{-1}).

Type	Run1	Run2	Run3	Run4	Run5	Run6	Total
Data On	20.4	61.1	32.3	100.3	132.9	66.1	413.0
Data Off	2.6	6.9	2.5	10.1	14.5	4.6	41.2
$c\bar{c}$ On	45.31	129.85	64.62	194.46	282.15	120.69	837.08
$c\bar{c}$ Off	1.62	8.15	2.85	10.31	24.77	8.38	56.08

Table 9.3: Mass and width parameters for the resonances in the MC.

	Neutral State Mass (GeV/c^2)	Neutral State Width (GeV)	Charged State Mass (GeV/c^2)	Charged State Width (GeV)
$D_1(2420)$	2.422	0.019	2.427	0.028
$D_0^*(2400)$	2.308	0.276	2.308	0.276
$D_1'(2430)$	2.461	0.290	2.461	0.290
$D_2^*(2460)$	2.459	0.030	2.459	0.025

Chapter 10

The $D^+\pi^-$ Final State

10.1 Event Reconstruction and Selection

For the reconstruction of $D^+\pi^-$ candidates we use the $D^+ \to K^-\pi^+\pi^+$ channel since this channel has the highest branching fraction and only three charged particles leading to a high reconstruction efficiency. The D^+ candidate is selected as follows:

- The Kaon candidate track is required to pass the Tight Kaon PID selector, while the pion candidate tracks are required to pass the `Loose` pion selector.
- A kinematic fit is applied to the tracks requiring them to originate from a common point and the fit probability must greater than 0.1%.
- The D^+ candidate is accepted if the invariant mass of the tracks is within 2.5σ of the mean value for the D^+ signal distribution. The mean and σ parameters are determined from a fit to the $K^-\pi^+\pi^+$ mass distribution using a Gaussian signal + linear background function (see Figure 10.1) and are found to be mean=1868.6 MeV, σ=6.7 MeV.
- In addition, the D^+ candidate must have a signed-flight-significance greater than 0 (see Figure 10.2). The signed-flight-significance is calculated using the transverse displacement of the $K\pi\pi$ vertex relative to the center of the IP region.

Once a D^+ candidate has been selected the $D^+\pi^-$ system is reconstructed as follows:

- D^+ passing the above selections are paired with an additional negatively charged track in the event. This track must pass the VeryTight pion selector.

- A kinematic fit is applied to the $D^+\pi^-$ system with a constrain on the vertex to be within IP region. A fit probability greater than 0.1% is required.
- The momentum of the $D^+\pi^-$ system in the e^+e^- rest frame is required to be greater than 3.0 GeV/c (see Figure 10.3) to reduce combinatorial and B meson decays.
- Finally, the cosine of the angle of the primary pion, in the $D^+\pi^-$ rest frame, relative to the $D^+\pi^-$ direction in the e^+e^- rest frame is required to be greater than -0.8 (see Figure 10.4). This angle is defined as shown in Figure 10.5 and the selection removes pion candidates which originate from the opposite jet.

For each $D^+\pi^-$ candidate the invariant-mass is computed using the mass difference with respect to the D^+ candidate:

$$M(D^+\pi^-) = m(K^-\pi^+\pi^+\pi^-) - m(K^-\pi^+\pi^+) + 1.8693 \text{ GeV}/c^2, \tag{10.1}$$

where the last number is the nominal value for the D^+ mass [17]. The resolution in this variable is about 2.5 MeV whereas the resolution on the total mass $m(K^-\pi^+\pi^+\pi^-)$ is about 10 MeV since the smearing due to the D^+ decay reconstruction is removed by taking the difference.

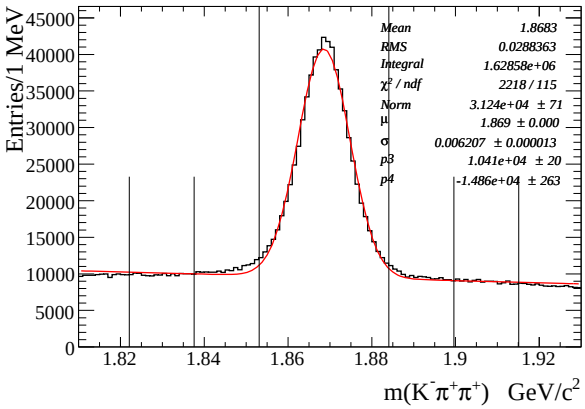

Figure 10.1: D^+ candidate mass distribution in data before the selections on the flight-significance and $\cos(\theta_\pi)$.

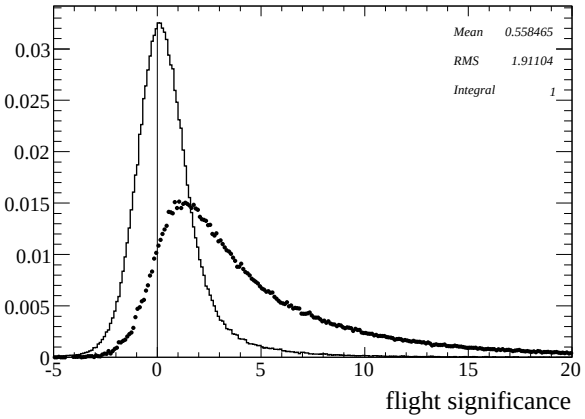

Figure 10.2: Distribution of D^+ candidate flight-significance in data before the $\cos(\theta_\pi)$ selection for signal (points) and D^+ mass side-band regions (histogram). The signal distribution is determined through a side-band subtraction for events in the signal region.

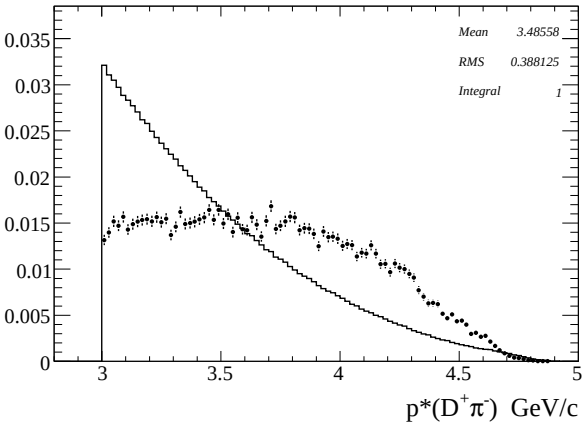

Figure 10.3: CM momentum distribution of the $D^+\pi^-$ candidates for truth-matched signal MC (points) and background(histogram) in the generic MC sample.

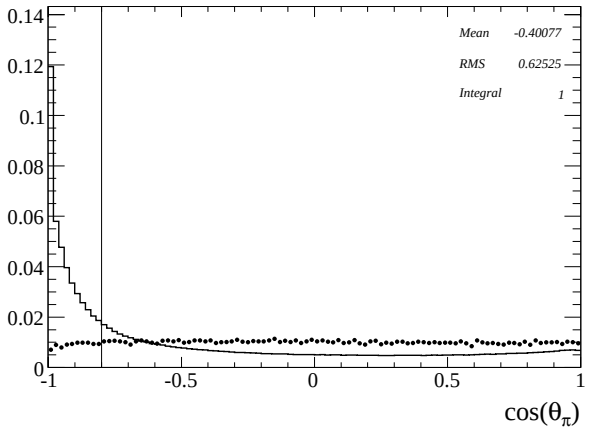

Figure 10.4: $\cos(\theta_\pi)$ distribution for truth-matched signal MC (points) and background (histogram) in the generic MC sample.

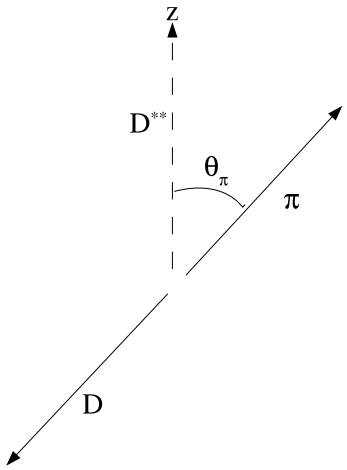

Figure 10.5: $\cos(\theta_\pi)$ is defined by the angle between the π and the D^{**} after boosting the π into the D^{**} frame. The direction of the D^{**} before the boost is used to define the z-axis.

10.2 Signal MC: Efficiency and Resolution

The signal MC for the decay of the $D_2^*(2460)$ into the $D^+\pi^-$ final state has been reconstructed using the procedure defined in the previous section. This MC sample is used to study the dependence of the efficiency and resolution as a function of the generated $D^+\pi^-$ invariant mass. Figure 10.6 shows the reconstructed mass distribution for this sample. In addition to true signal candidates, there is a small non-peaking background present even for signal events, for the determination of the efficiency and resolution only the true signal component is used. The true signal combinations are extracted through a truth-matching algorithm where the reconstructed tracks must be matched to the generated ones. Figure 10.7 shows the reconstruction efficiency as a function of the $D^+\pi^-$ mass, the efficiency increases linearly as the $D^+\pi^-$ mass increases since the momentum of the primary pion increases.

The resolution on M($D^+\pi^-$) is determined as function of the generated mass as there may be some dependence due to the varying momentum of the primary pion. The signal MC sample is divided into sub-samples each covering a range of 25 MeV, for each sub-sample the distribution in the difference between the reconstructed mass and the generated mass is parametrized using the following function:

$$R(x) = (1 - f_2 - f_3)\frac{e^{-\frac{1}{2}\frac{(x-\mu_1)^2}{\sigma_1^2}}}{\sigma_1\sqrt{2\pi}} + f_2\frac{\frac{\sigma_2}{\pi}}{(x-\mu_2)^2+\sigma_2^2} + f_3\frac{\frac{\sigma_3}{\pi}}{(x-\mu_3)^2+\sigma_3^2} \qquad (10.2)$$

The Breit-Wigner functions are necessary because the resolution distributions have very long tails. Figure 10.8 shows the fitted distribution for each sub-sample. Each piece in the function is normalized 1 so that f_2 and f_3 are the fractions in each Breit-Wigner component. Only the σ_1 parameter varies as a function of the generated mass, the other parameters can be fixed to the following values, determined from a fit to the total combined distribution:

- $f_2 = .084 \quad f_3 = .026$
- $\mu_1 = .06\ MeV \quad \mu_2 = -5.62\ MeV \quad \mu_3 = 6.0\ MeV$
- $\sigma_2 = 1.58\sigma_1 \quad \sigma_3 = .79\sigma_1$

The values for the parameter σ_1 are shown in Figure 10.9.

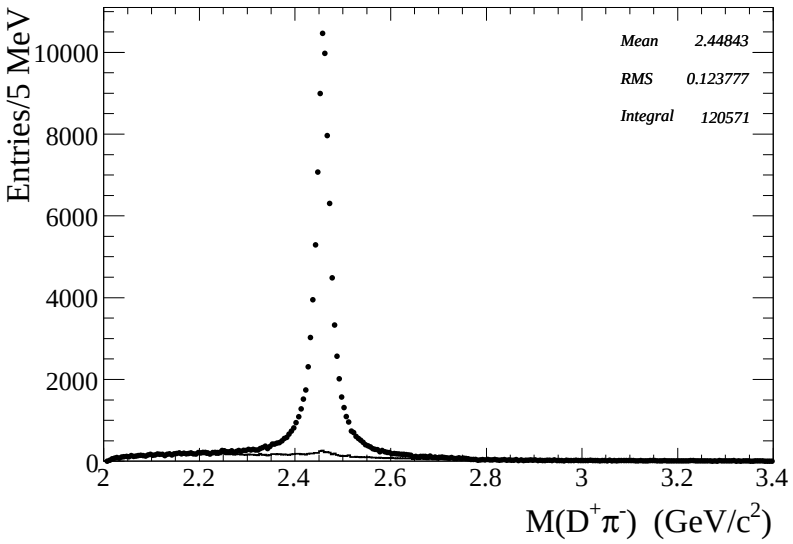

Figure 10.6: Reconstructed mass distribution (points), the histogram shows the candidates which are not truth-matched.

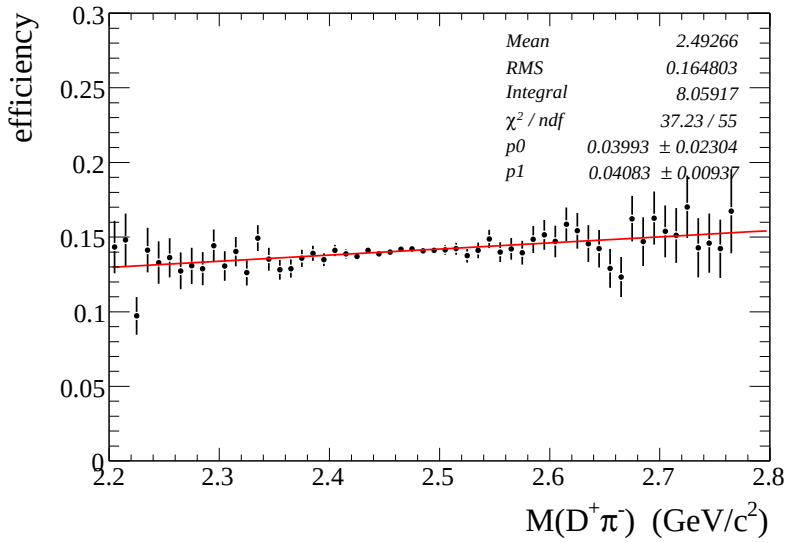

Figure 10.7: Efficiency as a function of generated $D^+\pi^-$ mass is computed using the truth-matched distribution over the generated distribution .

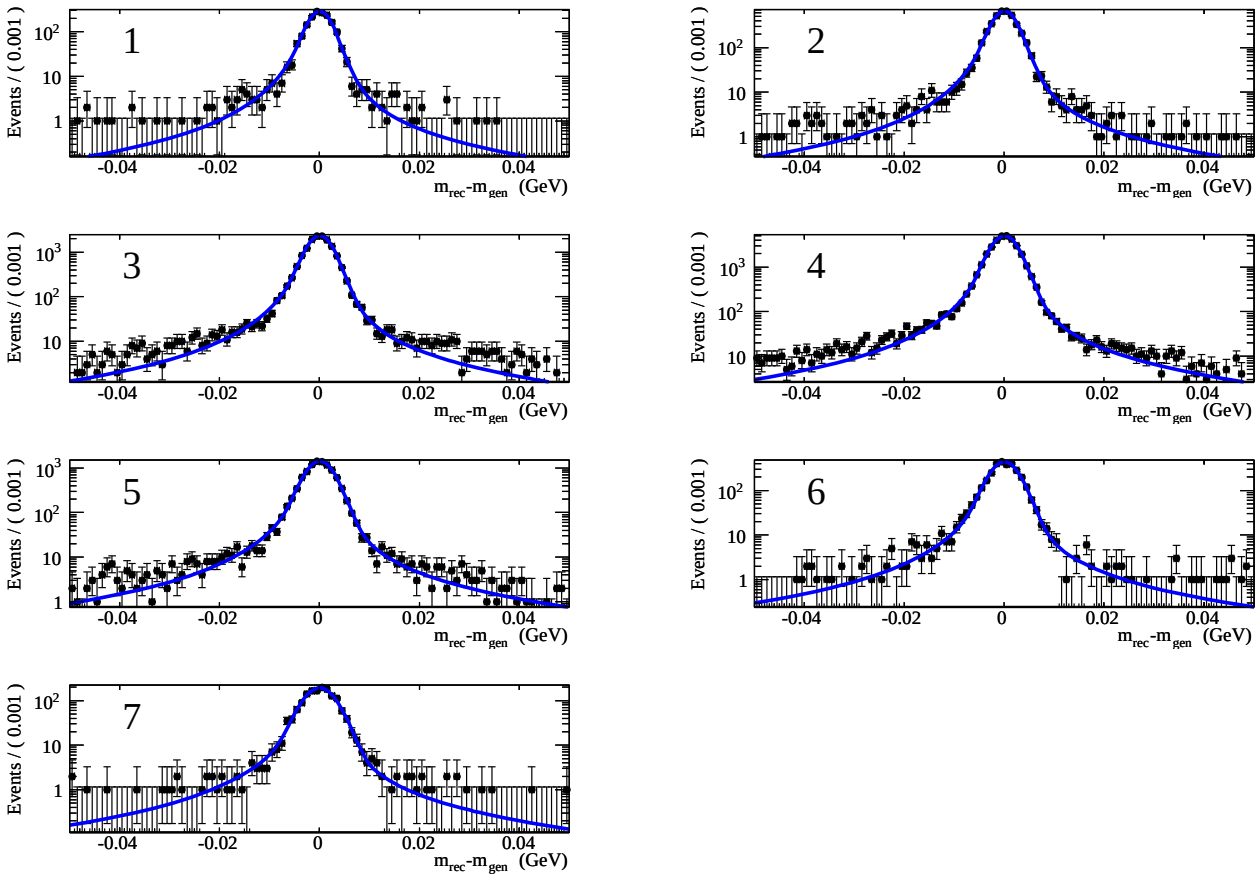

Figure 10.8: Fit to the distribution of reconstructed - generated $D^+\pi^-$ mass for each sub-sample.

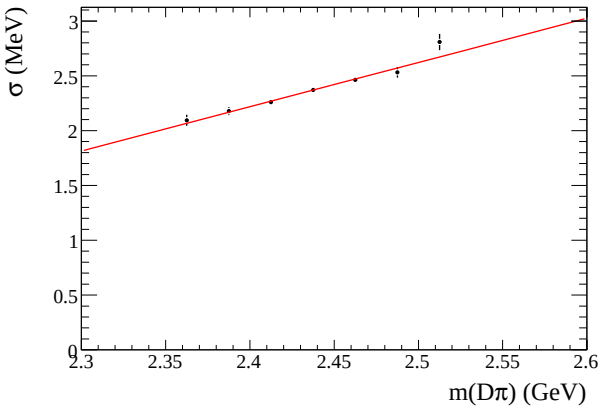

Figure 10.9: Values for σ_1 determined from each of the fits in Figure 10.8. The linear fit gives σ_1=(-8.04 + 4.31*x) MeV).

10.3 Generic MC

The study of the generic MC sample is an important part of this analysis as this sample is generated with the current knowledge on the states of the D meson spectrum and is therefore a good approximation to what one expects to observe in the data. It also shows what, if any, possible peaking backgrounds might be present in the data. Finally, it provides a testing ground for the method to be used for modeling the data distribution later.

The invariant-mass distribution of D^+ candidates after the full event selection is applied is presented in Figure 10.10. The purity of the D^+ signal is determined to be 81% by subtracting the background from the signal region using the sideband regions under the assumption of a linear background shape.

The M($D^+\pi^-$) distribution is shown in Figure 10.11. The known D meson excited states $D_1(2420)^0$, $D_2^*(2460)^0$, $D_0^*(2400)^0$, and $D_1'(2430)^0$ all contribute to this mass distribution either as signals or as a peaking background. The smooth background, shown in this plot, contains no other peaking structures and arises largely from events where there is a true D^+ which is paired with a pion produced in the fragmentation of the same jet. In Figure 10.12 the resonances have been separated from the smooth background by truth-matching and one can see a total of five peaking components. The main signal from the $D_2^*(2460)^0$ appears as the most prominent signal. A large broad signal component peaking at about 2300 MeV is due to the $D_0^*(2400)^0$, however, it has been generated with an artificial mass cut-off at about 2600 MeV . There are three peaking backgrounds (feed-down) arising from the decays of $D_1(2420)^0$, $D_2^*(2460)^0$, and $D_1'(2430)^0$ into $D^{*+}\pi^-$ where the D^{*+} decays to $D^+\pi^0$, but this π^0 is missing in the reconstruction. Due to the missing slow pion, the mass distribution of these components is shifted downward by about 147 MeV from their nominal mass values.

The modeling of the feed-down requires the determination of the bias and resolution for these components. A resolution function, to be used in the fit later, is determined by truth-matching these decays and computing the difference between the reconstructed and generated mass values as shown in Figure 10.13.

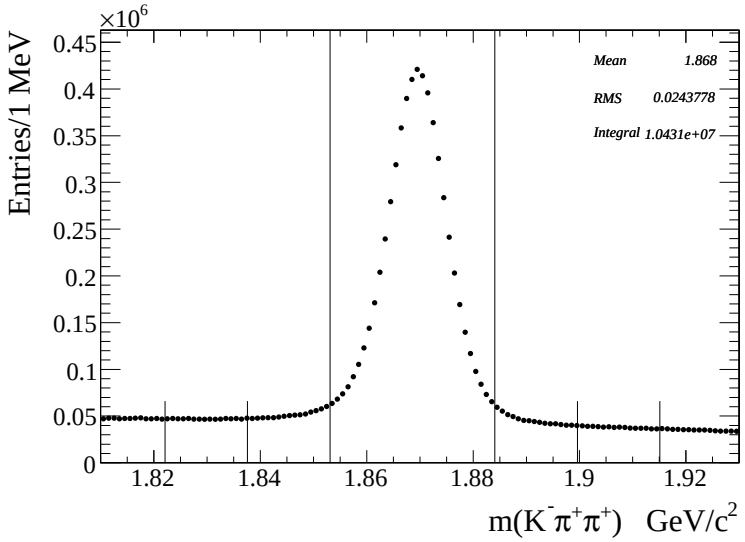

Figure 10.10: m($K\pi\pi$) distribution in generic MC for D^+ candidates passing the selections. The vertical lines show the signal and side-band regions.

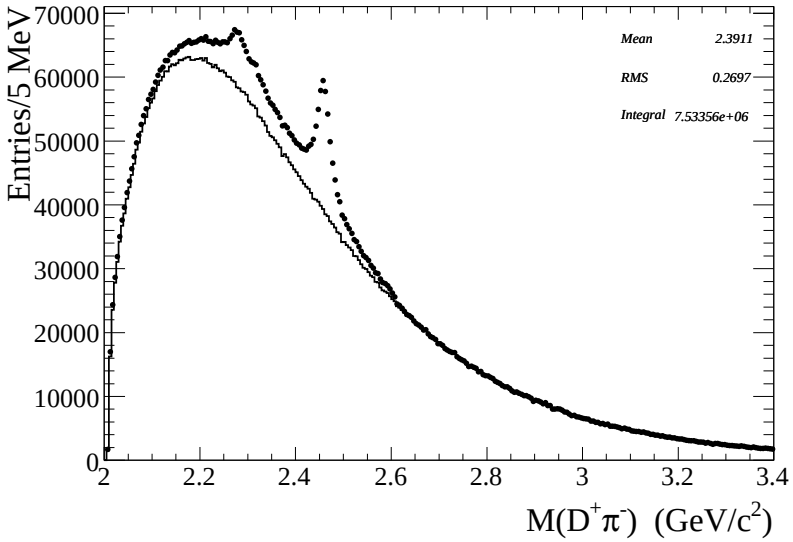

Figure 10.11: Reconstructed M($D^+\pi^-$) distribution for total generic MC (points) and candidates not passing the truth-match requirement (histogram).

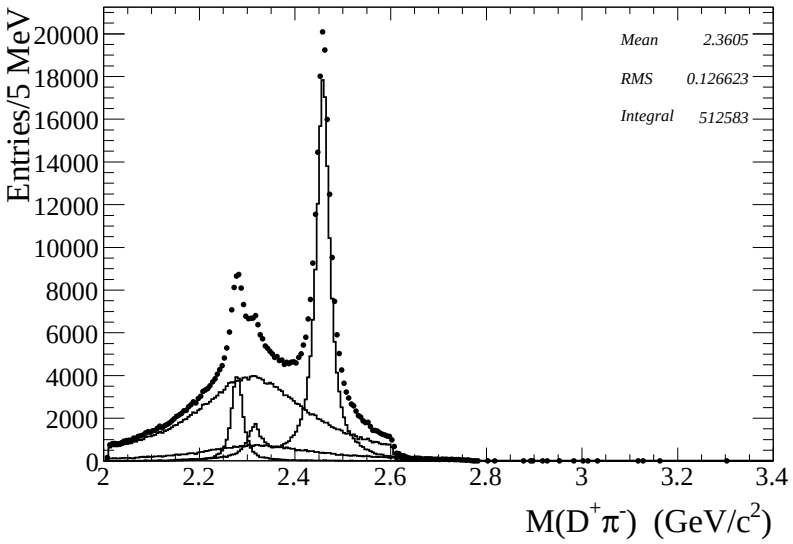

Figure 10.12: Reconstructed M($D^+\pi^-$) distribution for the signals in the generic MC.

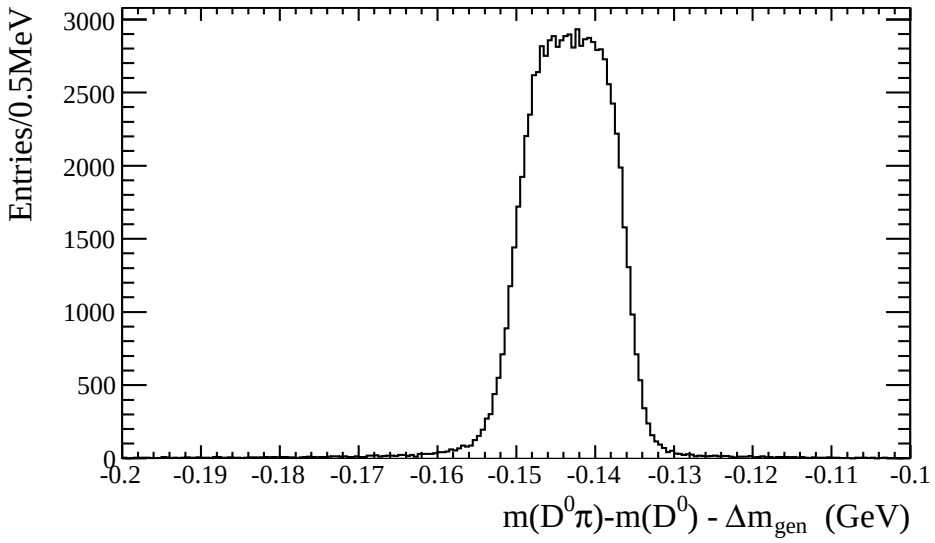

Figure 10.13: Distribution of reconstructed minus generated mass for the feed-down components. These decay $D^{*+}\pi^-$ and the slow pion from the D^{*+} is missing in the reconstruction.

10.3.1 Background Model

For the modeling of the smooth background an empirical formula $F_B(x)$ has been constructed. This formula is motivated by the behavior near threshold and the exponential decrease at high mass:

$$F_B(x) \propto P(x) \begin{cases} e^{c_1 x + c_2 x^2} & \text{for } x < x_0 \\ e^{d_0 + d_1 x + d_2 x^2} & \text{for } x > x_0 \end{cases} \tag{10.3}$$

where

$$P(x) \equiv \frac{1}{2x}\sqrt{[x^2 - (m_{D^+} + m_\pi)^2][x^2 - (m_{D^+} - m_\pi)^2]} \tag{10.4}$$

is the 2-body phase space factor for x=m($D^+\pi^-$). This factor gives the model a rising behavior near threshold. The transition point x_0 is floated between 2.2GeV and 2.7GeV. The parameters c_1, c_2, and d_2 are floated, while the parameters d_0 and d_1 are fixed from the requirement of continuity and differentiability at x_0.

This model has been tested using a sample of wrong-sign (WS) candidates $D^+\pi^+$ reconstructed in the same way as the right-sign (RS) candidates but requiring the pion to have the same charge as the D^+. A fit to the M($D^+\pi^+$) distribution is shown in Figure 10.14 and describes the data well as shown by the normalized residuals.

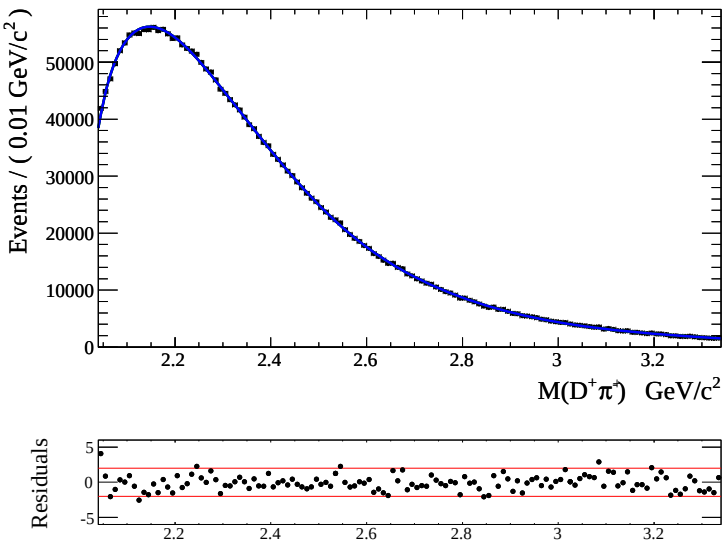

Figure 10.14: Fit to the WS distribution, the bottom plot shows the normalized residuals.

10.3.2 Fit to M($D^+\pi^-$) Distribution in Generic MC

To extract the parameters of the resonances a fit is performed to the M($D^+\pi^-$) distribution where a Breit-Wigner (BW) function is included for each resonance and the background is parametrized using the formula from the previous section. In order to remove the contribution due to fake D^+ candidates from the M($D^+\pi^-$) distribution a sideband subtraction is performed where the M($D^+\pi^-$) distribution corresponding to the D^+ mass sideband regions is subtracted from that of the signal region.

The complete model used in the fit is the following:

$$PDF(x) = \int \left[S_{D_2^*(2460)}(y) + S_{D_0^*(2400)}(y)\right] R(x-y)dy \quad (10.5)$$

$$+ \int \left[F_{D_1(2420)}(y) + F_{D_2^*(2460)}(y)\right] R_{Feed}(x-y)dy \quad (10.6)$$

$$+ F_B(x) \quad (10.7)$$

- Where the variables x and y here refer to the reconstructed and true mass of the $D^+\pi^-$ system respectively.
- The components $S_{D_2^*(2460)}(x)$ and $S_{D_0^*(2400)}(x)$ are non-relativistic BW functions corrected for the efficiency shape to model the signal components.
- The components $F_{D_1(2420)}(x)$ and $F_{D_2^*(2460)}(x)$ are non-relativistic BW functions for the feed-down components. The $D_1'(2430)$ resonance is weak and broad and can be ignored, its contribution is absorbed by the background function.
- $F_B(x)$ is the smooth background model described in the previous section.
- The $S_{D_0^*(2400)}(x)$ is convolved with the resolution even though it is very broad, this is because it has a mass cut-off as shown in figure 10.12. However, due to its width, its parameters are fixed to the true values.
- The feed-down resonances are convolved with the feed-down transfer function $R_{Feed}(x-y)$ shown in Figure 10.13 which accounts for the negative bias and resolution.
- The parameters of $F_{D_2^*(2460)}$ are constrained to those of $S_{D_2^*(2460)}$.

A binned minimum χ^2 fit was performed and a χ^2/NDF of 129/118 was obtained. The fit is shown in Figure 10.15 together with the normalized residuals which show good agreement between the fit and the MC distribution. The signal parameters extracted from the fit are listed in Table 10.1 and are in good agreement with the generated values.

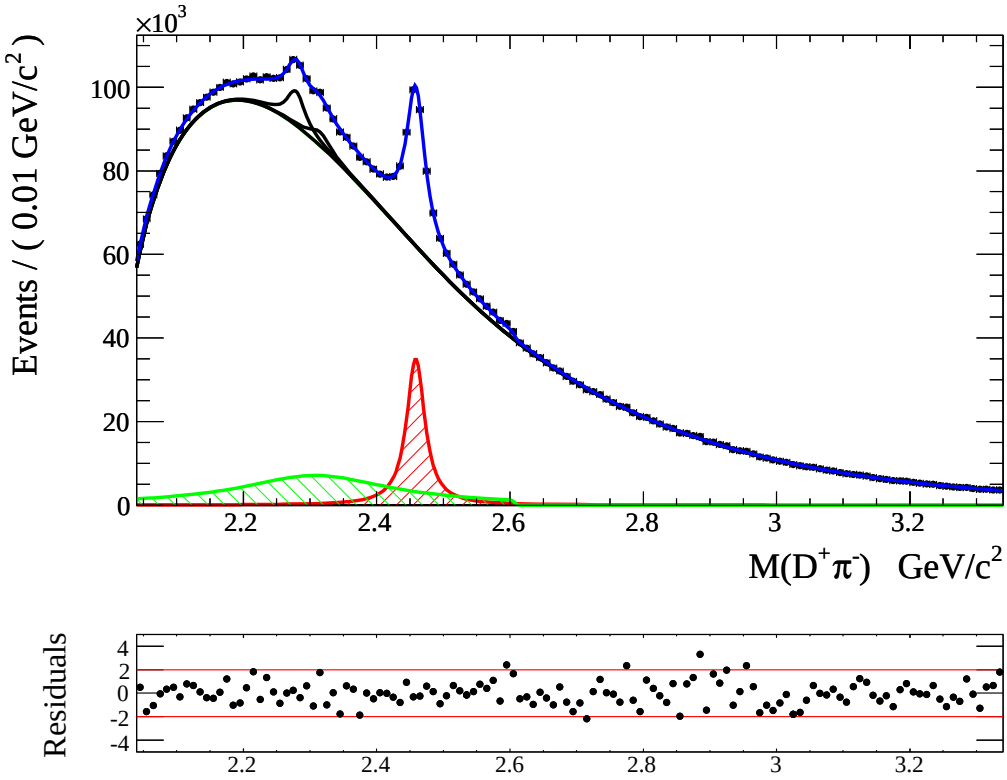

Figure 10.15: Fit to the M($D^+\pi^-$) distribution in generic MC.

Table 10.1: Reconstructed signal parameters. The error is statistical only. The last columns show the true values. The generated $D_2^*(2460)$ yield also includes the generated $D_2^*(2460)_{Feed}$ yield as the truth-match algorithm used did not to separate the two.

Resonance	Yield ($\times 10^3$)	M (MeV)	Γ (MeV)	Generated Yield ($\times 10^3$)	Generated M (MeV)	Generated Γ (MeV)
$D_2^*(2460)$	173.9 $\pm$ 3.1	2458.5 $\pm$ 0.1	30.8 $\pm$ 0.6	188.8	2459.0	30.0
$D_0^*(2400)$	228.2 $\pm$ 16.6	2308.0	276.0	246.8	2308.0	276.0
$D_1(2420)_{Feed}$	30.4 $\pm$ 1.3	2422.0	19.0	30.7	2422.0	19.0
$D_2^*(2460)_{Feed}$	18.4 $\pm$ 1.8	2458.5 $\pm$ 0.1	30.8 $\pm$ 0.6	-	2459.0	30.0

10.4 Data

The data sample has been processed following the procedure developed in the MC analysis. The D^+ candidate mass distribution, Figure 10.16, shows a signal peak with a lower purity (65%) than the MC. This is expected since the MC sample excluded non-peaking backgrounds from the light quark production $e^+e^- \to u\overline{u}, d\overline{d}, s\overline{s}$. Also, the D^+ production rate may be overestimated in the MC.

The M($D^+\pi^-$) distribution for data is presented in Figure 10.17. This distribution shows the feeddown and $D_2^*(2460)$ features expected from the analysis of the MC sample. In addition, the region above the $D_2^*(2460)$ shows new structures: an enhancement at about 2.6 GeV/c^2 and another one at about 2.75 GeV/c^2. The M($D^+\pi^-$) distribution obtained by selecting the D^+ mass sidebands is shown in Figure 10.18 and shows no peaking structures in this mass region. A small bump at the $D_2^*(2460)$ mass is due to $D_2^*(2460)$ signal events from the tails of the D^+ signal distribution.

The formula from section 10.3.1 is used to model the smooth background in the data. A fit to the data wrong-sign sample has also been done to test this formula and is shown in Figure 10.19. The residuals from this fit show a small discrepancy between the model and the distribution, this discrepancy will be accounted for in the systematic uncertainties of the results later.

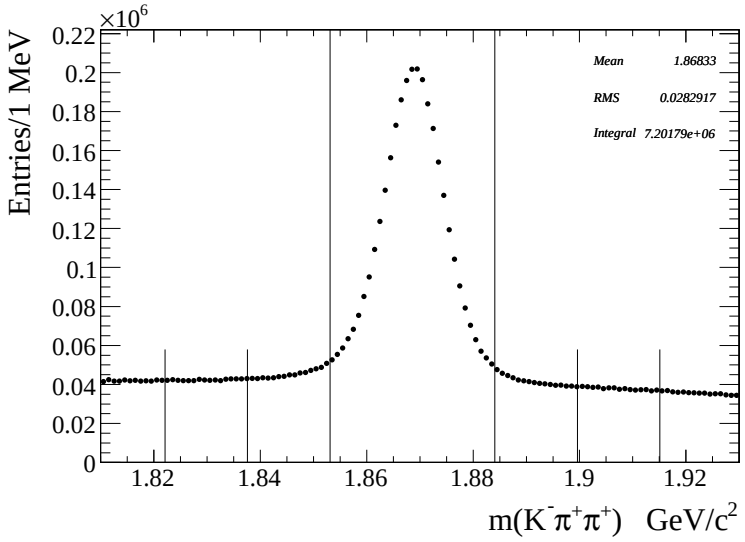

Figure 10.16: Reconstructed M($K\pi\pi$) distribution after the full selection. The vertical lines show the signal and side-band regions.

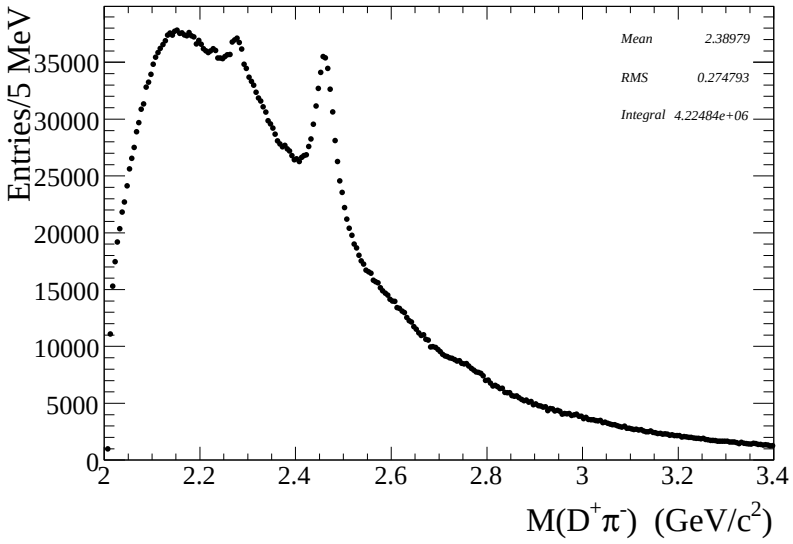

Figure 10.17: Reconstructed M($D^+\pi^-$) distribution.

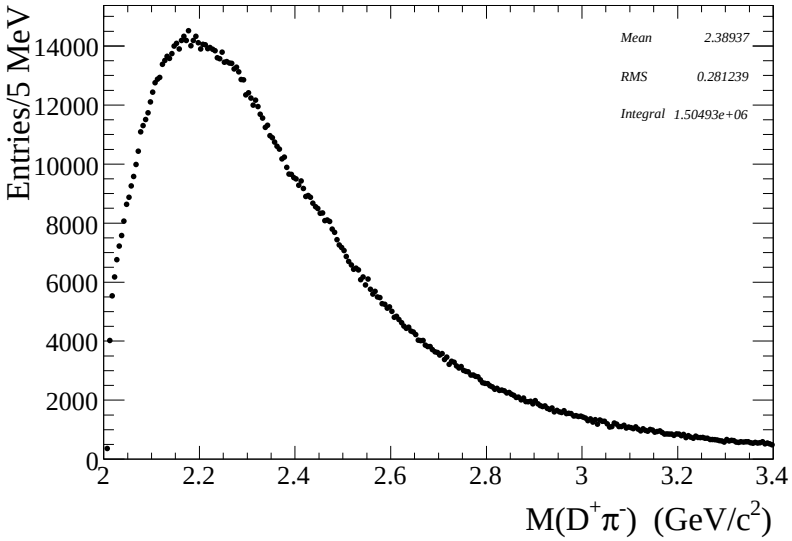

Figure 10.18: Reconstructed M($D^+\pi^-$) distribution for the D^+ side-band regions. The small bump at about 2.46 GeV is due to a small amount of D^+ signal leaking into the side-bands.

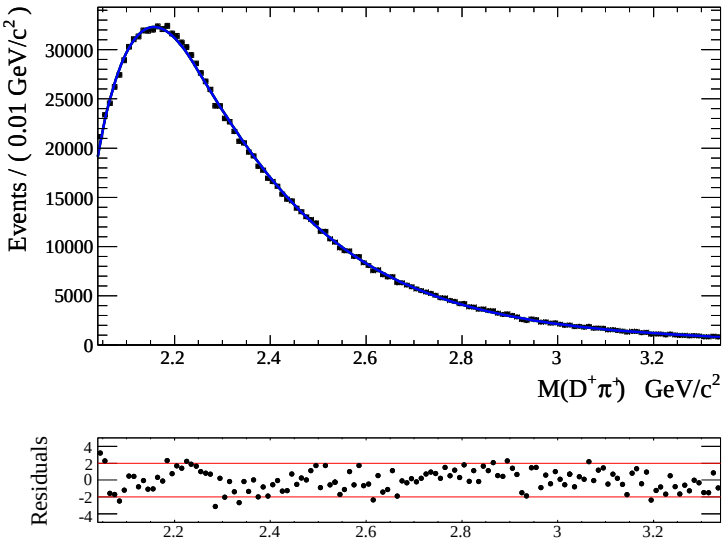

Figure 10.19: Fit to the WS data. The bottom plot shows the normalized residuals from the fit.

10.4.1 Fit to M($D^+\pi^-$) in Data.

A fit to M($D^+\pi^-$) distribution is performed after subtracting the contribution from fake D^+ by using the D^+ candidate mass sidebands. The model used in the fit is the following:

$$F(x) = \int \left[S_{D_2^*(2460)}(y) + S_{D_0^*(2400)}(x) + S_{D^*(2600)}(x) + S_{D^*(2760)}(x)\right] R(x-y)dy \quad (10.8)$$

$$+ \int \left[F_{D_1(2420)}(y) + F_{D_2^*(2460)}(y)\right] R_{Feed}(x-y)dy \quad (10.9)$$

$$+ F_B(x) \quad (10.10)$$

- The variables x and y refer to the reconstructed and true mass of the $D^+\pi^-$ system respectively.

- $S_{D_2^*(2460)}(x)$ and $S_{D_0^*(2400)}(x)$ are BW functions for the two expected signals, $S_{D^*(2600)}(x)$ and $S_{D^*(2760)}(x)$ are additional BW functions to account for the new structures. These functions are corrected for the efficiency shape.

- The feeddown components, $F_{D_1(2420)}(x)$ and $F_{D_2^*(2460)}(x)$, are BW functions and are convolved with the PDF R_{Feed} which accounts for the downward bias and resolution determined in the MC analysis. The parameters of $F_{D_1(2420)}(x)$ are fixed to the parameters found in the $D^{*+}\pi^-$ analysis later. Also, the parameters of $F_{D_2^*(2460)}(x)$ are shared with the function for the true signal $S_{D_2^*(2460)}(x)$.

- $F_B(x)$ is the smooth background model.

- Since the $D_2^*(2460)$ is a spin-2 particle decaying into two pseudoscalars, the BW function includes mass dependent factors to account for a D-wave decay:

$$S_{D_2^*(2460)}(x) \propto \frac{xP(x)\left(\frac{Q(x)}{Q(M)}\right)^4 \frac{B^2(M)}{B^2(x)}}{(x^2-M^2)^2 + M^2\Gamma^2(x)} \quad (10.11)$$

where

$$\Gamma(x) \equiv \Gamma \frac{P(x)}{P(M)} \left(\frac{Q(x)}{Q(M)}\right)^4 \frac{B^2(Q(M))}{B^2(Q(x))} \quad (10.12)$$

P(x) is the two-body phase-space factor and $Q(x) = xP(x)$ is the momentum of the

daughters in the $D^+\pi^-$ rest frame. The factor

$$B^2(Q) \approx 9 + 3(QR)^2 + (QR)^4 \tag{10.13}$$

is the D-wave Blatt-Weisskopf form factor with the radius R fixed to 4 GeV^{-1} [42].

- The $D_0^*(2400)$ is a spin-0 particle so the its BW function includes mass dependent factors for an S-wave decay:

$$S_{D_0^*(2400)}(x) \propto \frac{xP(x)}{(x^2 - M^2)^2 + M^2\Gamma^2(x)} \tag{10.14}$$

where

$$\Gamma(x) \equiv \Gamma\frac{P(x)}{P(M)} \tag{10.15}$$

- For the other components a simple relativistic Breit-Wigner (multiplied by a phase-space factor) is used.

- Due to the large width of the $D_0^*(2400)$, mass and width parameters are constrained to be within the range determined by the recent analysis of $B^- \to D^+\pi^-\pi^-$ [39]: $M = 2297 \pm 21MeV, \Gamma = 273 \pm 50MeV$.

The fit finds a minimum χ^2/NDF of 140/112. A plot of the fit is shown in Figure 10.20 and shows good agreement between the model and the data. The signal parameters are listed in Table 10.2.

A study has been performed to show that the fit requires the presence of the new signals as well as the wide resonance $D_0^*(2400)$. In this study each resonance is removed from the fit model to determine what is the change in the fit quality. Significant changes in the χ^2/NDF are observed as shown in Table 10.3, the residuals for each fit are shown in Figures 10.21-10.23 and show clear oscillations.

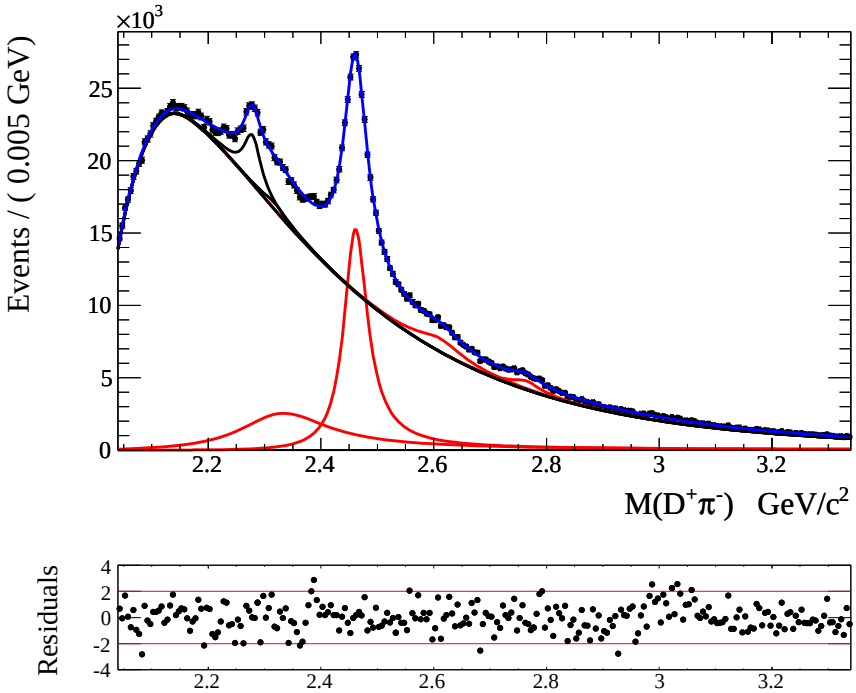

Figure 10.20: Fit to the M($D^+\pi^-$) distribution.

Table 10.2: Signal parameters extracted from the fit. Errors are only statistical.

Resonance	Yield ($\times 10^3$)	M (MeV/c^2)	Γ (MeV)
$D_0^*(2400)$	143.2± 4.7	2338.0± 1.0	195.0±5.9
$D_2^*(2460)$	242.8± 1.8	2462.2± 0.1	50.5± 0.6
$D^*(2600)$	26.0± 1.4	2608.7± 2.4	93± 6
$D^*(2760)$	11.3± 0.8	2763.3± 2.3	60.9± 5.1
$D_1(2420)_{Feed}$	36.1 ± 1.1	2421.5	31.0
$D_2^*(2460)_{Feed}$	7.5 ± 1.7	2462.2 ± 0.1	50.5 ± 0.6

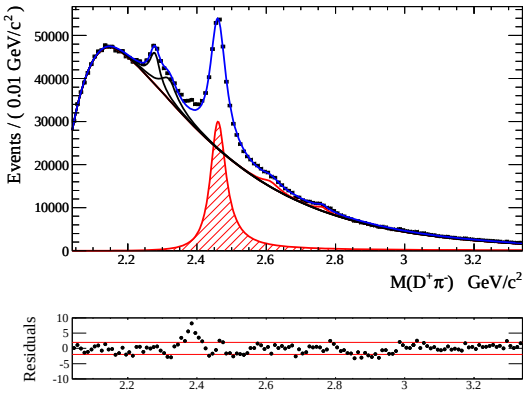

Figure 10.21: Fit to the M($D^+\pi^-$) distribution with $D_0^*(2400)$ removed from the PDF.

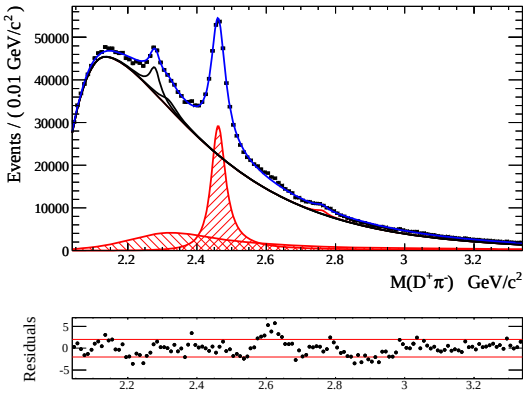

Figure 10.22: Fit to the M($D^+\pi^-$) distribution with $D^*(2600)$ removed from the PDF.

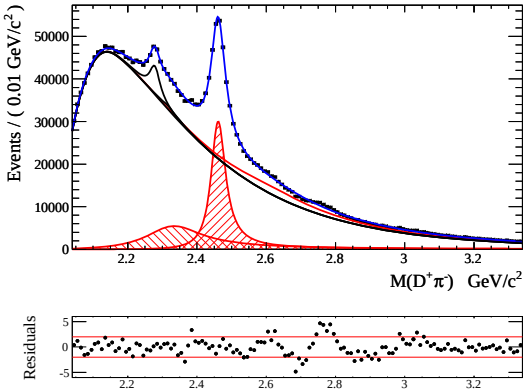

Figure 10.23: Fit to the M($D^+\pi^-$) distribution with $D^*(2760)$ removed from the PDF.

Table 10.3: χ^2/NDF for the fits where the resonance has been removed from the fit PDF.

Resonance Removed	χ^2/NDF
$D_0^*(2400)$	386/115
$D^*(2600)$	359/115
$D^*(2760)$	306/115

10.4.2 Systematic Uncertainties

Several sources of systematic uncertainty have been identified in the fit for the signal parameters. For each source the nominal fit is modified and the difference between the nominal parameters and the modified parameters is taken as the systematic error.

- The mass range of the histogram used in the fit is arbitrary so a modified fit is performed where the range is increased by 100 MeV.

- The binning of the histogram is arbitrary so a fit is performed with a bin size which is 2 times larger than the nominal.

- The new signals at 2600 MeV and 2750 MeV are modeled using relativistic BW functions, a modified fit is performed by modifying these shapes to D-waves.

- The parameters of the feed-down resonance $D_1(2420)$ are fixed from the $D^{*+}\pi^-$ analysis. Both the mean and the width of this resonance are varied according to the errors.

- The background model has limited flexibility as shown by the residuals from the fit to the Wrong-Sign distribution in figure 10.19. A systematic error is assigned by inserting the residuals obtained from that fit into nominal right-sign fit. The normalization of the inserted residuals is determined by requiring that the probability of the modified fit does not become worse than 0.1%.

- Uncertainties in the magnetic field of the solenoid are on the order of .02%. The magnitude of the solenoid B field has been decreased by this amount in the reconstruction stage. In addition, uncertainties on the SVT material density are of the order of 20% according to previous *BABAR* internal studies of the K_s mass variations. These variations are extremely cpu resource consuming because the jobs have to run in "refit" mode and therefore have been performed only on the sample of signal MC events. These modifications of the reconstruction lead to variations in the mean of the reconstructed mass distribution of 0.42 MeV for the B-field and 0.65 MeV for the SVT material.

- The $D_1'(2430)$ resonance has been ignored in the fit. To account for its possible contribution, the nominal fit is varied by including an additional Breit-Wigner whose mass and width are fixed to the nominal values for this resonance [17]. Because the

resonance is very broad the fit cannot determine its yield, its yield is fixed to the observed yield for the $D_1(2420)$ feed-down.

The systematic uncertainties on the fit parameters due to the above variations are listed in tables 10.4 and 10.5.

Table 10.4: Systematic errors on the parameters of the known signals.

	$D_0^*(2400)$ **Yield** ($\times 10^3$)	$D_2^*(2460)$ **Yield** ($\times 10^3$)	$D_2^*(2460)$ **M** (MeV)	$D_2^*(2460)$ Γ (MeV)
Mass Range	12.05	0.03	0.02	0.18
Bin Width	0.23	1.07	0.02	0.56
Breit-Wigner Shape	2.70	0.02	0.02	0.02
Feed-Down Mass	1.92	0.44	0.00	0.08
Feed-Down Width	1.85	0.31	0.00	0.03
Background Model	4.78	3.15	0.07	0.29
B field & SVT material	0.00	0.00	0.77	0.00
Feed-Down D(2430)	19.57	0.58	0.02	0.09
Total	23.8	3.4	0.8	0.7

Table 10.5: Systematic errors on the parameters of the new signals.

	$D^*(2600)$ **Yield** ($\times 10^3$)	$D^*(2600)$ **M** (MeV)	$D^*(2600)$ Γ (MeV)	$D^*(2760)$ **Yield** ($\times 10^3$)	$D^*(2760)$ **M** (MeV)	$D^*(2760)$ Γ (MeV)
Mass Range	2.67	0.47	5.38	0.85	0.08	3.03
Bin Width	0.70	0.33	2.37	0.13	0.44	0.51
Breit-Wigner Shape	0.26	2.22	0.55	0.37	0.60	1.33
Feed-Down Mass	0.13	0.03	0.22	0.03	0.00	0.11
Feed-Down Width	0.16	0.08	0.34	0.00	0.00	0.00
Background Model	5.93	0.28	11.25	0.30	0.52	1.40
B field & SVT material	0.00	0.77	0.00	0.00	0.77	0.00
Feed-Down D(2430)	0.79	0.27	1.52	0.09	0.02	0.23
Total	6.6	2.5	13	1.0	1.2	3.6

Chapter 11

The $D^0\pi^+$ Final State

The analysis of the $D^0\pi^+$ final state is an important part of this study on the excited D mesons. In addition to providing parameters for the isospin partners of the states observed in $D^+\pi^-$, it provides confirmation of the new structures observed in $D^+\pi^-$. The combinatorial backgrounds in this final state are of different nature than those in $D^+\pi^-$, therefore observing new structures consistent with those in $D^+\pi^-$ strongly supports the identification of the new structures as true resonances.

11.1 Reconstruction and Selection

The procedure for the reconstruction of this final state is similar to the procedure used in $D^+\pi^-$, however a few differences arise since the D^0 has somewhat different production and decay properties which affect the backgrounds. This final state is reconstructed using the $D^0 \to K^-\pi^+$ mode:

- D^0 candidates are created from two oppositely charged tracks, one is required to pass the Tight Kaon PID selector and the other is required to pass the Loose pion selector.
- A vertex fit is applied to the $K^-\pi^+$ tracks and a fit probability greater than 0.1% is required.
- A D^0 candidate is selected if its invariant mass is within 2.5 sigma of the mean of the signal distribution. The mean and sigma are determined to be 1863.7 MeV and 7.6 MeV from a fit using a Gaussian signal and linear background as shown in Figure 11.1.

- Any D^0 candidate which is reconstructed in the decay $D^{*+} \to D^0\pi^+$ is removed. The π^+ in these reconstructions must have lab momentum less than 600 MeV. A vertex fit is performed and a fit probability greater than 0.1% is required. The D^{*+} is detected if the mass difference, $\Delta m = m(D^0\pi^+) - m(D^0)$ is within 3.0 MeV of the mean value of the peak (145.43 MeV) as shown in Figure 11.2.

- Also, any D^0 candidate which is reconstructed in the decay $D^{*0} \to D^0\pi^0$ is removed. The π^0 are mass constrained and a vertex fit is performed on the D^{*0} candidate. The fit probability must be greater than 0.1%. The D^{*0} is detected if the mass difference $\Delta m = m(D^0\pi^0) - m(D^0)$ is within 3σ from the mean value of the peak, where the mean is 142.05 MeV and σ=1.12 MeV (see Figure 11.3).

After the D^0 candidates have been selected, $D^0\pi^+$ candidates are reconstructed as follows:

- A D^0 candidate is combined with an additional charged particle in the event which passes the Loose pion selector.

- A vertex fit is applied to the $D^0\pi^+$ candidate while constraining the vertex to be within the IP region. The fit probability must be greater than 0.1%.

- The momentum of the $D^0\pi^+$ system in the CM frame must be greater than 3.0 GeV.

- Finally, $\cos(\theta_\pi)$ must be greater than -0.8 to remove pions from the other side of the event, see Figure 11.4. The angle $\cos(\theta_\pi)$ was defined in the $D^+\pi^-$ analysis as the angle of the primary pion with respect to the $D^0\pi^+$ system direction.

To obtain fine resolution on the D^{**} candidate mass, the mass difference with respect to the D^0 is used:

$$M(D^0\pi^+) = m(K^-\pi^+\pi^+) - m(K^-\pi^+) + 1.8645 \text{ GeV} \tag{11.1}$$

where the last number is the nominal value for the D^0 mass [17].

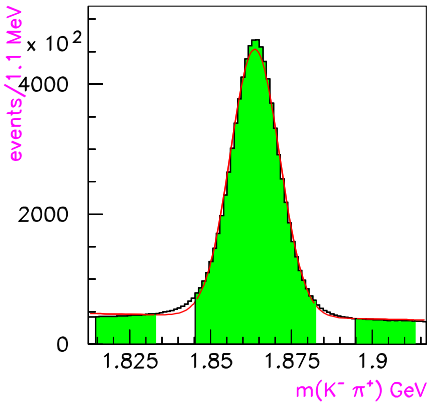

Figure 11.1: Mass distribution for D^0 candidates in data. The solid line shows the fit, the shaded bands show the signal and sideband regions.

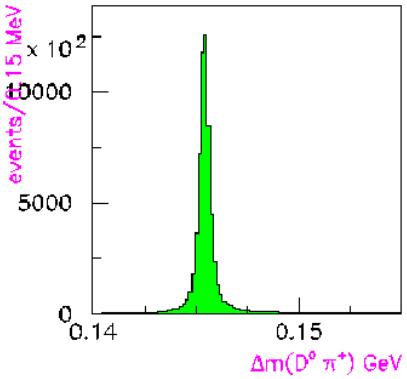

Figure 11.2: Δm distribution for $D^{*+} \to D^0\pi^+$ candidates.

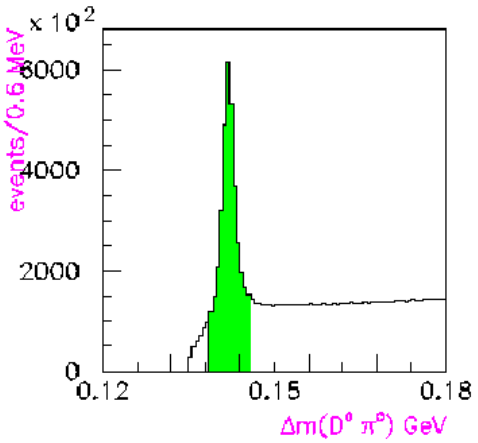

Figure 11.3: Δm distribution for $D^{*0} \to D^0\pi^0$ candidates.

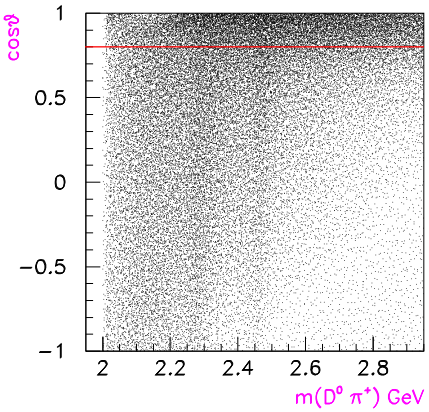

Figure 11.4: Scatter plot of the $\cos(\theta_\pi)$ ($=-cos\vartheta$) angle vs the $D^0\pi^+$ mass.

11.2 Generic MC

The generic MC sample has been processed using the reconstruction procedure defined in the previous section. The reconstructed D^0 candidate mass distribution after all the selections is shown in Figure 11.5. In this figure the signal and sideband regions are also shown. The sideband sample is particularly important in this final state due to a peaking background which must be removed using this sample.

The reconstructed M($D^0\pi^+$) distribution is shown in Figure 11.6. This distribution exhibits a sharp peak near threshold due $D^{*+} \to D^0\pi^+$ decays which remain even after the veto. Next, there is the peaking background at about 2.3 GeV as in the $D^+\pi^-$ analysis due to feed-down from the decays $D_1(2420)^+/D_2^*(2460)^+ \to D^{*0}\pi^+$ where the $D^{*0} \to D^0\pi^0$ and the π^0 is missing. The narrow peak at about 2.460 GeV is the true signal of $D_2^*(2460)^0 \to D^0\pi^+$. Finally at about 2.6 GeV another peaking background can be observed, this background is more clear in the M($D^0\pi^+$) distribution from the D^0 sideband sample shown in Figure 11.7.

The peaking background at 2.6 GeV is specific to this $D^0\pi^+$ analysis because the $D^0\pi^+$ candidate is created with two same charge pions: $(K^-\pi^+)\pi_f^+$ where the $K^-\pi^+$ is assumed to be the D^0, however the K^- can also create a D^0 with the second pion π_f^+: $(K^-\pi_f^+)\pi^+$. Events where there is a real D^0 in the $K^-\pi_f^+$ combination create this peaking structure. This background is more carefully studied in the data section later and is removed before the fit by subtracting the M($D^0\pi^+$) distribution obtained from the D^0 side-bands.

For this final state a wrong-sign sample is defined using $D^0\pi^-$ candidates and is shown in Figure 11.8. However, this sample is not completely free of signals due to feed-down from the decays of $D_1(2420)^0/D_2^*(2460)^0 \to D^{*+}\pi^-$ where the $D^{*+} \to D^0\pi^+$ and the slow π^+ is missing. The fit shown in the figure is a test to the background formula used in the $D^+\pi^-$ analysis and includes two BW functions to model the feeddown. Moreover this distribution does not show a peaking background at 2.6 GeV consistent with the fact that the K^- in this D^0 candidate cannot create a real D^0 with the primary pion π^- because it has the same sign.

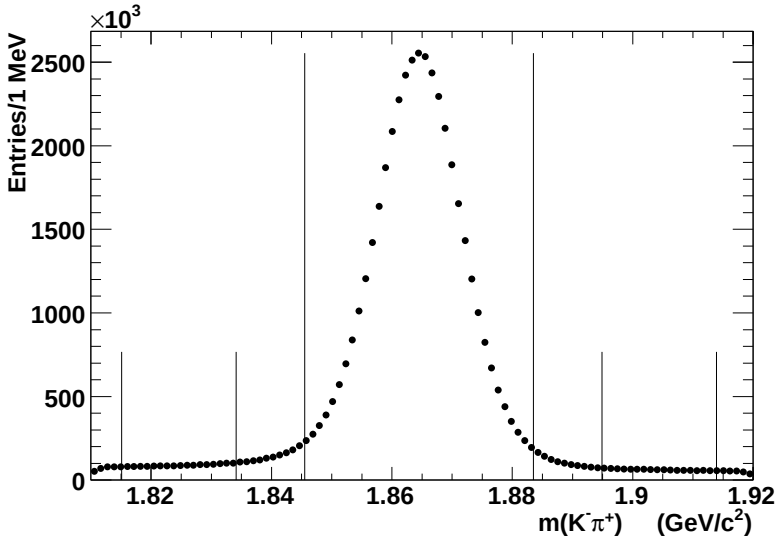

Figure 11.5: D^0 candidate mass distribution in generic MC, the lines show the signal and side-bands.

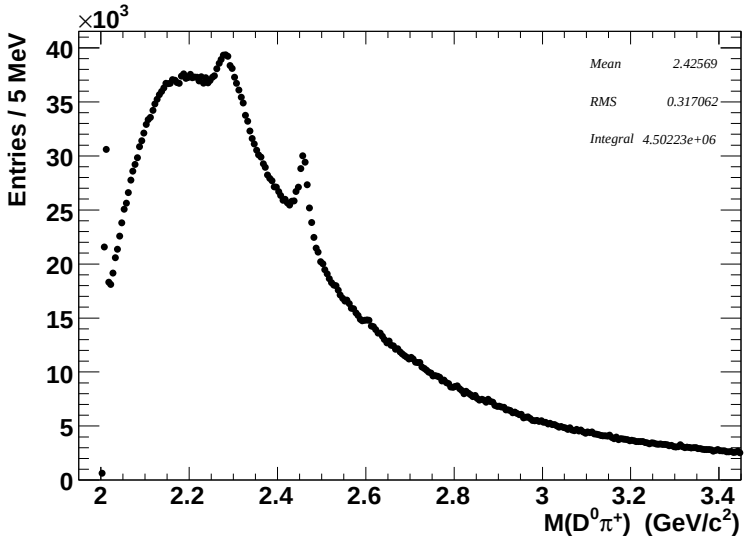

Figure 11.6: M($D^0\pi^+$) mass distribution in generic MC.

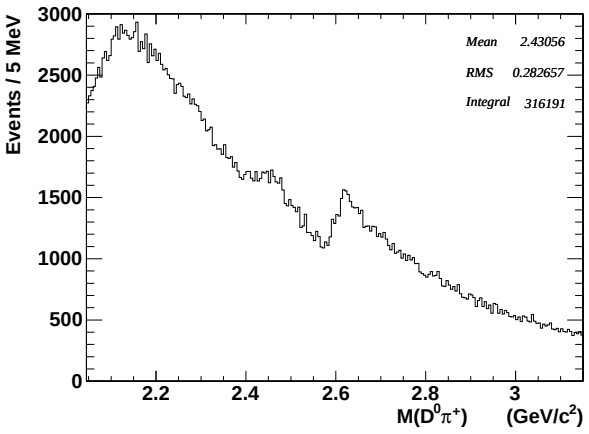

Figure 11.7: M($D^0\pi^+$) mass distribution for the side-bands of the D^0 mass in generic MC.

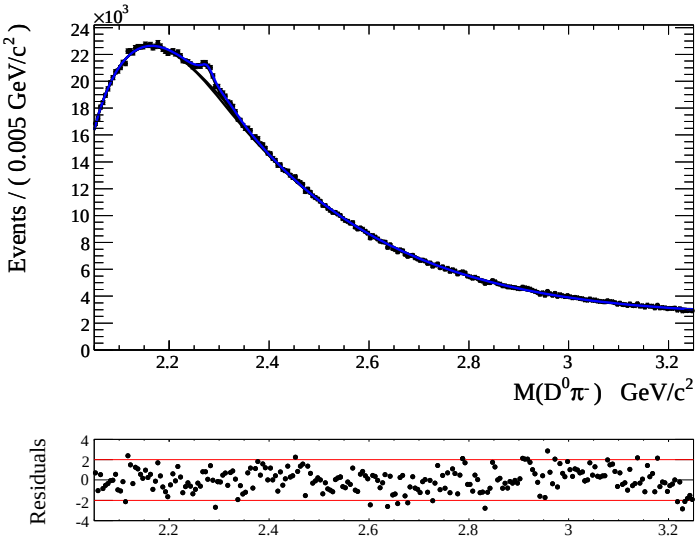

Figure 11.8: Fitted M($D^0\pi^-$) mass distribution in generic MC.

11.2.1 Fit to M($D^0\pi^+$) in MC.

The fit to the M($D^0\pi^+$) distribution in generic MC is performed after a sideband subtraction where the M($D^0\pi^+$) distribution obtained from the D^0 sidebands is subtracted from the M($D^0\pi^+$) distribution obtained from D^0 signal region. The following model is used to fit the resulting M($D^0\pi^+$) distribution:

$$\begin{aligned} F(x) &= \int \left[S_{D_2^*(2460)}(y) + S_{D_0^*(2400)}(y)\right] R(x-y)dy && (11.2)\\ &+ \int \left[F_{D_1(2420)}(y) + F_{D_2^*(2460)}(y)\right] R_{Feed}(x-y)dy && (11.3)\\ &+ F_B(x) && (11.4) \end{aligned}$$

- $S_{D_2^*(2460)}(x)$ and $S_{D_0^*(2400)}(x)$ are BW functions for the two expected signal components. The $D_0^*(2400)$ signal has an artificial mass cut-off at 2.611 GeV, also its mass and width parameters are fixed to the true values since it is very weak. The resolution and efficiency variation are expected to have negligible differences with respect to those found in $D^+\pi^-$ since these depend on the primary pion reconstruction only. Therefore, the signal MC for this final state was not processed and the resolution function and efficiency shape from the $D^+\pi^-$ analysis are used to correct the signals here.

- $F_{D_1(2420)}(x)$ and $F_{D_2^*(2460)}(x)$ are BW functions for the feed-down components. These are convolved with the function R_{Feed} described in the $D^+\pi^-$ analysis which accounts for the negative bias and resolution.

- $F_B(x)$ is the smooth background function constructed in the $D^+\pi^-$ analysis.

- The parameters of $F_{D_2^*(2460)}$ are fixed to those of $S_{D_2^*(2460)}$.

- The mass and width of the $F_{D_1(2420)}$ are fixed to the true values.

- The contribution from the $D_1'(2430)$ resonance is ignored in the fit due to its large width and small yield which allow it merge with the smooth background.

The fit is done by minimizing the χ^2 on a binned histogram and a minimum χ^2/NDF of 351/228 is found. Figure 11.9 shows the fitted M($D^0\pi^+$) distribution. The results of the fit are shown in Table 11.1, we find good agreement between the fitted and generated signal parameters.

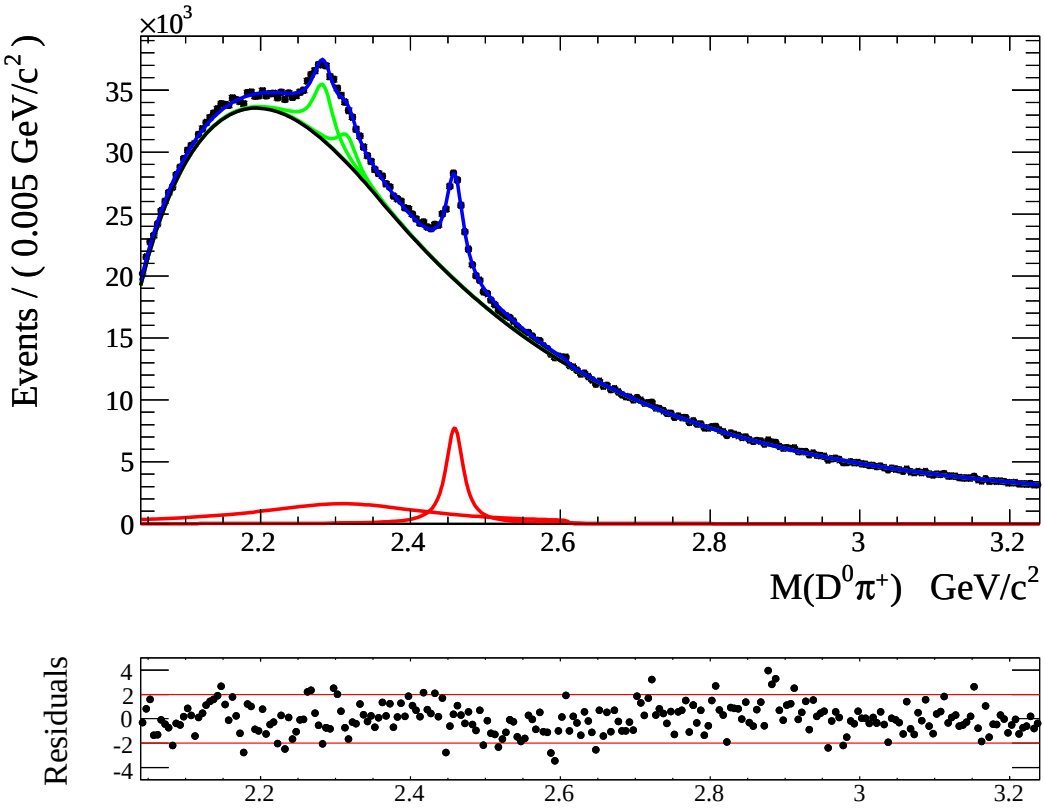

Figure 11.9: Fit to the M($D^0\pi^+$) distribution in MC, the bottom plot shows the normalized residuals.

Table 11.1: Parameter values extracted from the fit compared to the true values.

Resonance	Yield ($\times 10^3$)	Mass (MeV)	Γ (MeV)	Generated Mass (MeV)	Generated Γ (MeV)
$D_0^*(2400)^+$	99.9 ± 18.2	2308.0	276.0	2308.0	276.0
$D_2^*(2460)^+$	63.8 ± 0.8	2458.9 ± 0.1	24.8 ± 0.2	2459.0	25.0
$D_1(2420)^+{}_{Feed}$	43.0 ± 1.2	2427.0	28.0	2427.0	28.0
$D_2^*(2460)^+{}_{Feed}$	19.7 ± 1.3	2458.9 ± 0.1	24.8 ± 0.2	2459.0	25.0

11.3 Analysis of the Data

For the data sample the reconstructed D^0 candidate distribution after all selections is shown in Figure 11.10. The purity of D^0 candidates is determined to be 83% by determining the number background events in the signal region using the sideband regions.

The reconstructed M($D^0\pi^+$) distribution is shown in Figure 11.11. The features of the distribution are mostly as in the generic MC. The distribution exhibits a sharp peak near threshold due to remaining $D^{*+} \to D^0\pi^+$ decays which were not removed in the veto. Next, there is the feed-down at about 2.3 GeV due to the decays $D_1(2420)^+/D_2^*(2460)^+ \to D^{*0}\pi^+$ where the $D^{*0} \to D^0\pi^0$ and the π^0 is lost. The narrow peak at about 2.460 GeV is the true signal of $D_2^*(2460)^0 \to D^0\pi^+$.

The enhancement at about 2.75 GeV is labeled as $D^*(2760)^+$ and is a confirmation of the isospin partner signal observed in $D^+\pi^-$. The enhancement at 2.6 GeV is similar to the new structure $D^*(2600)^0$ observed in the $D^+\pi^-$ analysis, however due to the peaking background discussed in the generic MC section one needs to perform a sideband subtraction in order to see if there is a remaining enhancement which can be assigned to a true $D^*(2600)^+$ signal. Figure 11.12 shows the M($D^0\pi^+$) distribution from the D^0 sidebands where the peaking background shows clearly, in this plot we also see a small bump at the mass of the $D_2^*(2460)$ due to a small of amount signal leaking into the side bands.

To study the peaking background further the invariant mass distribution of the $K^-\pi_f^+$ system is plotted against the mass of the $K^-\pi^+$ combination in Figure 11.13. This scatter plot shows a horizontal accumulation of events at a value on the y-axis corresponding the D^0 mass. The distribution of events as a function of the $K^-\pi_f^+$ invariant mass is shown in Figure 11.14 and shows a clear peak at the D^0 mass value. As done for the generic MC, this peaking background can be removed through a sideband subtraction. The effectiveness of this method is shown more clearly by performing a sideband subtraction on the $K^-\pi_f^+$ mass distribution. A scatter plot of $m(K^-\pi_f^+)$ against $m(K^-\pi^+)$ is shown in Figure 11.15, the D^0 events from the peaking background are distributed linearly across the $K^-\pi^+$ mass distribution. The distribution of events as a function of the $K^-\pi_f^+$ mass after subtracting the distribution of events in this variable obtained from the D^0 sidebands is shown in Figure 11.16 and shows that the events from the peaking background are completely removed.

The wrong-sign sample obtained by reconstructing $D^0\pi^-$ candidates is shown in Figure 11.17. The fit performed uses the smooth background model and two BW components for the feeddown and reproduces the data well.

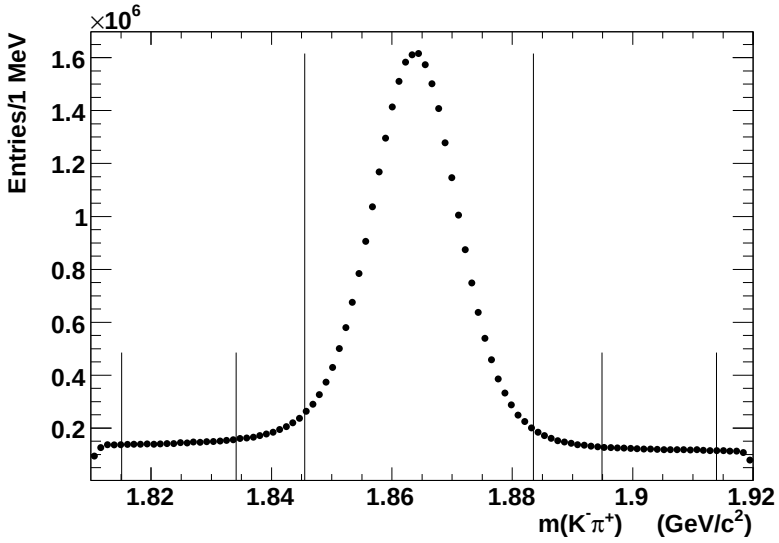

Figure 11.10: D^0 candidate mass distribution, the lines show the signal and side-band regions.

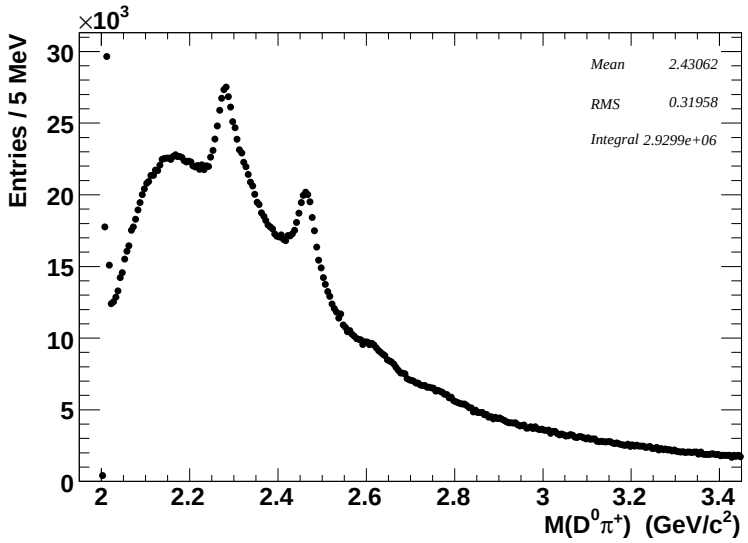

Figure 11.11: M($D^0\pi^+$) mass distribution.

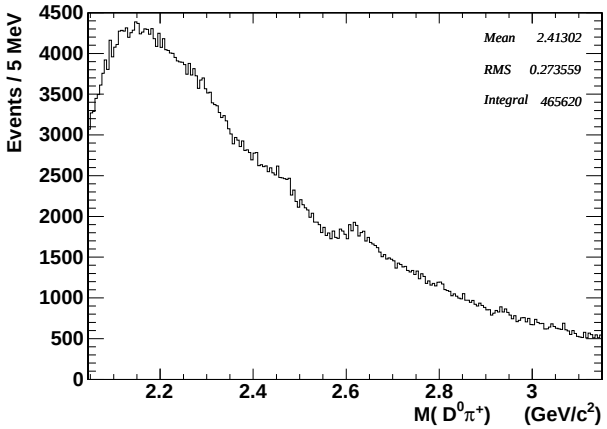

Figure 11.12: M($D^0\pi^+$) mass distribution for the side bands of the D^0 mass.

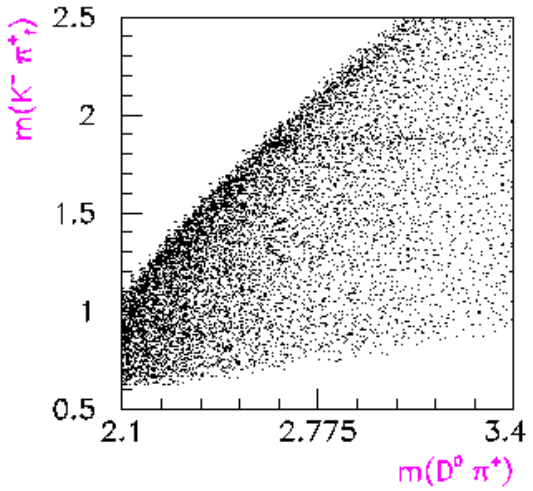

Figure 11.13: Scatter plot of m($K^-\pi_f^+$) vs. m($D^0\pi^+$) showing a horizontal band due D^0 decays.

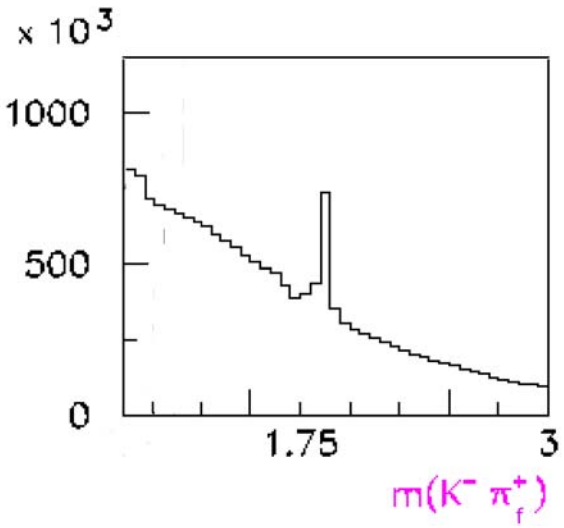

Figure 11.14: m($K^-\pi_f^+$) distribution showing a D^0 peak before side-band subtraction.

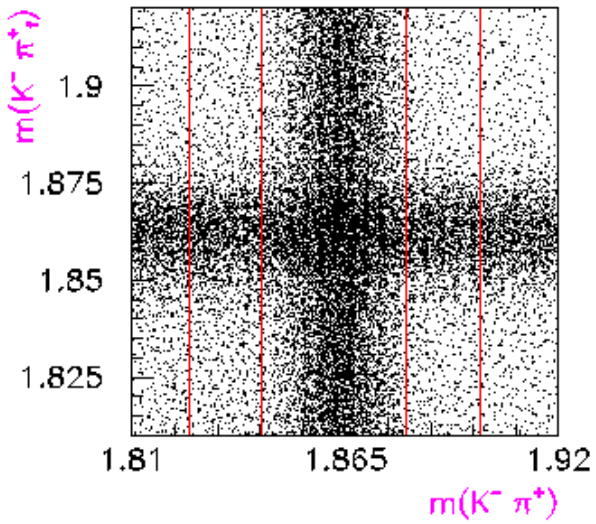

Figure 11.15: Scatter plot of m($K^-\pi_f^+$) vs. m($K^-\pi^+$). The red lines show the side-band regions.

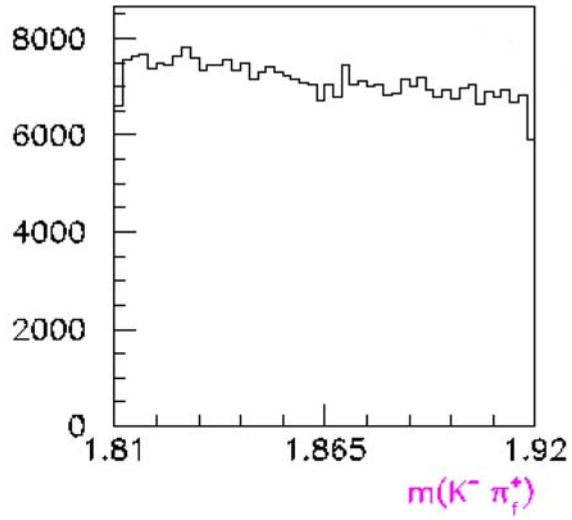

Figure 11.16: m($K^-\pi_f^+$) distribution after side-band subtraction showing the peaking background events have been removed.

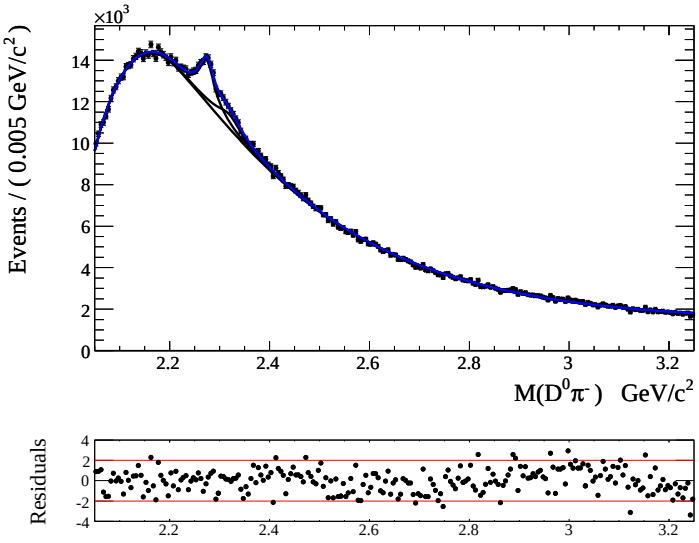

Figure 11.17: Fit to the M($D^0\pi^-$) distribution in the wrong-sign sample.

11.3.1 Fit to M($D^0\pi^+$) in Data.

A fit is performed to the M($D^0\pi^+$) distribution after subtracting the distribution in this variable obtained from the D^0 sidebands in order to remove the contribution from fake D^0 candidates which include the peaking background. The fit model is the following:

$$F(x) = \int \left[S_{D_2^*(2460)}(y) + S_{D_0^*(2400)}(y) + S_{D^*(2600)}(y) + S_{D^*(2760)}(y)\right] R(x-y)dy \quad (11.5)$$

$$+ \int \left[F_{D_1(2420)}(y) + F_{D_2^*(2460)}(y)\right] R_{Feed}(x-y)dy \quad (11.6)$$

$$+ F_B(x) \quad (11.7)$$

- $S_{D_2^*(2460)}(x)$ and $S_{D_0^*(2400)}(x)$ are BW functions for the known signal components and $S_{D^*(2600)}(x)$ and $S_{D^*(2760)}(x)$ are additional BW functions to account for the new structures. A significant enhancement at about 2.6 GeV remains after the sideband subtraction confirming the isospin partner observed in $D^+\pi^-$. The resolution and efficiency corrections are applied as described in the MC analysis.

- The $D_2^*(2460)$ BW function includes factors to account for a D-wave decay, while the $D_0^*(2400)$ BW function includes factors for an S-wave decay. The mass and width of the $D_0^*(2400)$ are limited to be within $\pm 2\sigma$ of the PDG values.

- In order to increase the significance of the new signals, the width parameters of the signal components for the $D_2^*(2460)$, $D^*(2600)$ and $D^*(2760)$ are fixed to those determined in the $D^+\pi^-$ analysis. The mean values are floated because in this final state we expect them to be higher by a few MeV since these resonances are the charged partners. However, by isospin symmetry the width parameters should have negligible differences.

- $F_{D_1(2420)}(x)$ and $F_{D_2^*(2460)}(x)$ are BW functions for the feed-down components and are convolved with the function which accounts for the negative bias and resolution for these events. The width parameter of $F_{D_1(2420)}(x)$ is fixed to the value from the $D^{*+}\pi^-$ analysis performed later while its mean value is free in the fit. The mass and width parameters of $F_{D_2^*(2460)}(x)$ are the same as those in the function $S_{D_2^*(2460)}(x)$ which describes the $D_2^*(2460)$ signal.

- $F_B(x)$ is the smooth background function described before.

The fit is done by minimizing the χ^2 on a binned histogram and a χ^2/NDF of 278/224 has been obtained. The fitted M($D^0\pi^+$) distribution is shown in Figure 11.18 and the

residuals in this figure show good agreement between the model and the data. The parameters extracted from the fit are listed in Table 11.2.

In order to test the effect of removing the BW functions which account for the new signals as well as the broad state from the fit, each function is removed from the fit model and the fit is redone. Figures 11.19 to 11.21 show the effect on the residuals, the degraded χ^2 for each fit is shown in Table 11.3.

Table 11.2: Parameter values extracted from the fit.

Resonance	Yield ($\times 10^3$)	Mass (MeV)	Width (MeV)
$D_0^*(2400)^+$	151.6± 1.2	2338± 2	202± 8
$D_2^*(2460)^+$	110.8± 1.3	2465.4± 0.2	50.5
$D^*(2600)^+$	13.0± 1.3	2621.3± 3.7	93
$D^*(2760)^+$	5.7± 0.7	2769.7± 3.8	60.9
${D_1(2420)^+}_{Feed}$	72.3 ± 1.1	2423.9 ± 0.3	31.0
${D_2^*(2460)^+}_{Feed}$	31.6 ± 2.1	2465.4± 0.2	50.5

Table 11.3: χ^2/NDF for the fits where the indicated resonance has been removed from the fit PDF.

Resonance Removed	χ^2/NDF
$D_0^*(2400)$	502/227
$D^*(2600)$	380/226
$D^*(2760)$	343/226

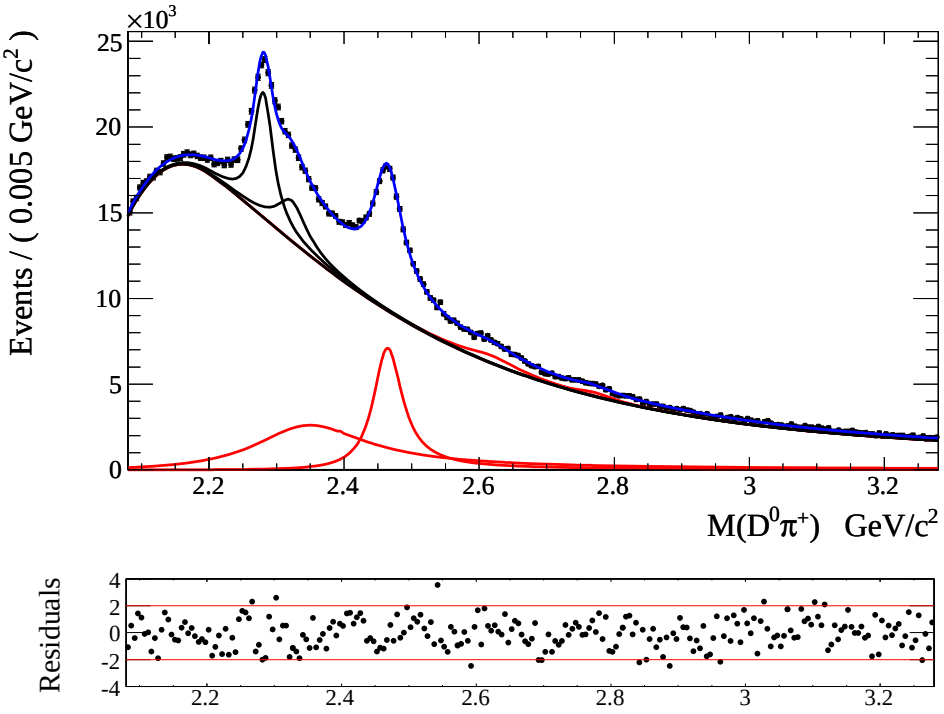

Figure 11.18: Fit to the M($D^0\pi^+$) mass distribution.

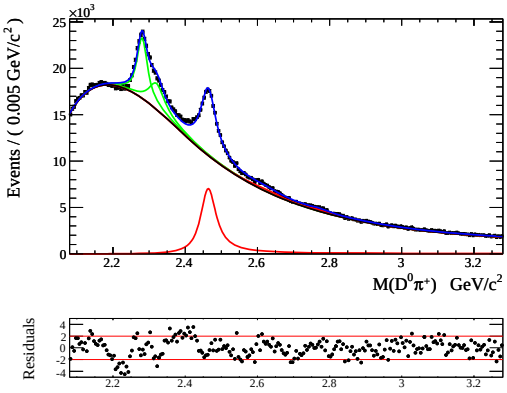

Figure 11.19: Fit to the M($D^0\pi^+$) distribution with the $D_0^*(2400)$ removed from the PDF.

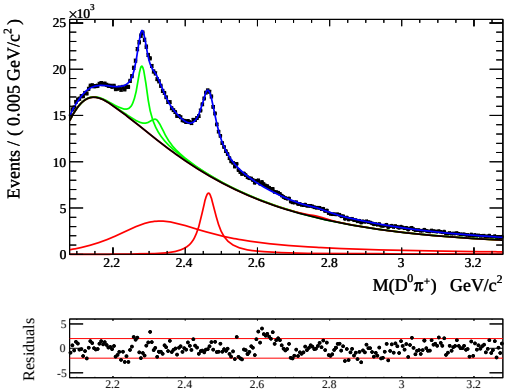

Figure 11.20: Fit to the M($D^0\pi^+$) distribution with the $D^*(2600)$ removed from the PDF.

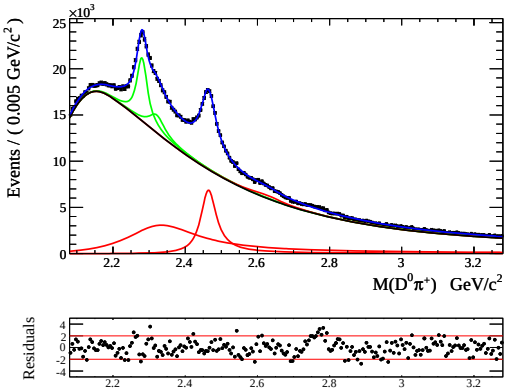

Figure 11.21: Fit to the M($D^0\pi^+$) distribution with the $D^*(2760)$ removed from the PDF.

11.3.2 Systematic Uncertainties

Systematic uncertainties on the signal parameters have been estimated from the following sources by modifying the nominal fit and taking the observed variation as the uncertainty:

- The mass range of the histogram is changed by 100 MeV on the higher side.
- The bin width of the histogram used in the fit is increased by a factor of two.
- The new signals at 2600 MeV and 2750 MeV are modeled using relativistic BW functions, in a modified fit these are replaced by BW functions for D-wave decay.
- The width parameter of the $D_2^*(2460)$, $D^*(2600)$, $D^*(2760)$, and $D_1(2420)$ resonances are fixed in the fit. These parameters are varied according to their errors.
- The smooth background model has limited flexibility as shown by the residuals from the fit to the Wrong-Sign distribution in Figure 10.19. A systematic error is assigned due to this possible mis-modeling by inserting the residuals obtained from the wrong-sign fit into the nominal fit.
- For the B field and SVT material uncertainties the values obtained for $D^+\pi^-$ are used.
- A systematic uncertainty is assigned due to a possible contribution from the $D_1'(2430)$ as described in the $D^+\pi^-$ systematics.

The variations in the signal parameters due to the above variations of the nominal fit are shown in Tables 11.4 and 11.5.

Table 11.4: Systematic errors on the parameters of the known signals.

	$D_0^*(2400)^+$ **Yield** ($\times 10^3$)	$D_2^*(2460)^+$ **Yield** ($\times 10^3$)	$D_2^*(2460)^+$ **M** (MeV)
Mass Range	6.2	3.0	0.34
Bin Width	9.5	1.5	0.25
Breit-Wigner Shape	8.3	2.0	0.21
Background Model	35.2	1.7	0.22
D(2460) Width	12.6	4.2	0.24
D(2620) Width	16.0	2.2	0.25
D(2750) Width	14.3	2.1	0.23
D(2420) Width	12.5	2.3	0.20
B field & SVT material	0.0	0.0	0.77
D(2430)	13.0	2.5	0.24
Total	48.3	7.5	1.1

Table 11.5: Systematic errors on the parameters of the new signals.

	$D^*(2600)^+$ **Yield** ($\times 10^3$)	$D^*(2600)^+$ **M** (MeV)	$D^*(2760)^+$ **Yield** ($\times 10^3$)	$D^*(2760)^+$ **M** (MeV)
Mass Range	1.8	2.05	1.3	0.34
Bin Width	0.3	0.79	0.2	0.09
Breit-Wigner Shape	0.5	1.37	0.1	0.41
Background Model	3.4	0.59	0.4	0.89
D(2460) Width	0.7	0.89	0.0	0.27
D(2620) Width	1.9	1.99	0.1	0.36
D(2750) Width	0.5	1.14	0.3	0.28
D(2420) Width	0.6	1.22	0.1	0.29
B field & SVT material	0.0	0.77	0.0	0.77
D(2430)	0.5	1.50	0.2	0.32
Total	4.5	4.2	1.5	1.5

Chapter 12

The $D^{*+}\pi^-$ Final State

The $D^{*+}\pi^-$ final state provides a more inclusive view of the excited D meson spectrum. As described in the introduction, the vector nature of the D^{*+} allows the $D^{*+}\pi^-$ system to accept more excited states since the spin angular momentum of the D^{*+} combined with the orbital angular momentum of the $D^{*+}\pi^-$ products forms a larger set of J^P values. Out of the 10 orbitally (L=1 and L=2) and radially excited states predicted only one state, the $D_0^*(2400)$, cannot decay to this final state.

The reconstruction of this final state, in any single decay chain, has lower signal yields when compared to the $D^+\pi^-$ final state. There are two reasons for this feature, one is the lower branching fractions for the excited states to decay into the $D^{*+}\pi^-$ channel because of the D^{*+} is heavier and this results in a smaller available phase space . The second reason is because even in the best reconstruction channel of the D^{*+}, $D^{*+} \to D^0\pi^+$, there is a slow pion track for which the reconstruction efficiency is relatively low. This efficiency loss is in addition to the efficiency loss due to the fact that the D^{*+} decays to $D^0\pi^+$ at a rate of only 67.7%. In order to improve the signal yield for this final state, two decay channels of the D^0 are combined in the reconstruction: $D^0 \to K^-\pi^+$ and $D^0 \to K^-\pi^+\pi^-\pi^+$. The decay rate of $D^0 \to K^-\pi^+$ is 3.7% while the decay rate of $D^0 \to K^-\pi^+\pi^-\pi^+$ is 8.1%, however, in the second channel the requirement of the additional two tracks results in signal yields which are about the same as for $D^0 \to K^-\pi^+$.

12.1 Event Reconstruction and Selection

For each event, D^0 candidates are reconstructed with the following requirements.

- In both, the $D^0 \to K^-\pi^+$ and $D^0 \to K^-\pi^+\pi^-\pi^+$ channels, the Kaon track must

pass the Tight Kaon PID selector.

- The tracks for each channel are fitted to a common vertex and a fit probability greater than 0.1% is required.
- For both channels, the D^0 candidate invariant mass must be within 30 MeV of the mean value as shown in Figure 12.1.

Once the D^0 candidates are selected, the D^{*+} candidates are reconstructed as follows.

- A charged track originating from the IP region is required and must have a momentum less than 700 MeV in the CM frame.
- A vertex fit is applied to the $D^0\pi^+$ combination while constraining the vertex to be within the IP region. The fit probability must be greater than 0.1%.
- D^{*+} mesons are best identified using the mass difference $\Delta m = m(D^0\pi^+) - m(D^0)$ because the signal is near threshold (as shown in Figure 12.2) and is very narrow. D^{*+} candidates are selected if the mass difference is within 3 MeV of the mean value.

Finally, the D^{**} candidates are reconstructed by combining the D^{*+} candidates with an additional π^- in the event.

- The π^- must originate from the IP region.
- A vertex fit is applied to the $D^{*+}\pi^-$ system while requiring the vertex to be within the IP region. The fit probability must be greater than 0.1%.
- The momentum of the $D^{*+}\pi^-$ system in the CM frame must be greater than 3.0 GeV to select the $c\bar{c}$ events (see Figure 12.3).
- Finally, the cosine of the angle of the primary pion, in the $D^{*+}\pi^-$ rest frame, with respect to the prior $D^{*+}\pi^-$ direction in the CM frame is required to be greater than -0.8. Figure 12.4 shows a comparison between background and signal events in this variable.

As in the $D\pi$ analyzes, the D^{**} candidate mass is calculated using the mass difference with respect to the D^{*+} mass to obtain improved resolution:

$$M(D^{*+}\pi^-) = m(D^0\pi^+\pi^-) - m(D^0\pi^+) + 2.01 \text{ GeV} \tag{12.1}$$

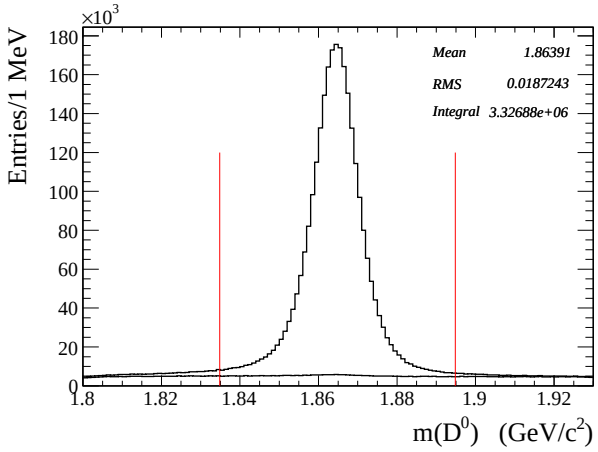

Figure 12.1: Distribution of the D^0 candidate mass after all other selections in the generic MC. The lower distribution shows the D^0 candidates which are not truth-matched. The vertical lines define the selected region.

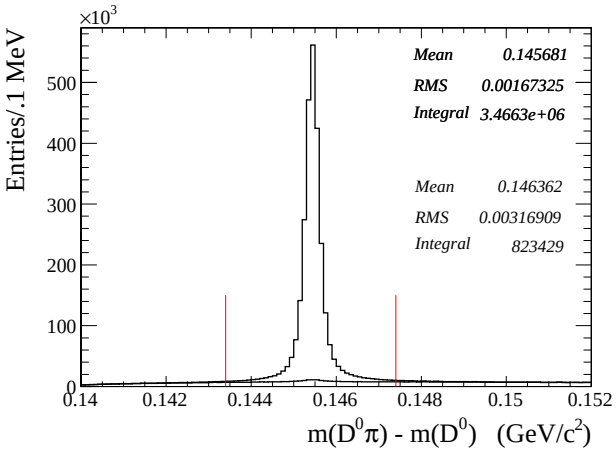

Figure 12.2: Distribution of D^{*+} ΔM in the generic MC after all other selections. The bottom distribution shows the D^{*+} candidates which are not truth-matched. The vertical lines define the selected region.

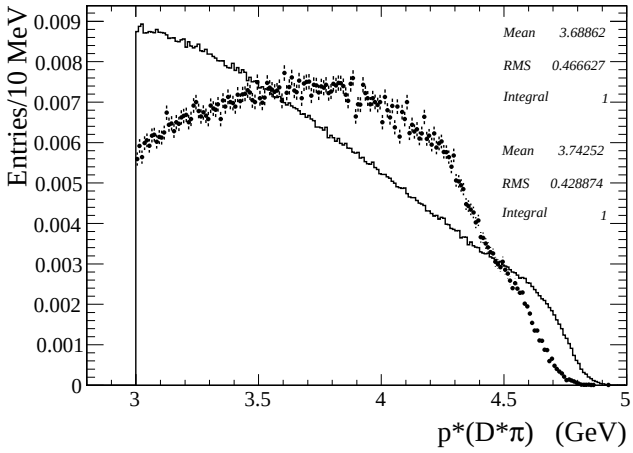

Figure 12.3: Comparison of the p* distribution between signal (points) and background (histogram) $D^{*+}\pi^-$ candidates in the generic MC. The background is obtained by removing the truth-matched signal candidates.

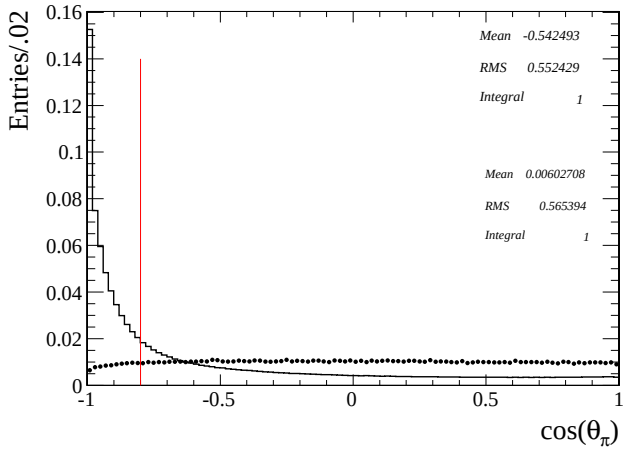

Figure 12.4: Comparison of the $\cos(\theta_\pi)$ distribution between signal (points) and background (histogram) $D^{*+}\pi^-$ candidates in the generic MC.

12.2 Signal MC

The signal MC samples generated for the $D_1(2420)^0$ and $D_2^*(2460)^0$ resonances decaying into the channels used in the reconstruction are used to determine the efficiency and resolution.

A total of four samples were generated, each resonance is simulated in the two D^0 decay channels. The samples corresponding to the $D^0 \to K^-\pi^+$ channels can be combined since they differ only by the generated mass values and have a common efficiency. This allows a determination of the efficiency across a wider mass range. Similarly, the two samples for the $D^0 \to K^-\pi^+\pi^-\pi^+$ channel are combined. The reconstructed mass distributions for the combined samples are shown in Figures 12.5 and 12.6 and the efficiencies determined from the truth-matched signal candidates are shown in Figures 12.7 and 12.8. The efficiency for the $D^0 \to K^-\pi^+\pi^-\pi^+$ channel is about two thirds the efficiency for the $D^0 \to K^-\pi^+$ channel due to the additional tracks.

For the determination of the resolution all four samples can be combined, since M($D^{*+}\pi^-$) is computed using the mass difference, the resolution depends only on the reconstruction of the primary pion. The distributions of reconstructed minus generated mass are parametrized using the same formula used in the analysis of the $D^+\pi^-$ signal MC. The constant parameters determined from the entire MC sample are the following:

- $f_2 = 0.090 \quad f_3 = 0.226$
- $\mu_1 = -.038\ MeV \quad \mu_2 = -2.6\ MeV \quad \mu_3 = 0.26\ MeV$
- $\sigma_2 = 4.2\sigma_1 \quad \sigma_3 = .70\sigma_1$

The parameter, σ_1, which varies as a function of the generated mass is determined from the subsamples shown in Figure 12.9. The values for σ_1 are shown in Figure 12.10.

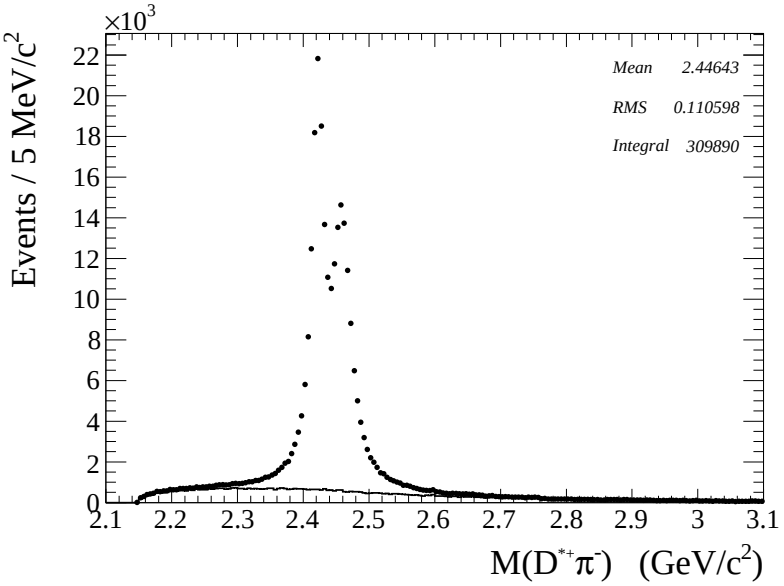

Figure 12.5: M($D^{*+}\pi^-$) distribution for the $D^0 \to K^-\pi^+$ Signal MC. The bottom distribution shows the candidates which do not pass the truth-match.

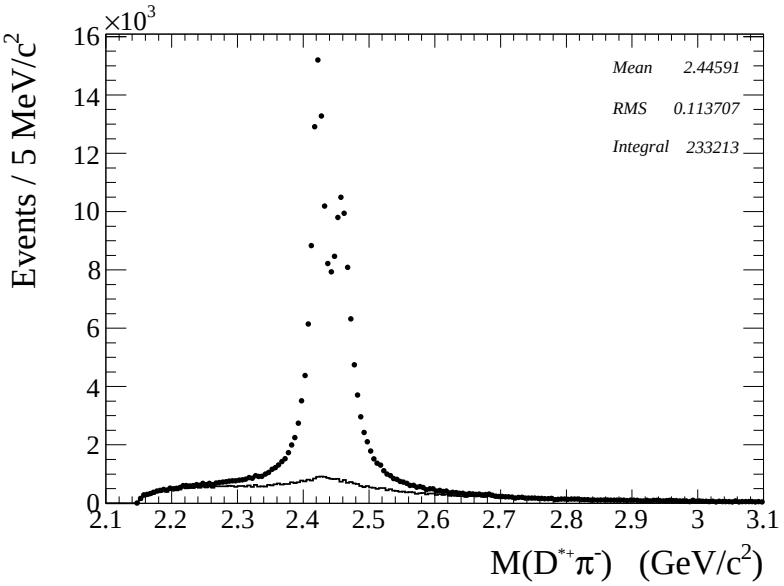

Figure 12.6: M($D^{*+}\pi^-$) distribution for the $D^0 \to K^-\pi^+\pi^-\pi^+$ Signal MC. The bottom distribution shows the candidates which do not pass the truth-match.

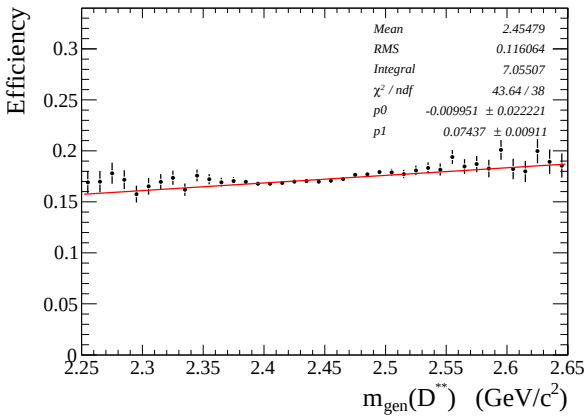

Figure 12.7: Ratio of the reconstructed signal candidates over the number generated as a function of generated mass for the $D^0 \to K^-\pi^+$ mode. The $D_1(2420)$ and $D_2^*(2460)$ MC samples are combined here.

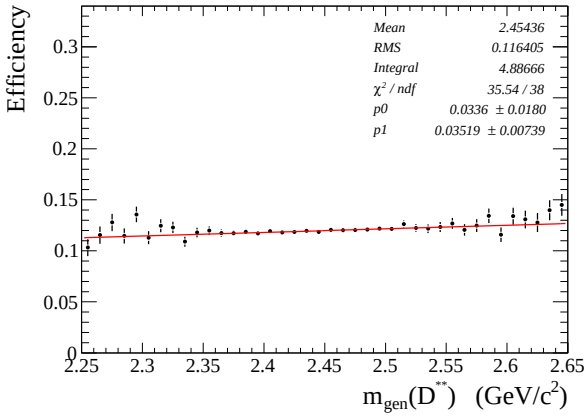

Figure 12.8: Ratio of the reconstructed signal candidates over the number generated as a function of generated mass for the $D^0 \to K^-\pi^+\pi^-\pi^+$ mode. The $D_1(2420)$ and $D_2^*(2460)$ MC samples are combined here.

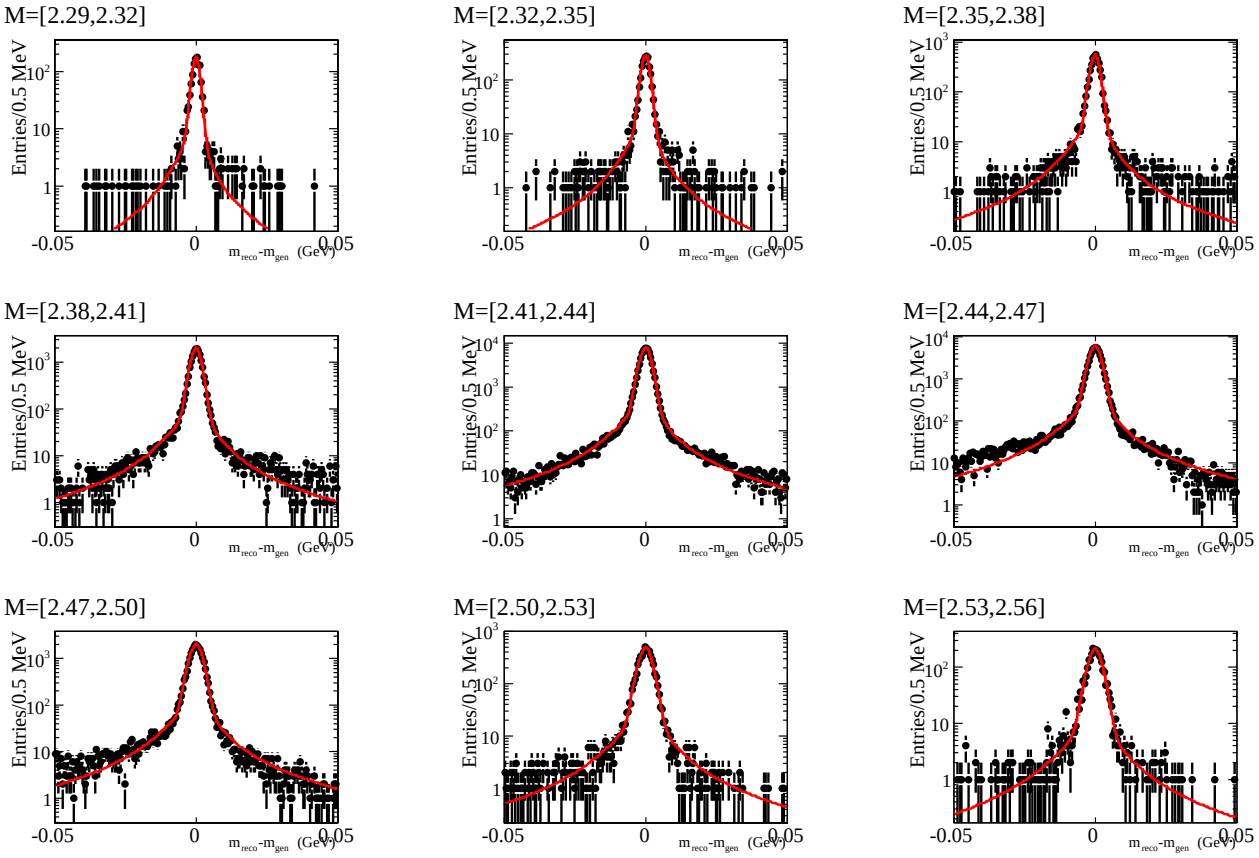

Figure 12.9: Distributions of reconstructed - generated mass as a function of $D^{*+}\pi^-$ mass in bins of 30MeV. The mass ranges are shown at the top of each plot. The $D_1(2420)$ and $D_2^*(2460)$ MC samples for both the $D^0 \to K^-\pi^+$ and $D^0 \to K^-\pi^+\pi^-\pi^+$ modes are combined here.

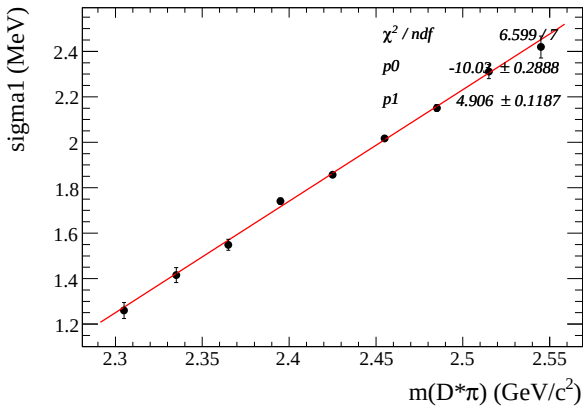

Figure 12.10: The parameter σ_1 as a function of mass.

12.3 Generic MC

The sample of D^0 candidates reconstructed in the generic MC sample after the full event selection are shown for the $D^0 \to K^-\pi^+$ and $D^0 \to K^-\pi^+\pi^-\pi^+$ channels in Figures 12.11 and Figure 12.12. For the $D^0 \to K^-\pi^+$ channel the requirement of a D^{*+} parent removes essentially all the fake D^0 candidates. In the $D^0 \to K^-\pi^+\pi^-\pi^+$ channel fake D^0 candidates remain due to the larger combinatorial background arising from the four tracks. The distribution of D^{*+} candidates as a function of Δm for the combined D^0 samples is shown in Figure 12.13. Since the purity of the D^{*+} signal is high and since there are no peaking backgrounds in this final state the sidebands of the D^{*+} distribution are not used in the analysis.

The generic MC sample simulates the three known resonances, $D_1(2420)$, $D_2^*(2460)$ and $D_1'(2430)$, which are expected to decay to the $D^{*+}\pi^-$ final state. These can be observed in the reconstructed M($D^{*+}\pi^-$) distribution shown in Figure 12.14. The smooth background arises mainly from events which contain a D^{*+} and the D^{*+} is combined with a pion from the fragmentation processes in same side of the event. Figure 12.15 shows the distribution of $D^{*+}\pi^-$ candidates which have been truth-matched to one of the resonances. The $D_1'(2430)$ component has an artificial mass cutoff at about 2.7 GeV.

A sample of wrong-sign candidates has been reconstructed by requiring that the primary pion have the same charge as the D^{*+}. The M($D^{*+}\pi^+$) for this sample is shown in Figure 12.16 and shows no peaking structures. The fit to this distribution has been done using the nominal background formula constructed in the $D^+\pi^-$ analysis.

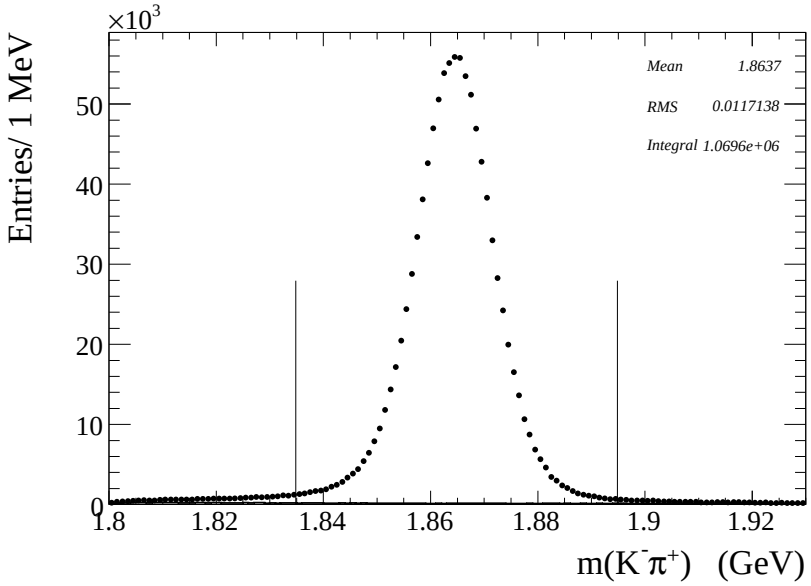

Figure 12.11: D^0 mass for the $D^0 \to K^-\pi^+$ channel in generic MC after all other selections. The background for this channel is negligible.

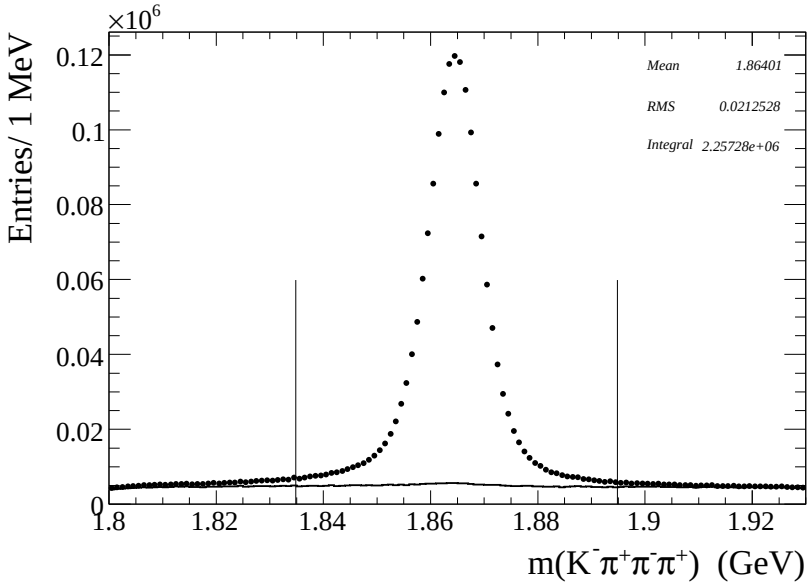

Figure 12.12: D^0 mass for the $D^0 \to K^-\pi^+\pi^-\pi^+$ channel in generic MC after all other selections. The bottom histogram shows the D^0 candidates which do not pass the truth-match.

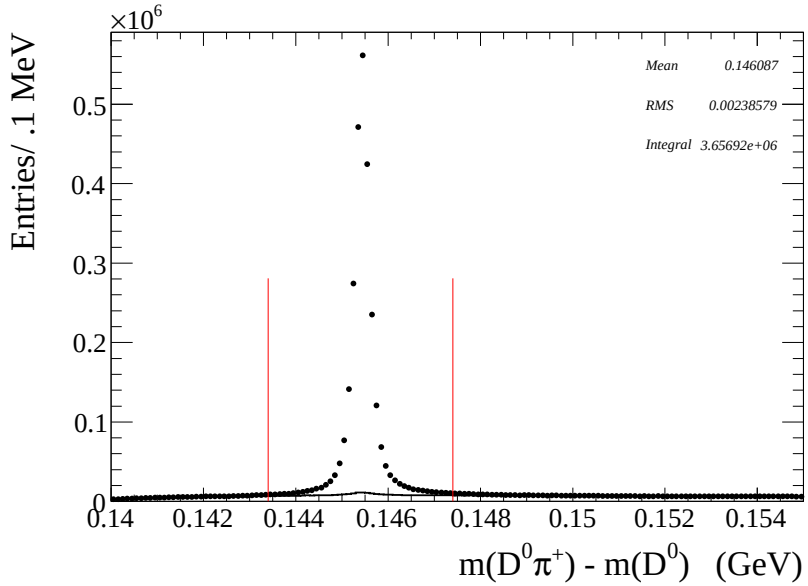

Figure 12.13: D^* ΔM in generic MC after all other selections. This distribution combines both D^0 modes. The bottom histogram shows the D^* candidates which do not pass the truth-match.

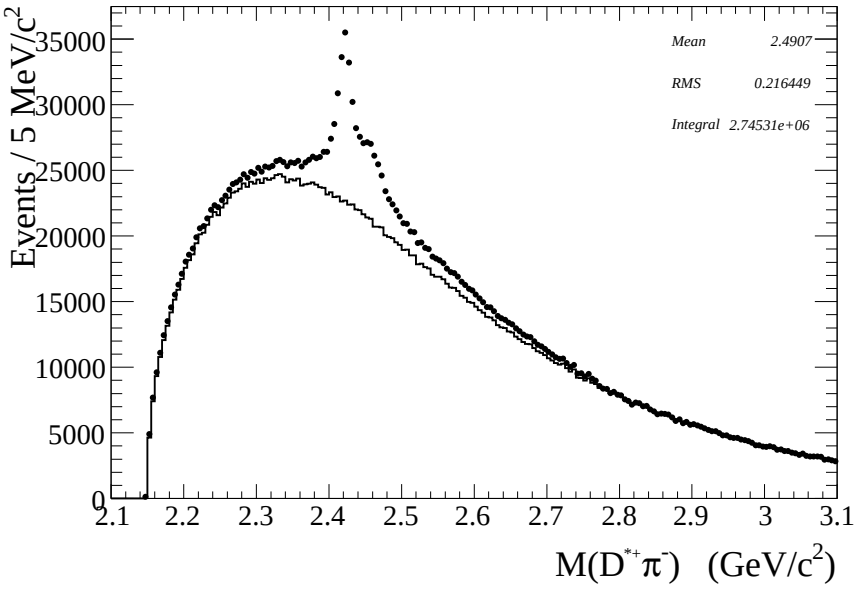

Figure 12.14: M($D^{*+}\pi^-$) in generic MC after all selections. The bottom histogram shows the D^{**} candidates which do not pass the truth-match.

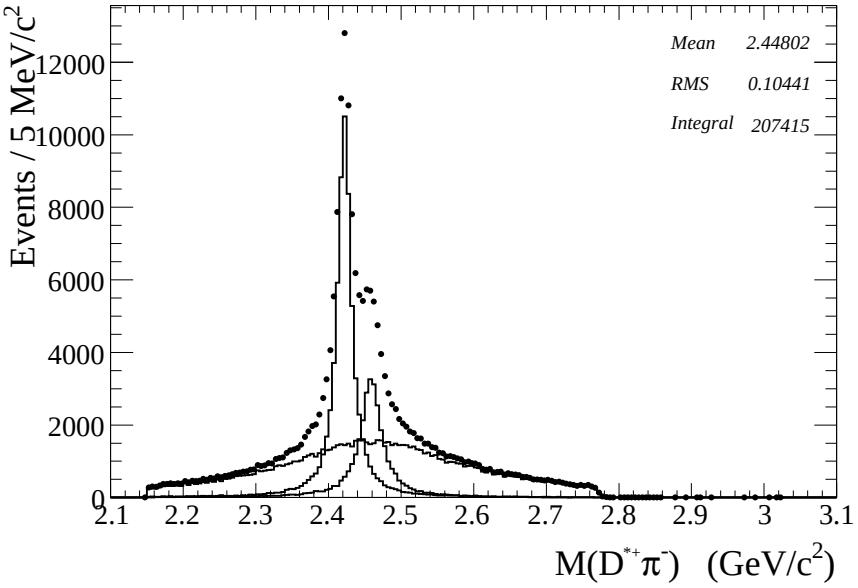

Figure 12.15: M($D^{*+}\pi^-$) after all selections for D^{**} candidates which are truth-matched to either a $D_1(2420)$, a $D_2^*(2460)$ or a $D_1'(2430)$. The individual components are also shown.

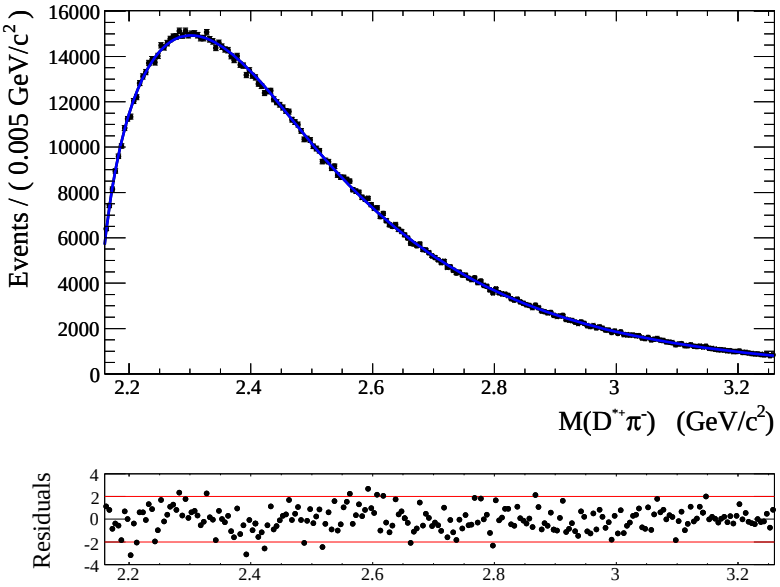

Figure 12.16: Fit to the M($D^{*+}\pi^+$) distribution in the wrong-sign generic MC sample.

12.3.1 Fit to M($D^{*+}\pi^-$) in MC

The fit to the M($D^{*+}\pi^-$) distribution is simpler than the in the $D\pi$ analyzes because this final state does not suffer from feed-down backgrounds and no sideband subtraction is necessary. The fit model contains the three signal components and the smooth background function:

$$F(x) = \int \left[S_{D_1(2420)}(y) + S_{D_2^*(2460)}(y) + S_{D_1'(2430)}(y)\right] R(x-y)dy + F_B(x) \qquad (12.2)$$

- The components $S_{D_1(2420)}(x)$, $S_{D_2^*(2460)}(x)$, and $S_{D_1'(2430)}(x)$ are non-relativistic BW functions corrected for the efficiency shape and are convolved with the resolution function.
- Due to its large width the mass width parameters of the $D_1'(2430)$ must be fixed to the true values. The sensitivity to this signal is mostly artificial arising from the mass cut-off.
- The background function $F_B(x)$ is described in the $D^+\pi^-$ analysis.

The fit is performed by minimizing the χ^2 on a binned histogram. The fit finds a minimum at χ^2/NDF of 241/209 and is shown Figure 12.17. The results, listed in Table 12.1, are in good agreement with the generated values.

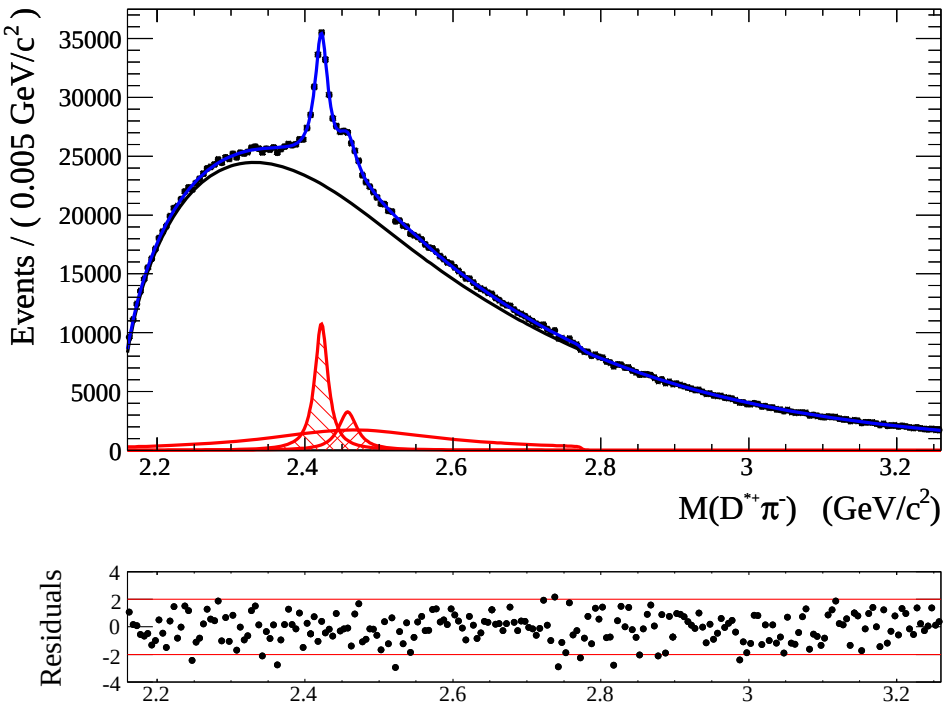

Figure 12.17: Fit to the M($D^{*+}\pi^-$) distribution in generic MC.

Table 12.1: Reconstructed signal parameters. The error is statistical only.

Resonance	Yield ($\times 10^3$)	M (MeV)	Γ (MeV)	Generated Yield ($\times 10^3$)	Generated M (MeV)	Generated Γ (MeV)
$D_1(2420)$	68.6 $\pm$ 1.5	2422.2 $\pm$ 0.2	19.5 $\pm$ 0.5	69.7	2422.0	19.0
$D_2^*(2460)$	29.3 $\pm$ 1.6	2457.8 $\pm$ 0.6	28.2 $\pm$ 1.7	32.1	2459.0	30.0
$D_1'(2430)$	112.0 $\pm$ 15.0	2461.0	290.0	103.7	2461.0	290.0

12.3.2 Helicity Distributions

Once the nominal fit to the M($D^{*+}\pi^-$) distribution is defined, the distribution of the signal yield as a function of $\cos\theta_H$ can be extracted. This is accomplished by creating 10 subsamples by selecting ranges in $\cos\theta_H$ of equal size between -1 and 1, and applying the nominal fit to the M($D^{*+}\pi^-$) distribution for each subsample. The fit to each subsample is performed with the mass and width parameters of the signals fixed to the values obtained from the fit to the entire sample. The M($D^{*+}\pi^-$) distribution and the fit for each subsample are shown in Figure 12.18, the signal yields obtained from each fit are shown in Figures 12.20 and 12.21. A fit to the signal distribution of the $D_1(2420)$ has been performed using a function $Y \propto 1 + Acos^2(\theta_H)$ with an additional shape correction for a slight dependence of the efficiency on $\cos\theta_H$ (see Figure 12.19). The result of the fit gives a value for A consistent with 3.0 which is the value used in the simulation. For the $D_2^*(2460)$ a fit is performed using the function $Y \propto sin^2(\theta_H)$ and a good agreement with the extracted distribution is found. The J^P quantum numbers for this resonance are believed to be 2^+ and fall in the class called *natural parity* defined by the relation $P = (-1)^J$. States with natural parity have a distribution in $\cos\theta_H$ which is proportional to $\sin^2\theta_H$.

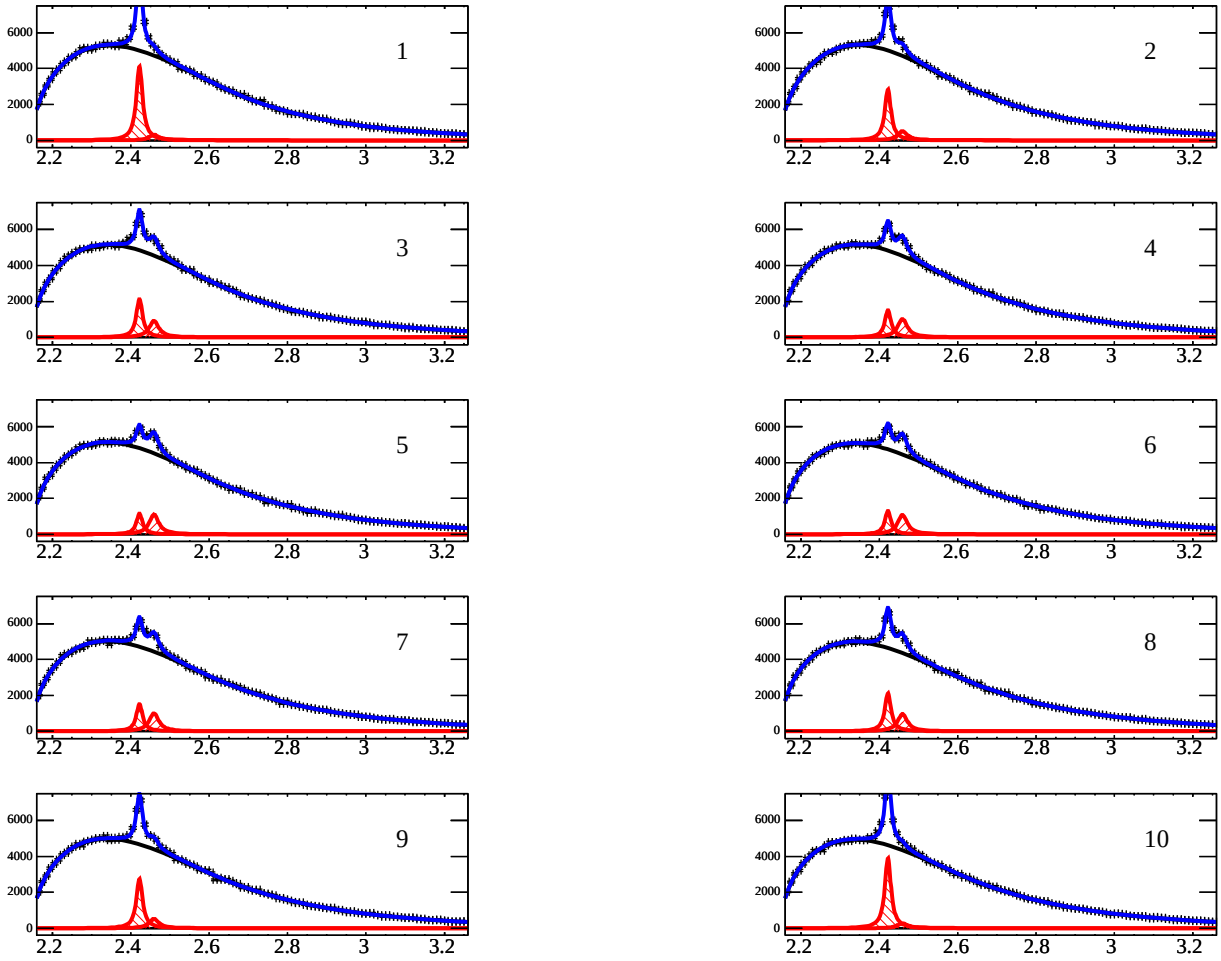

Figure 12.18: Fit to the generic MC M($D^{*+}\pi^-$) distribution in each interval of $\cos\theta_H$.

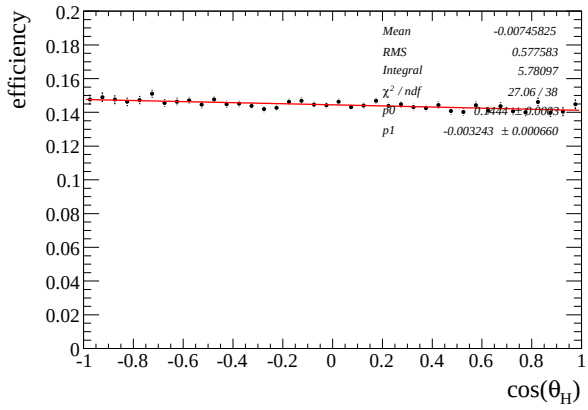

Figure 12.19: Efficiency as a function of $\cos\theta_H$ determined using the signal MC.

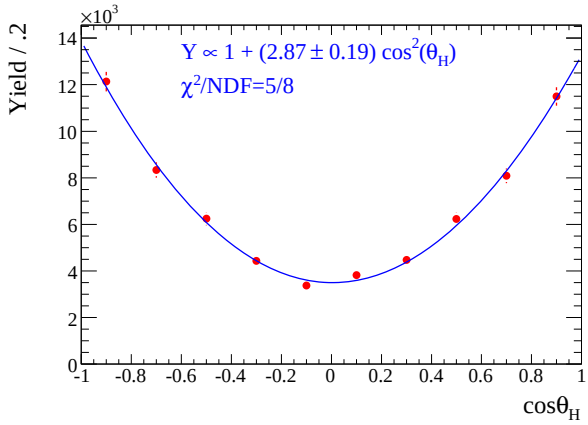

Figure 12.20: Yield as a function of $\cos\theta_H$ for the $D_1(2420)$.

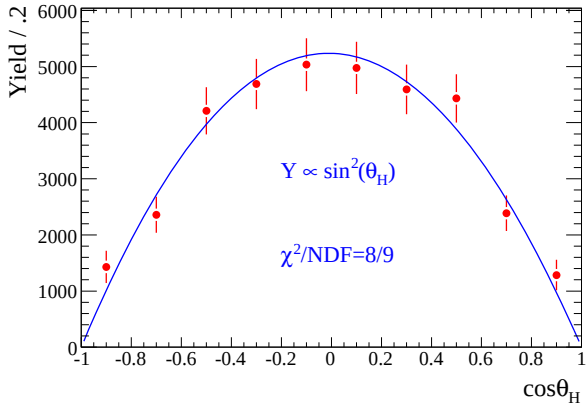

Figure 12.21: Yield as a function of $\cos\theta_H$ for the $D_2^*(2460)$.

12.4 Analysis of the Data

A similar analysis has been performed for the data sample. The distribution of D^0 candidates after the full event selection is shown for the $D^0 \to K^-\pi^+$ mode in Figure 12.22 and for the $D^0 \to K^-\pi^+\pi^-\pi^+$ mode in Figure 12.23. As in the MC the $D^0 \to K^-\pi^+$ mode is essentially background free while the $D^0 \to K^-\pi^+\pi^-\pi^+$ mode suffers from remaining combinatorial background.

The Δm distribution for the D^{*+} candidates, shown in Figure 12.24, has a signal purity of 89%. The purity is determined from a fit to this distribution in which the signal is modeled using a BW function added with a Gaussian function. The background is modeled using a 3rd order polynomial.

The M($D^{*+}\pi^-$) distribution for this final state is shown in Figure 12.25. In addition to the expected signals from the decays of the $D_1(2420)$ and $D_2^*(2460)$, there are additional structures in the mass range between 2.6 and 2.8 GeV/c^2. The interpretation of these structures is not straight forward since this final state can be populated by more excited states than those in the $D^+\pi^-$ spectrum and therefore the structure at about 2.6 GeV/c^2 and the one at about 2.75 GeV/c^2 are not necessarily the same ones observed in the $D^+\pi^-$ distribution. A study of the mass and width parameters and helicity distributions is necessary to understand better the origin of these structures.

The mass distribution for wrong-sign $D^{*+}\pi^+$ candidates is shown Figure 12.26 and is used as an additional test of the background model. The residuals of the fit to this distribution show a small oscillation, this disagreement is used to estimate systematic uncertainties later.

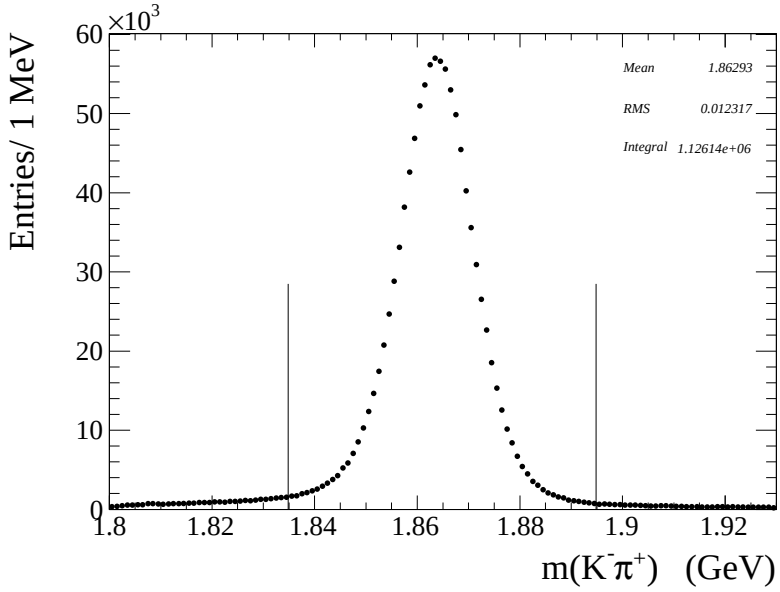

Figure 12.22: Invariant-mass distribution for the D^0 candidates in data for the $D^0 \to K^-\pi^+$ mode .

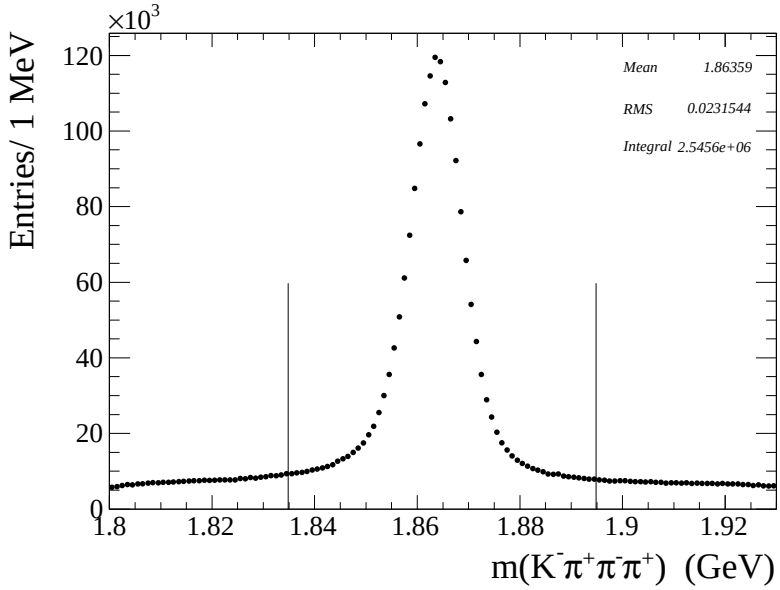

Figure 12.23: Invariant-mass distribution for the D^0 candidates in data for the $D^0 \to K^-\pi^+\pi^-\pi^+$ mode .

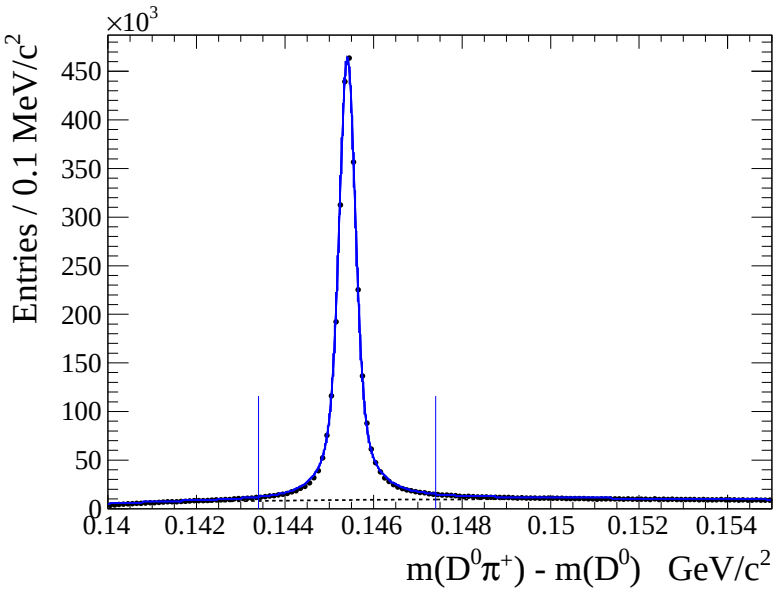

Figure 12.24: Fit to the Δm distribution in data. The signal is modeled using a Breit-Wigner function added with a Gaussian function with common mean parameter; the background is modeled with a polynomial (dashed curve). All functions are multiplied by a 2-body phase-space threshold factor.

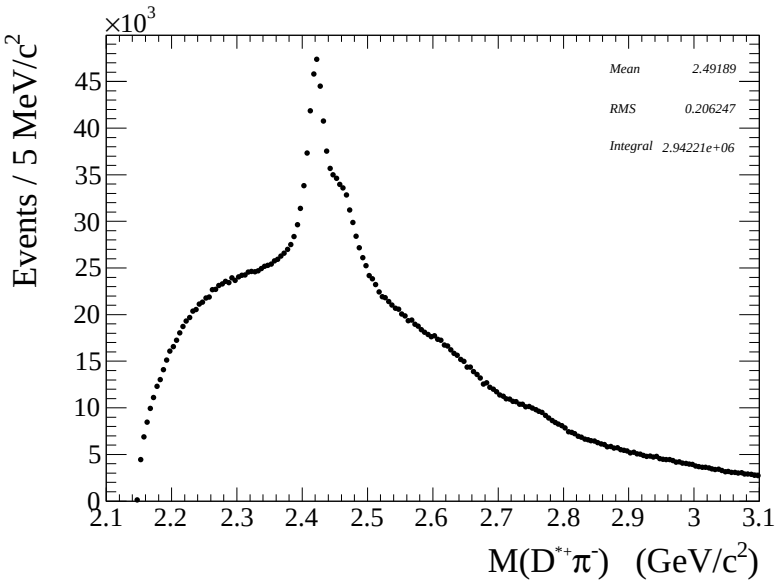

Figure 12.25: M($D^{*+}\pi^-$) distribution in data after all the event selections.

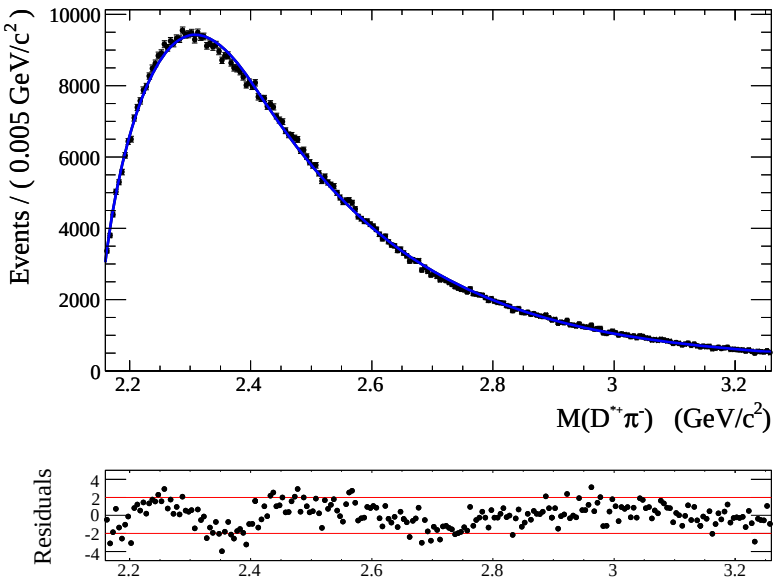

Figure 12.26: Fit to the wrong-sign M($D^{*+}\pi^+$) distribution in data.

12.4.1 Preliminary fit to the M($D^{*+}\pi^-$) in Data

A preliminary fit to the M($D^{*+}\pi^-$) distribution has been performed with a minimal number of signals included in the fit model. In addition to the known $D_1(2420)$ and $D_2^*(2460)$ signals, two more signal components for the higher mass structures are included:

$$F(x) = \int \left[S_{D_1(2420)}(y) + S_{D_2^*(2460)}(y) + S_{D^*(2600)}(x) + S_{D(2750)}(x)\right] R(x-y)dy \quad (12.3)$$
$$+F_B(x) \quad (12.4)$$

- The components for the known signals, $S_{D_1(2420)}(x)$ and $S_{D_2^*(2460)}(x)$, are BW functions with appropriate factors for a D-wave decay. The components for the new structures, $S_{D^*(2600)}(x)$ and $S_{D(2750)}(x)$, are relativistic BW functions. All components are corrected for the efficiency shape and are multiplied by a phase-space factor.

- The function $F_B(x)$ is the nominal background model constructed in the $D^+\pi^-$ analysis.

- The mass and width parameters of the $D_2^*(2460)$ are fixed to the parameters determined in the $D^+\pi^-$ analysis.

For this fit a minimum χ^2/NDF of 267/206 is obtained, Figure 12.27 shows the fitted distribution and the signal parameters are listed in Table 12.2.

Using this minimal fit model a study of the helicity dependence has been performed. As for the MC, 10 subsamples have been created by selecting on $\cos\theta_H$. The M($D^{*+}\pi^-$) distribution for each subsample has been fit using this minimal model, however, it is found that the mass parameter for the $D^*(2600)$ structure depends strongly on the helicity selection. The fits are presented in Figure 12.28 after subtracting the fitted background and with a y-axis scale that allows to see the variation of this signal. The dependence of the mass parameter is shown in Figure 12.29 and shows that the mass of this signal increases for values of $\cos\theta_H$ near 0.

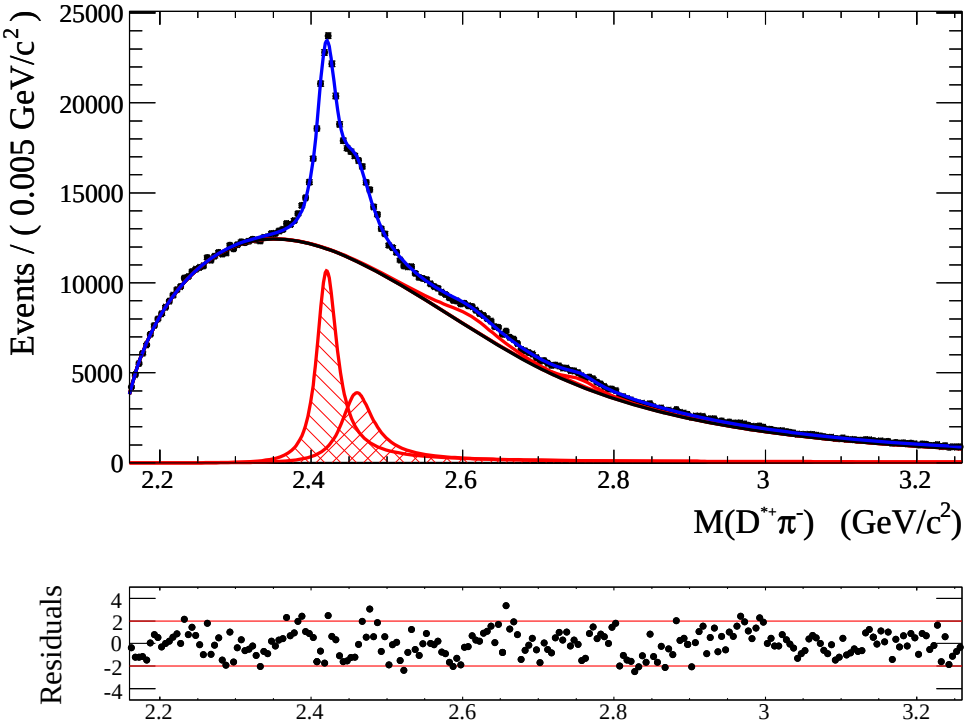

Figure 12.27: Preliminary fit to the M($D^{*+}\pi^-$) distribution in data.

Table 12.2: Signal parameters extracted from the preliminary fit to the M($D^{*+}\pi^-$) distribution in data. The error is only statistical.

Resonance	Yield ($\times 10^3$)	M (MeV)	Γ (MeV)
$D_1(2420)$	114.9 $\pm$ 0.9	2421.2 $\pm$ 0.1	30.6 $\pm$ 0.1
$D_2^*(2460)$	67.9 $\pm$ 1.3	2462.2	50.5
$D^*(2600)$	31.6 $\pm$ 6.1	2616.2 $\pm$ 2.6	115.2 $\pm$ 13.2
$D(2750)$	6.9 $\pm$ 0.9	2756.7 $\pm$ 2.7	54.4 $\pm$ 6.4

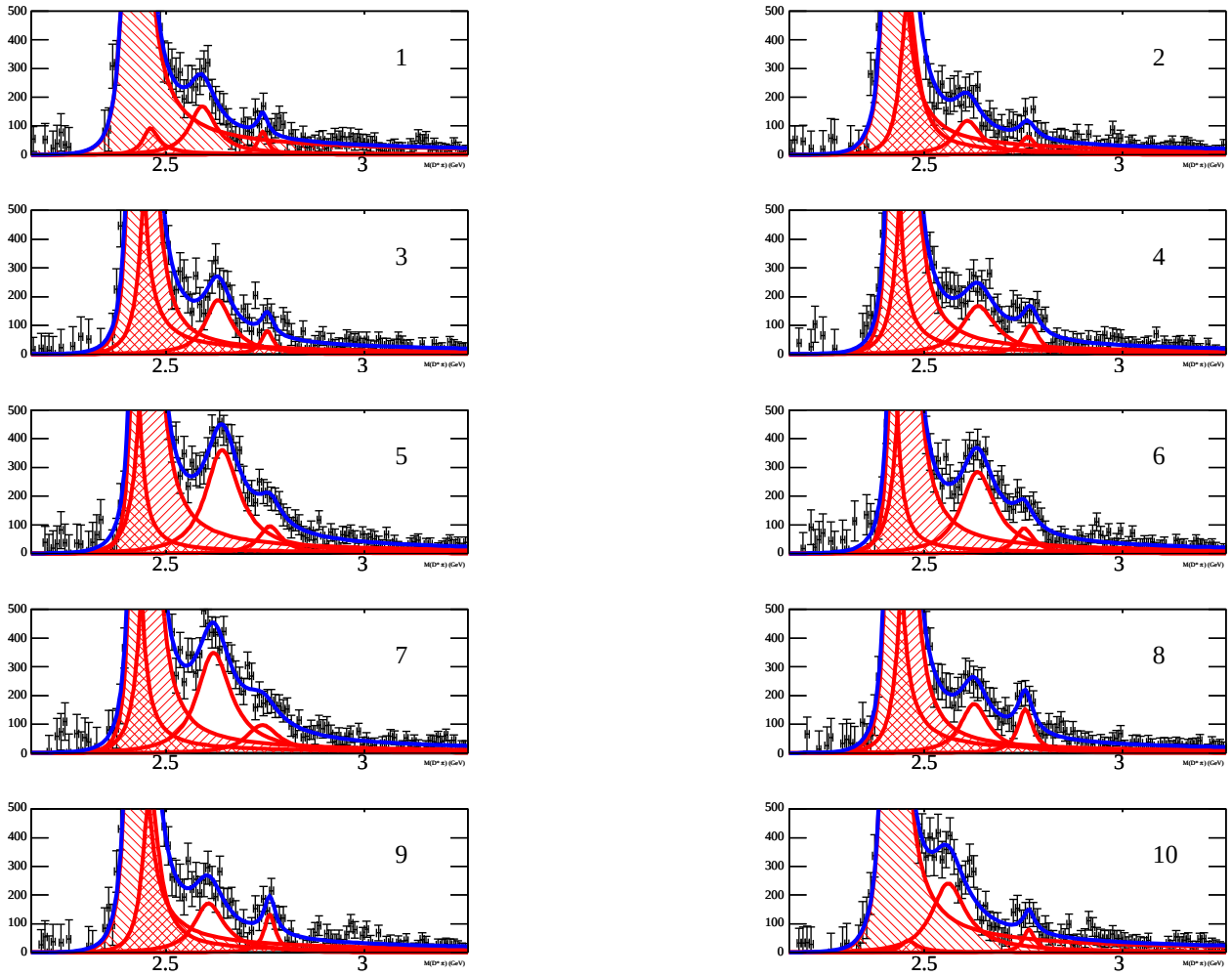

Figure 12.28: Fit to the M($D^{*+}\pi^-$) distribution in data for each helicity subsample. The fits are shown after subtracting the smooth background. The Y axis has been zoomed to show the new signals.

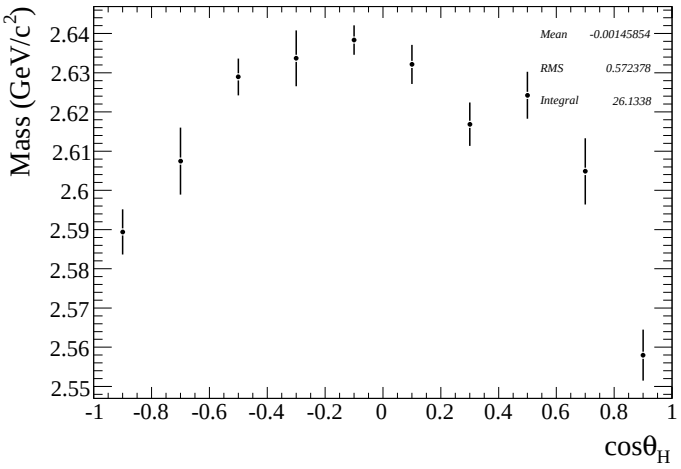

Figure 12.29: Dependence of the $D^*(2600)$ Mass as a function of $\cos\theta_H$.

12.4.2 Extraction of the $D(2550)$ signal

The behavior encountered for the $D^*(2600)$ signal indicates that multiple resonances may exist in this mass region. The observed behavior can be explained if two resonances with different helicity distributions populate this region. In order to proceed, we recall that the theoretical predictions indicated that the two radially excited states $D_0^1(2S)$ and $D_1^3(2S)$ have mass values at about 2.58 and 2.62 GeV/c^2. The $D_0^1(2S)$ has a helicity distribution proportional to $cos^2\theta_H$ while the $D_1^3(2S)$ has a helicity distribution which is proportional to $sin^2\theta_H$. Given these mass values and helicity distributions, these two resonances can produce precisely the observed behavior.

Since only the $D_1^3(2S)$ can decay to $D^+\pi^-$, the parameters for this state are identified as those found for the $D^*(2600)$ signal in $D^+\pi^-$. A new signal, denoted as $D(2550)$, is added to the minimal fit model with a mass at about 2.55 GeV/c^2. The mass and width parameters for the $D(2550)$ are determined from a fit to the M($D^{*+}\pi^-$) distribution after applying the selection $|\cos\theta_H| > 0.75$ which suppresses the neighboring $D_2^*(2460)$ and $D^*(2600)$ signals. This fit is shown in Figure 12.30 and the signal parameters are listed in Table 12.3. Since in this fit the mass and width parameters for the $D_2^*(2460)$ and $D^*(2600)$ are fixed to the values determined in $D^+\pi^-$, the excess events at about 2.55 GeV/c^2 determine the mass and width of the $D(2550)$. This fit also determines the $D_1(2420)$ mass and width parameters.

A complementary fit with the selection $|\cos\theta_H| < 0.5$ is also performed in order to test the consistency of the final fit model. This selection suppresses the $D_1(2420)$ and $D(2550)$ signals and allows a clearer observation of the $D^*(2600)$ signal. This fit is shown in Figure 12.31 and the signal parameters are listed in Table 12.4. In this fit the mass and width parameters for all signals except the $D(2750)$ are fixed to the values determined from the previous fits.

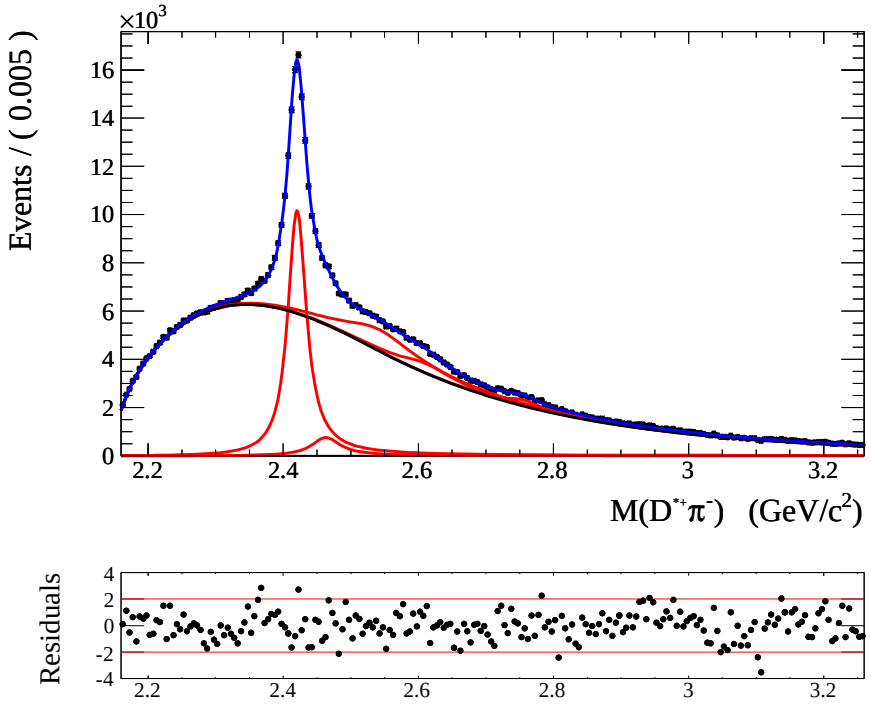

Figure 12.30: Fit to the M($D^{*+}\pi^-$) distribution in data with the selection $|\cos\theta_H| > 0.75$.

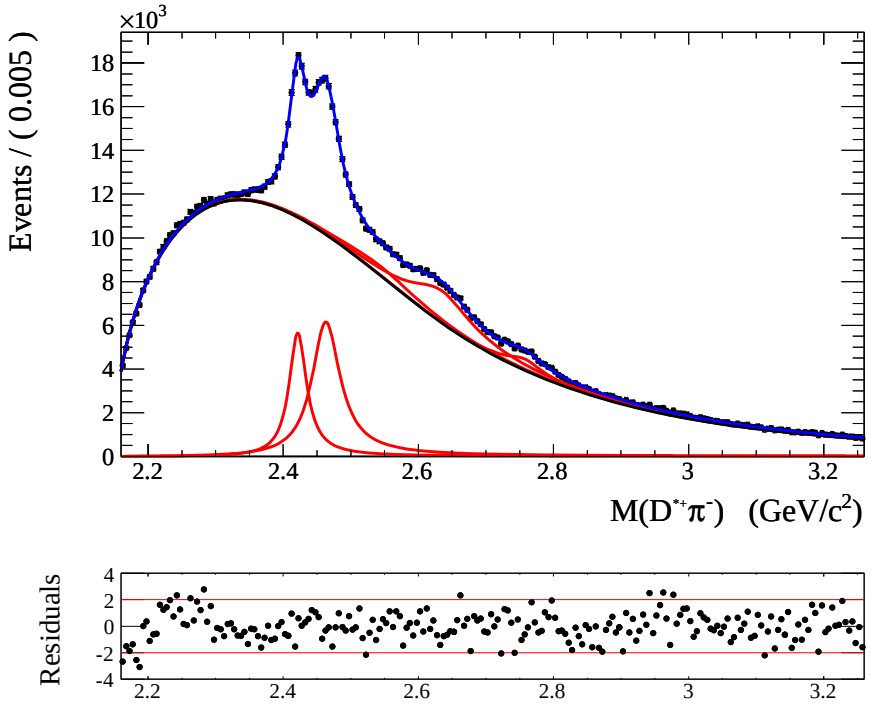

Figure 12.31: Fit to the M($D^{*+}\pi^-$) distribution in data with the selection $|\cos\theta_H| < 0.5$.

Table 12.3: Signal parameters determined in the fit with helicity selection $|\cos\theta_H| > 0.75$. The error is statistical only.

Resonance	Yield ($\times 10^3$)	M (MeV)	Γ (MeV)
$D_1(2420)$	102.8± 1.3	2420.1± 0.1	31.4± 0.5
$D_2^*(2460)$	136± 2	2462.2	50.5
$D(2550)$	34.3± 6.7	2539.4± 4.5	130± 12
$D^*(2600)$	11.3 ± 2.2	2608.7	93
$D(2750)$	4.5 ± 0.7	2755.1 ± 3.0	58.5 ± 8.7

Table 12.4: Signal parameters determined in the fit with helicity selection $|\cos\theta_H| < 0.5$. The error is statistical only.

Resonance	Yield ($\times 10^3$)	M (MeV)	Γ (MeV)
$D_1(2420)$	55.9 ± 0.8	2420.1	31.4
$D_2^*(2460)$	96.9 ± 1.1	2462.2	50.5
$D(2550)$	15.9 ± 2.9	2539.4	130
$D^*(2600)$	50.2± 3.0	2608.7	93
$D(2750)$	9.5 ± 1.1	2756.9 ± 4.5	61.2 ± 6.6

12.4.3 Final fit to the M($D^{*+}\pi^-$) Distribution

A fit to the M($D^{*+}\pi^-$) distribution for the entire $D^{*+}\pi^-$ event sample is necessary in order to assign final mass and width parameters to the $D(2750)$ signal. Also, the signal yields from this fit are used to compute ratios of the branching fractions for the decays of the states with natural parity. This fit is also a crosscheck on the final model to make sure that under varying event yields for the different resonances the model remains good.

In this fit, the mass and width parameters for the $D_2^*(2460)$ and $D^*(2600)$ are fixed to the values obtained in the analysis of $D^+\pi^-$. Also, the parameters of the $D_1(2420)$ and $D(2550)$ are fixed to the values obtained from the fit to M($D^{*+}\pi^-$) distribution with helicity selection $|\cos\theta_H| > 0.75$. The χ^2/NDF obtained for this fit is 244/207 showing that the constructed model can describe the total $D^{*+}\pi^-$ distribution well. The fit is shown in Figure 12.32 and the signal parameters are listed in Table 12.5.

Finally, throughout the analysis of the $D^{*+}\pi^-$ mass distributions, the $D_1'(2430)$ resonance, which is expected to decay to this final state, has not been included in the nominal fits. The fits to this final state are insensitive to this resonance due to the background shape. The background model parameters are floated and this allows this resonance to merge with the fitted background. A fit where a BW component for this resonance has been tried with its mass and width parameters fixed to the PDG values, however the fit quality does not improve and a signal yield consistent with zero was obtained.

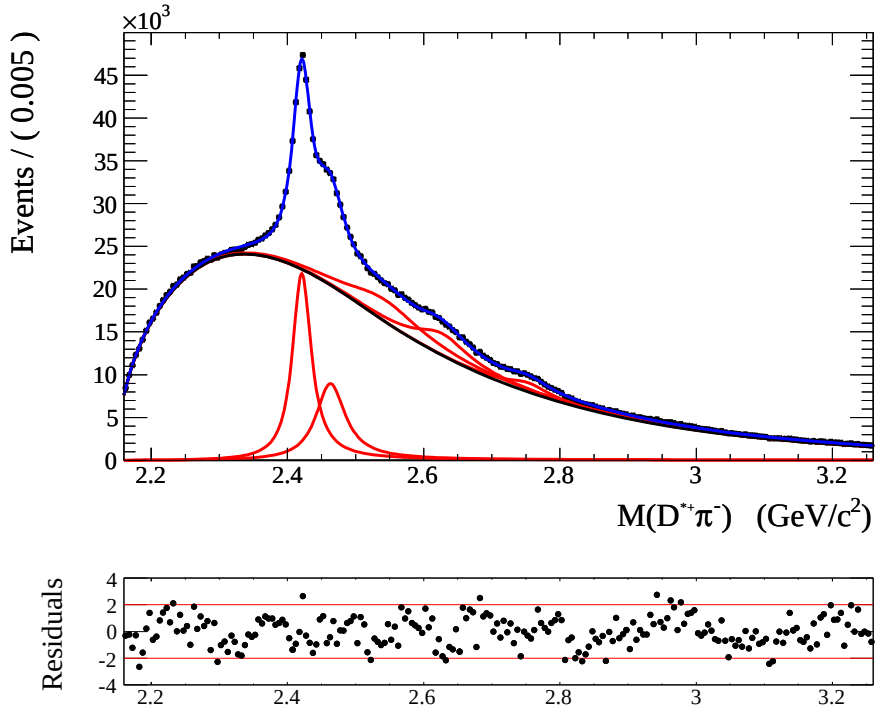

Figure 12.32: Fit to the entire $D^{*+}\pi^-$ sample using the final fit model.

Table 12.5: Signal parameters determined from the fit to the entire $D^{*+}\pi^-$ sample. The error is statistical only.

Resonance	Yield ($\times 10^3$)	M (MeV)	Γ (MeV)
$D_1(2420)$	214.6± 1.2	2420.1	31.4
$D_2^*(2460)$	136± 2	2462.2	50.5
$D(2550)$	98.4± 8.2	2539.4	130
$D^*(2600)$	71.4± 1.7	2608.7	93
$D(2750)$	23.5± 2.1	2752.4± 1.7	71± 6

12.4.4 Systematic Uncertainties

Systematic uncertainties have been estimated for all fit results obtained using the final fit model for the $D^{*+}\pi^-$ final state. Three fits have been performed in this final state. The first one with the helicity selection $|\cos\theta_H| > 0.75$ is used to extract the $D(2550)$ and the parameters of the $D_1(2420)$. The second one with the helicity selection $|\cos\theta_H| < 0.5$ is used mainly to check the consistency of the fit model as well as to observe the $D^*(2600)$ most clearly, therefore for this fit we are only interested in the variations of the this signal yield which is used to estimate the significance. In the final fit it is necesary to determine the uncertainties of all signal yields since these are used to compute ratios of branching fractions later, also this fit determines the parameters of the $D(2750)$.

For all fits, systematic uncertainties due to the following sources have been estimated by varying the fit as indicated:

- The range of the histogram is arbitrary and is varied by 100 MeV to determine the variation of the parameters.
- The bin size of the histogram is arbitrary and is increased by a factor of 2 to determine the variation of the parameters.
- The function shape for the new signals is a relativistic BW, this is changed to that for a D-wave decay.
- The background model shows some limitations when fitting the wrong-sign distribution as shown in the residuals of figure 12.26, these residuals are inserted into the nominal fit and the difference in the fitted parameters is assigned as the systematic error.
- The mean and width of the $D_2^*(2460)$ and $D^*(2600)$ are fixed to the parameters obtained in the $D^+\pi^-$ analysis. These parameters are varied according to their errors.
- Systematic uncertainties on the mass values due to the B field and SVT material uncertainties are assigned as those obtained in the $D^+\pi^-$ analysis since these depend only on the primary pion.
- A systematic uncertainty due to a possible contribution by the broad state $D_1'(2430)$ is assigned by including an additional signal component in the fit whose mass and width parameters are fixed to the PDG values for this resonance and the yield is

fixed to the $D_1(2420)$ yield. A fit where the yield for this signal is floated gives a yield which is consistent with zero.

In addition, in the fit with helicity selection $|\cos\theta_H| < 0.5$ and in the final fit the mass and width of the $D_1(2420)$ and $D(2550)$ are fixed in the fit to the parameters obtained in the fit with the selection $|\cos\theta_H| > 0.75$, systematic uncertainties are assigned by varying these parameters according their errors.

The variations on the fit parameters obtained from each fit are listed in Tables 12.6 to 12.9.

Table 12.6: Systematic uncertainties for the $D_1(2420)$ parameters obtained from the fit with helicity selection $|\cos\theta_H| > 0.75$.

	$D_1(2420)$ **Yield** ($\times 10^3$)	$D_1(2420)$ **M** (MeV)	$D_1(2420)$ Γ (MeV)
Mass Range	0.32	0.00	0.00
Bin Width	2.06	0.04	1.24
Breit-Wigner Shape	0.02	0.01	0.00
Background Model	0.37	0.03	0.06
D(2460) Mean	0.17	0.01	0.04
D(2460) Width	0.08	0.00	0.01
D(2600) Mean	0.06	0.01	0.01
D(2600) Width	0.12	0.00	0.03
B field & SVT material	0.00	0.77	0.00
D(2430)	0.56	0.01	0.12
Total	2.3	0.8	1.3

Table 12.7: Systematic uncertainties for the $D(2550)$ parameters obtained from the fit with helicity selection $|\cos\theta_H| > 0.75$.

	$D(2550)$ **Yield** ($\times 10^3$)	$D(2550)$ **M** (MeV)	$D(2550)$ Γ (MeV)
Mass Range	0.50	0.03	0.31
Bin Width	1.39	1.46	0.17
Breit-Wigner Shape	3.10	3.39	5.30
Background Model	4.09	0.10	1.15
D(2460) Mean	0.38	0.31	1.05
D(2460) Width	0.39	0.35	0.73
D(2600) Mean	7.11	5.63	11.20
D(2600) Width	1.56	0.40	2.91
B field & SVT material	0.00	0.77	0.00
D(2430)	1.43	0.59	2.31
Total	9.2	6.8	13

Table 12.8: Systematic variations on the $D^*(2600)$ yield obtained from the fit with the selection $|\cos\theta_H| < 0.5$.

	$D^*(2600)$ **Yield** ($\times 10^3$)
Mass Range	0.68
Bin Width	0.71
Breit-Wigner Shape	0.21
Background Model	1.38
D(2420) Mean	0.79
D(2420) Width	1.22
D(2460) Mean	0.85
D(2460) Width	0.59
D(2550) Mean	1.37
D(2550) Width	0.66
D(2600) Mean	2.65
D(2600) Width	2.63
D(2750) Mean	3.35
D(2750) Width	0.07
D(2430)	2.12
Total	6.7

Table 12.9: Systematic variations on the fit parameters obtained from the final fit to entire $D^{*+}\pi^-$ sample. The Yields are in thousands.

	$D_1(2420)$ **Yield**	$D_2^*(2460)$ **Yield**	$D(2550)$ **Yield**	$D^*(2600)$ **Yield**	$D(2750)$ **Yield**	$D(2750)$ **M** (MeV)	$D(2750)$ Γ (MeV)
Mass Range	0.15	0.52	2.64	0.15	0.37	0.25	1.13
Bin Width	1.87	0.25	3.41	0.60	0.94	0.17	1.74
BW Shape	0.37	0.51	6.66	0.02	0.48	0.40	0.76
Bkg. Model	5.47	12.42	31.36	2.86	4.33	1.56	8.53
D(2420) Mean	0.10	2.81	3.49	0.86	1.23	0.44	3.03
D(2420) Width	2.40	1.22	0.67	0.03	0.03	0.11	0.38
D(2460) Mean	1.01	0.19	0.25	0.57	0.18	0.02	0.01
D(2460) Width	0.41	0.67	3.12	0.05	0.29	0.23	0.95
D(2550) Mean	0.38	1.46	3.17	3.51	0.56	0.10	0.56
D(2550) Width	0.09	0.57	9.87	2.25	0.23	0.22	0.64
D(2600) Mean	0.92	1.19	16.62	0.14	1.24	0.97	1.55
D(2600) Width	0.07	0.44	1.35	5.14	1.85	1.60	4.80
B field & SVT	0.00	0.00	0.00	0.00	0.00	0.77	0.00
D(2430)	0.63	1.18	3.28	0.29	0.05	0.23	0.04
Total	6.4	13	38	7.3	5.2	2.7	11

12.4.5 Helicity Distributions

As discussed in the introduction, the $D^{*+}\pi^-$ final state can distinguish between different spin-parity quantum numbers of the excited states. The distributions of the signal yield as a function of $\cos\theta_H$ for the different expected states are predicted in Table 8.2.

In the data the helicity distributions are extracted by dividing the data into 10 subsamples corresponding to $\cos\theta_H$ intervals of size 0.2 between -1 and $+1$. For each subsample, a fit is performed as described in Section 12.4.3, while also fixing the $D(2750)$ signal parameters to those obtained in that fit. All signal shape parameters are fixed to the values previously determined, only the yields are allowed to vary. The fit results are shown in Figure 12.33. The yields obtained for each signal component are shown in Figures 12.34 to 12.38. For the $D_1(2420)$ we obtain a distribution which can be fitted with a function proportional to $Y = 1 + A\cos^2\theta_H$ and for the $D_2^*(2460)$ the distribution is well described by a function proportional to $\sin^2\theta_H$. Both of these results are as expected and give confidence that the results obtained for the new resonances are reliable. In these fits to the helicity distributions a correction has been applied to the function Y for a small dependence of the efficiency on $\cos\theta_H$ shown in Fig. 12.19. The fit is performed on the binned histogram shown where the errors on each point include both the statistical and systematic error. The χ^2 of these fits is evaluated using the integral of the fit function over the range of the bin in order to account for the coarse bin size. The systematic error is determined for each point as described in systematics of the "Final fit" with two additional systematics corresponding to the fixed $D(2750)$ shape parameters.

The $\cos\theta_H$ distribution for the new signal $D(2550)$ is well described by a function proportional to $\cos^2\theta_H$, which is expected for the predicted state $D_0^1(2S)$ the radial excitation of the D^0 meson. The helicity distribution for the new signal $D^*(2600)$ is described by a function proportional to $\sin^2\theta_H$, which is as expected for the predicted state $D_1^3(2S)$ the radial excitation of the D^{*0} meson. For the $D(2750)$ signal the $\cos\theta_H$ distribution is not a simple $\sin^2\theta_H$ or $\cos^2\theta_H$ and is therefore not conclusive. At the mass value obtained for this signal there are 4 states predicted, corresponding to the L=2 angular excitations shown in Table 8.2, this would imply that this signal may be composed of contributions from multiple states with different qunatum numbers and hence the helicity distribution would be not be simple.

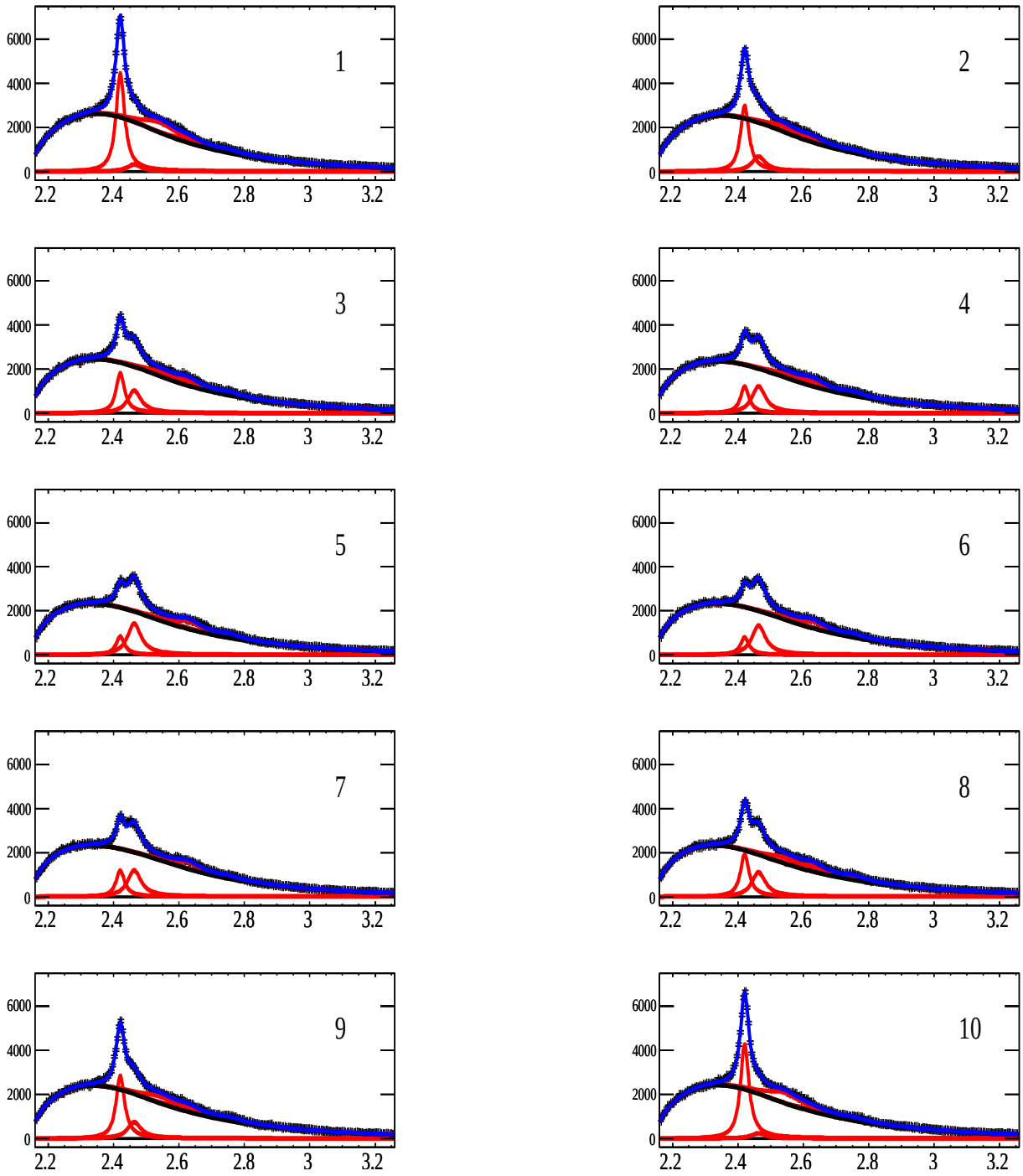

Figure 12.33: Fits to the M($D^{*+}\pi^-$) distributions for the sub-samples corresponding to 10 intervals in $\cos\theta_H$.

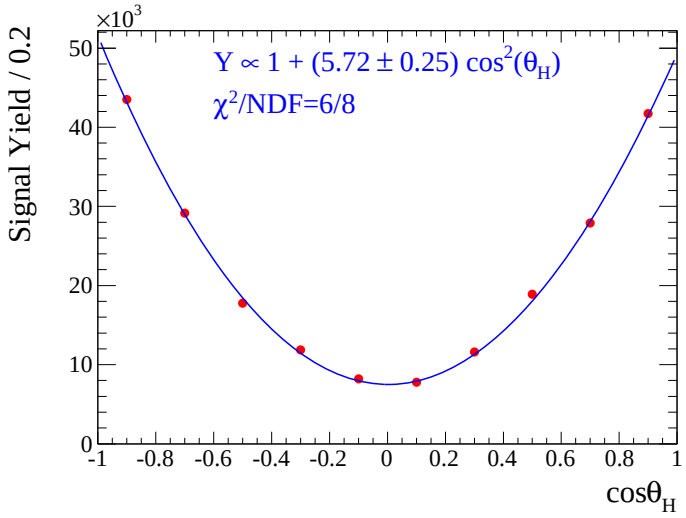

Figure 12.34: Yield as a function of $\cos\theta_H$ for the $D_1(2420)$.

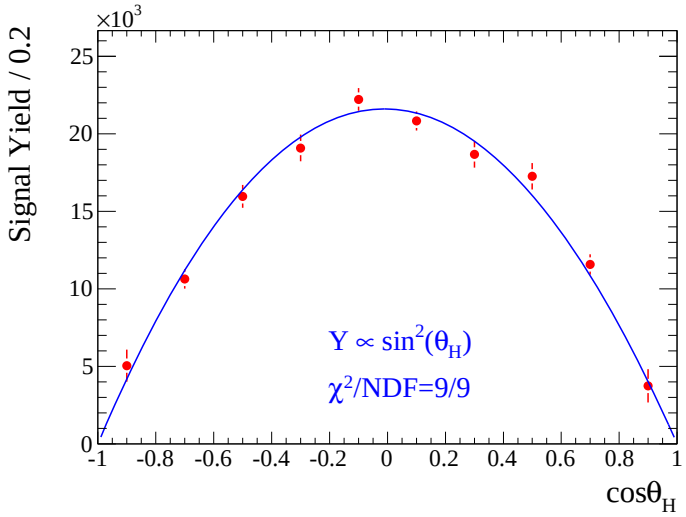

Figure 12.35: Yield as a function of $\cos\theta_H$ for the $D_2^*(2460)$.

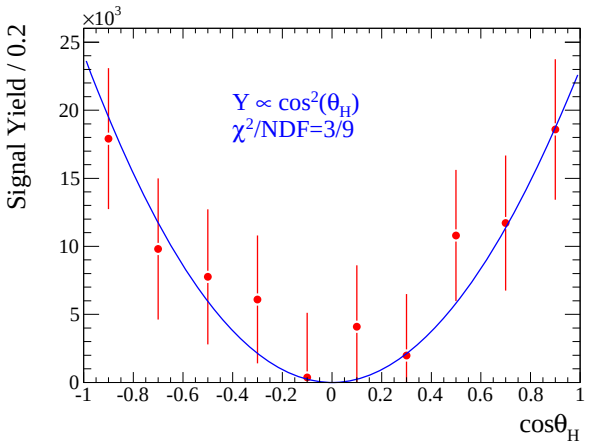

Figure 12.36: Yield as a function of $\cos\theta_H$ for the $D(2550)$.

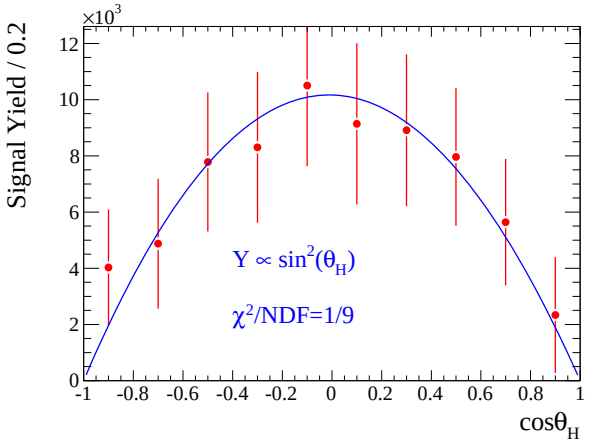

Figure 12.37: Yield as a function of $\cos\theta_H$ for the $D^*(2600)$.

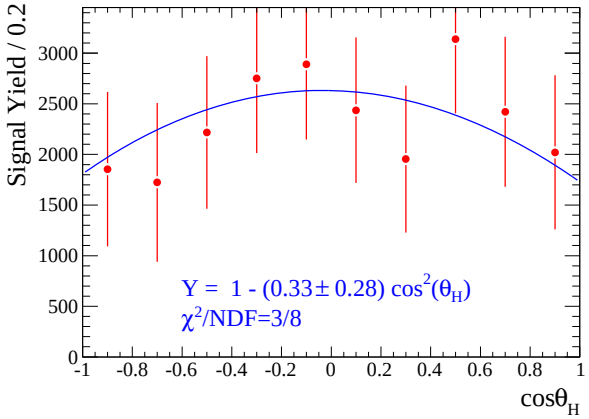

Figure 12.38: Yield as a function of $\cos\theta_H$ for the $D(2750)$.

Chapter 13

Branching Fraction Ratios

Resonances with natural spin-parity decay to both the $D^+\pi^-$ and $D^{*+}\pi^-$ final states. This allows a determination of the ratio of branching fractions

$$\frac{\mathcal{B}(D^{**} \to D^+\pi^-)}{\mathcal{B}(D^{**} \to D^{*+}\pi^-)},$$

where D^{**} denotes any one of these resonances. The individual branching fractions cannot be measured since the absolute number of produced signal events is not known, however this number cancels in the computation of the ratio. This ratio has been calculated for the $D_2^*(2460)$ and $D^*(2600)$ resonances observed in this analysis. The value obtained for the $D^*(2600)$ may be used in future theoretical calculations to help identify this state with a predicted state. Finally, the same calculation is also performed for the $D^*(2760)/D(2750)$ signals under the assumption that these originate from the same state(s). The agreement or disagreement of the value obtained may be used in future theoretical calculations to elucidate the nature of this signal.

The calculation of the branching fraction ratio is performed using the signal yields obtained from the total $D^+\pi^-$ and $D^{*+}\pi^-$ samples, and the absolute reconstruction efficiencies for each final state:

$$\frac{\mathcal{B}(D^{**} \to D^+\pi^-)}{\mathcal{B}(D^{**} \to D^{*+}\pi^-)} = \frac{N_{D\pi}^{D^{**}}}{\varepsilon_{D\pi}^{D^{**}}} \frac{\varepsilon_{D^*\pi}^{D^{**}}}{N_{D^*\pi}^{D^{**}}} \tag{13.1}$$

The absolute efficiencies must account for the reconstruction efficiency of the channel used as well as the branching fraction of the particular D or D^* decay channel. In the $D^+\pi^-$

analysis we use the channel $D^+ \to K^-\pi^+\pi^+$, therefore the efficiency is computed as:

$$\varepsilon_{D\pi}^{D^{**}} = \mathcal{B}(D^+ \to K^-\pi^+\pi^+)\varepsilon_{K\pi\pi}^{MC} \tag{13.2}$$

where $\mathcal{B}(D^+ \to K^-\pi^+\pi^+)$ is obtained from Ref [17] and $\varepsilon_{K\pi\pi}^{MC}$ was determined using the $D^+\pi^-$ signal MC sample. The $D^{*+}\pi^-$ efficiency, $\varepsilon_{D^*\pi}^{D^{**}}$, is more complicated because in this case the decay chain has an additional level, $D^{**} \to D^{*+} \to D^0$, and the D^0 is reconstructed in two channels. The formula for this efficiency is:

$$\varepsilon_{D^*\pi}^{D^{**}} = \mathcal{B}(D^{*+} \to D^0\pi^+)\left[\mathcal{B}(D^0 \to K^-\pi^+)\varepsilon_{K\pi}^{MC} + \mathcal{B}(D^0 \to K^-\pi^+\pi^-\pi^+)\varepsilon_{K\pi\pi\pi}^{MC}\right], \tag{13.3}$$

where $\varepsilon_{K\pi}^{MC}$ and $\varepsilon_{K\pi\pi\pi}^{MC}$ are determined using their dedicated signal MC samples in the $D^{*+}\pi^-$ analysis. The efficiencies $\varepsilon_{K\pi\pi}^{MC}$, $\varepsilon_{K\pi}^{MC}$, and $\varepsilon_{K\pi\pi\pi}^{MC}$ were found to have a small linear dependence on the mass of the $D^+\pi^-$ or $D^{*+}\pi^-$ system and are therefore evaluated at the mass value for the resonance. The values obtained for the efficiencies are the following:

$$\varepsilon_{D\pi}^{D_2^*(2460)} = (\ 1.294 \pm 0.031\ )\%, \tag{13.4}$$
$$\varepsilon_{D^*\pi}^{D_2^*(2460)} = (\ 1.115 \pm 0.035\ )\%, \tag{13.5}$$
$$\varepsilon_{D\pi}^{D^*(2600)} = (\ 1.353 \pm 0.054\ )\%, \tag{13.6}$$
$$\varepsilon_{D^*\pi}^{D^*(2600)} = (\ 1.175 \pm 0.048\ )\%, \tag{13.7}$$
$$\varepsilon_{D\pi}^{D^*(2760)} = (\ 1.408 \pm 0.085\ )\%, \tag{13.8}$$
$$\varepsilon_{D^*\pi}^{D(2750)} = (\ 1.232 \pm 0.065\ )\%, \tag{13.9}$$

where errors are due to the limited size of the signal MC samples as well as to the errors on the D^+, D^0, and D^{*+} branching fractions. The results for the branching fraction ratios are the following:

$$\frac{\mathcal{B}(D_2^*(2460)^0 \to D^+\pi^-)}{\mathcal{B}(D_2^*(2460)^0 \to D^{*+}\pi^-)} = 1.47 \pm 0.03 \pm 0.16, \tag{13.10}$$
$$\frac{\mathcal{B}(D^*(2600)^0 \to D^+\pi^-)}{\mathcal{B}(D^*(2600)^0 \to D^{*+}\pi^-)} = 0.32 \pm 0.02 \pm 0.09, \tag{13.11}$$
$$\frac{\mathcal{B}(D^*(2760)^0 \to D^+\pi^-)}{\mathcal{B}(D(2750)^0 \to D^{*+}\pi^-)} = 0.42 \pm 0.05 \pm 0.11, \tag{13.12}$$

where the first error is statistical and the second is systematic. The statistical errors are due to the statistical errors on the signal yields. The systematic errors are due to

systematic errors on the signal yields, the limited size of the signal MC samples, errors on the D^+, D^0, and D^{*+} branching fractions and to systematic errors on the efficiency ratio due to tracking and PID efficiency differences between MC and Data. Systematics due to the m(D^+/D^0), Δm, p^* and $\cos(\theta_\pi)$ selections have been estimated to be insignificant. The systematic uncertainties are dominated by the uncertainty on the signal yields.

Chapter 14

Conclusions

For this part of this thesis, a study of the inclusive production of the reactions

$$e^+e^- \to D^+\pi^- X, \quad e^+e^- \to D^0\pi^+ X, \quad \text{and} \quad e^+e^- \to D^{*+}\pi^- X$$

has been presented. In addition to the known resonances, $D_1(2420)^0$ and $D_2^*(2460)^0$, four new signals denoted by $D(2550)^0$, $D^*(2600)^0$, $D(2750)^0$, and $D^*(2760)^0$ have been observed for the first time. The analysis of the angular distribution in the $D^{*+}\pi^-$ final state provides additional information about the spin-parity quantum numbers of the resonances. For the signal $D(2550)^0$ observed in $D^{*+}\pi^-$, the mass and helicity distribution are consistent with the theoretical prediction for the first radial excitation of the D^0. Also, the signal $D^*(2600)^0$ observed both in $D^+\pi^-$ and $D^{*+}\pi^-$ has mass and helicity distribution consistent with the theoretical prediction for the first radial excitation of the D^{*0}. Together, the mass and helicity agreements provide strong evidence that these enhancements are due to these radially excited states. The $D^*(2760)^0$, in $D^+\pi^-$, is very close to the signal $D(2750)^0$ observed in $D^{*+}\pi^-$, however the mass values are different by about 2.8σ; the helicity distribution of the $D(2750)^0$ indicates that this enhancement may not be due to a single resonance. The theoretical predictions for the four L=2 excited states lie very close in mass to the mass observed for this signal. It is expected that all four decay to $D^{*+}\pi^-$ while only two decay to $D^+\pi^-$, this fact may explain the observed features. Also, the isospin partners $D^*(2600)^+$ and $D^*(2760)^+$ are observed in $D^0\pi^+$ and have mass values consistent with the signals observed in $D^+\pi^-$. This provides strong evidence that the signals are genuine, since they are observed under different background conditions. Table 14.1 summarizes the observed signal parameters. The significance shown in this table for each new resonance is estimated by dividing the signal yield by its total error, taking into account both the statistical and systematic uncertainties. Finally, for the

signals with natural parity, the ratio of the branching fractions for their decays to $D^+\pi^-$ and $D^{*+}\pi^-$ have been determined.

The results obtained in this study make a large step in our understanding of the excited D meson spectrum. Previously only candidates to the ground states and L=1 excited states existed. This study extends our knowledge to the higher L=2 and radially excited states. The observed mass values are in qualitative agreement with QCD predictions, however, these predictions are over 20 years old. Updated calculations are necessary and may reveal even better agreement with experiment. From the experimental side, the high luminosity B-factories expected to turn on in the near future should provide much more information on charm spectroscopy, and hence provide even more detailed challenges toe the QCD predictions.

Table 14.1: Summary of the signal parameter values obtained from the fits to the $D^+\pi^-$, $D^0\pi^+$, and $D^{*+}\pi^-$ final states. The first error is statistical and the second is systematic. "(fixed)" indicates that the value have been fixed to the values determined in $D^+\pi^-$ or the $D^{*+}\pi^-$ fit with selection $|\cos\theta_H| > 0.75$. "θ_H^1" indicates the fit with the selection $|\cos\theta_H| > 0.75$ and "θ_H^2" indicates the fit with the selection $|\cos\theta_H| < 0.5$.

Signal	**Channel**	**Yield (x10^3)**	**Mass (MeV/c^2)**	**Width (MeV)**	**Significance**
$D_0^*(2400)^0$	$D^+\pi^-$	143.2±4.7±23.8	2338.0	195.0	5.9σ
$D_1(2420)^0$	$D^{*+}\pi^-$ (θ_H^1)	102.8±1.3±2.3	2420.1±0.1±0.8	31.4±0.5±1.3	
	$D^{*+}\pi^-$	214.6±1.2±6.4	2420.1(fixed)	31.4(fixed)	
$D_2^*(2460)^0$	$D^+\pi^-$	242.8±1.8±3.4	2462.2±0.1±0.8	50.5±0.6±0.7	
	$D^{*+}\pi^-$	136±2±13	2462.2(fixed)	50.5(fixed)	
$D(2550)^0$	$D^{*+}\pi^-$ (θ_H^1)	34.3±6.7±9.2	2539.4±4.5±6.8	130±12±13	3.0σ
	$D^{*+}\pi^-$	98.4±8.2±38	2539.4(fixed)	130(fixed)	
$D^*(2600)^0$	$D^+\pi^-$	26.0±1.4± 6.6	2608.7±2.4±2.5	93±6±13	3.9σ
	$D^{*+}\pi^-$ (θ_H^2)	50.2±3.0±6.7	2608.7(fixed)	93(fixed)	7.3σ
	$D^{*+}\pi^-$	71.4±1.7±7.3	2608.7(fixed)	93(fixed)	
$D(2750)^0$	$D^{*+}\pi^-$	23.5±2.1±5.2	2752.4±1.7±2.7	71±6±11	4.2σ
$D^*(2760)^0$	$D^+\pi^-$	11.3±0.8±1.0	2763.3±2.3±2.3	60.9±5.1±3.6	8.9σ
$D_0^*(2400)^+$	$D^0\pi^+$	151.6±1.2±48.3	2338	202	3.1σ
$D_2^*(2460)^+$	$D^0\pi^+$	110.8±1.3±7.5	2465.4±0.2±1.1	50.5(fixed)	
$D^*(2600)^+$	$D^0\pi^+$	13.0±1.3±4.5	2621.3±3.7±4.2	93(fixed)	2.8σ
$D^*(2760)^+$	$D^0\pi^+$	5.7±0.7±1.5	2769.7±3.8±1.5	60.9(fixed)	3.5σ

Part III

R&D for a Next Generation DIRC

Chapter 15

Introduction

15.1 Motivation

Given the success of the DIRC detector in *BABAR* and the imminence of an upgraded B-factory experiment (Super-B) it is important to study the possibility of an upgraded DIRC detector (Focusing-DIRC). After more than a decade since the design of the DIRC, new pixel photon detectors (shown in Figure 15.1) have emerged which can substantially improve the performance of the current DIRC due to their small size and fast response.

The potential improvements to the current DIRC are several:

- an expansion region about 25 times smaller making the Focusing-DIRC more compact,
- lower photon backgrounds due to the smaller expansion region,
- a possible correction for the bar thickness aberrations on the θ_C resolution through the use of a focusing mirror,
- a resolution on the photon time-of-propagation (TOP) about 10 times better allowing for a background reduction of about the same factor,
- a chromatic correction (described below) on the θ_C resolution using the precise measurement of the TOP.

The above background reductions come about because most of the photon backgrounds in the current DIRC are due to stray particles (off-beam particles or neutrons captured by the water) ionizing the water in the expansion region and are proportional to the size of the expansion region. These backgrounds are random in the TOP measurement and can,

therefore, be discriminated from the true signals by measuring the difference between the measured and expected TOP. A hypothetical design for a section of the Focusing-DIRC is shown in the Figure 15.2.

In this chapter we study the performance of a prototype of the Focusing-DIRC in beam tests done in the years 2005 and 2006 at SLAC.

15.2 Chromatic Properties

A Focusing-DIRC equipped with photon detectors able to measure the TOP of the Cherenkov photons represents a break-through in the field of Cherenkov detectors. The measurement of the TOP can be converted into a measurement of the group velocity (v_g) of the photons simply through the relation v_g=L/TOP. The information contained by the v_g of the photons is equivalent to knowing the wavelength of the photons because the index of refraction of the material through which the photons travel is known as a function of the wavelength and v_g=c/n_g, however, for the purposes of this study it is not necessary to explicitly determine the wavelength. Until now no other detector is capable of measuring both the angle θ and the wavelength of the photons simultaneously.

According to the theory of Cherenkov radiation for the geometry of the DIRC [43] the distribution of the emitted photons is given by the following p.d.f.,

$$S(\theta,\omega) \propto \frac{n\ sin^2\theta\ sin^2(\omega t_0(1-\beta\ n\ cos\theta))}{(1-\beta\ n\ cos\theta)^2} \tag{15.1}$$

where ω is the frequency of the photons, n is the frequency dependent index of refraction, β is the speed of the particle traversing the bar (in units of c) and t_0 is the time the charged particle spends in the bar. In this experiment we consider values of β close to 1, very short t_0 values ($\sim 6\times10^{-11}$ s) and n$\sim$1.4. The frequency range of the observed photons is determined by the efficiency of the detector ϵ and is about $\omega \sim 4\times10^{15} rads^{-1}$. The resolution θ is about 5 mrad and, therefore, the argument of the sin^2 term varies by about 400 π. This large variation results in a fast oscillation which effectively averages to a constant; for the purposes of this analysis this term will be neglected. After rewriting the above formula in terms of the group velocity $v_g = c/n_g$ where $n_g = n - \lambda(dn/d\lambda)$ is a one-to-one map between n and n_g we obtain the following formula for the observed intensity,

$$\mathbf{S}(\theta,v_g) \propto \frac{\epsilon(v_g)\ n(v_g)\ sin^2\theta}{(1-\beta\ n(v_g)\ cos\theta)^2} \tag{15.2}$$

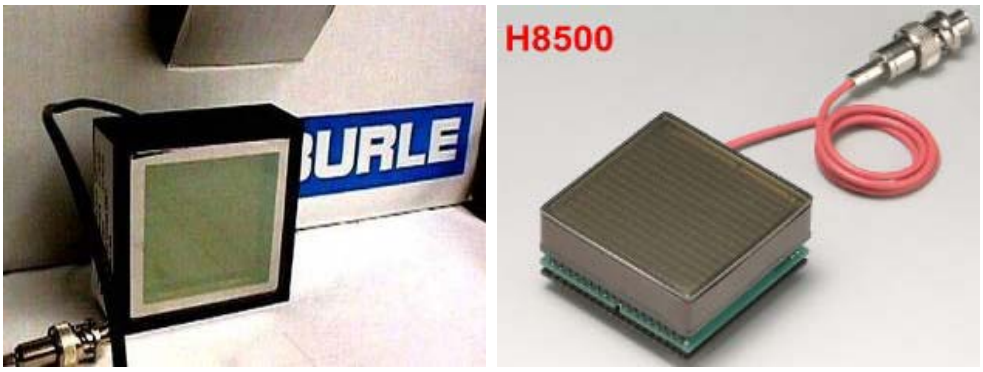

Figure 15.1: Left: 8x8 pixel detector produced by the BURLE company (MCP-PMT 85011-501). Right: 8x8 pixel detector produced by the Hamamatsu company (MaPMT H-8500). Both detectors have pixels which are 6 mm x 6 mm. The edges of the Hamamatsu detector are thinner allowing less dead space between stacked detectors.

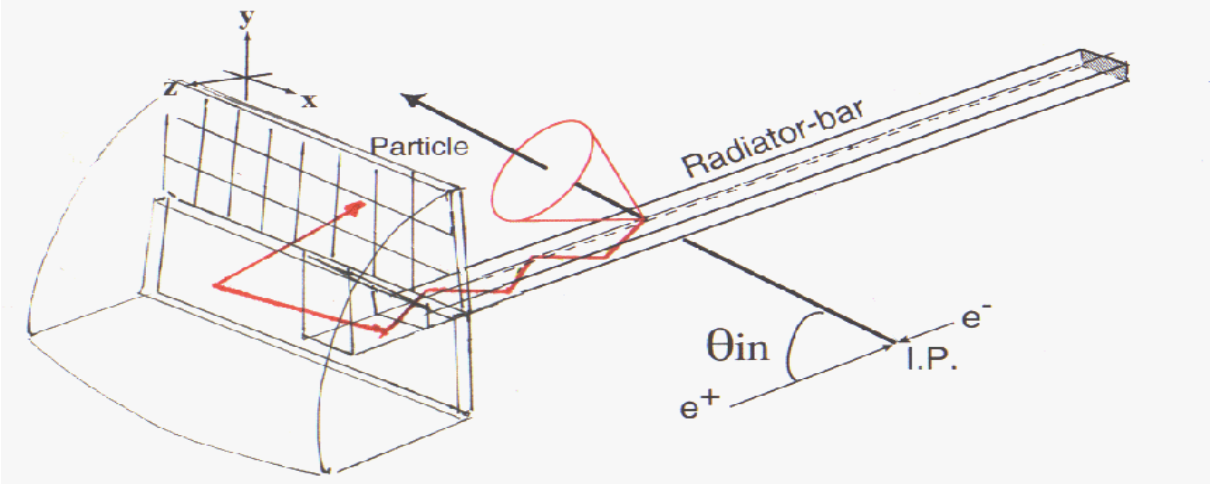

Figure 15.2: Conceptual design of a section of a Focusing-DIRC. The curved mirror allows the focusing and bending of the Cherenkov light on the detector plane, thereby reducing the SOB size. Ideally the SOB will be made out of fused silica just like the radiator bar to reduce imperfections in the material traveled by the photons.

where the wavelength dependent efficiency has also been inserted. Note that the distribution is dominated by the denominator term and the observed photons follow the well known relation $cos\theta = 1/(n\beta)$.

To understand the chromatic correction it is useful to consider two particles of different masses, a π^+ and a K^+ for example, with the same momentum (5 GeV) traversing a radiator bar as shown in Figure 15.3. Each particle gives a 2-dimensional distribution of photons as shown in Figure 15.4(left). In a traditional Ring Imaging CHerenkov (RICH) detector one only measures the angle θ equivalent to the projection of the 2-dimensional distribution onto the θ axis Figure 15.4(middle). With a Focusing-DIRC one measures both the angle θ and v_g, one can then perform a "chromatic correction" by rotating the distribution and then projecting it onto the θ axis. The separation between the π^+ and the K^+ distributions after the correction is much better as shown in Figure 15.4(right). In this example we have assumed an ideal resolution on θ and v_g of only about 1%. In practice, however, the resolution on θ and v_g are significantly larger and the separation of pions and kaons is not as good.

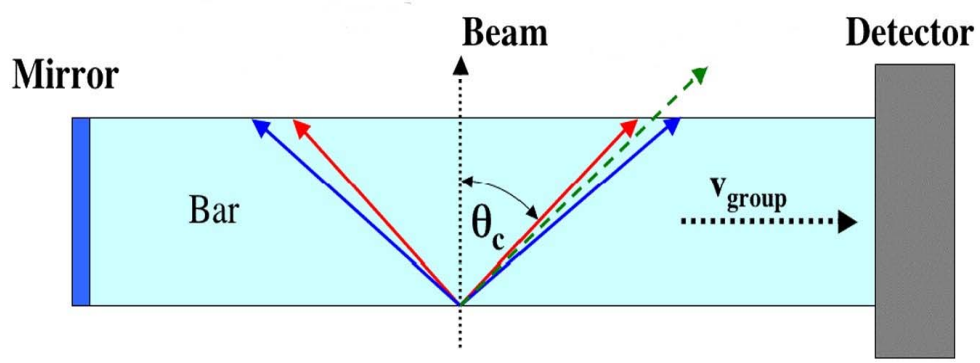

Figure 15.3: Illustration of the production of Cherenkov radiation in the bar by a particle track. Photons with longer wavelengths are produced at smaller opening angles. The photons emitted to the left undergo a reflection on the end mirror. The photon camera box with the detectors is shown as a simple block here.

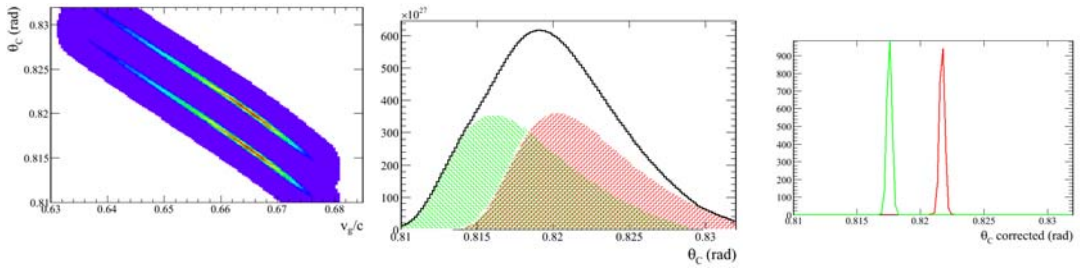

Figure 15.4: Left: Distribution of Cherenkov radiation on the θ vs. v_g plane for a pion and a Kaon of 5 GeV momentum. Middle: projection of the 2-dimensional distribution onto the θ axis. Right: projection of the 2-dimensional distribution onto the θ axis after rotating the distribution according the correlation.

Chapter 16

Development of the Focusing DIRC

16.1 Photon Detectors

Three types of pixel PMT detectors have been studied in the Focusing-DIRC prototype, a MCP-PMT 85011-501 produced by the BURLE company and two by the Hamamatsu company: MaPMT H-8500 and MaPMT H-9500.

The size of each pixel in the detector produced by the BURLE company is 6x6 mm and the pixels are arranged in an 8x8 array. The detector consists of a film coated front glass (Bialkali photocathode) which emmits a photoelectron when a Cherenkov photon strikes the surface. The electron is then accelerated with an electric field through two multi-channel-plate (MCP) containing an array of 25 micron holes. As the electrons pass through the holes they create secondary electrons and an avalanche is formed. After the MCP is an 8x8 array of anodes which collect the charge.

The detectors from the Hamamatsu company are similar to the BURLE detector except that the MCP is replaced by a sequence of 12 fine dynodes. The MaPMT H-8500 consists of pixels which are 6x6 mm while the MaPMT H-9500 consists of fine 3x3 mm pixels. However, for this experiment the 3x3 mm pixels have been shorted in segments of 4 in the x direction; the effective size of the pixels is 12x3 mm retaining the fine size along the θ direction.

Studies of the efficiency and timing resolution have been performed previously [45] using a fast PiLas laser [46] which has a trigger response resolution of only about 15 picoseconds. Scans of the detection uniformity of each detector are shown in Figure 16.1 and timing resolutions are shown in Figure 16.2. The timing resolutions are on the order of 100 ps and represent an improvement of more than 10 times compared to the 1.7 ns

resolution of the PMT's used in the *BABAR* DIRC. The precise time resolution derives from the much more compact region between photocathode and anode which is only a few millimeters while the *BABAR* PMT's are a few centimeters in size.

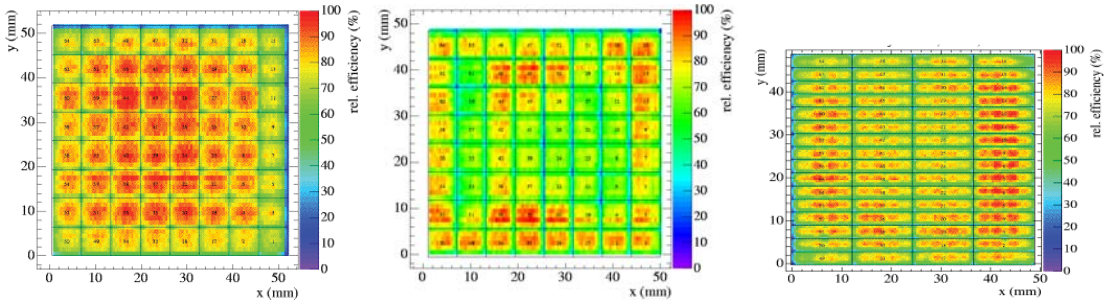

Figure 16.1: Scans of the detection uniformity across the face of the detectors for the MCP-PMT 85011-501(left), MaPMT H-8500(middle), and MaPMT H-9500(right) performed in Ref. [45]. The z axis shows the efficiency relative to the highest point.

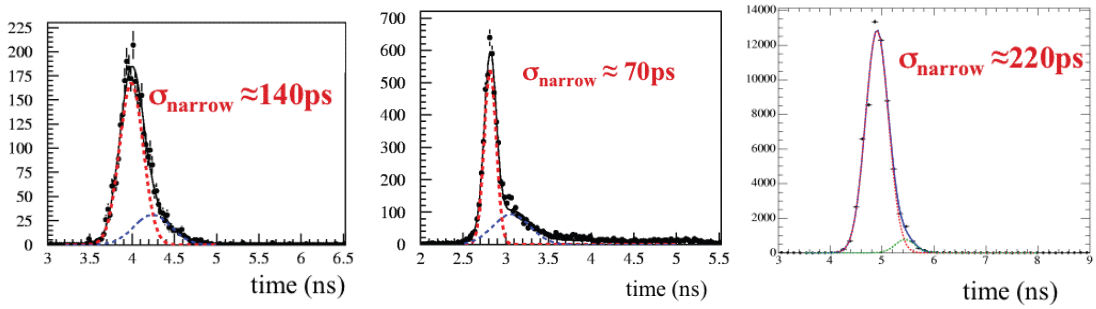

Figure 16.2: Timing resolution of the MCP-PMT 85011-501(left), MaPMT H-8500(middle), and MaPMT H-9500(right) obtained in Ref. [45]. The test was done by shining the PiLas laser on the center of a pixel. The resolution on pixel edges is somewhat worse due to charge sharing between pixels.

16.2 Prototype

A prototype of the Focusing-DIRC has been designed and built by J. Va'Vra *et al.*at SLAC [44]. The prototype was built using 3 Fused Silica bars (1.2 m long), of the same quality as the bars used in *BABAR*, glued together to make a full size segment (3.6 m long) as in the *BABAR* DIRC. At one end is a mirror which reflects the photons to be collected at the other end in a photon camera box (PCB). A schematic of the PCB is shown in Figure 16.4. It consists of a Fused Silica block which joins the PCB to the radiator bar. A section of a spherical mirror is used to focus the photons onto a detector plane at the

top. The PCB casing is made from aluminum and is filled with mineral oil with an index of refraction close to that of fused silica [44].

The detectors are placed on a focal plane as shown in Figure 16.5 [44]. Five MCP-PMT 85011-501 , one MaPMT H-8500 , and one MaPMT H-9500 photon detectors have been arranged in a ring pattern covering the expected Cherenkov ring. Only the channels around the expected ring are instrumented to minimize the costs. The readout electronics are described elsewhere and consist of SLAC-made amplifiers providing a voltage gain factor of 130 [44]. The signal is digitized using a constant-fraction-discriminator (CFD) and converted to a raw time measurement count using a Philips TDC7186. The overall timing resolution of the electronics is about 35 ps [44].

The efficiency for detection of the Cherenkov photons with the prototype ranges between 300 and 600 nm and peaks at a wavelength of about 410 nm (Figure 16.3) [44]. The lower end is restricted by the (EPOTEK) glue joining the bars, the mineral oil transmission, as well as the quantum efficiency of the PMT's. The high end of the spectrum is restricted by the PMT efficiency.

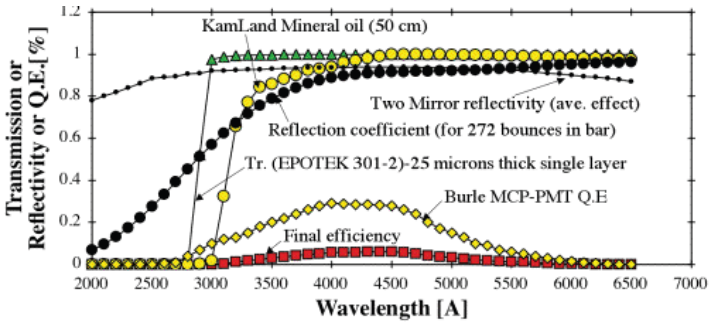

Figure 16.3: The curves show the different components of the prototype photon efficiency as a function of wavelength [44]. The overall efficiency is shown by the bottom curve.

16.3 Prototype Calibration

Calibration of the prototype is performed using the PiLas laser [46] (operating at a wavelength of 430 nm) by inserting light pulses into the photon camera box (PCB) as shown the schematic. The light pulses are randomized onto the detector plane when they strike the etched aluminum surface of the PCB. Both the laser and the TDC's are triggered simultaneously and this provides the start time for the calibration. Two calibrations are performed, one to study the factor used to convert the raw TDC count of each channel

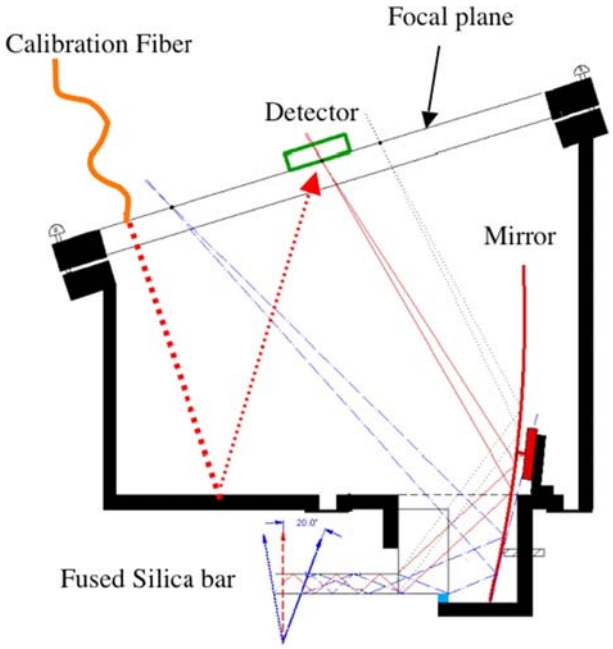

Figure 16.4: Schematic of the Focusing-DIRC prototype PCB. The region PCB region is enclosed in an aluminum case and filled with mineral oil. The spherical mirror has a radius of 97.211 cm. The orange curve shows how the PiLas laser was used to insert calibration pulses. The dashed line crossing the bar shows the possible particle track, the photons emitted straight down the bar are focused onto the detector plane.

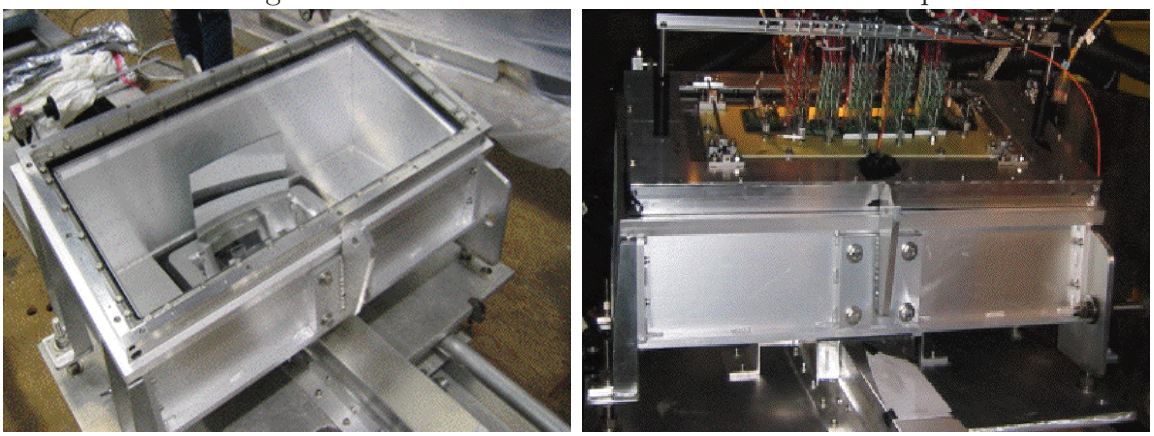

Figure 16.5: Left: Picture of the actual prototype before placing the detectors on the detection plane. Right) Picture after installing the detectors and their readout adapters.

into a time measurement, the second calibration is done to align all the channels in time.

The conversion factor calibration is performed by inserting delays of precisely known steps (∼7 ns) into the trigger line of the PiLas laser. In this way one moves the position of the observed signal on the raw TDC count as shown in Figure 16.6(left). We determine the difference in TDC counts between each step and divide the known time delay by this difference to determine the conversion factor. This factor is determined as a function of the TDC count as shown in Figure 16.6(right) to verify the linearity of the TDC. The data sheet for the TDC's quotes a conversion factor of 25ps/count; in this calibration we find a small non-linearity about the expected value. A similar study is performed for all channels in the prototype.

The alignment calibration is performed simply by illuminating the detectors and determining the time delay of the detected signal for each channel. The delay should be the same for all channels since the difference in paths of the photons hitting different channels results in negligible time differences. Figure 16.8 shows the peak positions for the observed laser signals for one MCP detector (32 channels instrumented in Slot#4). Large variations are observed resulting from different cable lengths in the readout electronics. The time offset for each channel is determined by fitting the signal distribution as shown in Figure 16.8. The offset values for all channels are shown in Figure16.9. This channel-by-channel calibration is crucial for the TOP measurement of the Cherenkov photons in the beam test below.

16.4 Beam Test

The performance of the Focusing-DIRC prototype has been tested using Cherenkov radiation produced by electron tracks traversing the radiator bar in a beam-test setup at the SLAC Endstation A facility in the years 2005 and 2006.

The electrons are secondary particles produced by colliding the main SLAC Linac electron beam onto a fixed target. The products of the collision are collimated and transported to the Endstation A hall, Figure 16.10 shows the end of the beam line and the prototype assembly. At the Endstation the beam consists mainly of electrons of approximately 10 GeV energy, the energy and particle type is selected upstream using a magnetic field and collimator setup. The prototype is mounted and aligned on a support structure such that the electrons enter the bar at a 90^o angle and the distance of the track from the PCB can be modified to seven equally spaced positions by sliding the support

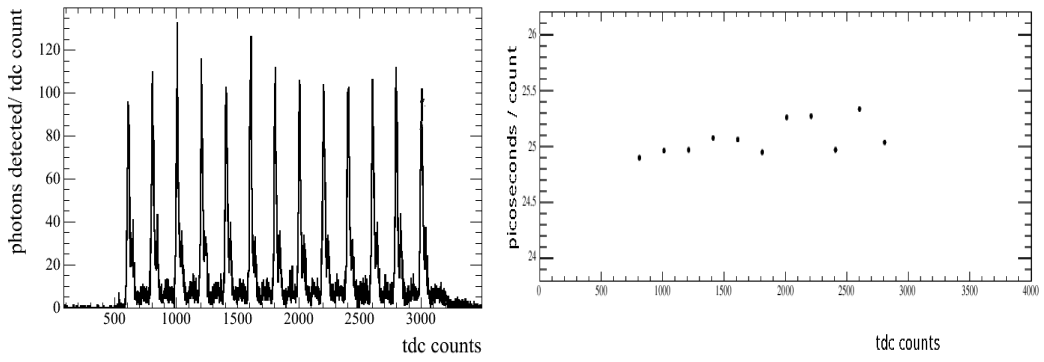

Figure 16.6: Left: Distributions of the laser signals on one detector pixel with different trigger delays relative to the readout electronics. Right) Conversion factor (for the same pixel in the left plot) between the raw TDC count to actual time determined as a function of the TDC counts using the known time differences of the laser trigger delay steps.

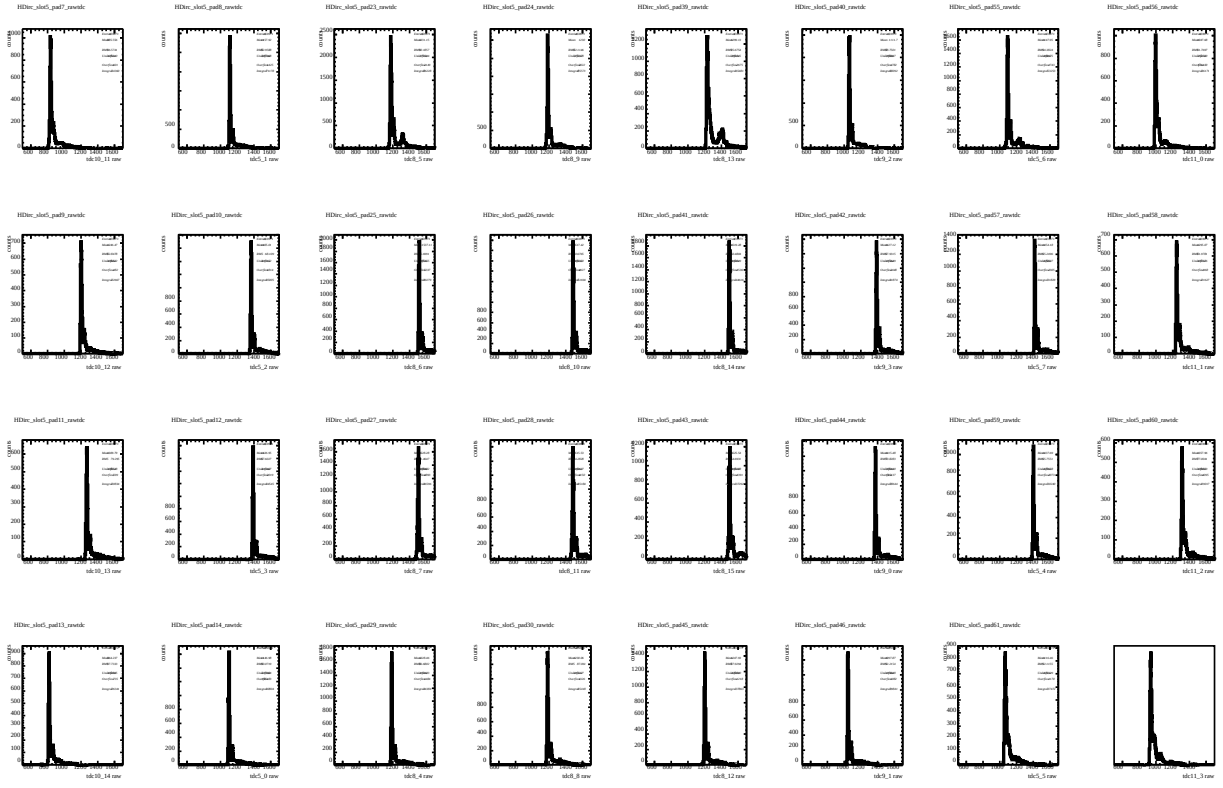

Figure 16.7: Distribution of laser calibration signals for all instrumented pixels in slot#4 of the detector plane. The peak positions are at different places on the TDC count range due to different cable lengths in the readout electronics.

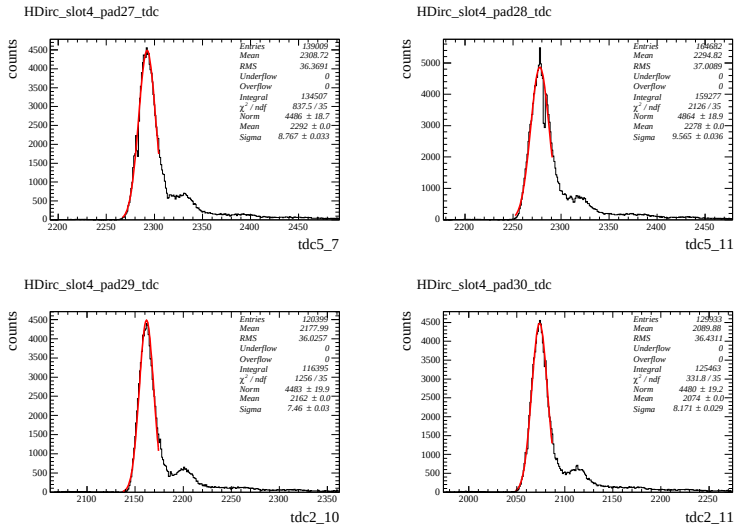

Figure 16.8: Distributions of the laser calibration signals for 4 pixels of the detector in slot#4. The distributions are fitted using a single Gaussian whose mean value determines the time alignment of the pixel relative an arbitrary reference pixel.

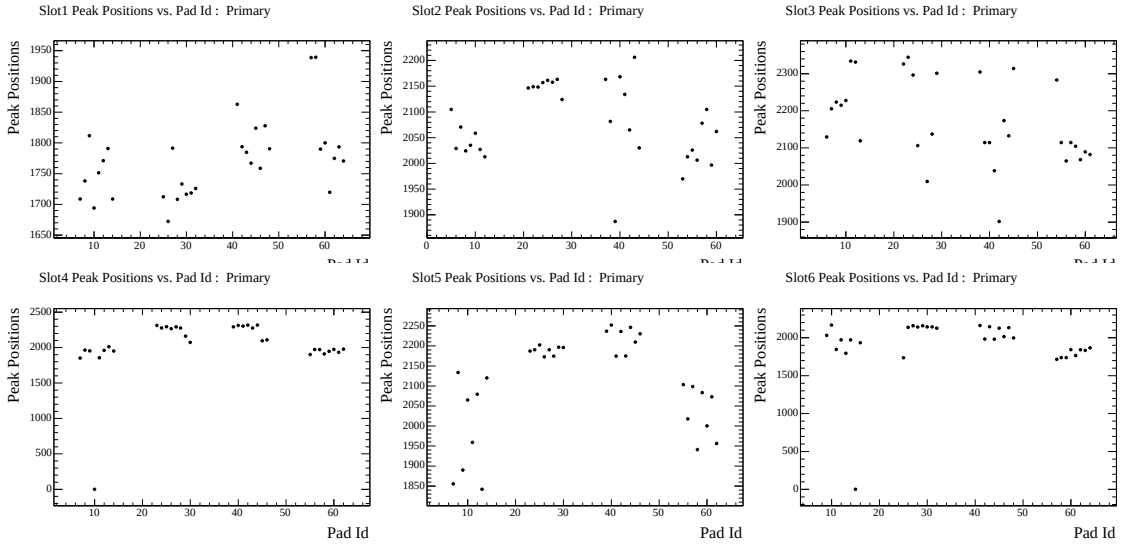

Figure 16.9: Time alignment constants for all detectors in the prototype. Each plot shows the constant (in TDC counts) as a function of the pixel id within the detector.

structure.

A schematic of the test setup is shown in Figure 16.11.

- In front of the beam pipe is a hodoscope consisting of 16 vertical and 16 horizontal square scintillation fibers (2mm x 2mm). The fibers were readout by a 64 pixel MaPMT. The hodoscope monitors the x and y coordinates of the beam with minimal material to avoid any scattering of the beam.

- After traversing the radiator bar the beam is detected using a fast Cherenkov counter (Quartz counter) composed of a small block of Fused Silica and a 2x2 pixel MCP-PMT (with 10 micron holes). This detector is used to monitor the stability of the trigger signal which is provided by the Linac.

- Behind the Quartz counter is another detector (Scintillator counter) made from a block of Scintillation material and two photon detectors: on one end is another 2x2 pixel PMT while at the other end is a traditional PMT. The Scintillator counter is mainly used as a redundant beam diagnostic.

- At the end is a Lead Glass calorimeter which determines the energy of the beam pulse. This was useful for discriminating against pulses containing multiple particles.

- The beam pulsing operated with a frequency of 10 hz, but we operated with a low particle probability of 10% leading to a trigger rate of only 1 hz.

Figure 16.10: Picture of the actual beam test setup in Endstation A. The aluminum pipe is the end of the beam line delivering 10 GeV electrons. The Focusing-DIRC prototype is mounted on the steel structure, the PCB is covered with a black cloth.

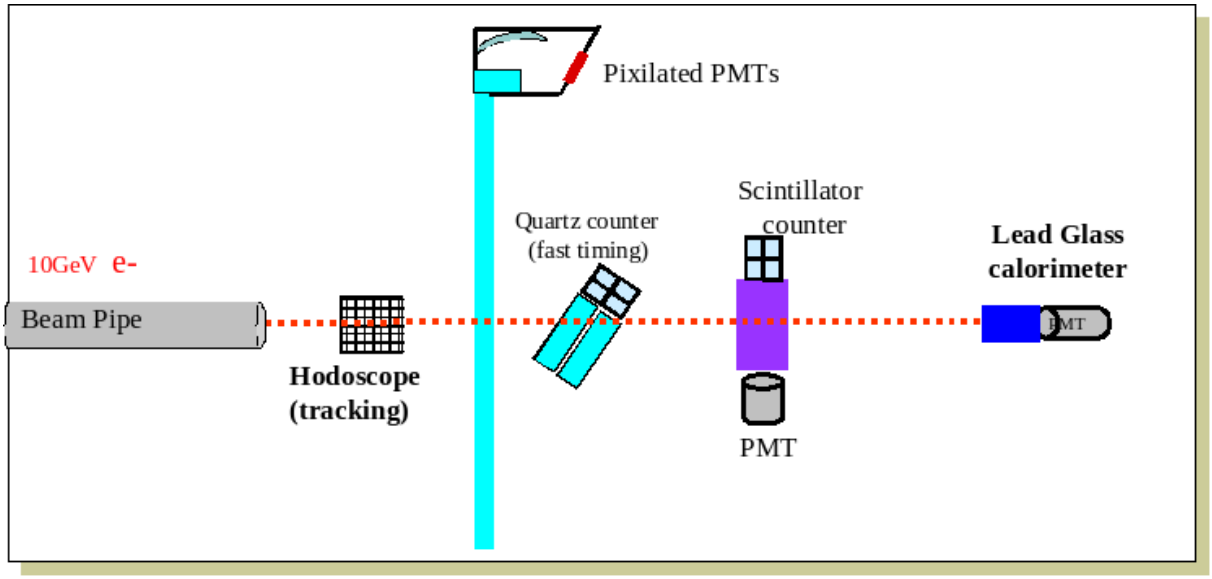

Figure 16.11: Schematic of the beam test setup showing all the relevant beam detectors and the layout of the prototype. Note that the prototype is placed on its side in order for the electron track to enter the radiator bar at the desired orientation. The different detectors are described in the text.

Chapter 17

Analysis of the Beam Test Data

17.1 Event selection

We select good beam pulses using the signals from the beam diagnostic detectors:

- we require that only one track has been detected by the hodoscope,
- the Quartz counter must have recorded a timing signal,
- the energy deposited in the calorimeter must be consistent with a single electron energy,
- there must be at least one photon detected by the Focusing-DIRC.

The 2-dimensional distribution of Hodoscope hits (Figure 17.1(left)) shows that the beam was well contained within the acceptable region and had a size of about 12x5 mm. Using the Quartz counter we found the trigger signal was stable with time to a 35 ps precision (Figure 17.1(right)). The energy deposited in the calorimeter (Figure 17.2(left)) showed three different features: a strong single electron signal, to the right an accumulation of double electron pulses and to the left a signal which we identify as coming from pion contamination. Finally, the number of photons detected in the Focusing-DIRC is shown in Figure 17.2(right), on average there were about 4 photons.

After the above selections we retained more than 50 thousand single electron pulses for each beam position.

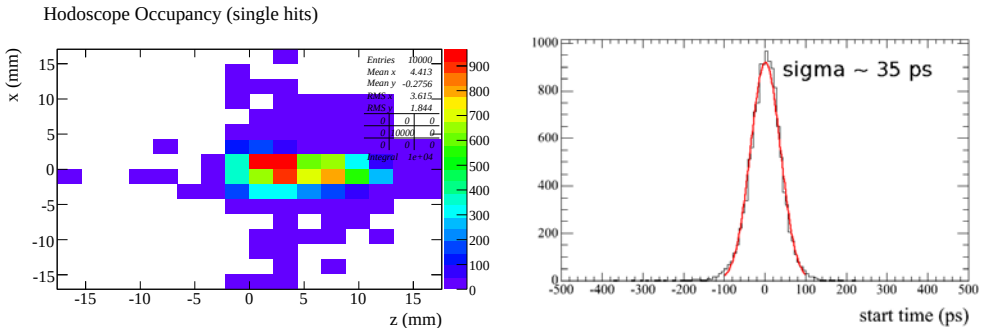

Figure 17.1: Left: Distribution of beam coordinates on the Hodoscope. Right: Distribution of beam signals (obtained after converting to actual time and applying a global offset) as detected by the Quartz start counter detector whose start trigger was given by the Linac beam signal. This good resolution shows the stability of the Linac signal.

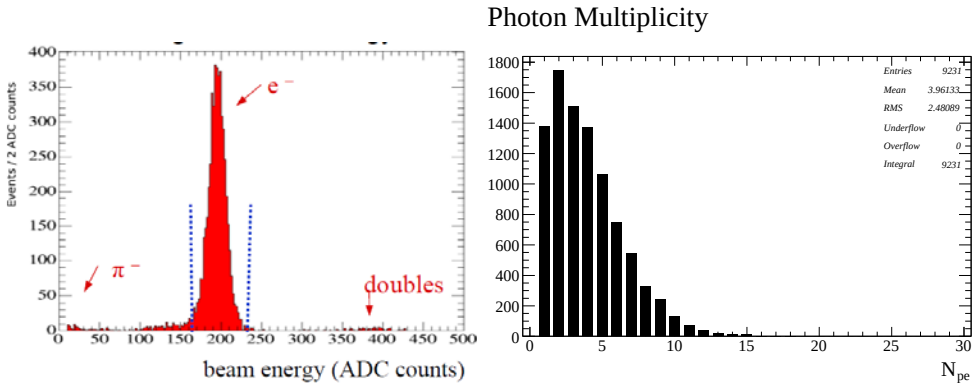

Figure 17.2: Left: Distribution beam energy measured using the Lead Glass calorimeter. The distribution shows some contamination from pions and pulses containing two electrons. Right: Distribution of the number of detected Cherenkov photons in the prototype.

17.2 Geometry of the Focusing-DIRC

The determination of the Cherenkov angle resolution and the chromatic correction require a determination of the angles θ and ϕ, and path length L of the photon.

The angles θ and ϕ corresponding to the angles of emission of the photon with respect to the electron track direction can be assigned through a ray tracing algorithm as shown in the schematic of the PCB (Figure 16.4). The algorithm uses the known positions and orientations of the spherical mirror and pixel detectors with respect to the end of the radiator bar. A ring of simulated photons is emitted from the center of the bar end face and propagated through the PCB onto the detector plane. The black curve in Figure 17.3 shows a hypothetical ring emitted at a 47^o angle with respect to the electron track direction. By comparison a ring emitted from inside the bar (beam position 1) creates an image as shown in the same Figure by the broad red distribution. The distribution of the ring from inside the bar is affected by geometrical aberrations due to the bar crossection, the image is modified by the mirror such that the central region is focused but broadens as a function of the ϕ coordinate.

A continuous assignment of the θ and ϕ coordinates can be determined for each point on the detector plane as shown in Figures 17.4 and 17.5. This is accomplished by simulating rings as above in small discrete steps.

The assignment of the path length L traveled by the photon can be done for any given beam position (and for any track orientation but here we restrict to the perpendicular case) by calculating the distance the photon needs to travel while inside the bar and adding the distance between the bar-end and the detector pixel. The distance inside the bar is given simply by the formula $l/(sin(\theta)sin(\phi))$ where l is the distance from the beam position to the bar end and ϕ is chosen to be 90^o at the center of detector plane. The distance traveled in the PCB is determined using the ray tracing algorithm.

17.3 Cherenkov Ring and TOP distributions

A typical occupancy of Cherenkov photons on the detector plane is shown in Figure 17.6. The photons can be divided into *d*irect and *i*ndirect depending on weather they are emitted in the direction of the PCB or in the opposite direction and undergo a reflection on the mirror. The measured signal time is significantly longer for the indirect photons and each detector pixel gives a time distribution with two peaks as shown in Figure 17.7.

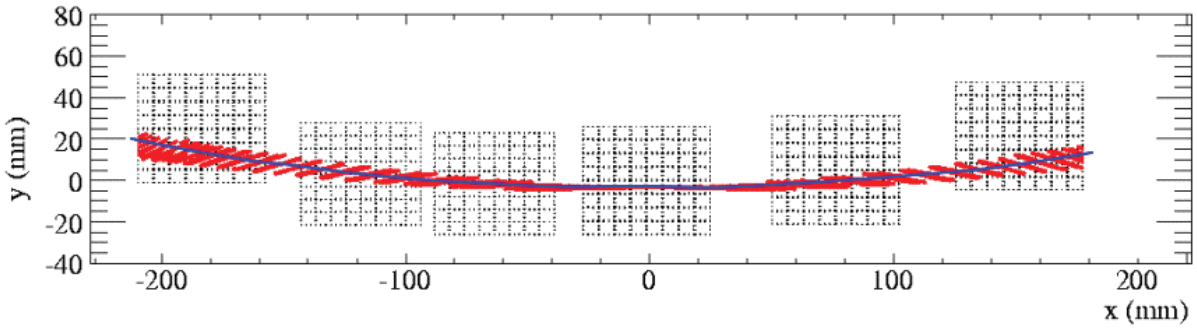

Figure 17.3: Black curve shows an image of a Cherenkov ring produced at the end of the radiator bar with an opening angle of 47^o and propagated using a simple ray tracing algorithm onto the detector plane. The broad red distribution shows the image of the same Cherenkov ring produced within the bar at beam position 1. The broadening as a function of ϕ shows the effect of the geometrical aberrations due to the bar size.

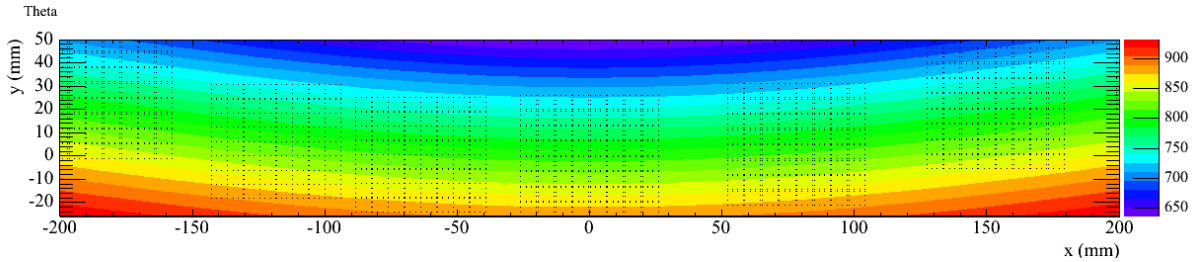

Figure 17.4: Assignment of the θ coordinate to each position on the detector plane. The z coordinate (color) gives the θ value in mrad. The center of the detector plane corresponds to approximately 47^o in the beam-test setup.

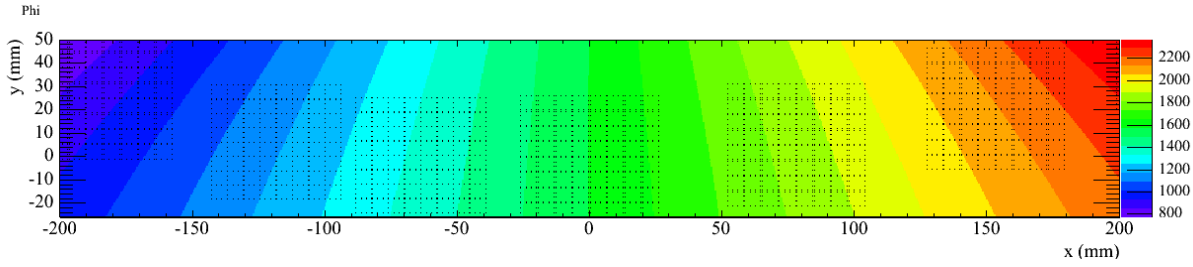

Figure 17.5: Assignment of the ϕ coordinate to each position on the detector plane. The z coordinate (color) gives the ϕ value in mrad, $\phi = 90$ is chosen at the center of the detector plane.

The effect of the pixel alignment calibration is shown in Figure 17.8 where the time distribution of all pixels has been plotted before and after applying the calibration offsets. The Cherenkov pulse time distribution is expected to have a sharp front rise corresponding to the photons traveling straight down the bar with no bounces on the sides and a tail corresponding to photons traveling longer distances detected in the wings of the detector plane. In this Figure we see that the corrected pulse time distribution is not smooth, this is caused by gaps between the detectors due to their thick edges.

In this experimental setup we cannot make an absolute TOP measurement due to an unknown global offset between the trigger signal and the readout electronics. To determine the absolute TOP for each photon we apply a global offset determined by requiring that the average TOP for all photons be equal to the expected TOP (=L/$v_g(410nm)$) calculated using the known average wavelength (410 nm). Figure 17.9 shows the difference between the measured TOP and the expected TOP (ΔTOP) for beam position 1 indirect photons after applying the global offset.

In Figure 17.10 all beam positions have been combined (using an equal number of events for each) to show the chromatic broadening due to the dispersion of the Cherenkov pulse as the distance traveled by the pulse increases. In this Figure the width of the pulse time distributions has two components (ignoring the time resolution), one due to the chromatic broadening and one due to the effect of the different path lengths corresponding to different pixels. The path length difference between pixels at the center of the detector plane and pixels in the far wings is about 3 meters for beam position 1 indirect photons. The effect of the path length difference can be removed by plotting ΔTOP as shown in Figure 17.11. We can then extract the pure Chromatic broadening of the time distribution as a function of path length by determining the width of these distributions. A fit is performed using a single Gaussian plus a 2nd order polynomial to account for the long tail as shown in the Figure. In Figure 17.12 we see that the width of the Cherenkov pulse increases linearly from about 250 ps to about 1 ns between the shortest path length and the longest path length.

17.4 Chromatic Correction

Using the θ assignments of each detector pixel we can determine the resolution of the prototype σ_{θ_C}. The resolution σ_{θ_C} is defined as the width of the distribution of detected photon θ angles. Note that this resolution is not the same as σ_θ because the detected

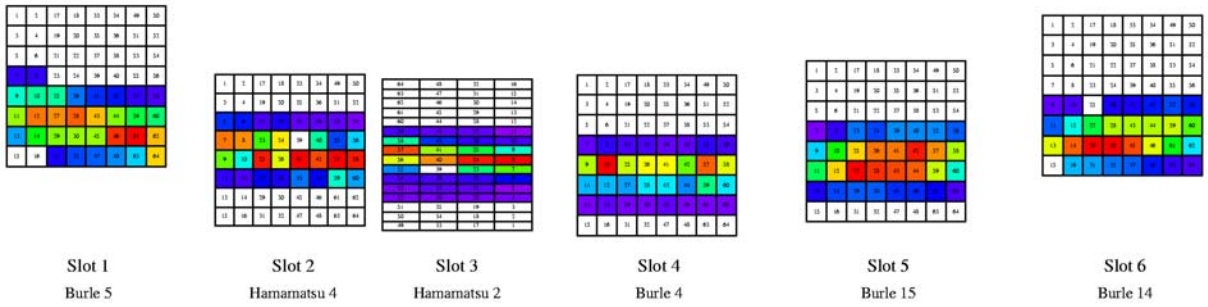

Figure 17.6: Cherenkov ring occupancy on the detector plane for data from beam position 1.

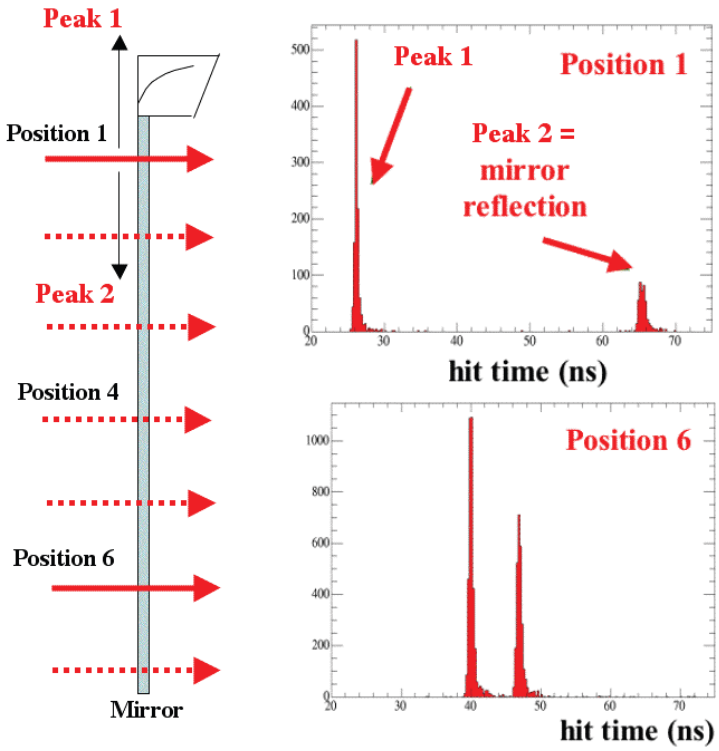

Figure 17.7: Left: Illustration of the different prototype positions relative to the beam. Right Top: Time distribution of photons detected in one pixel in slot#4 for beam position 1. The first peak is from direct photons while the second peak is due to indirect photons reflected from the mirror at the opposite end of the bar. Right Bottom: Time distribution of photons detected in one pixel in slot#4 for beam position 6. The separation between the peaks decreases due to the shorter path length difference between direct and indirect photons.

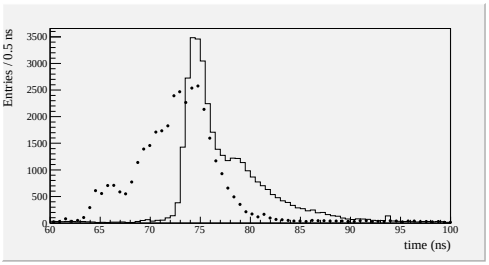

Figure 17.8: Comparison of the raw time distribution for the Cherenkov pulse obtained by combining all pixels in the detector before (points) and after (histogram) applying the time alignment calibration constants.

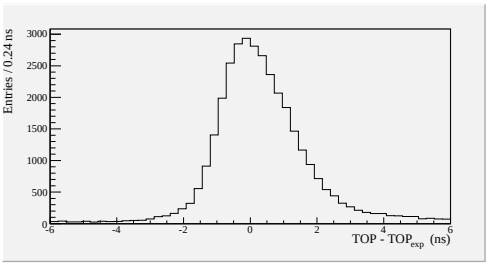

Figure 17.9: Distribution showing ΔTOP for all photons after applying the global time offset.

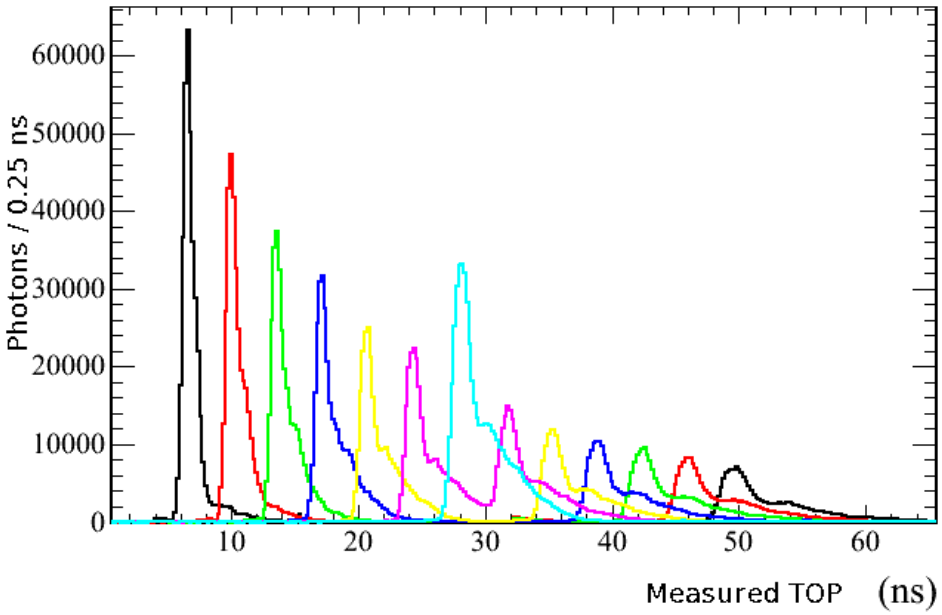

Figure 17.10: Comparison of the Cherenkov pulse distributions of all beam positions obtained using an equal number of events. The distributions broaden as the path length increases due to chromatic dispersion. The middle distribution is from beam position 7 and shows that direct and indirect photons cannot be distinguished here due to the small path length difference.

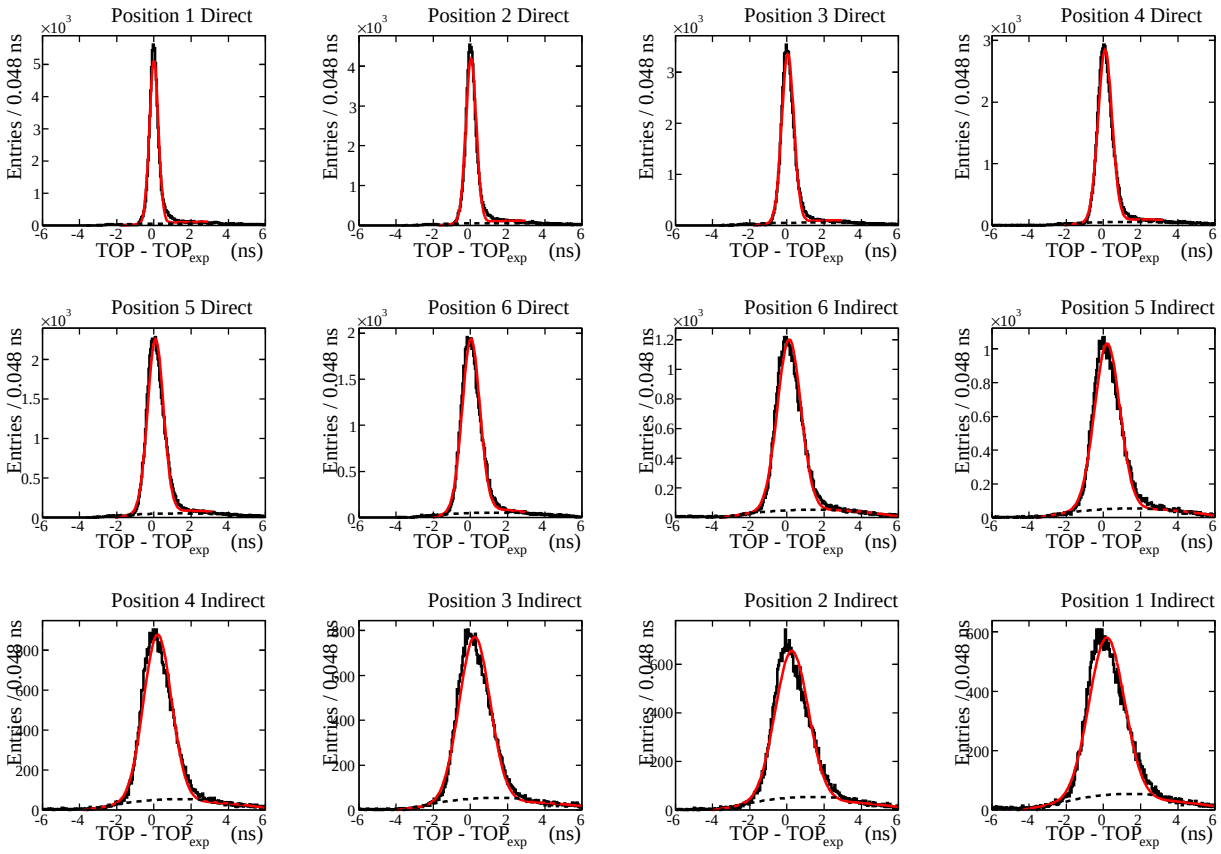

Figure 17.11: Distributions of ΔTOP as a function of increasing photon path length. The red curve shows the fit described in the text.

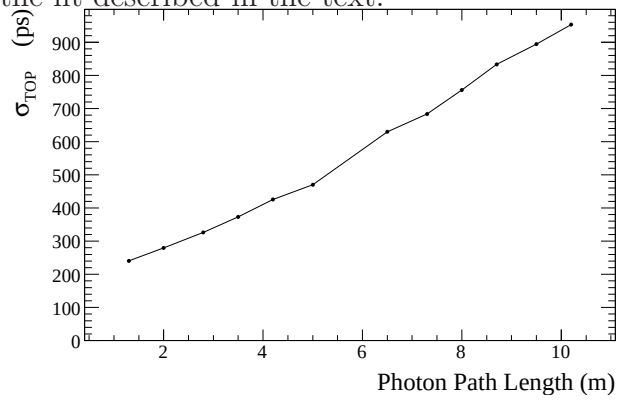

Figure 17.12: Width of the ΔTOP distributions as a function of path length determined from the Gaussian fit. The broadening shows the effect of the chromatic dispersion.

Cherenkov photons have an intrinsic distribution in θ as determined by the production intensity and the efficiency of the detector discussed in section 15.2. In this section we study the effect of the chromatic correction described earlier on the resolution σ_{θ_C}.

A feature of the prototype data is the strong discretization in the θ distribution due to the relatively large width of the pixels with respect to the intrinsic width of the Cherenkov ring as can be observed in the detected ring distribution in Figure 17.6. This effect does not happen for a sample of tracks whose orientation with respect to the bar is continuously changing as in the BaBar experiment. In the present case, one can produce a distribution which can be used to assign a width to the detected Cherenkov ring only after combining all pixel columns which are positioned at different θ angles. The width of the Cherenkov ring has been determined to be about 10.2 mrad [47] using θ assignments to each pad from a GEANT4 simulation in which photons are isotropically emitted at the track beam position and propagated through the material onto the detector plane. In this simulation the θ angle assigned to each pad is determined as the average angle of all detected photons in the pixel. A fit to the θ distribution where the angles have been assigned using this simulation is shown in Figure 17.13. The fit uses two Gaussians with common mean, the second broad Gaussian is necessary to account for a background in the prototype data. The width of this Gaussian has been determined to be about 50 mrad by instrumenting pixels far from the expected Cherenkov ring where no photons are expected. The source of this background is not understood, possible explanations include imperfections in bar material imperfections, bar joints reflections, and contributions from delta rays [48]. In addition, the fit to the θ distributions does not cover the edges of the distributions because these edges are affected by the limited instrumentation of the detector pixels.

For this note an alternate procedure is used where the θ angle assigned to each detected photon is determined by employing the simple ray tracing algorithm described in Section 17.2. As described earlier a continuous map of the θ and ϕ coordinates has been created as shown in Figures 17.4 and 17.5. Using these maps one can remove the discretization by randomizing the position of the detected photon uniformly within the pixel and obtaining the θ and ϕ coordinates using the fine maps. This procedure is useful for visualizing the measured correlation between θ and v_g, however the resolution determined after this randomization is worse by about 2 mrad as shown in Figure 17.14.

The measurement of the correlation between θ and v_g is shown for each beam position in Figure 17.15. In these plots one can observe that the correlation disappears for short path lengths, because Cherenkov pulse becomes very narrow and the time resolution of the detectors can no longer distinguish between different wavelengths. The projections

onto the θ and v_g axes are shown in Figures 17.16 and 17.17. The θ resolution measured as a function of path length degrades by about 1 mrad between the shortest path length and the longest. This feature is not understood and might be caused by an improper modeling of the photon background. The v_g distribution shows broadening as the path length gets short due to the degradation of the relative time resolution.

The chromatic correction is applied by rotating the 2-dimensional distribution according to the observed correlation in the θ vs. v_g plane, the resulting distributions are shown in Figure 17.18. Figure 17.19 compares σ_{θ_C} before and after the correction. For the longest path lengths we obtain an improvement of about 2 mrad while the improvement vanishes for the short path lengths where the time resolution is not good enough. Although this improvements are qualitatively as expected the improvement observed for the long path lengths is larger than the expected which is about 1 mrad.

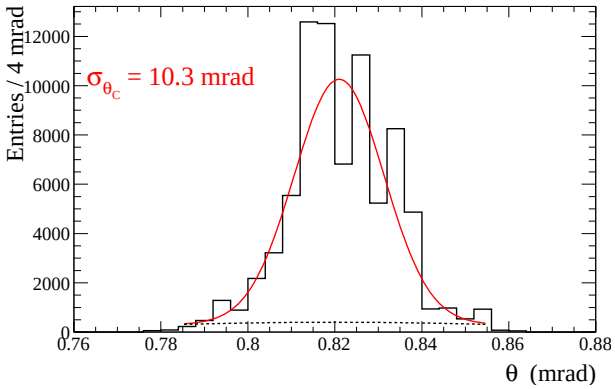

Figure 17.13: Distribution of Cherenkov photon θ angles using a GEANT4 simulation to assign discrete angles to each detector pixel. The fit is described in the text.

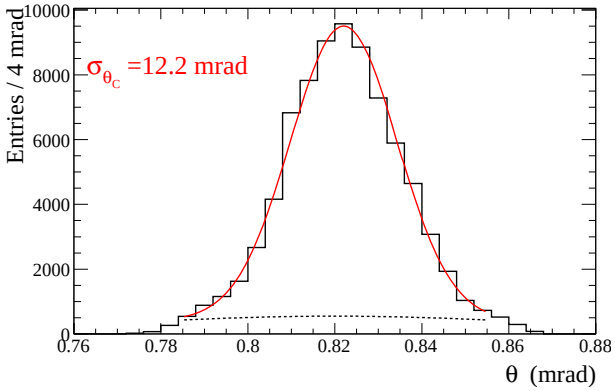

Figure 17.14: Distribution of Cherenkov photon θ angles using the continuous θ and ϕ maps and randomization of the photons within the detector pixel.

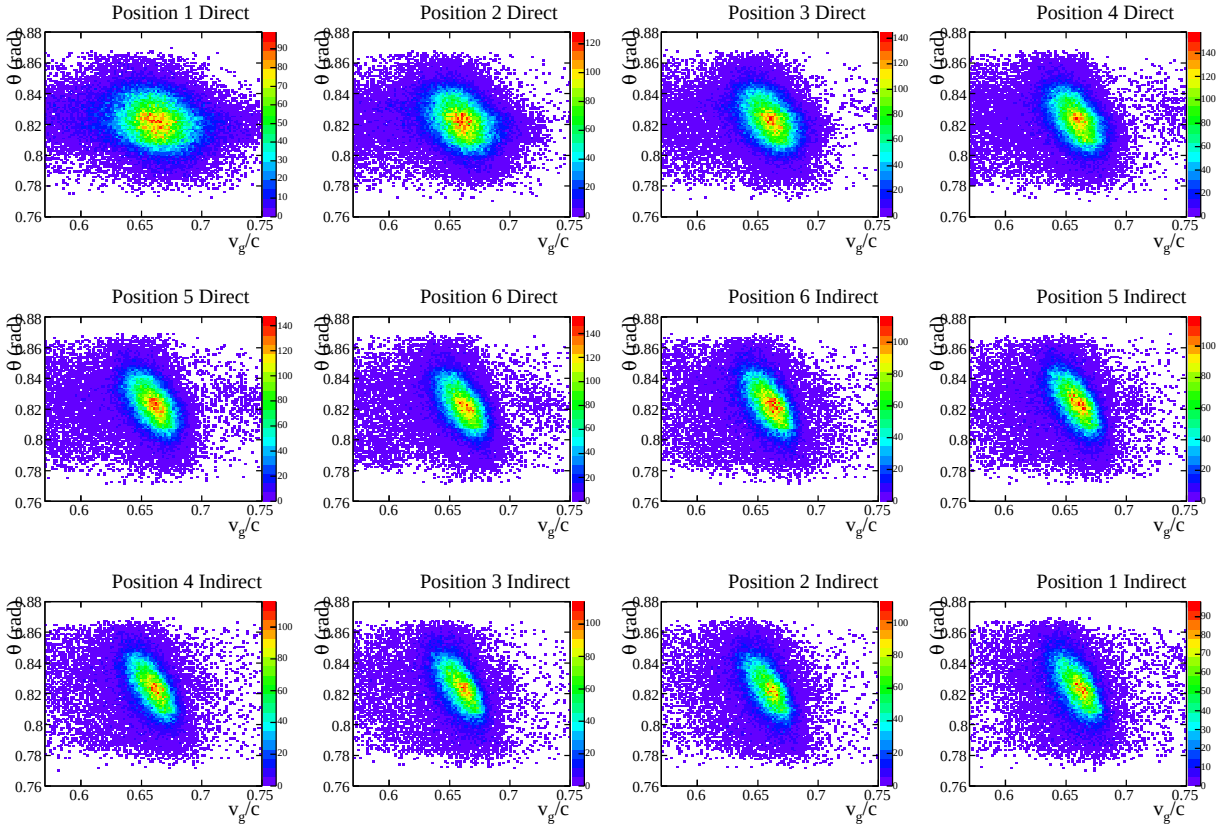

Figure 17.15: Measured distribution of θ vs. v_g as a function of L. The observed correlation disappears at short path lengths due to degradation in the timing resolution with respect to the width of the Cherenkov pulse.

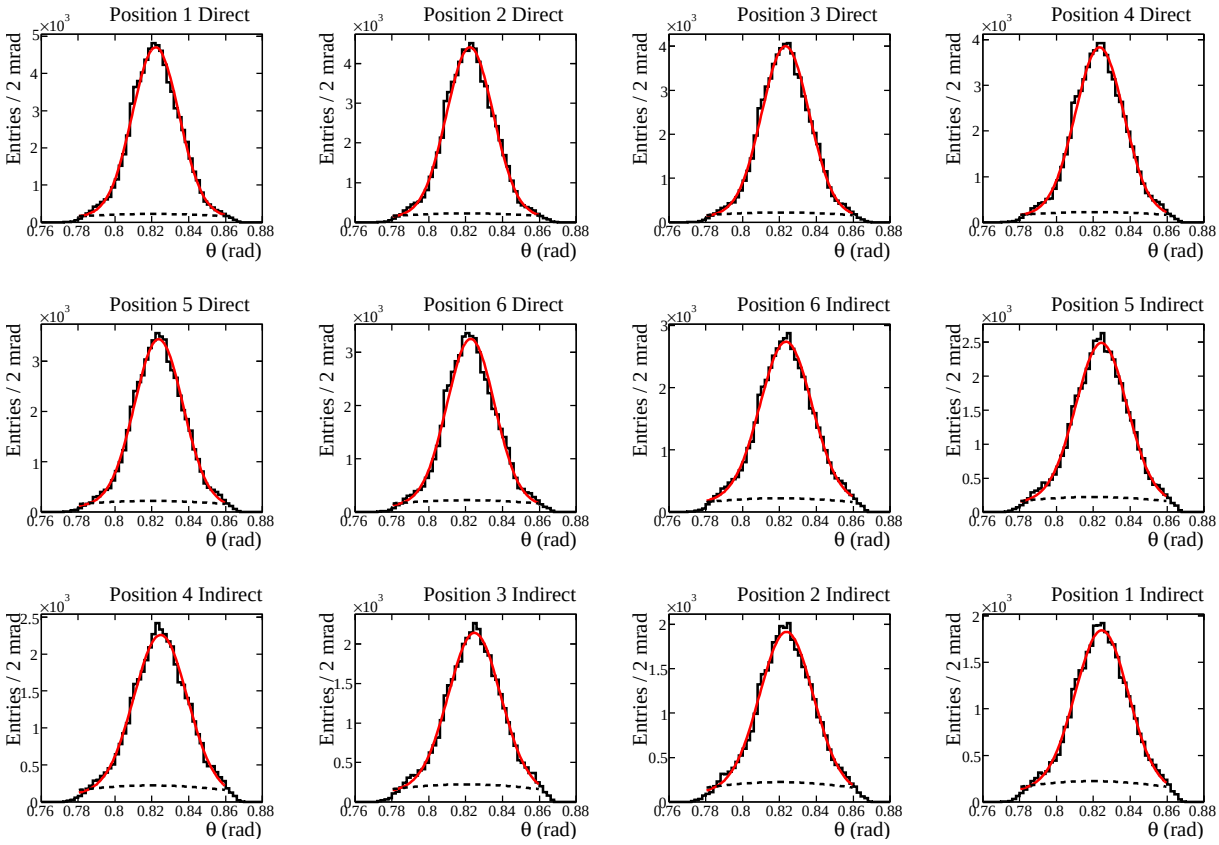

Figure 17.16: Projections of the measured 2-dimensional distributions onto the θ axis as a function of the path length. The red curve shows the fit described in the text.

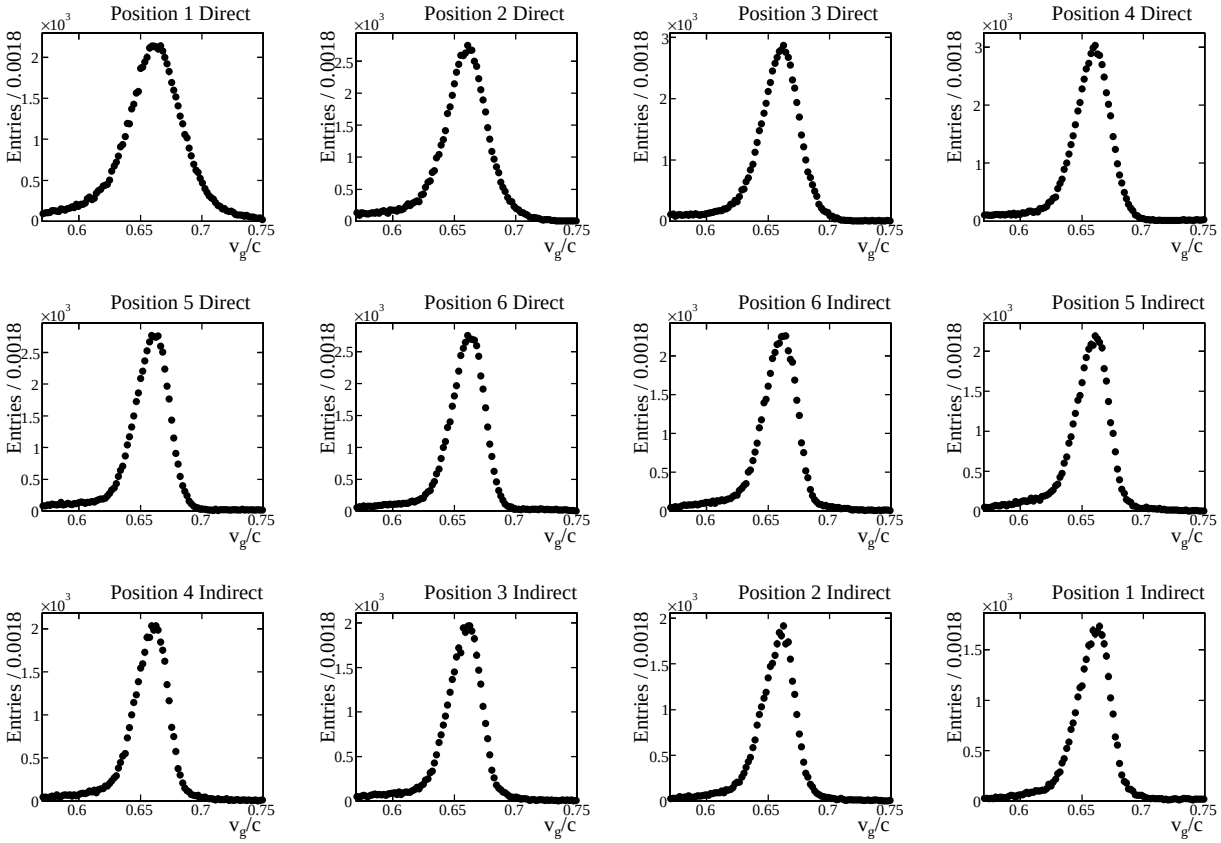

Figure 17.17: Projections of the measured 2-dimensional distributions onto the v_g axis as a function of the path length.

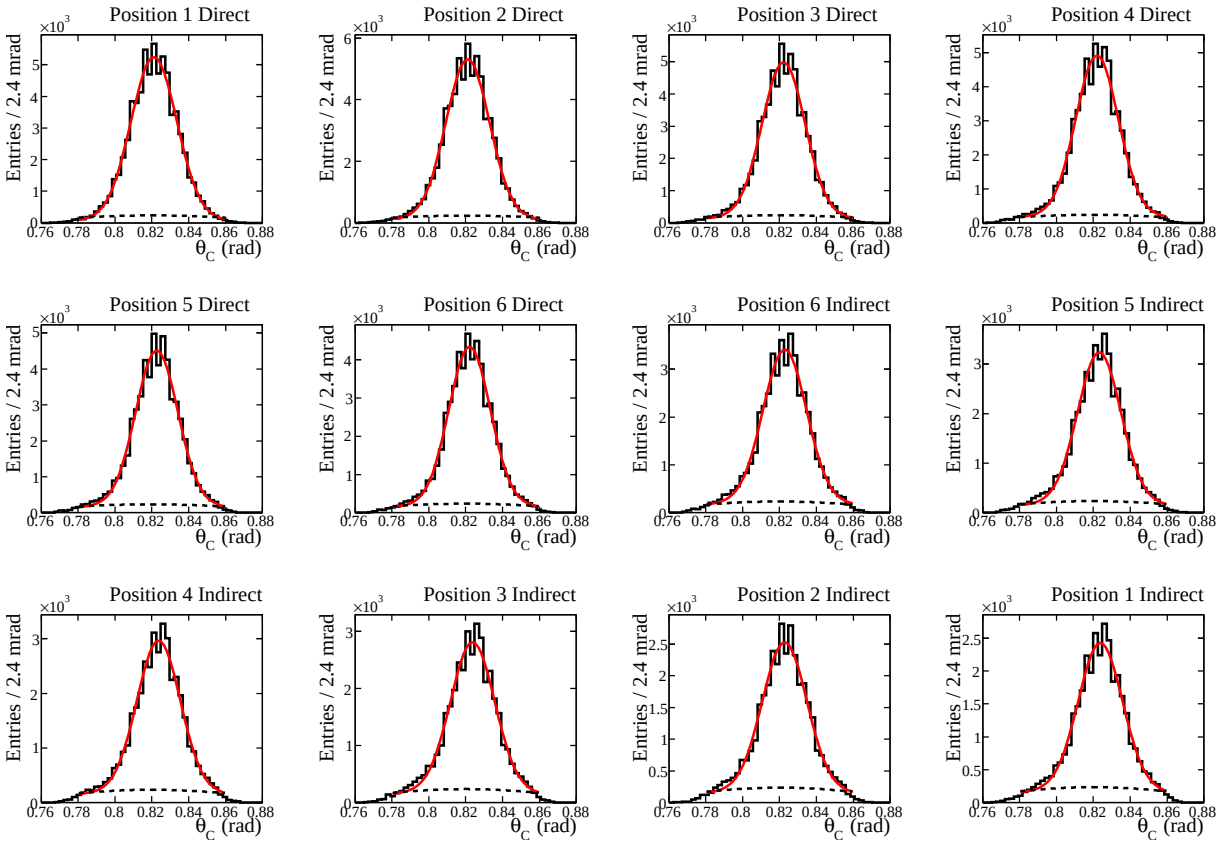

Figure 17.18: Distributions of the θ distributions after applying the chromatic correction. The red curve shows the fit.

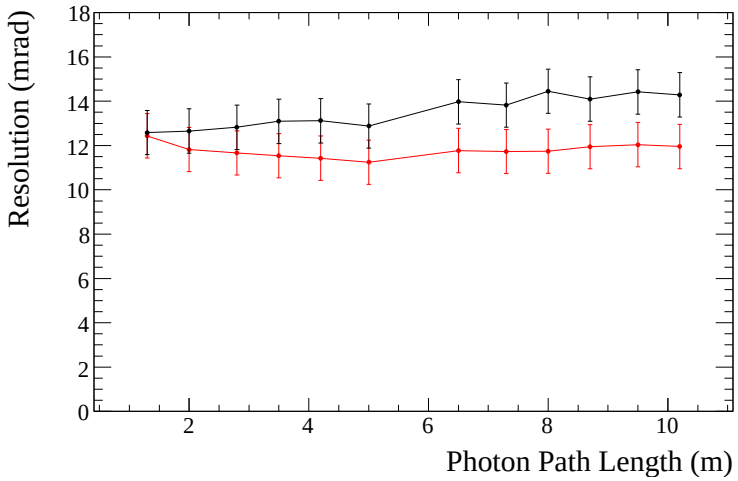

Figure 17.19: Comparison between the raw width of the θ distribution and the width of the distribution after the chromatic correction. The improvement observed at long path lengths vanishes for short path lengths where better timing resolution is needed.

Chapter 18

Conclusions

In summary, we have studied the performance of a Focusing-DIRC prototype. The use of new photon detectors allows a next generation DIRC to have many improvements including a large reduction in backgrounds and improved resolution as results of a reduction in the size of the PCB and a $\sim$10$\times$ improvement in the timing resolution. In the beam test of the prototype we have been able operate the prototype instrumented with about 300 channels and we measure the properties of the detected Cherenkov photons as a function of the photon path length. We have been able to measure the chromatic broadening of the Cherenkov pulse as a function of photon path length and therefore perform a chromatic correction to the Cherenkov ring resolution. The measured resolution of the prototype in the beam test is comparable to the resolution of the DIRC in *BABAR*. However, further studies are needed to understand the backgrounds as well as the magnitude of the chromatic correction.

In this study we have been able measure for the first time the correlation between the production angle and the group velocity of Cherenkov photons predicted by Maxwell's equations. This is interesting on its own at an academic level as it is generally assumed that Cherenkov radiation has a well defined angle θ_C. The study done here illustrates the 2-dimensional nature of this radiation.

Appendices

Appendix A

Measurement of $\mathcal{B}(D_s^- \to K^+K^-\pi^-)$

A.1 Motivation

Currently the branching fraction for the hadronic decay $D_s^- \to K^+K^-\pi^-$ is known to be $(5.50 \pm 0.28)\%$ [17]. This is almost 9 times larger than the $D_s^- \to \mu^-\bar{\nu}_\mu$ branching fraction and the relative error is only $\sim 5\%$. The expected number of signal $D_s^- \to \mu^-\bar{\nu}_\mu$ events in this analysis is ~ 300, one can therefore expect $\sim$2000 reconstructed $D_s^- \to K^+K^-\pi^-$ events since the efficiency for the additional tracks is about 60%. Given this statistical precision, the overall precision for a measurement of this decay branching fraction is expected to be at the level of 5% using the analsis method from Part I in this thesis. With this precision this mode provides a test of the complex analysis procedure used in the measurements of the leptonic D_s^- decays. Moreover, this hadronic mode is sometimes used as a reference mode for relative measurements of other D_s^- decays (when absolute measurements are not feasible) so a precise knowledge of this decay mode is necessary to obtain precise measurements of other decay modes. The measurement provided in this study improves the uncertainty on the world average value for this branching fraction.

A.2 Strategy

The measurement of this channel is performed in a similar manner as the measurements of the leptonic D_s^- decays. We start with the sample of inclusive D_s^- mesons is known in the sample of events reconstructed in Chapter 5. The remaining steps are to determine how many $D_s^- \to K^+K^-\pi^-$ events are in that sample and what is the reconstruction efficiency for these events. In order to keep the systematic uncertainties to a

minimum, a study of an "untagged" sample of $D_s^- \to K^+K^-\pi^-$ events has been performed. In this study a fraction of the total Data set is used for which the inclusive (tagged) D_s^- reconstruction has not been applied. The $D_s^- \to K^+K^-\pi^-$ events in this study are reconstructed using the same procedure as will be used for tagged events, however a much higher number $D_s^- \to K^+K^-\pi^-$ events are available and precise comparisons between MC and Data can be performed in order to determine systematic biases which may affect the efficiency.

A.3 Study of Untagged $D_s^- \to K^+K^-\pi^-$ Events

For the study of events which have not been tagged it is sufficient to use only the Run3 OnPeak data. The reconstruction of these events is performed as follows:

- Three tracks are required in the event, two of which must pass the VeryLoose Kaon PID selector. No PID requirements are placed on the pion candidate.

- A kinematic vertex fit is performed to the three tracks, but no requirement on the fit probability is applied. This selection is studied below.

- A requirement on the CM momentum of the $K^+K^-\pi^-$ system to be greater than 3.0 GeV is applied in order to be consistent the tagged D_s^- reconstruction.

- Decays of $D^{*+} \to D^0\pi^+$ where $D^0 \to K^+K^-$ appear as a peaking background next to the D_s^- signal peak in $m(K^+K^-\pi^-)$. These decays are completely removed by anti-selecting the mass difference 140 <m($K^+K^-\pi^-$)-m(K^+K^-)< 150 MeV/c^2.

- $D_s^- \to K^+K^-\pi^-$ events are selected if their invariant-mass is in the range 1.93 < m($K^+K^-\pi^-$) < 2.00 GeV/c^2. This selection is studied below.

The selection of the signal events must account for the fact that in the tagged D_s^- reconstruction only D_s^- events which are produced through a D_s^{*-} parent are accounted. In order to select these decay processes in this untagged sample a photon is required with the same selections as were applied to the signal photon in the tagged reconstruction. D_s^{*-} candidates are then constructed from the above D_s^- candidates and the additional photon.

A.3.1 $m(K^+K^-\pi^-)$ Selection Study

In order to determine any possible bias on the efficiency arising from the selection on the mass of the $K^+K^-\pi^-$ system a study has been performed where a fit is applied to the D_s^- signal peak in this variable. Using the fit, a comparison can be made between the efficiency in MC and the efficiency in Data. The fit to the $m(K^+K^-\pi^-)$ distribution is performed using a signal model which is composed of two Gaussian functions. The background is modeled using a linear polynomial. The fit to the MC distribution is shown in Figure A.1 and the fit to the Data is shown in Figure A.2, both distributions are well modeled. The efficiency of the selection on this variable is determined from the integral of the signal function within the selection region relative to the total integral. For MC this efficiency is found to be 99.80% while for Data the efficiency is found to be 99.75%, therefore the systematic uncertainty due to this selection can be ignored.

A.3.2 PID efficiency Systematic

A possible bias may arise from differences in the PID efficiency between MC and Data. A precise estimate of the efficiency of the selector applied to the *Kaons* can be made by determining the D_s^- signal yield before and after applying the selector to one of the *Kaons*. Fits to the $m(K^+K^-\pi^-)$ distribution before and after the Kaon selector is applied are shown for the MC sample in Figure A.3. From the ratio of the signal yields determined from these fits the average efficiency is determined to be 0.9529±0.0049. Likewise fits are performed to the Data sample in Figure A.4 and the efficiency is determined to be 0.9402±0.0098. The ratio of these efficiencies 0.987±0.011 must be applied as a correction factor (per Kaon) to the efficiency determined later from MC for the branching fraction calculation.

A.3.3 Vertex fit probability Study

A study has been performed to compare the probability of the vertex fit applied to the $K^+K^-\pi^-$ system between MC and Data. The distribution of signal events in Data as a function of this probability is extracted through a sideband subtraction. A lower side-band region in $m(K^+K^-\pi^-)$ is defined by the interval [1.891,1.926] GeV/c^2 and a higher side-band region is defined by the interval [2.04,2.39] GeV/c^2. The vertex fit probability distribution for both sidebands is shown to be the same in Figure A.5, this implies the distribution for the background in the signal region must be the same and the

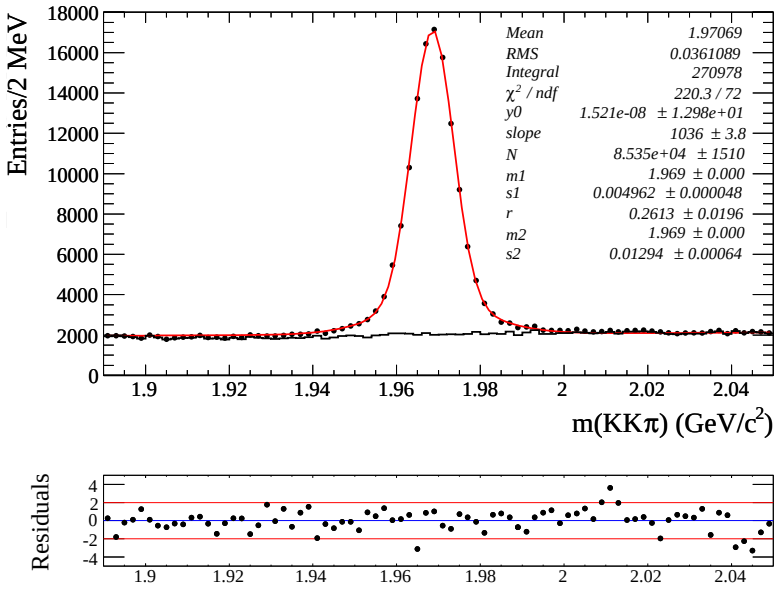

Figure A.1: Fit to the $m(K^+K^-\pi^-)$ distribution in generic MC.

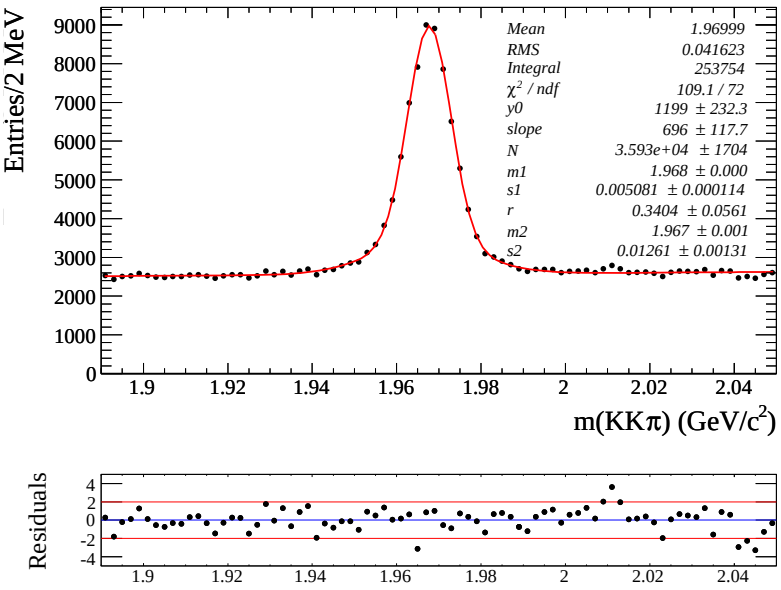

Figure A.2: Fit to the $m(K^+K^-\pi^-)$ distribution in Data.

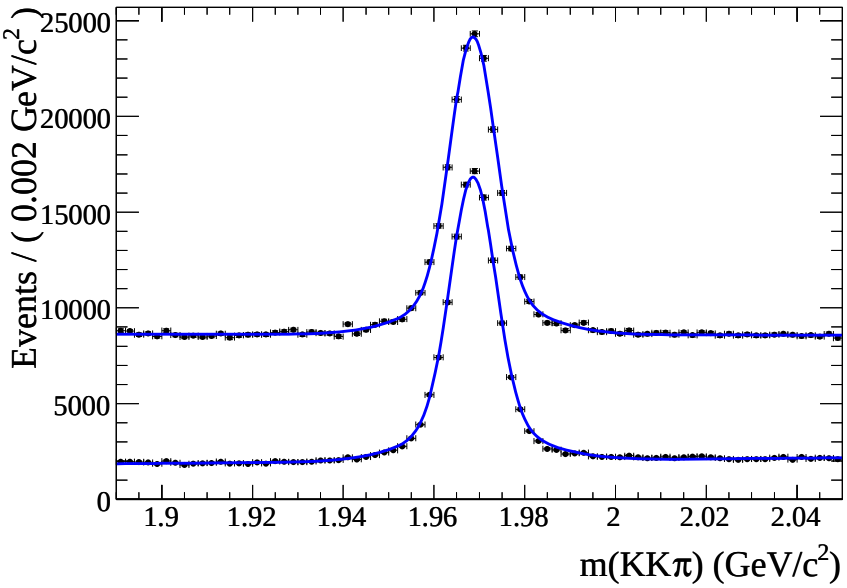

Figure A.3: Fit to the $m(K^+K^-\pi^-)$ distribution in generic MC with (bottom curve) and without (top curve) PID selector on one Kaon

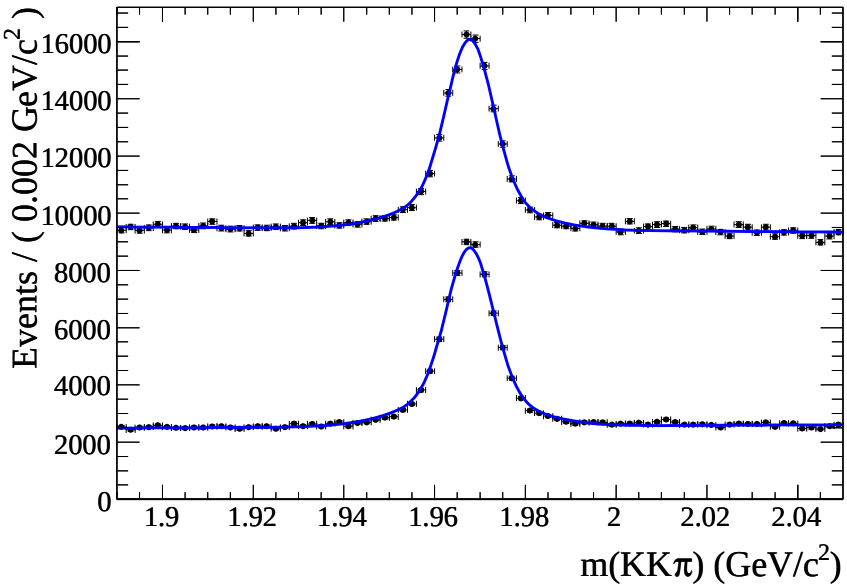

Figure A.4: Fit to the $m(K^+K^-\pi^-)$ distribution in Data with (bottom curve) and without (top curve) PID selector on one Kaon.

background subtraction is reliable. The fit probability distribution for the signal region after the sideband subtraction (i.e. for signal events) is compared to the probability distribution of signal MC events in Figure A.6 (after normalizing to the same integral), and Figure A.7 shows a ratio of these two distributions. The ratio shows a significant slope implying a disagreement between MC and Data. Since there is little separation between signal events and background events in this variable, and in order to avoid a bias in the efficiency, no selection is applied to this fit probability.

A.3.4 Dalitz Correction Weights

The efficiency for reconstructing $D_s^- \to K^+K^-\pi^-$ events is expected to depend on the position of the event in the Dalitz plot. However, the signal MC used for the determination of the efficiency is generated using a uniform distribution across the Dalitz plot while real Data events contain resonances which populate specific regions preferentially. Therefore an average efficiency determined from the signal MC will not be equal to the average efficiency for Data. In order to correct for this difference the efficiency will be determined for the three main regions of the Dalitz plot corresponding to $D_s^- \to \phi\pi^-$, $D_s^- \to K^{*0}K^-$, and the rest; these regions are defined in Table A.1. The efficiencies can then be averaged according to proper signal weights for each region. The signal weight for each Dalitz region can be determined precisely using this untagged sample of $D_s^- \to K^+K^-\pi^-$ events. Figures A.8 to A.10 show the distribution of $D_s^- \to K^+K^-\pi^-$ events in each of the three Dalitz plot regions, the fit performed to these distributions is used to extract the fraction of signal events in each region. These fractions are compared in Table A.2 to the true weights. In this table there is also a comparison between weights determined using the true 4-momentum vectors and the reconstructed 4-momentum vectors to show that there is no significant flow of events from one region to another due to the resolution on the momentum vectors. The fits to the Data distributions are shown in Figures A.11 to A.13 and the weights are listed in the same table.

A.3.5 Fit Model

The extraction of signal events in the tagged sample must be performed such that only D_s^- events produced through a D_s^{*-} parent are counted. For this reason the signal must be extracted from the distribution of D_s^{*-} candidates in the $m(K^+K^-\pi^-\gamma)$distribution. The distribution of Data events in this untagged sample is shown in Figure A.14. It can be observed that the background in this region is linear. For the signal model the

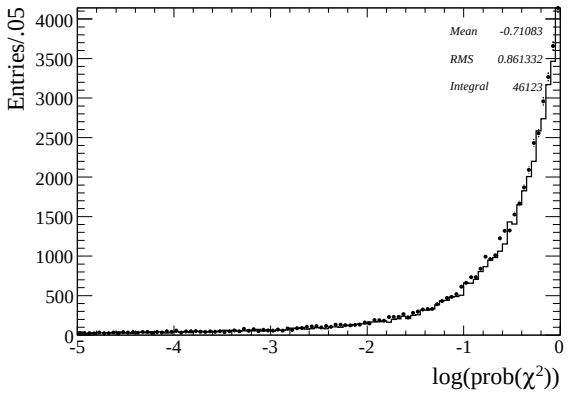

Figure A.5: Comparison of the vertex fit probability distributions between the lower (points) and higher (histogram) D_s mass sidebands.

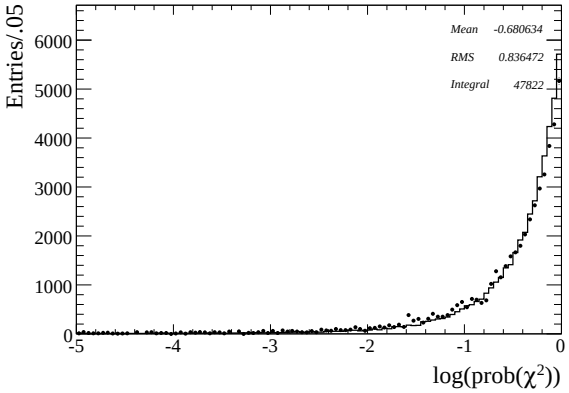

Figure A.6: Comparison of the vertex fit probability distributions between background subtracted Data (points) and truth-matched signal MC (histogram).

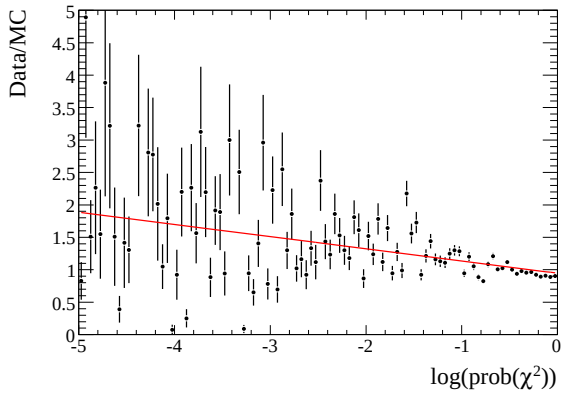

Figure A.7: Ratio of background subtracted Data to truth-matched signal MC yield v.s. vertex fit probability.

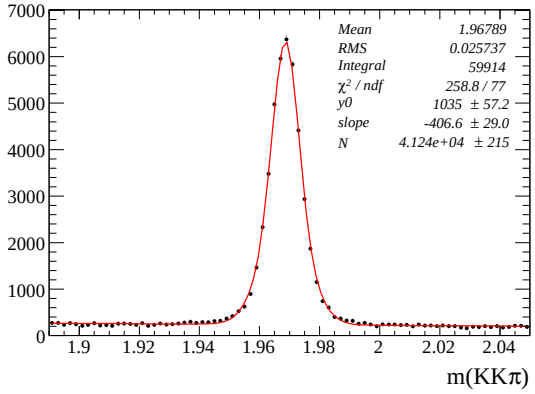

Figure A.8: Fit for the signal yield in Dalitz Region 0 for the generic MC.

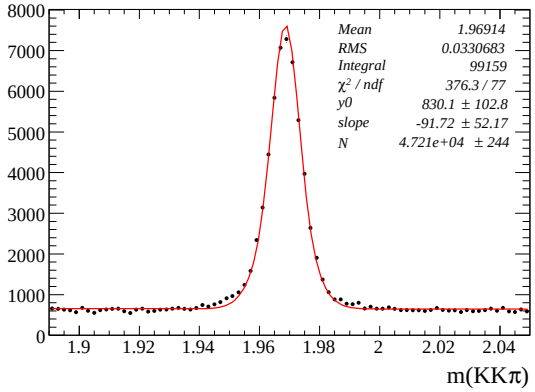

Figure A.9: Fit for the signal yield in Dalitz Region 1 for the generic MC.

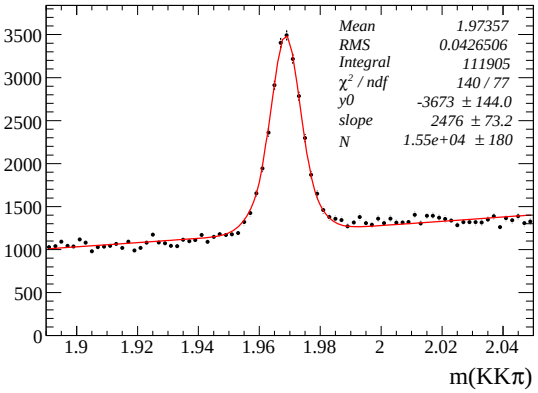

Figure A.10: Fit for the signal yield in Dalitz Region 2 for the generic MC.

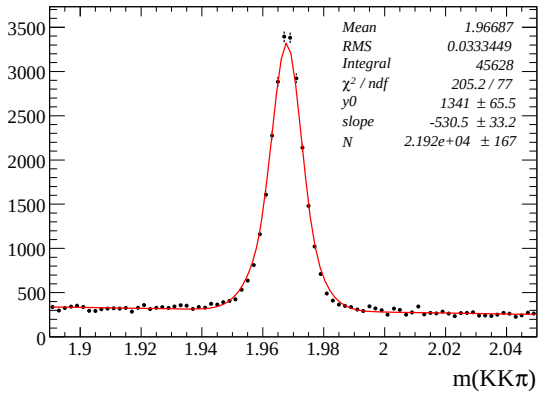

Figure A.11: Fit for the signal yield in Dalitz Region 0 for Data.

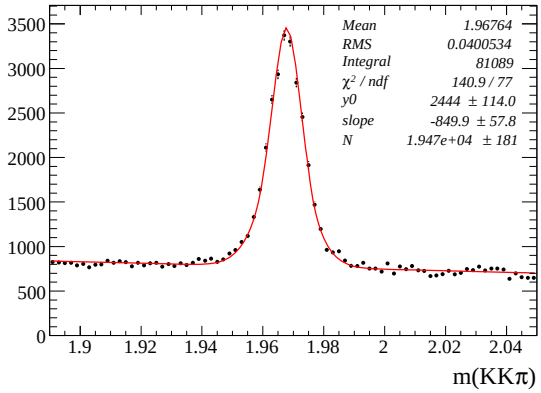

Figure A.12: Fit for the signal yield in Dalitz Region 1 for Data.

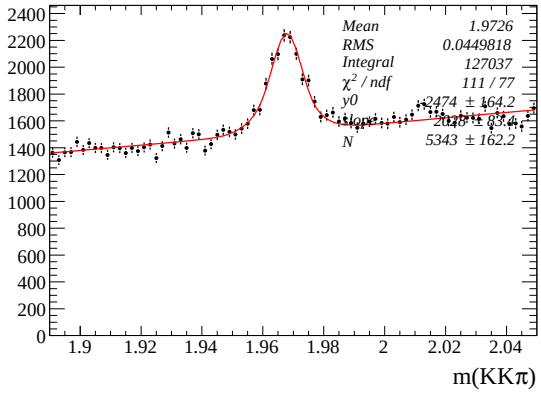

Figure A.13: Fit for the signal yield in Dalitz Region 2 for Data.

reconstructed signal MC events can be used to create a histogram PDF. The fit shown in this Figure is performed using these models and shows good agreement with this high statistics Data sample, the χ^2/NDF of the fit is 112/126. This models will be used in the tagged sample.

	$m^2(K^+K^-)$ **range (GeV^2)**	$m^2(K^+\pi^-)$ **range (GeV^2)**
Dalitz Region 0	(0.95,1.15)	(1.08,2.16)
Dalitz Region 1	(1.20,3.40)	(0.6,1.0)

Table A.1: Definition of the Dalitz regions. Dalitz Region 2 is defined as the remainder after the other regions.

	Gen.MC True Weight	Reco.MC True Weight	Reco.MC Fitted Weight	**Reco.Data Fitted Weight**
Dalitz Region 0	0.3926 ± 0.0019	0.3924 ± 0.0019	0.3967 ± 0.0036	0.4691 ± 0.0062
Dalitz Region 1	0.4556 ± 0.0020	0.4554 ± 0.0020	0.4542 ± 0.0041	0.4166 ± 0.0067
Dalitz Region 2	0.1518 ± 0.0012	0.1522 ± 0.0012	0.1491 ± 0.0030	0.1143 ± 0.0060

Table A.2: Comparison between MC and Data Dalitz weights.

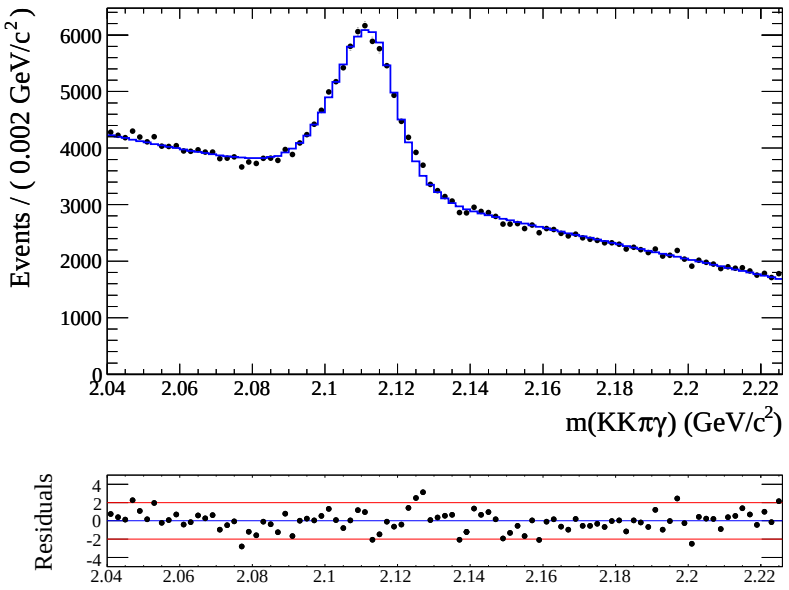

Figure A.14: Fit to the $m(K^+K^-\pi^-\gamma)$distribution in Data using the truth-matched signal MC as signal PDF and a linear background model.

A.4 Tagged $D_s^- \to K^+K^-\pi^-$

To determine $\mathcal{B}(D_s^- \to K^+K^-\pi^-)$, $D_s^- \to K^+K^-\pi^-$ decays must be counted in the inclusive D_s^- sample and the efficiency must be determined from the reconstructed signal MC events where the full event reconstruction procedure has been applied. The reconstruction procedure to extract the these decays has been applied to the inclusive D_s^- samples as well as to the signal MC sample listed in Section 4.2, the results are presented below.

A.4.1 Signal MC

The signal MC sample used to determine the reconstruction efficiency for these decays is generated with the requirement that each event contain the decay process $D_s^{*-} \to D_s^-\gamma$ where $D_s^- \to K^+K^-\pi^-$. Figure A.15 shows the resulting $m(K^+K^-\pi^-)$ distribution after the full event reconstruction has been applied. The peaking background shown in this plot arises from reconstructions where the $K^+K^-\pi^-$ system forms a true D_s^- but the photon candidate is not from the D_s^{*-} decay. The distribution of events as a function of $m(K^+K^-\pi^-\gamma)$ is shown in Figure A.16 and shows a well defined signal peak and linear background as in the untagged study. For this study signal events are counted only if the $K^+K^-\pi^-\gamma$ is fully truth-matched to the D_s^{*-} decay products.

The distribution of signal events over the Dalitz plot is shown in Figure A.17 and the number of events in each of the regions is used to determine the raw absolute efficiencies listed Table A.3. These efficiencies show a significant variation between the three regions. The average efficiency computed using the total number of signal events is 5.403×10^{-4} while the efficiency determined by a weighted average of these efficiencies, where the signal weights for Data are used in the average, is 5.470×10^{-4}. The ratio between the weighted efficiency and the simple efficiency is 1.0169 and will be applied as a correction to the efficiencies used in the branching fraction calculation later.

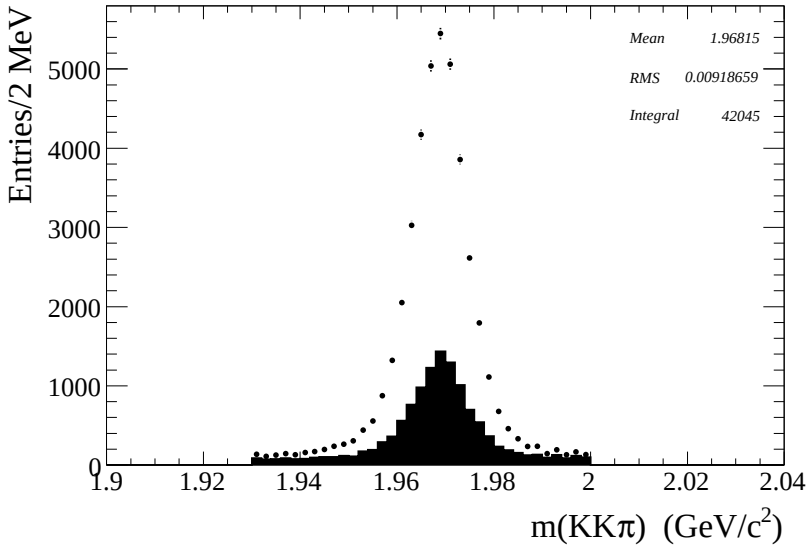

Figure A.15: Reconstructed $m(K^+K^-\pi^-)$ distribution in for signal MC. The black filled histogram are candidates which are not truth-matched to the full decay $D_s^* \to D_s\gamma(D_s \to KK\pi)$, but includes true $D_s \to KK\pi$.

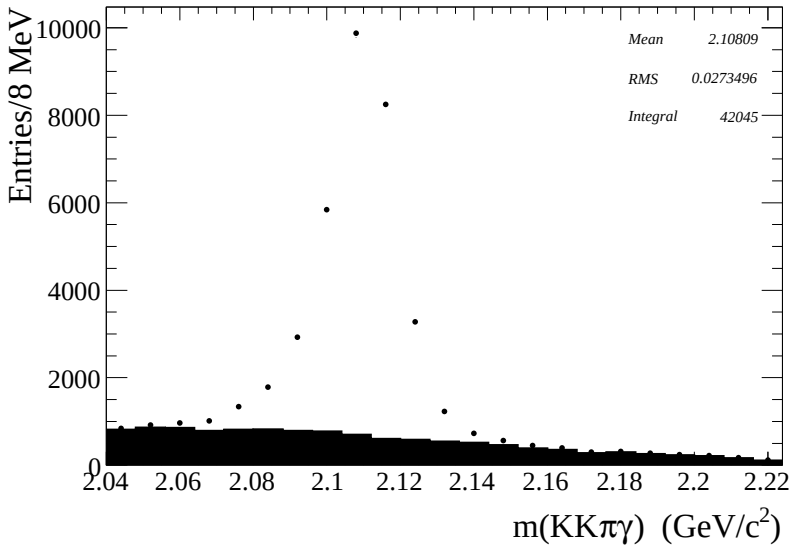

Figure A.16: Reconstructed $m(K^+K^-\pi^-\gamma)$ distribution for signal MC. The black histogram are $K^+K^-\pi^-\gamma$ candidates which are not truth-matched to a D_s^*.

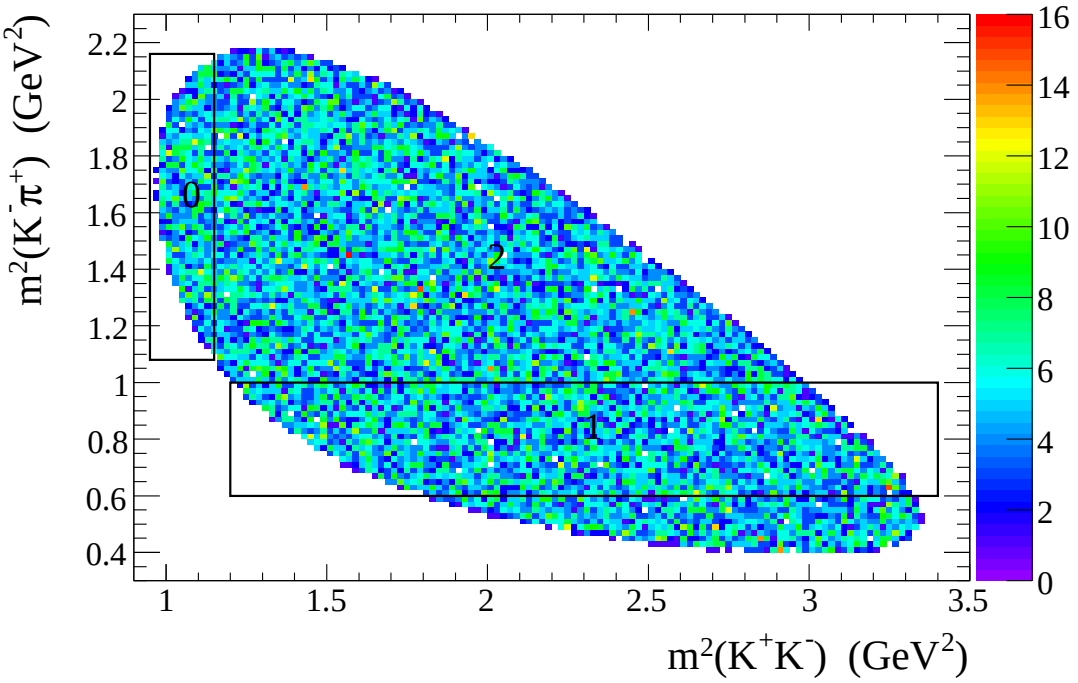

Figure A.17: Dalitz plot for truth-matched signal MC events. The boxes show the efficiency regions.

	Efficiency ($\times 10^{-4}$)
Dalitz Region 0	5.691 ± 0.144
Dalitz Region 1	5.289 ± 0.061
Dalitz Region 2	5.429 ± 0.041

Table A.3: Absolute reconstruction efficiency for each Dalitz plot region.

A.4.2 Generic Monte Carlo and Data

For the generic MC and Data samples the distribution of $K^+K^-\pi^-$ candidates remaining after the full event reconstruction are shown in Figures A.18 and A.19. In the generic MC, a the peaking background due to candidates where the signal photon does not correspond to a D_s^{*-} decay is quite large showing why the extraction of signal yield must be done using the $m(K^+K^-\pi^-\gamma)$ distribution. The Dalitz plot distributions are shown in Figures A.21 and A.21. Both the generic MC and Data most of the events are located at the $\phi\pi^-$ or $K^{*0}K^-$ regions. The distribution of D_s^{*-} candidates is shown for generic MC and Data in Figures A.22 and A.23, these distributions have not been reweighted by the reconstruction multiplicity to properly count the events.

The distribution of events after applying a weight to each candidate event to account for the reconstruction multiplicity is shown in Figures A.24 and A.23. These distributions have been fitted using the signal and background model determined in the untagged study. For the MC the signal yield is 4864 ± 64(stat) which is consistent with the true value of 4902. For the Data a signal yield of 1866 ± 40(stat) is obtained.

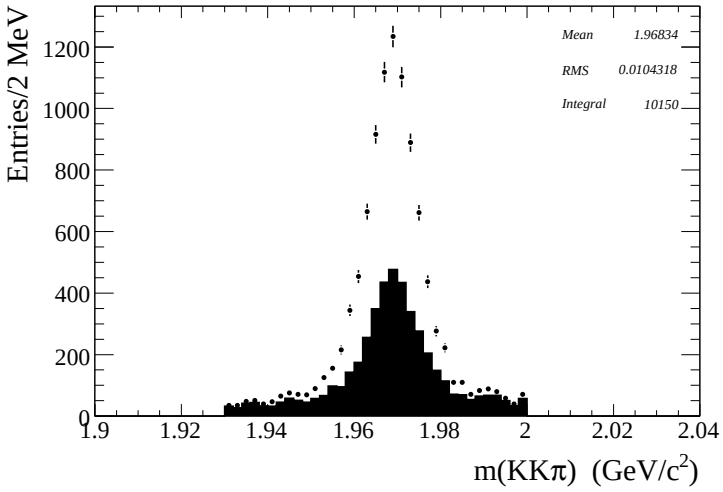

Figure A.18: Reconstructed $m(K^+K^-\pi^-)$ distribution in the generic MC sample. The black filled histogram are candidates which are not truth-matched to the full decay $D_s^{*-} \to D_s^-\gamma$ where $D_s^- \to K^+K^-\pi^-$, but includes true $D_s^- \to K^+K^-\pi^-$.

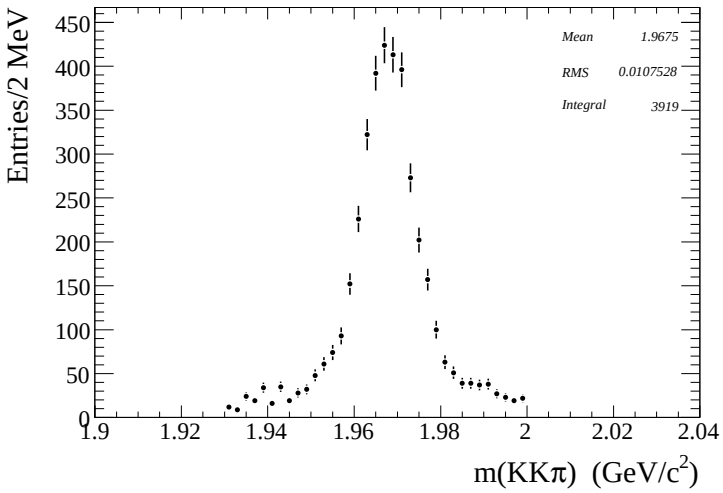

Figure A.19: Reconstructed $m(K^+K^-\pi^-)$ distribution in the Data sample.

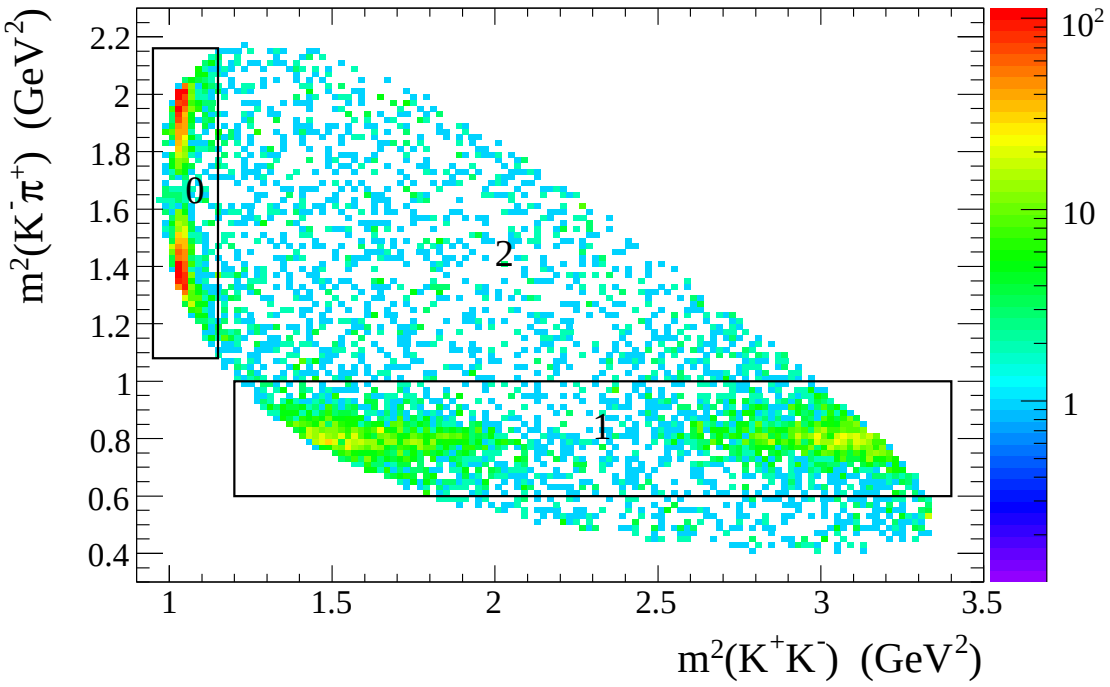

Figure A.20: Dalitz plot for generic MC. The boxes show the regions defined for the efficiency correction.

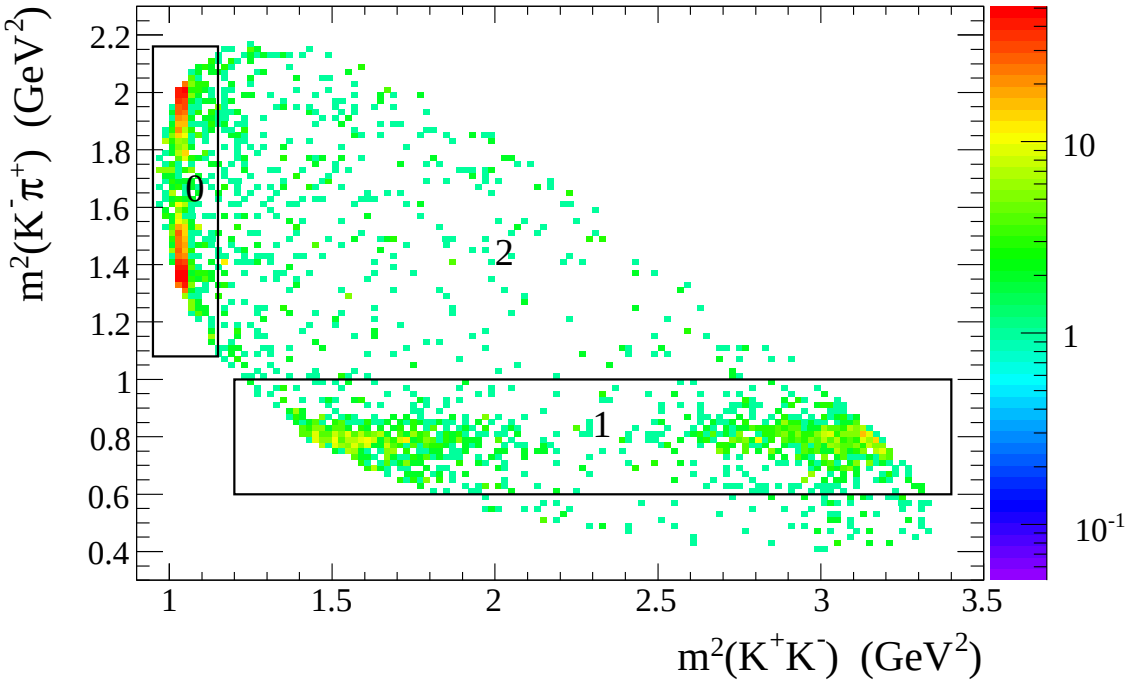

Figure A.21: Dalitz plot for Data.

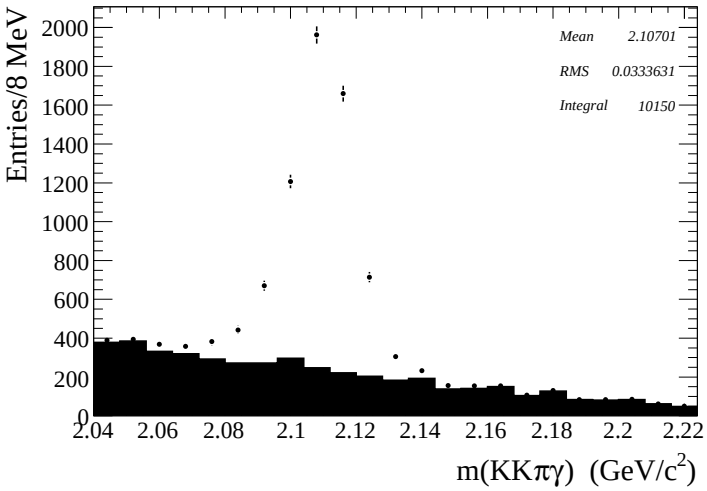

Figure A.22: Reconstructed $m(K^+K^-\pi^-\gamma)$ distribution for the generic MC sample. The black histogram are candidates which are not truth-matched to a D_s^* decay.

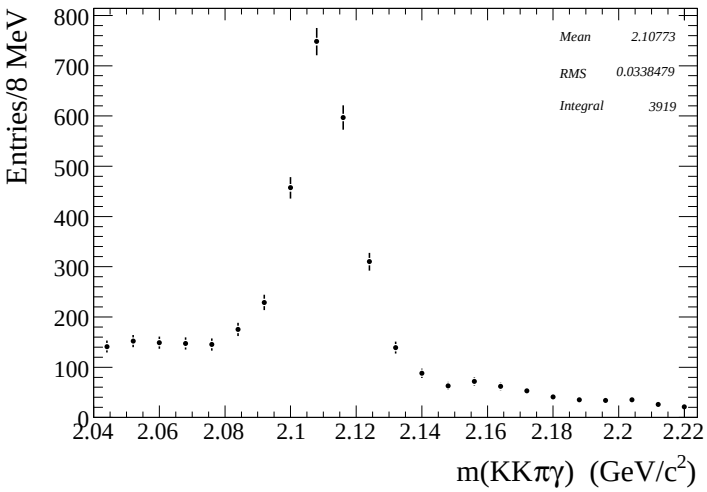

Figure A.23: Reconstructed $m(K^+K^-\pi^-\gamma)$ distribution for the Data sample. These event candidates have not been weighted for the reconstruction multiplicity.

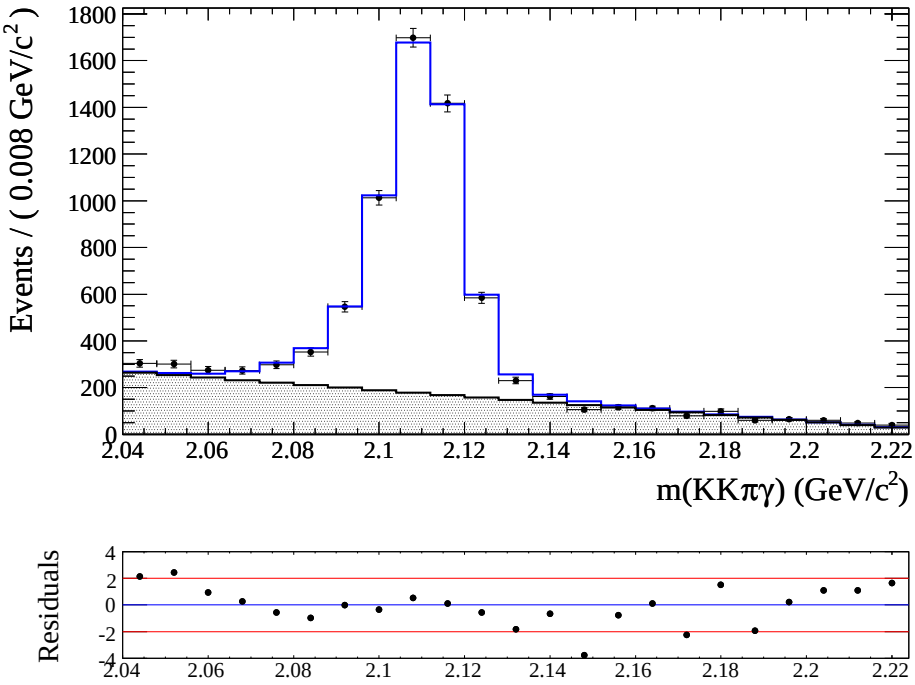

Figure A.24: Fit to the $m(K^+K^-\pi^-\gamma)$ distribution in MC.

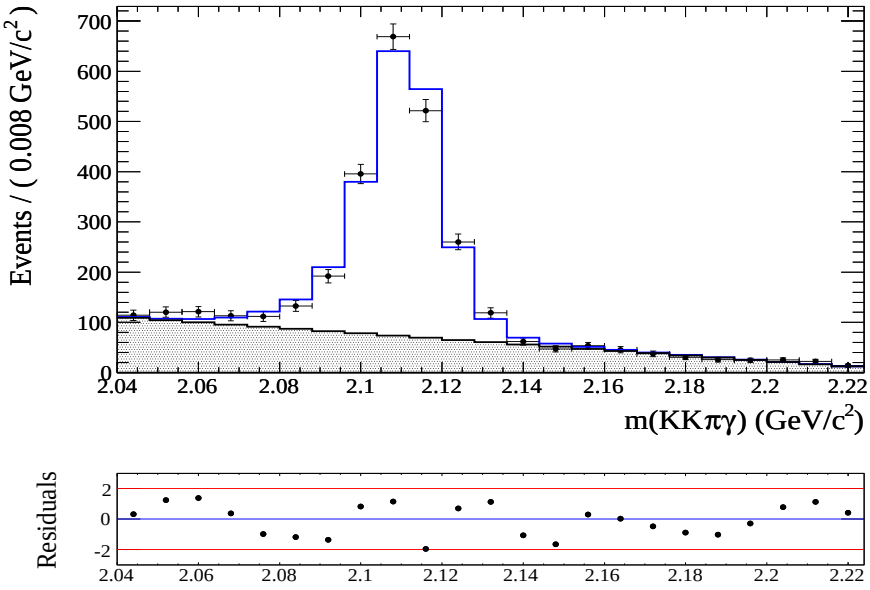

Figure A.25: Fit to the $m(K^+K^-\pi^-\gamma)$ distribution in Data.

A.4.3 Computation of the branching fraction

The calculation of the $D_s^- \to K^+K^-\pi^-$ branching fraction is performed using the same formula as was used for the leptonic decays:

$$B(D_s^- \to K^+K^-\pi^-) = \frac{N_{KK\pi}}{N_{D_s}\sum_{j=0}^{6} w_j \frac{\varepsilon^j_{KK\pi}}{\varepsilon^j_{D_s}}}$$

where $N_{KK\pi}$ is the number of $D_s^- \to K^+K^-\pi^-$ events extracted from the inclusive D_s^- sample and $\varepsilon^j_{KK\pi}$ is absolute efficiency determined using the signal MC for each value of n_X^T. The values for the efficiency ratios $\varepsilon^j_{KK\pi}/\varepsilon^j_{D_s}$ are shown in Table A.4. The efficiencies shown in this table have been corrected for the variation of the efficiency across the Dalitz plot as well as for the PID efficiency bias determined in the untagged study. The average efficiency ratio determined using the n_X^T weights determined in the inclusive reconstruction of the Data is found to be $\varepsilon = 0.295$ and the calculation of the branching fraction gives

$$B(D_s^- \to K^+K^-\pi^-) = (5.78 \pm 0.20)\%$$

The error is statistical and is obtained by propagating the statistical errors from the inclusive D_s yield and weights, their correlations are taken into account using the covariance matrix obtained from the fit. It also includes the statistical error on the $K^+K^-\pi^-$ signal yield.

As a crosscheck, a similar calculation has been performed using the signal yields obtained in the generic MC sample and the value $\mathcal{B}(D_s^- \to K^+K^-\pi^-) = (6.28 \pm 0.16)\%$ obtained agrees with the true value of 6.04% used in the generation of the MC.

A.4.4 Systematic Uncertainties

Systematic uncertainties for this measurement arise from the uncertainties on the determination of the inclusive D_s^- yield, the fit for the $D_s^- \to K^+K^-\pi^-$ signal events and the efficiency determination. The determination of the uncertainties on the inclusive D_s^- yield and the n_X^T weights has been described in chapter 5 and these uncertainties have been propagated into the $D_s^- \to K^+K^-\pi^-$ branching fraction as listed in the first 7 items in Table A.5. Systematic uncertainties due to the background and signal model used in the extraction of the $D_s^- \to K^+K^-\pi^-$ signal events, also listed in the table, have been estimated by changing the background model to a second order polynomial and by varying the signal PDF by the error on the nominal D_s^{*-} mass. Finally, systematic

uncertainties in the determination of the reconstruction efficiency for this mode have been estimated. The only two sources of uncertainty, after performing the untagged study, are from possible differences in track reconstruction efficiency which have been estimated at the level of 0.5% for the three tracks. Also, a correction needed to be applied due to the PID efficiency differences, the uncertainty on this correction factor is assigned as a residual uncertainty per Kaon. The overall systematic uncertainty remains at about 5% which was the goal in this measurement.

Table A.4: Efficiency ratio for each n_X^T value. The errors are due to the statistics of the signal MC sample.

n_X^T	$\varepsilon_{KK\pi}/\varepsilon_{D_s}$
0	0.377 ± 0.007
1	0.339 ± 0.004
2	0.301 ± 0.004
3	0.265 ± 0.004
4	0.241 ± 0.005
5	0.214 ± 0.006
6	0.140 ± 0.007

Table A.5: Summary of systematic uncertainties for the $D_s^- \to K^+K^-\pi^-$ branching fraction.

Systematic	**Difference in the B.F. (x10^{-2})**	**Difference/Nominal**
WS n_X^T weights	(-0.061,+0.000)	(-1.053,+0.000)%
RS n_X^T weights	(-0.001,+0.000)	(-0.018,+0.002)%
D_s Signal Shape	(-0.085,+0.085)	(-1.467,+1.467)%
Peaking Backgrounds	(-0.100,+0.102)	(-1.735,+1.765)%
Background Model	(-0.016,+0.010)	(-0.269,+0.167)%
n_X Resolution	(-0.052,+0.049)	(-0.906,+0.847)%
Signal Photon Backgrounds	(-0.206,+0.220)	(-3.570,+3.811)%
KKπ Background Model	(-0.040,+0.040)	(-0.700,+0.700)%
KKπ Signal Model	(-0.017,+0.017)	(-0.300,+0.300)%
KKπ Tracking Efficiency	(-0.029,+0.029)	(-0.510,+0.510)%
KKπ PID Efficiency	(-0.128,+0.128)	(-2.220,+2.220)%
Total	**(-0.29,+0.30)**	**(-5.07,+5.13)%**

Bibliography

[1] Complex conjugate modes are implied throughout this document unless otherwise stated.

[2] M. Peskin and D. Schroeder, *An Introduction to Quantum Field Theory*, Westview Press (1995).

[3] J. Bordes, J. Penarrocha, and K. Schilcher, JHEP 0511, 014 (2005).

[4] A. Ali Khan *et al.* (QCDSF Collab.), Phys. Lett. B **652**, 150 (2007).

[5] E. Follana *et al.* (HPQCD and UKQCD Collabs.), Phys. Rev. Lett. **100**, 062002 (2008).

[6] C. T. H. Davies *et al.* (HPQCD Collab.), arXiv:1008.4018 (2010).

[7] A. Gray *et al.*, Phys. Rev. Lett. **95**, 212001 (2005).

[8] M. Artuso *et al.*, (CLEO Collab), Phys. Rev. Lett. **99**,071802 (2007).

[9] P. U. E. Onyisi *et al.* (CLEO Collab.), Phys. Rev. D **79**, 052002 (2009).

[10] J. P. Alexander *et al.* (CLEO Collab.), Phys. Rev. D **79**, 052001 (2009).

[11] B.I. Eisenstein *et al.* (CLEO Collab.), Phys. Rev. D **78**, 052003 (2008).

[12] K. Abe *et al.* (Belle Collaboration), Phys. Rev. Lett. **100**, 241801 (2008).

[13] B. Aubert *et al.* (*BABAR*Collab.), Phys. Rev. Lett. **98**, 141801 (2007).

[14] A. Heister *et al.* (ALEPH Collab.), Phys. Lett. B **528**, 1 (2002).

[15] G. Abbiendi *et al.* (OPAL Collab.), Phys. Lett. B **516**, 236 (2001).

[16] HFAG (Collab. 2009),
http://www.slac.stanford.edu/xorg/hfag/charm/PIC09/f_ds/results.html

[17] K. Nakamura *et al.* (Particle Data Group), *Review of Particle Physics*, Journal of Physics G 37, 075021 (2010).

[18] B. A. Dobrescu and A. S. Kronfeld, arXiv:0803.0512 (2008).

[19] A.G. Akeroyd and C.H. Chen, Phys. Rev. D **75**, 075004 (2007).

[20] H. E. Haber, G. L. Kane and T. Sterling, *The Fermion Mass Scale and Possible Effects of Higgs Bosons On Experimental Observables*, Nucl. Phys. B **161**, 493 (1979).

[21] J. F. Donoghue and L. F. Li, *Properties of Charged Higgs Bosons*, Phys. Rev. D **19**, 945 (1979).

[22] T. P. Cheng and M. Sher, *Mass Matrix Ansatz and Flavor Non Conservation in Models with Multiple Higgs Doublets*, Phys. Rev. D **35**, 3484 (1987).

[23] I. Dorsner *et al.*, arXiv:0906.5585v2 (2009).

[24] "PEP-II: An Asymmetric B Factory", Conceptual Design Report, SLAC-R-418 (1993).

[25] B. Aubert *et al.* (*BABAR* Collaboration), Nucl. Instrum. Methods Phys. Res., Sect. A **479**, 1 (2002)

[26] W. Menges, IEEE Nuclear Science Symposium, Picataway, NJ, Conference Record **5** p.1470 (2006).

[27] R. Frühwirth, *Application of Kalman Filtering to Track and Vertex Fitting*, Nucl.Instr. and Meth. A **262**, (1987) 444.

[28] Thomas G. Dietterich and Ghulum Bakiri, *Solving Multiclass Learning Problems via Error-Correcting Output Codes*, Journal of Artificial Intelligence Research 2, p.263 (1995).

[29] I. Narsky,*Optimization of Signal Significance by Bagging Decision Trees*, arXiv:physics/0507157

[30] D.J. Lange, Nucl. Instrum. Methods A **462**, 152 (2001).

[31] T. Sjostrand, Computer Physics Commun. **82**, 74 (1994).

[32] S. Agostinelli *et al.* (GEANT4 Collab.), Nucl. Instrum. Methods A **506**, 250 (2003).

[33] E. Richter-Was, Phys. Lett. B **303**, 163 (1993).

[34] L. Lyons, D. Gibut, P. Clifford, Nucl. Instrum. Methods A **270**, 110 (1988).

[35] J. P. Alexander *et al.* (CLEO-c Collab.), Phys. Rev. Lett. **100**, 161804 (2008).

[36] S. Godfrey and N. Isgur, Phys. Rev. D **32**, 189 (1985).

[37] A. Falk and M. Peskin, Phys. Rev. D **49**, 7 (1994).

[38] G. Breit and E. Wigner, Phys. Rev. D **49**, 519 (1935).

[39] B. Aubert *et al.* (*BABAR* Collaboration), Phys. Rev. D **79**, 112004 (2009).

[40] K. Abe *et al.* (BELLE collaboration), Phys. Rev. D **69**, 112002 (2004).

[41] P. F. Harrison and H. R. Quinn, The BaBar Physics Book, SLAC-R-504 (1998).

[42] J. Blatt and V. Weisskopf, Theoretical Nuclear Physics, John Wiley & Sons Inc. (1952).

[43] V. P. Zrelov, Cherenkov Radiation In High-Energy Physics, Israel Program for Scientific Translations Ltd. (1970).

[44] J. Benitez *et al.*, Development of a Focusing DIRC, SLAC-PUB-12236 (2006).

[45] C. Field *et al.*, Status of the Fast Focusing DIRC, Nuclear Instruments and Methods in Physics Research A **553**, 96 (2005).

[46] Made by Advanced Laser Diode Systems, D-12489, Berlin, Germany (www.alsgmbh.com/pilas.htm).

[47] J. Benitez *et al.*, Development of a Focusing DIRC, 2006 IEEE Nuclear Science Symposium Conference Record (2006).

J. Benitez *et al.*, Status of the Fast Focusing DIRC, Nuclear Instruments and Methods in Physics Research A **595**, 104107 (2008).

[48] K. Yarritu, S. Spaniard, J. Va'Vra, Photon Background in DIRC Fused Silica Bars, DIRC internal group note #141 (2001).